PHOTODISSOCIATION AND O(^{1}D) REACTIONS OF NITROUS OXIDE

A Dissertation

Presented to the Faculty of the Graduate School

of Cornell University

in Partial Fulfillment of the Requirements for the Degree of

Doctor of Philosophy

by

Onur Tokel

August 2011

PHOTODISSOCIATION AND O(^{1}D) REACTIONS OF NITROUS OXIDE

Onur Tokel, Ph.D.

Cornell University 2011

The focus of this dissertation is on the application of the velocity map imaging (VMI) technique to photodissociation and reaction dynamics. The multiplexing advantage of the VMI technique enables us to gather both angular and translational energy distributions simultaneously, with product quantum mechanical state selectivity.

The first part of the thesis focuses on the ion-imaging experiments investigating the 130 nm dissociation of N_2O and spectroscopic studies of its reactions with O(^{1}D). The results are explained in conjunction with Hopper's *ab initio* MCSCF calculations in the linear and bent configurations. Our analysis provide the spin-orbit ratios, relative branching ratios and β anisotropy parameters. We study the NO product channel of the O(^{1}D)+N_2O reaction with REMPI techniques and provide the first analysis of the rotational distribution of this channel. We will conclude the discussion of the full and half reactions of the N_2O molecule by explaining the observed bimodal vibrational distribution in the NO channel.

The second part focuses on the design and development of a dual-beam apparatus for the application of the VMI technique to reaction dynamics in a state-selective manner. We provide the ion-optics design considerations and ion trajectory simulations for satisfying the VMI conditions. Furthermore, a delayed extraction scheme will be described which will be important in future state-selective dual-beam VMI studies, allowing the critical low background environments for these type of experiments.

BIOGRAPHICAL SKETCH

The author was born in Trabzon, Turkey in 1980. He moved to Izmir to attend Izmir Science High School (IFL), where he developed strong interest in the physical sciences. He entered Bilkent University, Ankara majoring in Electrical Engineering. There he studied electronics and physics. He spent a year at the ALS photonic crystals lab as an undergraduate researcher. His senior thesis was about the fundamental limits in optical interconnections.

After college, he began his graduate studies at Cornell University and soon after he joined Prof. Paul Houston's research group there. His research focused on the photodissociation and $O(^1D)$ reactions of nitrous oxide and on the development of a dual-beam apparatus for the application of velocity map imaging technique to reaction dynamics. He helped setting up the Houston Lab at Georgia Institute of Technology, Atlanta after moving the laboratory from New York.

To my family

ACKNOWLEDGEMENTS

I was influenced by many people throughout my education. I should first thank to my mother and father, Bircan and Zekai Tokel, without whom I wouldn't be this person. My brother, Çağlar, also taught me a lot.

This thesis benefited from a number of people with excellent qualities. Mark Lambert's impressive knowledge of every aspect of the lab was very valuable at the beginning of my graduate career. His help on aligning lasers, experimental planning, setting up optics and various setups was extremely helpful. I worked very closely with Clarice (Clare) Kelleher and Jun (Jack) Chen during the development of the dual beam apparatus, both at Cornell and later at Gatech. During the days (and nights) we spent together, I appreciated their resilience, creativity and enthusiasm as great scientists. I can not overestimate their contributions to this thesis. I wish them best of luck.

During the Cornell years, we hold joint group meetings with the Davis Group. These lively meetings provided insightful analysis and comments on our progress. I would like to thank the other members of both Davis and Houston groups for their useful comments especially on these meetings. Also, I would like to thank Prof. Davis and Prof. Rana for being helpful and encouraging special committee members.

I am indebted to Prof. Houston for his invaluable role he played as my advisor. His critical and timely comments, scientific guidance and support made the graduate school experience enjoyable and worthwhile. I have great respect for him both scientifically and personally. Thanks Paul.

Lastly, I would like to thank a number of friends, some of whom I know since high school, who made the PhD years much more enjoyable and meaningful for me. Özhan Özatay, my long time room mate was always interesting company. Ekin

Kocabaş, Özden Yalçın, Mustafa Özuysal, Aslı Ayaz, Tuğba Bağcı, Tayfun Gürel, Gökhan Arıkan, Serhan Ardanuç, Ömer İlday, Artun Alparslan, Cenk Ural, Ömer Hançer, Nancy Fidyk and Nevce Gürkan were all very supportive and helpful in various stages. I hope we continue our interaction with all these people.

There is no wild charisma in physics, but honest carpentry.

-Attributed to *Hans Bethe* [a]

[a] I heard this quote from Prof. Ambegaokar at a lecture. Along the same lines, R. N. Zare tells us, the best advice given to him is that "the equation for success is the integral of ability over time. Even the most talented scientists have to work hard."

TABLE OF CONTENTS

LIST OF TABLES

LIST OF FIGURES

CHAPTER 1

INTRODUCTION

Light has a special place in our relation to the world. In our attempts to understand the universe from the macroscopic to the microscopic phenomena, we find light as a subject of interest in itself and simultaneously as a tool to manipulate and gather information. Newton's *Opticks* was an attempt to understand the light as a particle. Maxwell's unification of electric and magnetic fields in the 19^{th} century let us understand the light as a wave phenomenon. Perhaps, it is no coincidence that the last big unsolved problems of physics at the beginning of 20^{th} century, the Michelson-Morley experiment and the blackbody radiation, were puzzles about light. The first puzzle led to the development of special relativity and the second led to the development of quantum mechanics.

In the context of molecular physics, the most natural question to ask is, what happens when light interacts with a molecule or atom. In the case of a molecule, does it fall apart, if so, what products does it create? What are the angular and velocity distributions of these products? What internal energies do these products have? What are the dynamical details of the event?

As for using the light as a "manipulator", one can think of colliding these photolysis products with some target molecules and then asking the same questions for the products of the collision processes. To gather information, we again turn to light: It is a perfect analogy to think of the probe light as fingers on a hand. The thickness and the type of fingers can be thought as the bandwidth and wavelength of light. In any experiment, these properties let you probe the scalar or vector properties that you are after.

While, conceptually, the preceding two fields of photodissociation events and bimolecular reactions, seem disjoint at first, the wave packet theories establish a direct link between them. It can be shown that electronic absorption and emission spectroscopy, probing tools in photodissociation events, are in fact resonance phenomena resulting from the recurrences in the wave packet behavior.[1,2] Even if resonances in reactive scattering are rarely seen experimentally, they have the same origin, in terms of the wave function behavior. From this perspective, the photodissociation event can actually be used to gain selective access to a reactive potential energy surface, in particular, to the transition state region, where much of the fate of the dynamics is decided. This is why sometimes we call photodissociation, a "half-collision" event.

The development of the experimental study of these fields follows two main parallel paths. The Ion-Imaging Experiments now set the standard for photodissociation experiments, in which the whole event can be "seen" at once with the ability of internal energy selectivity. The Crossed Molecular Beam Experiments with universal detection schemes are the main method for studying reactions. The measurements of crossed molecular beam experiments are done by rotating the detector around the lab. They result in a wealth of information about the reaction, even with the limitation of not knowing the internal energies of the reaction products, since a state selective method is not used.

It is both conceptually and aesthetically appealing that these two experimental methods are coming together now. The Velocity Map Imaging Method is starting to be applied to image the state selected products of reactive collisions with well defined initial velocities. In a way, the experimental duality of photodissociation and reactive collisions are being resolved by a direct experimental link in between,

a hybrid of them if you will, which lets you see the relation between these two types of experiments.

The state selectivity in reactive collisions comes at a price: The use of lasers to ionize the reaction products at a specific quantum state results in a small number of ions, compared to a photodissociation event. This limits the experimentalist, and sometimes unskimmed molecular beams are used to increase the signal, only to cause low beam quality and less resulting information. One strategy to increase the signal would be to increase the laser intensity initiating the reaction. Even in high vacuum, this will result in an increased background, which is a very important drawback considering the small signal. To circumvent this background problem, we devised an electrode pulsing scheme for the ion optics in a dual-beam setup, which will be detailed later.

To put how the types of experiments come together in a context, we need to look at these two fields in more detail.

1.1 Photodissociation Experiments

The earlier development of "molecular rays" by Otto Stern allowed researchers to create atoms and molecules with well defined velocities. This method was later improved by expanding the sample gas in vacuum, resulting in rotationally and vibrationally cold states. Around 1950s, the method of flash photolysis allowed our initial probing of the dynamics in the gas phase.[3] In 1969, Busch et al.[4] and Diesen et al.[5] almost simultaneously developed photofragment translational spectroscopy, which allowed the first measurements of velocity distributions of photofragments. They dissociated a target prepared in a molecular beam with a linearly polarized ruby laser and detected the products with electron-impact ionization. The arrival

times of these products then could be converted to center-of-mass velocities. The detection method did not have state selectivity but it was sensitive and universal and resulted in a wealth of information. Their method allowed angular measurements of the products as well, by rotating either the detector or the polarization of the laser. But important technological developments were on their way.

At the end of 1970s, the tunable wavelength dye lasers became available. The control on the wavelength of the laser allowed one to probe internal quantum mechanical energies of molecular or atomic products of photolysis or bimolecular reaction events, such as rotational, vibrational, electronic or spin-orbit interaction energies. This freedom soon resulted in several tools such as LIF (Laser Induced Fluorescence)[6], REMPI (Resonance Enhanced Multi Photon Ionization)[7] and CARS (Coherent Anti-Stokes Raman Spectroscopy)[8], which allowed population distribution measurements in these states. These techniques depend on the absorption of light by the product in a single quantum mechanical state.

Combining REMPI and LIF techniques with Doppler spectroscopy allowed the first measurements of velocity distributions with quantum state selectivity. The Doppler effect is well known in our daily life. The sound of a fast moving ambulance comes at a higher frequency as it approaches. This effect for sound waves, first found by Christian Doppler in 1842 turned out to be valid for light waves as well. Armand Fizeau in 1848 first noted that the light frequency absorbed by the product is $\nu_{abs} = \nu_0[1 \pm (v/c)]$, where v is the projection of the recoil velocity on the probe laser direction, c is the speed of light and ν_0 is the absorption frequency at rest. It can be shown that the lineshape of the probe absorption will be a function of this 1-D velocity projection.[9] From the observed signal, then one can reconstruct the velocity distribution in the center-of-mass frame. Two different initial distributions

can have similar probe lineshapes, so interpretation needs care. A variant of the method, with time of flight spectrometer and the core-sampling allowed Ogorzalek and coworkers to measure anisotropic angular distributions of the I or CD_3 products from the 266 nm photodissociation of CD_3I.[10]

To extend these techniques one needs a 2-D projection of the velocity distribution. This was possible by another technological advance, i.e. development of microchannel plate detectors and charge coupled device (CCD) cameras, in the mid-1980s. The first ion imaging experiment was done by D. W. Chandler and P. L. Houston in 1987.[11] They imaged the $CH_3(v{=}0)$ products from photolysis of CH_3I by 266 nm photolysis light. The state selective sampling was done by 2+1 REMPI and the resulting ion cloud accelerated through a TOF mass spectrometer to impinge on a position sensitive detector. The technique provided angular and velocity distribution at the same time. State selectivity constrained the energetics in a way to get information on the unobserved photolysis products.

After this initial ground breaking work, the improvements on the technique allowed the reconstruction of full 3-D velocity distribution in the center-of-mass frame. A mathematical method called inverse Abel transform, can directly reconstruct the ion cloud after the photolysis event, from the projected image. This method requires cylindrical symmetry in the product distribution and absence of alignment in the products, i.e. $J = 0$ and $J{=}1/2$. [a] Development advanced inversion algorithms continues, but we have very stable algorithms available. pBasex program uses polar basis functions to fit the image, while accumulating the noise to the center of the image, whereas Basex program uses well behaved gaussian

[a] If there is any "alignment" in the product, either a combination of detection geometries in the lab frame is used or forward convolution algorithms are used to analyze the image. An initial distribution is guessed and iterations are repeated until satisfactory agreement with the image is attained.

functions as basis functions, while accumulating the noise on a central line.[12,13] Both programs find wide usage.

Another very important advance came with The Velocity Mapping technique. In the earlier experiments, no correction was done to circumvent the blurring problem resulted from the fact that the interaction area of the laser and molecular beam is finite. This caused ions created with the same velocities at slightly different positions hit on different positions on the detector, causing some blurring in the image. In 1997, Eppink and Parker added an Einzel lens to focus these ions to the same position on the detector.[14] This allowed removing the grids used in the previous experiments in the acceleration region, letting even lower ion densities to be detected. Obviously this focusing, just like adjusting the objective lens on a photography camera, allowed the images to be sharper and contain more information.

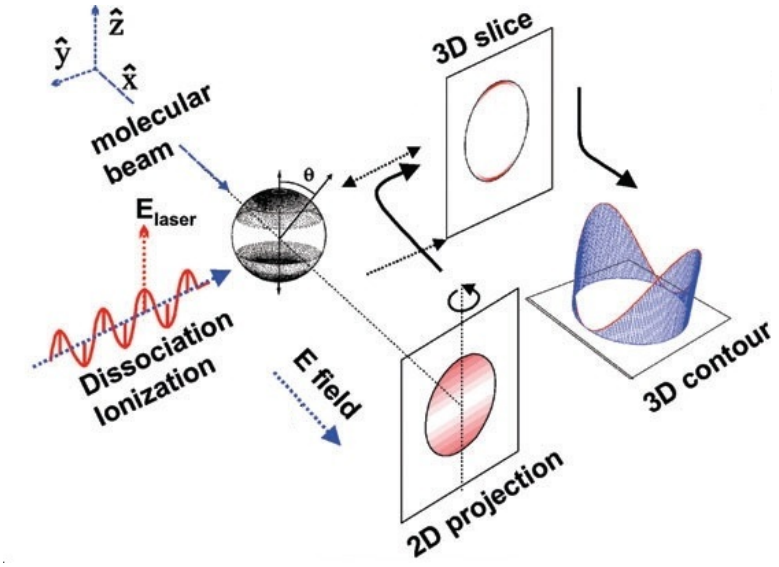

Figure 1.1: Photodissociation with linearly polarized light. The ion cloud is expanded through the ion optics in an electric field. The pancaked ions onto the detector are recorded by a computer and then reconstructed to give the nascent distribution in the center-of-mass frame. Adapted from reference[15].

Another improvement in the resolution came by making the detection step smarter, by analyzing the pixels on the CCD at each laser shot. For each ion hitting on the detector, 5-10 pixels were excited on the camera. Selecting the center of these pixels and recording in real time, resulted in higher resolution in the final ion counted image. Chang et al. implemented the technique in 1998, named Ion-Counting.[16]

Figure 1.1 shows the imaging experiment concept. The recent advances in experiments provided an alternative to the reconstruction step in the analysis stage. A. G. Suits and coworkers, in 2003 showed that the thin central slice of this ion cloud can be measured experimentally preserving the velocity mapping condition, so the reconstruction step can be bypassed.[17] They added extra electrodes in the ion optics, so that the ion cloud expanded more than the conventional spread size. Using a fast gated detector allowed selecting the central part of the ion cloud, which is a good approximation to the actual 3-D distribution. This removes the constraints of cylindrical symmetry or no alignment from the preceding reconstruction algorithms. Other methods for slicing the ion cloud also exist and are being improved such as optical slicing, pulsed slicing and Doppler Slicing.

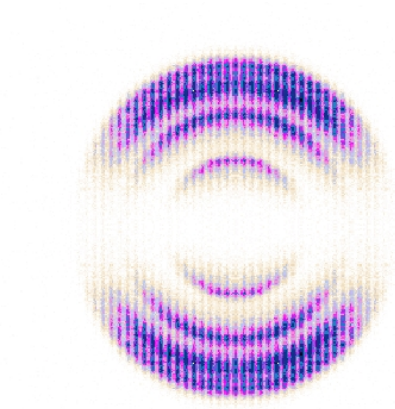

Figure 1.2: Imaging O(^{1}D) atoms from ozone dissociation at 266 nm.

Figure 1.2 shows the type of images we get from photodissociation experiments. The image shows the raw image of O(^{1}D) atoms detected by 2+1 REMPI processes after dissociating ozone molecules in a molecular beam with 266 nm laser light. One can see four rings with anisotropic angular distributions, corresponding to vibrational quanta in the O_2 cofragment. The radius of these rings are directly proportional to the speed O(^{1}D) atoms. The rings identify the unmeasured O_2 fragments internal energies from the conservation of angular momentum and energy, so the energetics of the photolysis event will be well defined.

The angular distributions of these rings contain another kind of information, which is a special case of so called vector-correlations. The angular distribution is given by,[18]

$$I(\theta) = (1 + \beta P_2 cos(\theta))/4\pi \tag{1.1}$$

In this equation θ is the angle between the polarization of the photolysis laser and the recoil velocity in the lab frame as shown in Figure 1.1, β is the anisotropy parameter and $P_2(x)$ is the second Legendre polynomial ($P_2(x) = (3x^2 - 1)/2$). β is a measure of the anisotropy, which takes values between -1 and 2. The limiting values correspond to simple sine and cosine squared distributions, corresponding to the case of prompt dissociation. The intermediate β values, i.e. β close to 0, would indicate a longer lifetime compared to the rotational period in the intermediate. [b]

We should note that other correlations exist between the following relevant vectors in the photolysis event: Product angular momentum **J**, recoil velocity **v** and transition dipole moment of the parent molecule, $\boldsymbol{\mu}$. These quantities come

[b] β can also take values around 0, if there are overlapping transitions or if there is alignment in the intermediate state. In that case, higher order terms in the angular distribution should be taken into account. In the experiments involving data in Figure 1.2, this was the case, so the analysis required a full quantum mechanical treatment, to extract the O(^{1}D) $|m_J|$ populations corresponding to different vibrational states of $O_2(^1\Delta_g)$ cofragments.

with a sense of directionality attached to them so correlations among them, namely $\boldsymbol{\mu}$-**J** , $\boldsymbol{\mu}$-**v** and **v**-**J** vector correlations, give us information about the geometry and forces at the dissociative state.[19]

The interplay between theory and experiment helps to identify the mechanisms and responsible channels in photodissociation events. A recent example involves the use the VMI technique together with new electronic structure and dynamics calculations by Schinke and coworkers.[20] The $O(^3P_J)$ images from deep UV dissociation of ozone show a broad peak maximum around 2 eV corresponding to vibrational states $v \approx$ 10-15 in the $O_2(^3\Sigma_g^-)$ cofragment. $O(^3P_J)$+$O_2(^3\Sigma_g^-)$ channel constitutes about 10% of this photolysis event. Classical surface hopping trajectories show transition from the B state to the R state about 10% of the time and is attributed to this feature observed in the images. However, at around 233 nm an additional sudden sharp peak starts to be observed. Previously, this feature had been attributed to the $O(^3P_J)$+$O_2(^3\Sigma_g^-)$ channel with O_2 forming in $v \geq$26.[21] An alternative explanation is suggested now in light of the simulations on the newest constructed surfaces.[c] They predict that the trajectories correlate to the Herzberg channels ($O(^3P_J)$+$O_2(A'\ ^3\Delta_u)$ and $O(^3P_J)$+$O_2(A^3\Sigma_u^+)$) about 4% of the time, corresponding to the extremely low energy products observed in the $O(^3P)$ images. This phenomena is described graphically in Fig. 1.3.

The energy threshold for opening these channels (234.1 nm for $O_2(^3\Delta_u)$ forming channel) coincide with the sudden onset (near 234.5 nm) of the experimental observation of these peaks. In addition to the two preceding observations, there is a good fit between the measured and calculated peak edge positions, assuming that

[c]They used adiabatic surfaces in which exact final populations in the Herzberg states can not be obtained. For this purpose, truly diabatic surfaces which asymptotically correlate to each channel individually are required. Such a construction including a multitude of curve crossings is currently impracticable.[20]

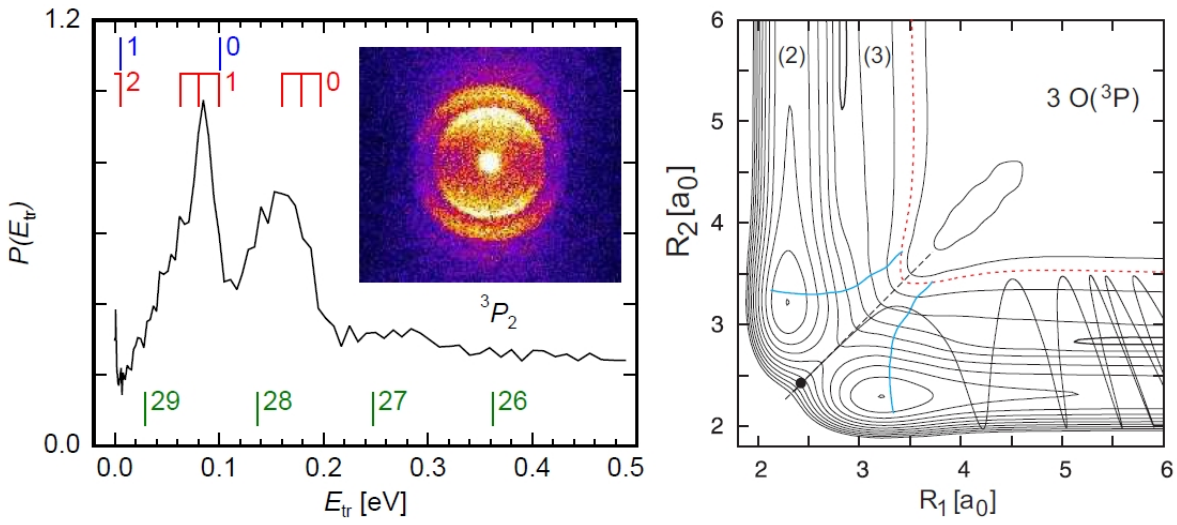

Figure 1.3: The inset in the left figure shows the low translational energy part of the $O(^3P_2)$ image taken from the 226 nm dissociation of ozone. The corresponding translational energy distribution from the image is shown in the left figure. The red and blue combs show the expected position of the peaks from the Herzberg channels whereas the green comb shows the positions for the $O_2(X)$ channel assigned previously. The figure on the right shows a sample trajectory leading to one of the Herzberg channels, indicated with (3) in the figure, as opposed to the dominant $O(^1D)$ channel, indicated with (2). Figure taken from reference[20].

the slow products are forming in the Herzberg channels. All these reasons taken together provide convincing evidence that these channels are good candidates for the explanation of this phenomena.

According to the dynamics simulations, after starting at the Franck-Condon region, indicated with the black dot in the figure, the trajectories first make a symmetric stretch motion and later are deflected to the dissociation channel. Most of the energy is in the vibration so the dissociation is slower compared to the main reaction channel.

1.2 Crossed Molecular Beam Experiments

The field of reaction dynamics studies the motions of atoms after a reactive encounter of atoms or molecules. Since many electrons and nuclei are moving at the same time during any collision event, it is necessary to simplify the problem, to be able to make predictions about the outcome. The solution came with the Born-Oppenheimer approximation in the 1930s, which assumes the motion of the nuclei is slow and therefore separate from the rapidly rearranging electrons.

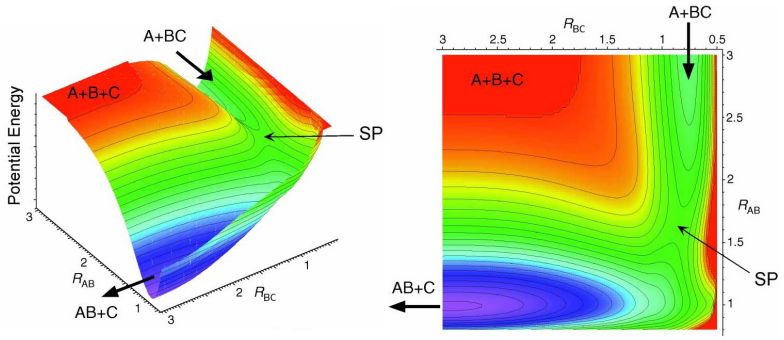

Figure 1.4: Two views of a hypothetical potential energy surface. Figure taken from reference.[22]

This allowed theoreticians to calculate realistic topological structures which govern the motion of atoms. [d] Figure 1.4 illustrates the potential energy surface (PES) concept. The collision of an atom A with a molecule BC is imagined to take place in a collinear geometry. R_{AB} and R_{BC} are bond lengths and the contours show the potential energy surface over which the reaction takes place. The reactants enter the PES from one side and exit from the other. The dynamics of their rearrangement is analogous to a marble rolling on a surface having the same

[d] It is somewhat ironic that this approximation served so well in calculations when one remembers Oppenheimer's complaints about the troubles in calculating anything in 1933: "As you undoubtedly know, theoretical physics- what with the haunting ghosts of neutrinos, the Copenhagen conviction, against all evidence, that cosmic rays are protons, Born's absolutely unquantizable field theory, the divergence difficulties with the positron, and the utter impossibility of making a rigorous calculation of anything at all - is in a hell of a way." [23]

topology. Since atoms obey the rules of quantum mechanics, one can imagine rolling a drop of water on a similar surface, instead of a marble, to bring the analogy closer to the true atomic behavior. One should remember that there can be multiple surfaces with different characteristics available reaction. Their combined effect determines the products.

From an experimental point of view, one would want to watch the reaction take place during the event. This approach is conceptually appealing but the lasers used to probe those time scales turn out to have "thick fingers" so the interpretation of the data is not straightforward, lacking spectroscopic information for loosely bound systems. [e] Another method is to watch what happens after the event takes place, which is the path we follow.

Initial experiments in the 1960s studied high yield alkali reactions. In the late 1960s, the field started developing rapidly in the Herschbach lab. Y. T. Lee led the development of a machine with sophisticated mass spectroscopy and J. Fenn and J. Anderson initiated the use of supersonic molecular beams in this machine. They installed two molecular beams crossing each other and the reaction products created at their intersection were detected by rotating a universal mass spectrometer inside a vacuum chamber. The detector was insensitive to internal energy of the detected products but some reactions allowed them to resolve angular scattering of different vibrational levels.

In 1980s these type of experiments were matured enough to generate the iconic flux data of HF(v) products from the reaction of F + H_2, shown in Figure 1.5.[24] The HF products as a function of the scattering angles are visible. (More specifically,

[e]This approach was possible to follow with the advent of femtosecond lasers and resulted in a new field, femto-chemisty. The work of A. Zewail and his coworkers was awarded a Nobel Prize in 1999.

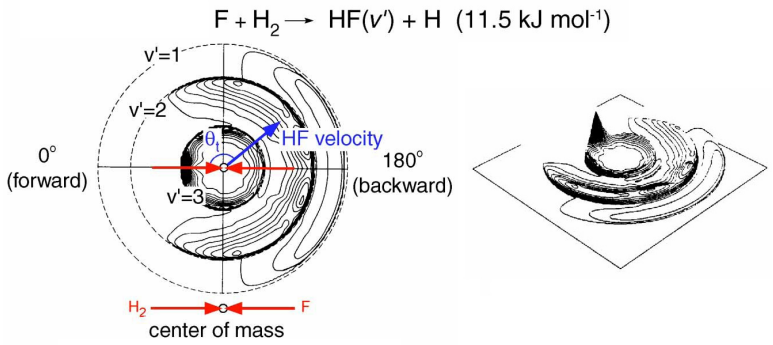

Figure 1.5: The flux of HF molecules recoiling at different CM angles. The dashed curves show the maximum available velocities at the labeled internal HF energies. Figure taken from reference.[22]

Differential Cross Section or Flux-Velocity Plots are the reported quantities in these experiments) This reaction became a benchmark for all crossed beam experiments. And the work of Y. T. Lee and D. R. Herschbach culminated in a Nobel Prize in 1986, shared with J. C. Polanyi.

A well studied system with this method is the reaction H + H_2 and its isotopic variants. Skodje and coworkers have studied the H + HD → D + H_2 reaction in a crossed-beams setting.[25] The D atom center-of-mass product contour plot from the reaction is shown in Figure 1.6.

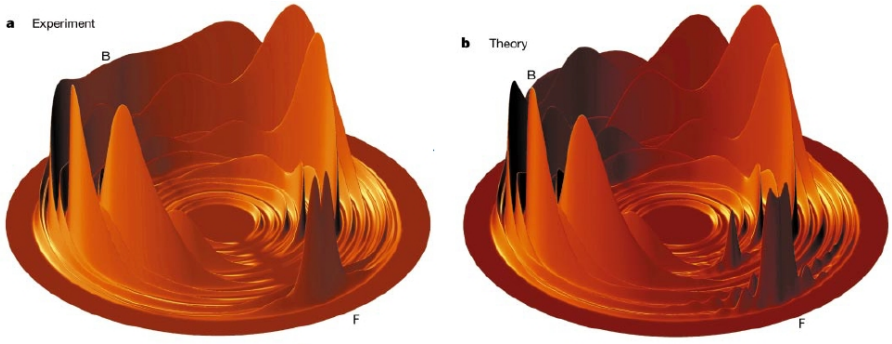

Figure 1.6: Experimental (on the left) and theoretical (on the right) product contour plots of D atom from H + HD reaction. The height of the contours gives the magnitude of the DCS. The radius represents the product translational energy. From reference[25]

The figure on the left shows the experimental data and the one on the right shows the theoretical calculation. H(D) atom Rydberg time-of-flight technique is used for detecting the D product. Theoretically, quantum-reactive scattering methods were used on a refined potential energy surface. The forward scattering peaks observed (indicated by F in the figures) are attributed to a slowdown of the motion of the system as it approaches to the reaction barrier. This effect is similar to a Feshbach resonance, in the sense that it requires a particular collision energy to be observed but different in its dynamical mechanism. In the former the motion is trapped in an effective potential well, whereas in the latter, the system does motion perpendicular to the reaction coordinate, causing a delay. Both may end up creating a similar forward scattering peak so the theory is important here to separate the two cases.

In 1992 the first report of the use of The Velocity Mapped Imaging (VMI) Technique in a crossed beam experiment appeared.[26] Suits et al. imaged the rotationally inelastic scattering of NO by Argon atoms. Soon after, a reactive process was imaged by Kitsopoulos et al. in 1993.[27] They used two color 1+1′ REMPI schemes to image D atoms from the $H+D_2 \rightarrow HD + D$ reaction. H(D) and NO are the only species we can use 1+1 REMPI schemes. 2+1 REMPI detection can be used for a larger set of molecules but suffers from lower sensitivity. However, Liu and coworkers managed to use 2+1 REMPI detection to great effect when they imaged CD_3 products from the reaction of CD_4 with F, in 2003.[28] The images they got were converted to contour plots that remind us of the one shown in Figure 1.5. Moreover, they were able to provide evidence for scattering resonances in several reactions.[29] Their pair-correlated data require accurate many body quantum dynamical theories to fully interpret but already shed some light on the dynamics of complicated systems.

The application of the Velocity Map Imaging Technique is providing deep insights into the nature of chemical reactions both with the ability to show us a snapshot of the event and by testing the theoretical calculations. The compact setup and fixed detector are other important advantages of the technique, which will broaden the area of applicability of the method. The examples given in this introduction cover only the milestones of the field. For an excellent review on the application of velocity map imaging on bimolecular reactions see Greaves, Rose and Orr-Ewing's excellent review.[30]

This dissertation is composed of two parts. In the first part, we describe the application of the VMI technique to the photodissociation of N_2O molecule at 130 nm and the results from the spectroscopic studies of $O(^1D) + N_2O \rightarrow NO + NO$ reaction in the high collision energy - low pressure region. The second part describes the design and development of a dual-beam apparatus for the application of the VMI technique to reaction dynamics.

In Chapter 2, we start by reviewing the dissociation of N_2O around 200 nm, which proceeds on the $1\ ^1A''$ ($A\ ^1\Sigma^-$) and $2\ ^1A'$,$2\ ^1A''$ ($B\ ^1\Delta$) surfaces and around 130 nm which proceeds mostly on the $^1A'$ ($D^1\Sigma^+$) surface. In chapter 3, we will describe how applying the ion imagine technique to $\approx$ 130 nm dissociation of N_2O gives us the translational energy and angular distributions of all the product channels in this event. We will describe the clues we get in regards to the contributing potential energy surfaces from measuring the β parameters of the product channels. Chapter 4 will be about our work on the $O(^1D) + N_2O \rightarrow NO + NO$ reaction. We provide the first detailed spectroscopic analysis of the rotational distribution of this reaction and explain the observed bimodal vibrational distribution in relation to high pressure studies of the same reaction.

After having talked about the application of the ion-imaging technique and laser spectroscopy to photodissociation and $O(^1D)$ reactions of N_2O, we will focus on the development of a dual-beam apparatus for the application of the VMI technique to reaction dynamics. We will give the electrode design considerations for slicing techniques, ion trajectory simulations for velocity mapping and calibration methods for optimum performance. Furthermore, we will describe a particular delayed extraction scheme that cuts all the background from the dissociation laser in a photo-initiated reaction, which takes advantage of the spatiotemporal separation of the lasers in the dual-beam experiments.

Chapter 3 been published in the Journal of Chemical Physics[31] and Chapter 4 in the Journal of Physical Chemistry A as part of the Klaus-Müller-Dethlefs Festschrift.[32] Both works are products of collaborative efforts in our lab. [f]

[f]Figure 1.1 is adapted from reference[15], by permission of the PCCP Owner Societies. http://dx.doi.org/10.1039/B509304J. Figure 1.3 is reprinted with permission from R. SCHINKE, G. C. McBANE, L. SHEN, P. C. SINGH and A. G. SUITS, THE JOURNAL OF CHEMICAL PHYSICS, 131, 11101, 2009. Copyright 2009. American Institute of Physics. Figure 1.4 and 1.5 are reprinted with permission from A. J. ALEXANDER and R. N. ZARE, JOURNAL OF CHEMICAL EDUCATION, 75, 9, 1998. Copyright 1998. American Chemical Society. Figure 1.5 is adapted from D. M. NEUMARK, A. M. WODTKE, G. N. ROBINSON, C.C. HAYDEN, Y. T. LEE, THE JOURNAL OF CHEMICAL PHYSICS, 82, 3045, 1985. Copyright 1985. American Institute of Physics. Figure 1.6 is reprinted by permission from Macmillan Publishers Ltd: NATURE, S. A. Harich et al. Nature, vol 419, page 281. Copyright 2002.

BIBLIOGRAPHY

[1] E. J. Heller *J. Chem. Phys.*, vol. 65, pp. 2066–2075, 1978.

[2] E. J. Heller *J. Chem. Phys.*, vol. 88, pp. 3891–3896, 1978.

[3] G. Porter *Proc. R. Soc. London. Ser. A.*, vol. 60, p. 60, 1950.

[4] G. E. Busch, R. T. Mahoney, R. I. Morse, and K. R. Wilson *J. Chem. Phys.*, vol. 51, p. 837, 1969.

[5] R. W. Diesen, J. C. Wahr, and S. E. Adler *J. Chem. Phys.*, vol. 50, p. 3635, 1969.

[6] R. N. Zare and P. J. Dagdigan *Science*, vol. 185, p. 739, 1974.

[7] M. N. R. Ashfold and J. D. Howe *Annu. Rev. Phys. Chem.*, vol. 45, p. 57, 1994.

[8] J. J. Valentini, *Spectrometric Techniques.* Academic, London, 1985.

[9] R. Schmiedl, H. Dugan, W. Meier, and K. H. Welge *Z. Phys.*, vol. A304, p. 137, 1982.

[10] R. Ogorzalek, G. E. Hall, H. P. Harri, and P. L. Houston *J. Chem. Phys*, vol. 92, p. 5, 1988.

[11] D. W. Chandler and P. L. Houston *J. Chem. Phys*, vol. 87, pp. 1445–1447, 1987.

[12] G. A. Garcia, L. Nahon, and I. Powis *Rev. Sci. Instr.*, vol. 75, p. 4989, 2004.

[13] V. Dribinski, A. Ossadtchi, V. A. Mandelshtam, and H. Reisler *Rev. Sci. Instr.*, vol. 73, p. 2634, 2002.

[14] A. Eppink and D. H. Parker *Rev. Sci. Instr.*, vol. 68, p. 3477, 1997.

[15] M. N. R. Ashfold, N. H. Nahler, A. J. Orr-Ewing, O. P. J. Vieuxmaire, R. L. Toomes, T. N. Kitsopoulos, I. A. Garcia, D. A. Chestakov, S. Wu, and D. H. Parker *Phys. Chem. Chem. Phys.*, vol. 8, pp. 26–53, 2006.

[16] B. Y. Chang, R. C. Hoetzlein, J. A. Mueller, J. D. Geiser, and P. L. Houston *Rev. Sci. Instr.*, vol. 69, pp. 1665–1670, 1998.

[17] D. Townsend, M. P. Minitti, and A. G. Suits *Rev. Sci. Instr.*, vol. 74, p. 2495, 2003.

[18] R. N. Zare *Mol. Photochem.*, vol. 4, p. 1, 1972.

[19] P. L. Houston *J. Phys. Chem.*, vol. 91, p. 5388, 1987.

[20] R. Schinke, G. C. McBane, L. Shen, P. C. Singh, and A. G. Suits *J. Chem. Phys.*, vol. 131, p. 11101, 2009.

[21] R. L. Miller, A. G. Suits, P. L. Houston, R. Toumi, J. A. Mack, and A. M. Wodtke *Science*, vol. 265, p. 1831, 1994.

[22] A. A. Alexander and R. N. Zare *J. Chem. Ed.*, vol. 75, pp. 1105–1118, 1998.

[23] P. L. Galison, *How Experiments End.* The University of Chicago Press, 1987.

[24] D. M. Neumark, A. M. Wodtke, G. N. Robinson, C. C. Hayden, and Y. T. Lee *Phys. Rev. Lett.*, vol. 53, p. 226, 1984.

[25] S. A. Harich, D. Dai, C. C. Wang, X. Yang, S. D. Chao, and R. T. Skodje *Nature*, vol. 419, p. 281, 2002.

[26] A. G. Suits, L. S. Bontuyan, P. L. Houston, and B. J. Whitaker *J. Chem. Phys.*, vol. 96, p. 8618, 1992.

[27] T. N. Kitsopoulos, M. A. Buntine, D. P. Baldwine, R. N. Zare, and D. W. Zare *Science*, vol. 260, p. 1605, 1993.

[28] J. J. Lin, J. Zhou, W. Shiu, and K. Liu *Science*, vol. 300, p. 966, 2003.

[29] X. Yang *Annu. Rev. Phys. Chem.*, vol. 58, p. 433, 2007.

[30] S. J. Greaves, R. A. Rode, and A. J. Orr-Ewing *Phys. Chem. Chem. Phys.*, vol. 12, p. 9129, 2010.

[31] H. M. Lambert, E. W. Davis, O. Tokel, A. A. Dixit, and P. L. Houston *J. Chem. Phys.*, vol. 122, p. 174304, 2005.

[32] O. Tokel, J. Chen, C. K. Ulrich, and P. L. Houston *J. Phys. Chem. A.*, vol. 114, p. 11292, 2010.

CHAPTER 2

PREVIOUS WORK ON N_2O PHOTODISSOCIATION

2.1 Motivation

In the last century, an important source of concern was the destruction of the ozone layer. The Montreal Protocol (MP) was successful in regulating the most important sources of ozone depleting substances (ODS) by regulating their emissions. In particular the chlorine- and bromine- containing hydrocarbons were regulated. Nitrous Oxide shows similar characteristics in terms of ozone depletion but it is not regulated by MP. N_2O is the main source of nitric oxides, which destroy the ozone catalytically as shown by Crutzen and Johnston via:

$$NO + O_3 \rightarrow NO_2 + O_2 \quad (1)$$

$$O + NO_2 \rightarrow NO + O_2 \quad (2)$$

$$\text{net: } O + O_3 \rightarrow 2\ O_2 \quad (3)$$

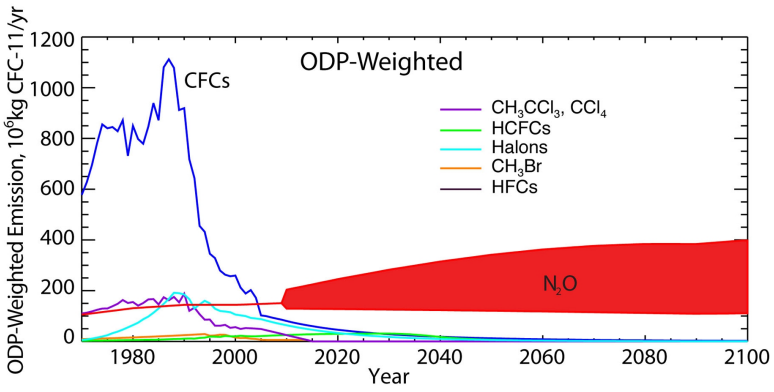

Figure 2.1: Weighted ozone depletion potential. Historical and projected values are shown. From Ravishankara et al. Science, 326, 123, 2009[1]. Reprinted with permission from AAAS.

Currently the anthropogenic emissions of Nitrous Oxide are the largest source of ozone depleting emissions. Moreover, Ravishankara et al. showed that this trend will continue making N_2O the largest ozone depleting substance in this century. Figure 2.1 shows the ozone depletion potential (ODP) values of the important ODS, weighted by their emissions to the atmosphere. The ODP is a measure that quantifies the amount of ozone destroyed by a unit release of that substance to the atmosphere. It is clear from the figure that if unregulated, N_2O will be a significant problem, comparable to the CFC's. N_2O is also an important greenhouse gas. Currently, it is second to methane in terms of climate forcing and its effect is much larger than all the others.

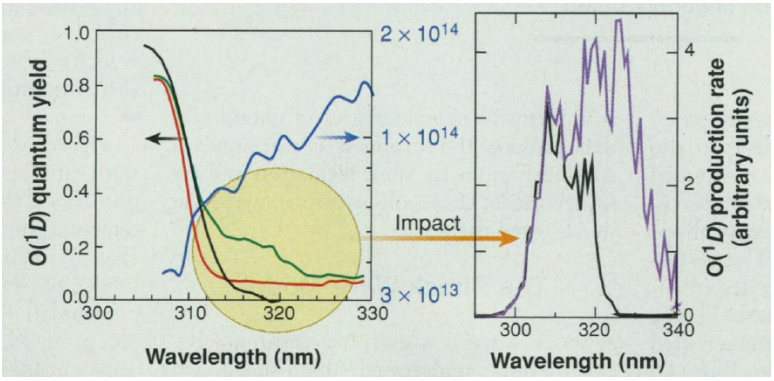

Figure 2.2: The left figure shows the quantum yield of $O(^1D)$ production from ozone photolysis as a function of wavelength. The black curve is the previously recommended values. The red curve shows the updated value at 200K and the green curve shows the yield at 250K. The blue curve shows the photon flux. The impact of this update is shown in the right figure. Black older, purple newer recommended values. From Ravishankara et al. Science, 280, 60, 1998[2]. Reprinted with permission from AAAS.

The contribution of N_2O to the NO_x in the atmosphere either is through its photodissociation to the $N(^2D)$ + $NO(X^2\Pi)$ and $N(^2P)$ + $NO(X^2\Pi)$ channels or thru its reaction with an excited state of the oxygen atom: $O(^1D) + N_2O \rightarrow 2\ NO(X^2\Pi)$. The $O(^1D)$ is produced in the atmosphere mostly by the $O_3 + h\nu \rightarrow$

$O(^1D) + O_2(^1\Delta)$ with a threshold of 310 nm. At longer wavelengths it was thought to be ignorable. However, it was later shown that the channel $O_3 + h\nu \rightarrow O(^1D) + O_2(^3\Sigma)$ is contributing to $O(^1D)$ production at long wavelengths, as shown in Figure 2.2.

This additional channel has a large impact on the calculated $O(^1D)$ production rate. It is clear from the figure that the formation of $O(^1D)$ at a larger range will have implications on the ozone cycle through its reactions with N_2O.

2.2 Previous studies on the photodissociation of N_2O

2.2.1 200 nm dissociation on the B $^1\Delta$ and A $^1\Sigma^-$ surfaces

The dissociation of N_2O in the 200 nm region has been extensively studied before. This photolysis event mostly results in the $N_2(X^1\Sigma) + O(^1D)$ channel.[3–6] Felder, Haas and Huber used time of flight spectroscopy, Shafer et al. and Springsteen et al. used Doppler profile spectroscopy to measure the angular and translational energy distributions of the photofragments.[7–9] Felder determined β=0.48±0.02. Springsteen et al. determined β=0.50±0.05. Both of these groups give an average translational energy of about 1.17 eV, 42% of the total available energy. In contrast, Shafer et al. determined β=2. Their measurement is done at a slightly different wavelength but the discrepancy arises from the uncertainty in their assumption for the rotational energy of N_2 fragment. This prompted Hanisco and Kummel to measure the N_2 distribution.[10] Their results confirmed Felder et al. and Springsteen et al.'s measurements: 43±4% of the available energy is in translational energy and 57±4% of it ends up in rotation. No vibrational excitation is

observed.

Suzuki et al. measured the velocity distribution of O(^{1}D) atoms from 205 nm photodissociation of N_2O by using the ion-imaging technique in conjunction with 2+1 REMPI processes to detect the O(^{1}D).[11] They reported two components in the translational energy distributions, indicating two different pathways: A main narrow energy peak at $\approx$ 25kcal/mol with a higher β and a wider distribution (0 to 60 kcal/mol) with a low value of β. They observed β values to increase from 0 to 1 up to 26kcal/mol and then decrease to lower values.

Chang et al. used the first ion-counting method with the imaging technique and it that work provided two separate translational energy products arising from the 203.2 nm dissociation of N_2O.[12] Two distinct but similar rings were observed in the N_2(v=0,J $\approx$74) images which were attributed to the ground and first excited bending states of the N_2O molecule. These results are also supported by the experiments of Teule et al. in which a hexapole field is used to select individual rotational states of vibrationally excited N_2O molecules.[13,14]

Neyer et al. studied the N_2 fragments by the imaging technique.[15] They found that the anisotropy parameter β is decreasing with increasing rotational quantum number, J, if N_2O is dissociated by $\approx$ 203 nm. They found that the β is around 1 for J <50 and it is decreasing slowly to 0.7 for N_2(J=74). Then it quickly falls to 0, for N_2(J=90). Since the two photofragments are coupled by the conservation of momentum, this change should present itself in the β measurements of the O(^{1}D) experiments. However, there is some orbital alignment hints in the measurements of Suzuki et al. Since the results from the 2+1 REMPI Q-branch imaging of N_2 fragments are less sensitive to alignment effects, Neyer et al. state that their β values will be more reliable.

Neyer et al. also used the imaging technique to directly measure the O(^{1}D) translational and angular distributions at 3 different but similar wavelengths from N_2O photolysis.[16] The dependency of the images on the polarization of the laser indicated orbital alignment of O(^{1}D) fragments. $I_{image} \propto I_{det}$ x $(1+\beta P_2 cos(\theta))$ and I_{det} is a function of the angular momentum distribution of the fragment. By using two-photon detection functions and coupling this data with rotationally selected N_2 imaging experiments, they were able to to extract populations in the magnetic sub-levels, m, as a function of the speed. They report almost negligible |m|=2. |m|=0 is observed mostly with high N_2 rotational levels (slow O translational energy) and |m|=1 is observed mostly with low N_2 internal energy (high O atom translational energies). The bent dissociation on the 2 ^{1}A′ surface is predicted to create O fragments with |m|=0 and |m|=1 while the bent dissociation on the 1 ^{1}A" surface is predicted to create |m|=1. Therefore, |m|=0 fits are used to get the β parameter for the 2 ^{1}A′ surface as a function of the O speed. The |m|=1 fits were used to find the branching ratio between the 1 ^{1}A" and 2 ^{1}A′ surfaces as a function of the O speed. Their reported speed dependent m populations provided strict constraints to be tested by trajectory calculations. Suits et al. also observed coherences between the m sub-levels of the $^1D_2$ state from the 193 nm dissociation of N_2O.[17]

Anouk et al. did rotationally resolved photoelectron spectroscopy of N_2 in the 203 nm photolysis of N_2O and improved the REMPI assignments of N_2.[18]

Similar to the O(^{1}D) alignment studies, Brouard et al. used the ion imaging technique to study the alignment of the O(^3P_J) products in the O(^3P_J)+N_2 channel, following the photolysis at 193 nm.[19] They found that 60% of the available energy is appears in the translation and the rest goes to N_2 internal energy. Nishida

et al. reported the quantum yield of the $O(^3P)$+$N_2(X)$ channel as 0.005± 0.002, from 193 nm dissociation of N_2O, found during their studies of the $O(^1D)$+N_2O $\rightarrow$ $O(^3P)$ + N_2O reaction.[20]

Suzuki et al. reinvestigated the 203-205 nm dissociation of nitrous oxide with an improved imaging apparatus.[21] They were able to get rotational resolution directly on the $O(^1D)$ images and were able to correlate their results with rotational data from the N_2 images. They also quantified that the absorption from the first bending excited level in the 203-205 nm region is seven times larger than that from the ground vibrational level.[22]

On the theoretical side, Daud et al. calculated the *ab initio* potential energy surfaces and did some dynamical studies on them.[23] They have calculated the rotational N_2 distribution from 203 nm photolysis and found that there is excellent agreement to previous experiments.

The theoretical focus was mainly on calculating accurate potential energy surfaces. The detailed calculations were done by Hopper[24], Brown et al.[25] and Janssen et al[26] but no extensive dynamical studies had been done on these surfaces.

2.2.2 130 nm dissociation on the D $^1\Sigma^+$ and $^3\Pi_v$ surfaces

At shorter wavelenghts, N_2O can be excited to the $C(^1\Pi)$ state near 145 nm or to the $D(^1\Sigma^+)$ state near 130 nm. These dissociation processes are less well understood. For photodissociation at 130 nm, the following channels are thought to be important:

$$N_2O + h\nu \rightarrow O(^1S) + N_2(X^1\Sigma_g^+) \qquad (4)$$

$$\rightarrow N(^2D) + NO(X^2\Pi) \qquad (5)$$

$$\rightarrow N(^2P) + NO(X^2\Pi) \qquad (6)$$

$$\rightarrow O(^3P) + N_2(A^3\Sigma_u^+) \qquad (7)$$

$$\rightarrow O(^3P) + N_2(B^3\Pi_g) \qquad (8)$$

Black et al. investigated the $O(^1S)$, $N(^2D)$, and $N_2(A^3\Sigma_u^+)$ products in the photodissociation of N_2O from 110 to 150 nm.[27] While the $O(^1S)$ was detected directly from its emission at 557.7 nm, the $N(^2D)$ was detected indirectly from its reaction with N_2O to give $NO(B^2\Pi)$, which decays radiatively. Similarly, $N_2(A^3\Sigma_u^+)$ was detected indirectly from its energy transfer to NO, yielding $NO(A\ ^2\Sigma^+)$, which decays radiatively. They report that the $O(^1S)$ quantum yield is near unity in the 128-138 nm range, that the $N(^2D)$ quantum yield is nearly zero at 130 nm, and that the quantum yield for $N_2(A^3\Sigma_u^+)$ is less than 10% at 130 nm. No information is available from these experiments on the dynamics of the dissociation, i.e., on what the kinetic energy release is for any of the channels studied.

Kinetic-energy release data is available, although at low resolution, from the experiments of Gilpin and Welge (GW)[28] and of Stone, Lawrence, and Fairchild (SLF).[29] In both studies, a molecular beam of N_2O was dissociated with a flash lamp operating near 130 nm, and the arrival time of metastable fragments at an ionizer was recorded. In the SLF study, data for the 130 nm photodissociation indicate that the vibrational distribution for the $N_2(X\ ^1\Sigma)$ product extends from v =0 to v =6 with a peak at v =3.[29] None of the other channels was investigated. In the GW study, processes (4) and (7) were observed, but the limited resolution precluded detailed energy analysis.

All previous studies of nitrous oxide dissociation benefited greatly from the theoretical work of Hopper, who performed extensive multiconfiguration self-consistent-field/configuration interaction (MCSCF/CI) calculations identifying some 30 electronic states of nitrous oxide.[24]

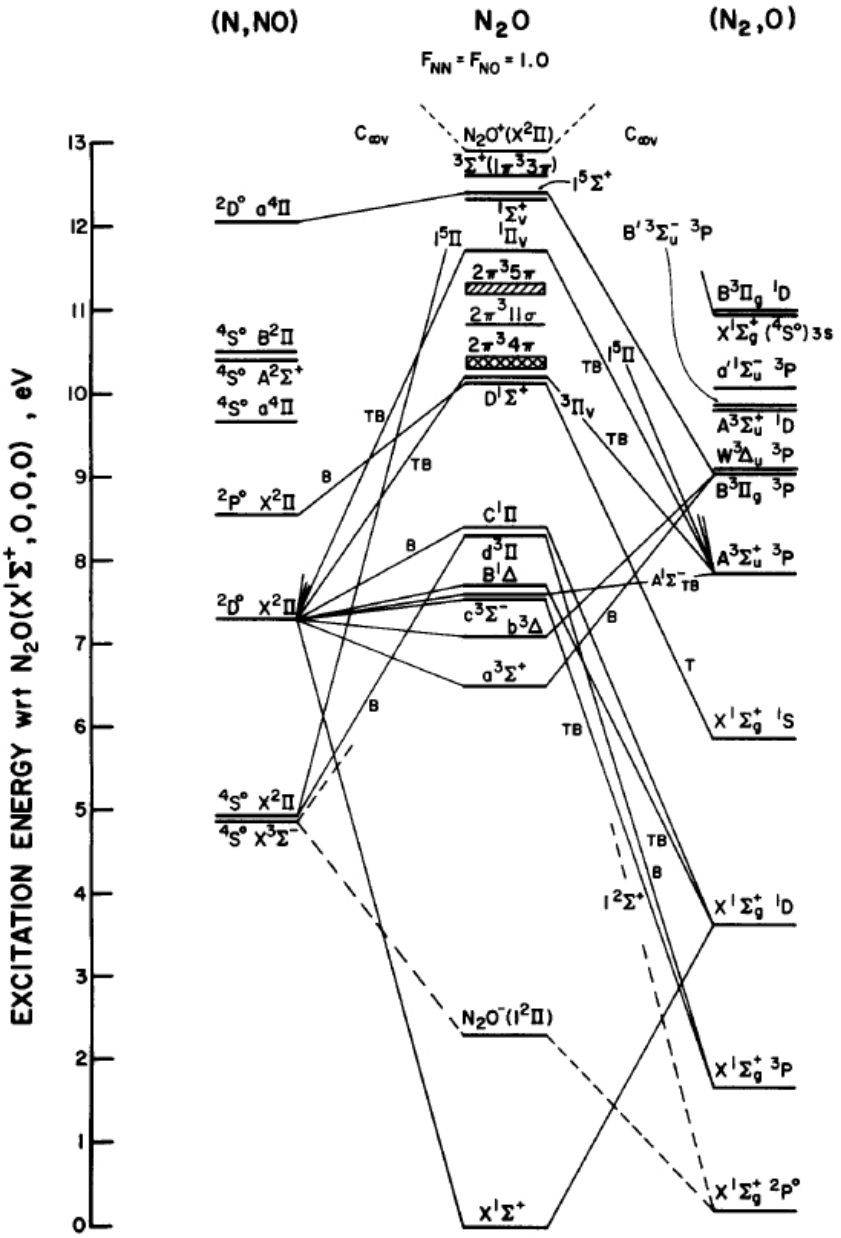

Figure 2.3: $C_{\infty v}$ adiabatic correlation diagram for N_2O. Symbol B is for relative barrier in the dissociation pathway. Symbol T indicates a two electron transition is required. Figure reprinted from ref[24]

In Fig. 2.3, Hopper's Figure 9 is reproduced, showing the $C_{\infty v}$ adiabatic configuration diagram for N_2O. In particular, the correlation diagrams of Figs. 9 and 10 in his paper show that the $N_2O(D^1\Sigma^+)$ state reached at 130 nm correlates with dissociation channels (4) and (6), while excitation to a nearby $^3\Pi_v$ state correlates to channels (7) and (5). Channel (8) correlates with a bent geometry of the $^3\Pi_v$ state, not seen in this figure. The $D^1\Sigma^+$ state is of A' symmetry when the molecule is bent away from a linear geometry, while the $^3\Pi_v$ state separates into two configurations, one of A' symmetry and of A'' symmetry. These results will be used in our analysis of the photodissociation event at this wavelength range, in the next chapter. [a]

[a]Figure 2.3 is reprinted with permission from D. G. HOPPER, THE JOURNAL OF CHEMICAL PHYSICS, 80, 4290, 1984. Copyright 1984. American Institute of Physics.

BIBLIOGRAPHY

[1] A. R. Ravishankara, J. S. Daniel, and R. W. Portmann *Science*, vol. 326, p. 123, 2009.

[2] A. R. Ravishankara, G. Hancock, M. Kawasaki, and Y. Matsumi *Science*, vol. 280, p. 60, 1998.

[3] K. F. Preston and R. F. Barr *J. Chem. Phys.*, vol. 54, p. 3347, 1971.

[4] G. Paraskevopoulos and R. J. Cvetanovic *J. Am. Chem. Soc.*, vol. 91, p. 7572, 1969.

[5] Y. F. Zhu and R. J. Gordon *J. Chem. Phys.*, vol. 92, p. 2897, 1990.

[6] M. Zelikoff, K. Watanabe, and E. C. Y. Inn *J. Chem. Phys.*, vol. 21, p. 1643, 1953.

[7] P. Felder, B. M. Haas, and J. R. Huber *Chem. Phys. Lett.*, vol. 186, p. 177, 1991.

[8] N. Shafer, K. Tonokura, Y. Matsumi, S. Tasaki, and M. Kawasaki *J. Chem. Phys.*, vol. 95, p. 6128, 1991.

[9] L. L. Springsteen, S. Satyapal, Y. Matsumi, L. M. Dobeck, and P. L. Houston *J. Phys. Chem.*, vol. 97, p. 7239, 1993.

[10] T. F. Hanisco and A. C. Kummel *J. Phys. Chem.*, vol. 97, p. 7242, 1993.

[11] T. Suzuki, H. Katayanagi, Y. Mo, and K. Tonokura *Chem. Phys. Lett.*, vol. 256, p. 90, 1996.

[12] B. Y. Chang, R. C. Hoetzlein, J. A. Mueller, and J. D. Geiser *Rev. Sci. Instr.*, vol. 69, p. 1665, 1998.

[13] J. M. Teule. PhD thesis, Vrije Universiteit, 1997.

[14] J. M. Teule, G. C. Groenenboom, D. W. Neyer, D. W. Chandler, and M. H. M. Janssen *Chem. Phys. Lett.*, vol. 320, p. 177, 2000.

[15] D. W. Neyer, A. J. R. Heck, and D. W. Chandler *J. Chem. Phys.*, vol. 110, p. 3411, 1999.

[16] D. W. Neyer, A. J. R. Heck, D. W. Chandler, J. M. Teule, and M. H. M. Janssen *J. Phys. Chem. A.*, vol. 103, p. 10388, 1999.

[17] M. Ahmed, E. R. Wouters, D. S. Peterka, O. S. Vasyutinskii, and A. G. Suits *Faraday Discuss.*, vol. 113, p. 425, 1999.

[18] A. M. Rij, E. H. G. Backus, C. A. Lange, M. H. M. Janssen, K. Wang, and V. McKoy *J. Chem. Phys.*, vol. 114, p. 9413, 2001.

[19] M. Brouard, A. P. Clark, C. Vallance, and O. S. Vasyutinskii *J. Chem. Phys.*, vol. 119, p. 771, 2003.

[20] S. Nishida, K. Takahashi, Y. Matsumi, N. Taniguchi, and S. Hayashidai *J. Phys. Chem. A.*, vol. 108, p. 2451, 2004.

[21] T. Nishide and T. Suzuki *J. Phys. Chem. A.*, vol. 108, p. 7863, 2004.

[22] H. Kawamata, H. Kohguchi, T. Nishide, and T. Suzuki *J. Chem. Phys.*, vol. 125, p. 133312, 2006.

[23] M. N. Daud, G. G. B. Kurti, and A. Brown *J. Chem. Phys.*, vol. 122, p. 54305, 2005.

[24] D. G. Hopper *J. Chem. Phys.*, vol. 80, p. 4290, 1984.

[25] A. Brown, P. Jimono, and G. G. Balint-Kurti *J. Phys. Chem.*, vol. 103, p. 11089, 1999.

[26] M. H. M. Janssen, J. M. Teule, D. W. Neyer, D. W. Chandler, and G. C. Groenenboom *Faraday Discuss.*, vol. 113, p. 473, 1999.

[27] G. Black, R. L. Sharpless, T. G. Slanger, and D. C. Lorents *J. Phys. Chem.*, vol. 62, p. 4266, 1975.

[28] R. Gilpin and K. H. Welge *J. Chem. Phys.*, vol. 55, p. 975, 1971.

[29] E. J. Stone, G. M. Lawrence, and C. E. Fairchild *J. Chem. Phys.*, vol. 65, p. 5083, 1976.

CHAPTER 3

PHOTODISSOCIATION CHANNELS FOR N_2O NEAR 130 NM STUDIED BY PRODUCT IMAGING

Nitrous oxide is an important component of the earth's natural atmosphere, produced primarily by biological processes in soils and oceans. Mostly inert in the troposphere, it is transported to the stratosphere where it is destroyed both by photodissociation and by reaction. Its mixing ratio falls from about 300 parts per 10^9 by volume (ppbv) at the tropopause to about 20 ppbv at 40 km, with a sharp decline beginning at about 25 km. This decline is partially due to the photodissociation

$$N_2O + h\nu \rightarrow N_2(X^1\Sigma) + O(^1D) \qquad (1)$$

This process occurs at wavelengths below about 220 nm, but is most effective in the atmospheric window at about 200 nm. N_2O is also destroyed in the stratosphere by reaction with $O(^1D)$ produced either in (1) or from the dissociation of ozone

$$N_2O + O(^1D) \rightarrow N_2 + O_2 \qquad (2)$$

$$\rightarrow NO + NO \qquad (3)$$

NO produced in (3) is the primary catalytic agent destroying the stratospheric ozone in the natural atmosphere, as noted by Crutzen.[1]

For photodissociation at 130 nm, the following channels are thought to be important:

$$N_2O + h\nu \rightarrow O(^1S) + N_2(X^1\Sigma_g^+) \qquad (4)$$

$$\rightarrow N(^2D) + NO(X^2\Pi) \qquad (5)$$

$$\rightarrow N(^2P) + NO(X^2\Pi) \qquad (6)$$

$$\rightarrow O(^3P) + N_2(A^3\Sigma_u^+) \qquad (7)$$

$$\rightarrow O(^3P) + N_2(B^3\Pi_g) \qquad (8)$$

In the results described below, we have investigated channels (4)-(8) by using product imaging to detect the angular distributions for the five channels as well as the kinetic-energy release for each of the product atoms or diatoms. The atomic products were probed by resonant (1+1′) ionization using vacuum-ultraviolet excitation for the first step, while the diatomic products were probed by nonresonant ionization. Our work is part of a larger effort at Cornell to characterize this photodissociation process. Witinzki, Ortiz-Suárez, and Davis have used oxygen Rydberg time-offlight spectroscopy to study channels (7) and (8), with results that are in reasonable agreement with ours.[2]

3.1 Experiment

A skimmed molecular beam of N_2O was introduced along the axis of a time-of-flight mass spectrometer (TOFMS), through the central holes in a set of three parallel, circular electrodes. Midway between the high-voltage repeller and accelerator plates, the beam was crossed at right angle by three or more copropagating laser beams. Along the intersection cylinder, the laser radiation photolyzed N_2O and ionized the recoiling dissociation products. The resulting ion cloud was accelerated through the opening in the third plate, held at ground, into a field-free region, all the while expanding at the velocities from the dissociation. The voltages and spacing of the electrodes were chosen to focus ions born with the same velocity onto a position-sensitive, dual microchannel plate assembly coupled to a fast phosphor screen at the end of the time-of-flight (TOF) tube. Gating the detector allowed a fast charge-coupled device (CCD) camera to record the resulting two-dimensional image of the ion cloud on the detector for a particular ion mass. This ion-imaging technique has been described in detail elsewhere.[3–5]

Vacuum-ultraviolet (VUV) laser radiation was used both to photodissociate N_2O and to detect the products by multiphoton ionization techniques. VUV photons were generated by a nonlinear four-wave mixing scheme at the difference frequency ($2\omega_1$-ω_2) between a two-photon resonance in krypton and a tunable photon in the visible to infrared region. Ultraviolet laser radiation (ω_1) at 212.55 nm ($\approx$ 0.8 mJ/ pulse) was employed to excite the 5p[0,1/2,0] $\leftarrow\leftarrow$ $4p^6$ transition in Kr by frequency doubling with a betabarium borate (BBO) crystal the output of a neodymium:yttrium aluminum garnet (Nd:YAG) (third harmonic) pumped Scanmate dye laser. The tunable (ω_2) photon employed in the VUV generation was produced by a second dye laser, pumped by the second harmonic of the same

Nd:YAG laser. The ω_1 and ω_2 lasers were spatially and temporally overlapped by means of dichroic mirrors and a delay line, respectively, and focused by an achromatic lens into a stainless steel tube containing 10-20 Torr Kr. The resulting VUV and the residual incident laser light entered the TOFMS through a MgF_2 collimating lens, which served as the exit window of the Kr cell. With horizontal and vertical polarizations of ω_1 and ω_2, respectively, the resulting polarization of the VUV was vertical and parallel to the plane of the detector.

N_2O was dissociated near the peak of the absorption curve at wavelengths around 130 nm, which were convenient for detection of atomic products by $(1+1')$ resonance enhanced multiphoton ionization (REMPI), namely, $O(^3P_{2,1,0})$ at 130.2, 130.5, and 130.6 nm and $N(^2P_{3/2})$ at 131.05 and 131.09 nm, respectively. In each case, the VUV dissociation wavelength was coincident with an atomic resonance to an excited electronic state, which could then be ionized by absorption of the residual 212.55 nm UV laser light. The detection of atomic products at dissociation wavelengths other than an atomic resonance required the generation of a second VUV wavelength. This was accomplished by sending a second visible laser into the Kr cell, coincident in time and spatially overlapped with the previously mentioned UV and visible lasers, which generated the first VUV wavelength. The scheme has been described more fully in a previous report.[6] With the photolysis laser tuned just off the $O(^3P_2)$ resonance near 130.2 nm, $N(^2D)$ and $O(^1S)$ photofragments could be detected with the second VUV laser by $(1+1')$ REMPI schemes at 124.3 and 121.76 nm, respectively. The ω_2 photons required to generate the VUV wavelengths were 578 nm for $O(^3P_2)$, 561 nm for $N(^2P)$, 731 nm for $N(^2D)$, and 835 nm for $O(^1S)$. The latter wavelength was obtained as the first Stokes line from Raman shifting 620 nm in H_2. Typical laser pulse energies were 2-5 mJ for the visible light and 1-2 mJ for the Raman-shifted infrared light.

Due to appreciable absorption by N_2O at 124.3 and 121.76 nm, product images recorded by two VUV color schemes were a composite of dissociation processes at both pump and probe wavelengths. The contribution to the dissociation at the detection wavelength was minimized by optimizing the Kr pressure for more efficient VUV generation at the dissociation wavelength. The remaining contribution at the detection wavelength was removed by a background subtraction scheme, involving the use of electronic shutters in each ω_2 laser. This allowed images to be collected on alternate sequences of laser shots, with dissociation and detection wavelengths together and then each separately.

Several experiments were undertaken with a photomultiplier tube replacing the camera and without gating the detector. The TOF mass spectra were recorded in this way for the mass peaks at N^+, O^+, N_2^+, and NO^+ as a function of the laser power for each of the ω_1 and ω_2 lasers. This was repeated for NO and N_2 gases to determine the origin of the observed molecular ions. The scans of the ω_2 laser wavelength were useful in determining the spin-orbit branching ratios by comparison of the integrated ion signals at each of the fine structure levels for $O(^3P_J)$, $N(^2D_J)$, and $N(^2P_J)$. The relative sensitivity for VUV detection of $O(^3P_2)$ and NO(X,v=0,1) at 130.2 nm was established by dissociating NO_2 at 355 nm and was used to calibrate the corresponding O:NO branching ratio obtained from N_2O dissociation.

The composition of the molecular beam was nominally 100% N_2O (99% min, Matheson C.P. grade), except for the experiments detecting the major $O(^1S)$ product channel for which a 10% N_2O mixture in Ar (99.999 5%, Spectra Gases) was prepared. In a diagnostic experiment, a premade 10% NO/ He mixture (9.97%, Matheson) was used. The Krypton was research grade (99.998 5%, Praxair).

3.2 Results

Following the dissociation of N_2O at 130.2 nm, the TOF mass spectrum showed product peaks at N^+ or O^+ whenever the ω_2 laser was tuned to the appropriate (1+1′) REMPI transition for detection of $N(^2D_J)$, $N(^2P_J)$, $O(^3P_J)$, or $O(^1S)$. Spectral scans over the fine structure levels yielded relative spin-orbit populations for $O(^3P_J)$, $N(^2D_J)$, and $N(^2P_J)$ after normalization for variations in the laser powers. These are given in Table I. Product peaks also were observed for the molecular ions, N_2^+, NO^+, and N_2O^+, due to nonresonant multiphoton ionization processes. Power dependence experiments established that NO^+ was produced by sequential absorption of UV and visible photons by the neutral photoproduct and not by predissociation of N_2O^+. Experiments with a N_2 beam confirmed that N_2^+ could not be produced optically from the ground state, inferring that the signal was due to the ionization of an excited state, likely by VUV absorption. The ratio of mass peaks for O^+ and NO^+ can be converted to the branching ratio between the dissociation channels, leading to $O(^3P) + N_2$ and N + NO by calibrating against the O^+:NO^+ mass peak ratio obtained from the dissociation of NO_2 at 355 nm. The ion signals were normalized for variations in laser intensities, using the measured power dependences, and corrected for the fraction of the spin-orbit population appearing as $O(^3P_2)$.[7] The resulting branching ratio is given in Table I. [a]

[a]This work has been published as *Photodissociation channels for N_2O near 130 nm studied by product imaging*, H. M. Lambert, E. W. Davis, O. Tokel, A. A. Dixit and P. L. Houston, The Journal of Chemical Physics, 122, 174304, 2005. It is reprinted with permission from The Journal of Chemical Physics, American Institute of Physics. Copyright 2005.

TABLE I. Product branching ratios: Spin-orbit populations and dissociation channels.

Atomic spin-orbit population ratios ($\pm 2\sigma$)	
$N(^2D_{5/2}):N(^2D_{3/2})$	1.37 ± 0.11
$N(^2P_{3/2}):N(^2P_{1/2})$	1.9
$O(^3P_2):O(^3P_1):O(^3P_0)$	$(0.51 \pm 0.09):(0.41 \pm 0.15):(0.08 \pm 0.02)$
Dissociation product channel ratios ($\pm 2\sigma$)	
$O(^3P_2)+N_2(A):O(^3P_2)+N_2(B)$	0.71 ± 0.16
$O(^3P_1)+N_2(A):O(^3P_1)+N_2(B)$	0.95 ± 0.06
$O(^3P_0)+N_2(A):O(^3P_0)+N_2(B)$	1.32 ± 0.25
$N_2(A)+O(^3P_J):N_2(B)+O(^3P_J)$	0.84 ± 0.09
$O(^3P)+N_2(A,B):N(^2D,^2P)+NO$	1.4 ± 0.5
$N(^2D_J)+NO:N(^2P_J)+NO$	3

Velocity-mapped ion images were recorded for the dissociation products of N_2O near 130 nm. The O + N_2 product channels are represented by the $O(^1S)$, $O(^3P_2)$, and N_2^+ images in Fig. 3.1. The N + NO product channels are represented by the $N(^2P_{3/2})$, $N(^2D_{5/2})$, and NO^+ images in Fig. 3.2. Inverse Abel transformation of the images recovers a slice through the original three-dimensional velocity distribution. Integration over angles yields the speed distributions. The magnification due to the camera lens and ion optics was determined by a calibration of the system with the dissociation of O_2. Conversion to total kinetic-energy released (TKER) allows for comparison between product channels and reveals the internal energy distributions in the unobserved dissociation coproduct. The O + N_2 TKER distributions derived from the images in Fig. 3.1 are shown in Fig. 3.3. The $O(^3P_0)$ TKER distribution was included to show the effect of the spin-orbit level. Similarly, the N + NO TKER distributions derived from the images in Fig. 3.2 are shown in Fig. 3.4. The energy combs in Figs. 3.3 and 3.4 were derived from the photon energy, bond energies, and spectral constants.

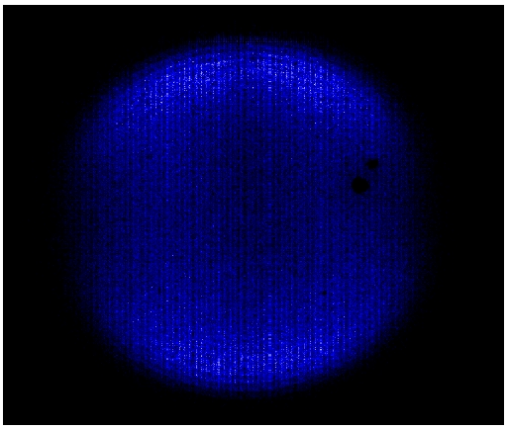

(a) $O(^1S)$

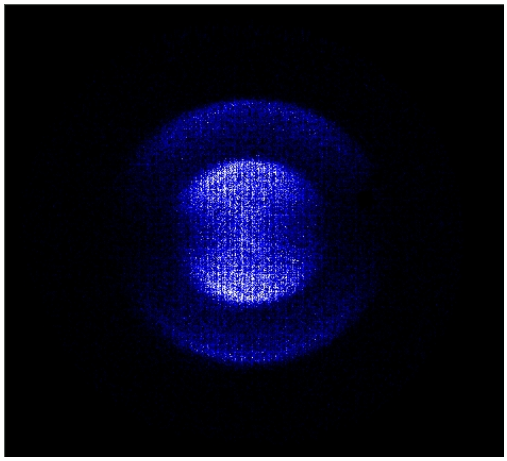

(b) $O(^3P_2)$

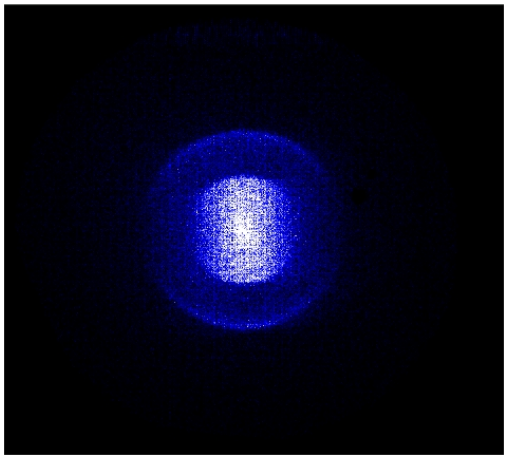

(c) N_2

Figure 3.1: O + N_2 product images from N_2O dissociation at 130.2 nm

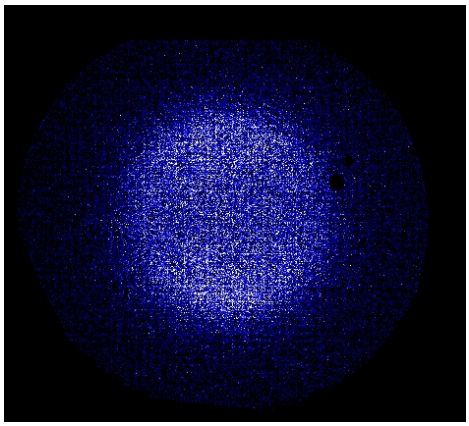

(a) $N(^2D)$

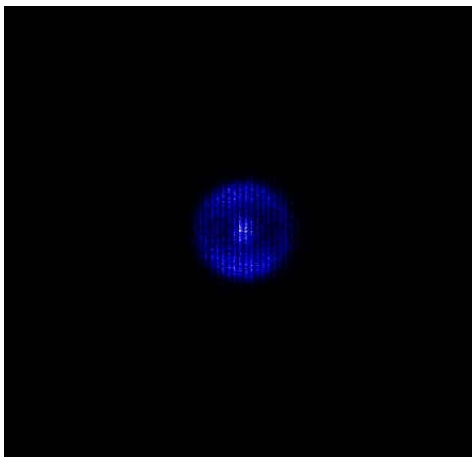

(b) $N(^2P)$

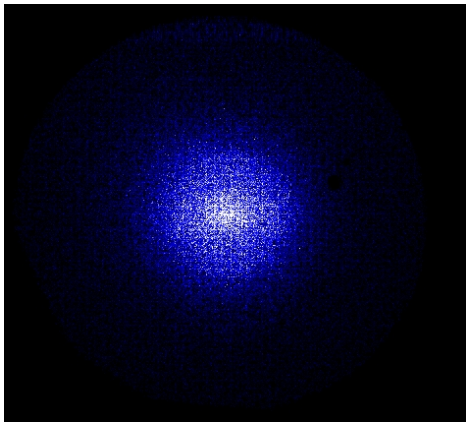

(c) NO^+

Figure 3.2: N + NO product images from N_2O photolysis at 130.2 nm (The dissociation wavelength for (b) is 131.05nm).

Inspection of the TKER distributions for the O + N_2 dissociation channels shows that the observed N_2^+ results from the ionization of N_2 in both the $A^3\Sigma_u^+$ and $B^3\Pi_g$ electronically excited states, as coproducts with $O(^3P_J)$. $O(^1S)$ is coproduced with unobserved N_2 in the ground electronic state. Electronically excited atoms/diatoms are coupled with ground state diatoms/atoms, respectively. The N_2 A:B branching ratio is easily determined by integration over the two peaks in the O atom TKER, and appears to differ with the atomic fine-structure level. Assuming that the ionization steps are equally efficient, the same information is obtained from the peak areas in the N_2^+ TKER. The N + NO data indicate that the NO^+ image is a composite of two dissociation channels, leading to the two electronically excited states of atomic nitrogen, with the $N(^2P)$ correlating with slower NO and the $N(^2D)$ with faster NO. The $N(^2P)$ products were shown to be bimodal with a minor contribution at very low kinetic energy. The $N(^2D)$:$N(^2P)$ branching ratio may be determined from scaling the TKER distributions from the nitrogen atoms to fit the NO distribution, and accounting for the spin-orbit populations. These branching ratios are also given in Table I. For electronically excited atomic nitrogen and oxygen, the peak kinetic energy is substantially lower than the maximum allowed by conservation of energy, indicating that the diatoms have significant internal excitation.

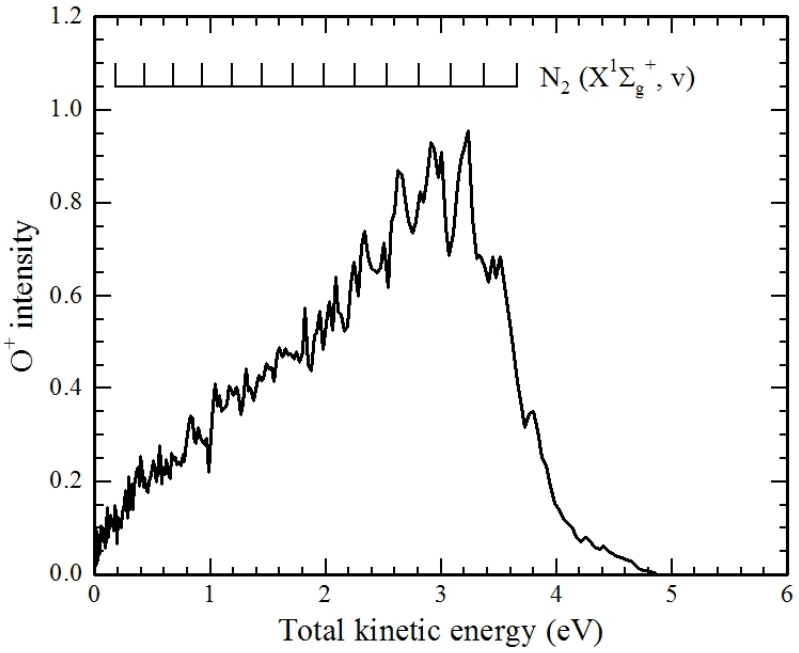

(a)

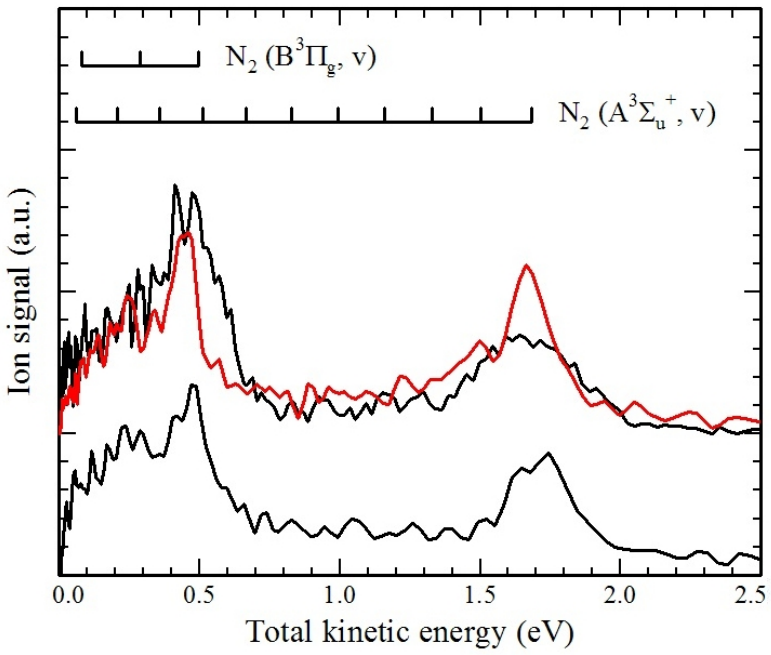

(b)

Figure 3.3: Total kinetic energy released for O + N_2 producets from the dissociation of N_2O at 130.2nm. (a) O(^{1}S) and (b) O($^3P_2$) top black curve, O($^3P_0$) top red curve and N_2^+ bottom curve.

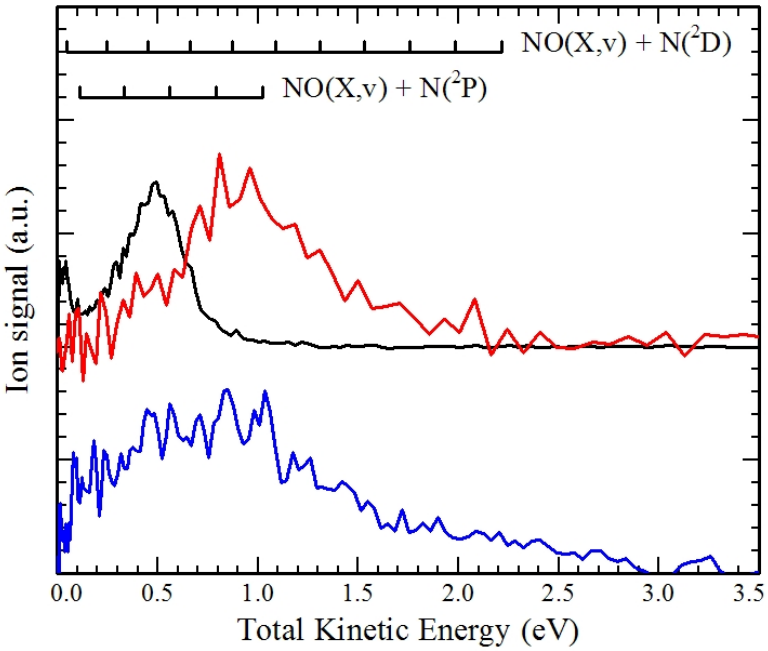

Figure 3.4: Total kinetic energy released for N+NO products from the dissociation of N_2O at 130.2 nm: $N(^2P_{3/2})$ top black curve (at 131.054 nm), $N(^2D_{5/2})$ top red curve, and NO^+ bottom curve.

Product angular distributions were obtained from the inverse Abel-transformed image by fitting the following function to annuli of eight to ten pixels in width:

$$I(\theta) = c\ [1+\beta\ P_2(\cos\theta)] \qquad (9)$$

where c is a scaling constant, β is the anisotropy parameter, which has the limiting values of 2 for a parallel transition and -1 for a perpendicular transition, and $P_2(x)$ is the second-order Legendre polynomial, 1/2 ($3x^2$-1). For the O + N_2 dissociation channels, the fitted anisotropy parameters are large and positive, indicating that the dissociating state is reached by a parallel transition. With increasing vibrational excitation in the N_2 coproduct, however, the anisotropy parameter decreases substantially. The good agreement of the $O(^3P_2)$ and $O(^3P_0)$ angular distributions indicates that there is no alignment of the atomic angular

momentum. The N + NO dissociation channels yielded angular distributions for the N(^{2}D,^{2}P) products, which are characterized by positive values of β, whereas the NO^+ image appeared to be very nearly isotropic. An alignment of the N(^2P_J) fragments could not be confirmed by comparison of the angular distributions since both J=1/2 and J=3/2 fragments gave similar β's within the fairly large ($\pm 2\sigma$) uncertainties. Angular distributions together with the resulting fit of Eq. (9) to the data are displayed in Fig. 3.5, while the determined anisotropy parameters are given in Table II.

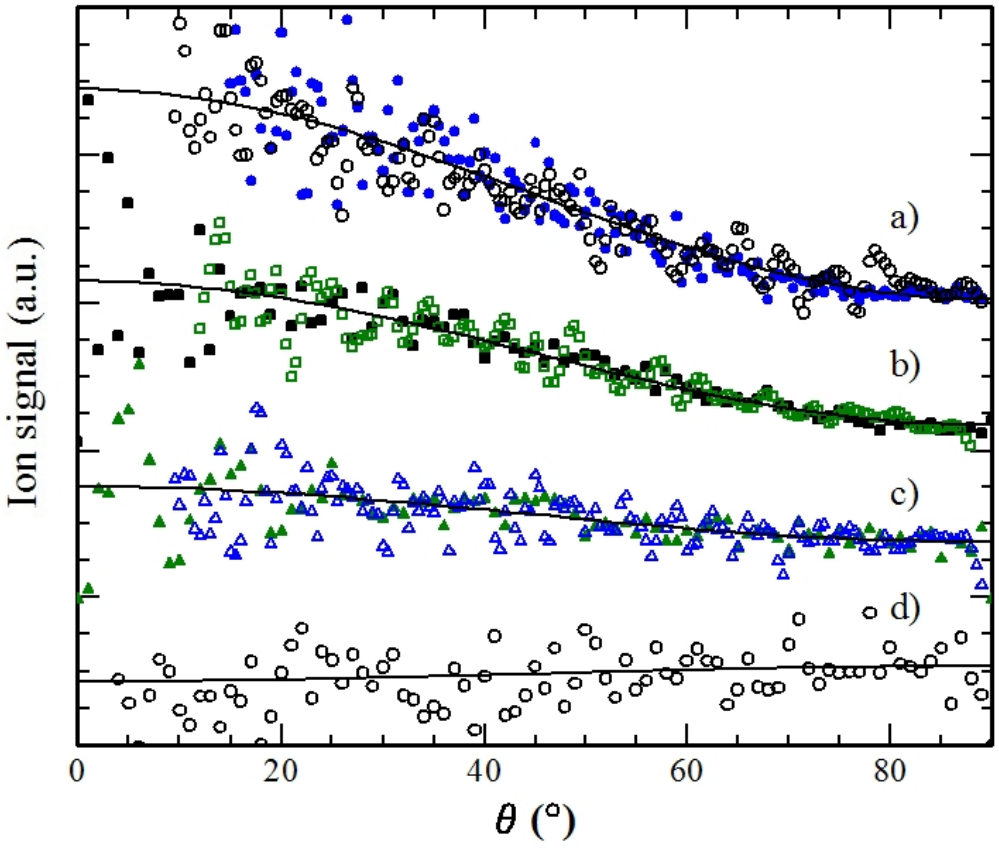

Figure 3.5: Angular distributions and fit of $1+\beta P_2(\cos(\theta))$: (a) β=1.9, • $O(^3P_2)+N_2(A,v=0)$, ∘ N_2^+ outer ring; (b) β=1.3, ■ $O(^1S)+N_2(X,v=0)$, □ $O(^3P_0)+N_2(B,v=0)$; (c) β=0.5, ▲ $N(^2P_{1/2})+NO(X)$, △ $N(^2D_{5/2})+NO(X)$; and (d) β=-0.14, ∘ NO^+. The zero of the scale is shifted so that al the data can be displayed on one plot.

TABLE II. Anisotropy parameters determined from fitting Eq. (9) to the angular distributions of various N_2O dissociation product channels.

Product channel	Anisotropy parameter $\beta(\pm 2\sigma)$
$O(^1S)+N_2(X,v)$	(v=0) 1.3±0.2; (v=1) 1.3±0.2; (v=2) 1.1±0.1; (v=3) 0.9±0.1
$O(^3P_2)+N_2(A,v)$	(v=0) 2.0±0.2
$O(^3P_0)+N_2(A,v)$	(v=0) 1.8±0.2; (v=1) 1.6±0.3
$N_2(A,v)+O(^3P_J)$	(v=0) 1.8±0.2
$O(^3P_2)+N_2(B,v)$	(v=0) 1.3±0.2; (v=1) 0.7±0.1
$O(^3P_0)+N_2(B,v)$	(v=0) 1.3±0.1; (v=1) 0.9±0.1
$N_2(B,v)+O(^3P_J)$	(v=0) 1.4±0.1; (v=1) 0.9±0.1
$N(^2D_{5/2})+NO(X)$	0.48±0.15
$N(^2P_{3/2})+NO(X)$	0.68±0.12 (fast); 0.03±0.31 (slow)
$N(^2P_{1/2})+NO(X)$	0.51±0.12 (fast); −0.39±0.26 (slow)
$NO(X)+N(^2D^2P)$	−0.14±0.13

3.3 Discussion

3.3.1 Branching Ratios

A product branching ratio for $O(^3P)$:NO(X) of 1.4±0.5 was obtained for the 130.2 nm dissociation of N_2O. The VUV detection scheme for O and NO was calibrated by using it with the dissociation of NO_2, which has O + NO as the sole product channel. This required the normalization of the O^+ and NO^+ ion signals for variations in the laser powers, using measured power dependences both for N_2O and NO_2 photodissociations. The O^+:NO^+ ratio was taken as

$$O^+/\ NO^+ = (S_O/S_{NO}) = f_{SO}[O(^3P)]/[NO]$$

where S_O/S_{NO} is the experimental sensitivity relating the ion signal to number densities, [ ] refers to the number densities, and f_{SO} is the spin-orbit fraction of $O(^3P_J)$ with J=2. For the dissociation of NO_2 at 355 nm, the relative sensitivity factor is determined because $[O(^3P)]/[NO]$ is unity and f_{SO} has been previously measured to be 0.82.[7] With the relative sensitivity factor known and the spin-orbit fraction measured as 0.51 for N_2O dissociation, the above relationship yields $[O(^3P)]/[NO]$. The $\pm 2\sigma$ uncertainty includes contributions from f_{SO} and the relative ion signals from more than 50 TOF mass spectra recorded at various laser powers. The resulting branching ratio relies on the assumption that the relative sensitivity for O + NO measured with NO(v= 0,1) in the NO_2 system does not change significantly over the NO(v= 0-9) range of vibrational levels accessible in the N_2O system. That this assumption is reasonable is demonstrated by the good agreement of the TKER distributions of NO^+ with $N(^2D,^2P)$, for which the detection efficiency is independent of the vibrational level of the NO partner.

A product branching ratio for $N(^2D)$:$N(^2P)$ of 3 was obtained for the 130.2 nm dissociation of N_2O from comparison of the TKER distributions of the N atoms with that of NO^+. Beginning with TKER distributions normalized to unit area, the $N(^2D)$ TKER was scaled to fit the NO^+ TKER at energies between 1 and 2 eV. Below 1 eV, $N(^2P)$ begins to make a contribution, especially near 0.5 eV. Scaling the $N(^2P)$ TKER to make up the difference between the results for NO^+ and $N(^2D)$ yields the branching ratio. The sum of the contributions from the N atoms accounts for about 90% of the NO^+ TKER. The regions of mismatch fall in the high energy wing of the $N(^2D)$ distribution and in the valley of the bimodal $N(^2P)$ distribution (this bimodality appears to be real). It is unlikely that the NO(v) detection efficiency behaves strangely at these particular internal energies. It is more likely that the difficulties in determining and subtracting the background

contribution to the weak NO^+ image are the source of the problem. Considering the poor signal-to-noise ratio of both the NO^+ and the $N(^2D)$ TKER distributions, the agreement of the fit is very reasonable. While no uncertainty for the branching ratio is given in Table I, the fit was recognizably worse with $N(^2D)/N(^2P)$ ratios of 2 or 4. The fit assumes that the TKER distributions do not differ between atomic spin-orbit levels. Although this is not the case for $O(^3P_J)$, analysis of $N(^2P_{1/2,3/2})$ images gave insignificantly different TKER distributions. Despite the branching ratio favoring $N(^2D)$ production, the $N(^2P)$ signal was stronger due to the relatively inefficient VUV generation at 124.3 nm compared to 131.05 nm. As well, the ionization step for $N(^2D)$ relied solely on the residual ω_1 ultraviolet laser light, whereas the ionization step for $N(^2P)$ could be effected by the ω_2 visible laser light, which was at least a factor of 5 greater in power.

Product branching ratios for $N_2(A\ ^3\Sigma_u^+)$:$N_2(B\ ^3\Pi_g)$ were determined from the analysis of the $O(^3P_J)$ and N_2^+ images. The ratio of the integrated peaks in the TKER distributions was on the order of unity, although the ratio did depend strongly on the O atom spin-orbit level detected, favoring the $N_2(A\ ^3\Sigma_u^+)$ state for $O(^3P_0)$ and the $N_2(B\ ^3\Pi_g)$ state with $O(^3P_{1,2})$. Witinski et al. also observed this difference with spin-orbit level and our branching ratio results are in reasonable agreement.[2] The branching ratio obtained from the N_2^+ data incorporates contributions from each of the $O(^3P)$ spinorbit levels and is consistent with the weighted average (0.86 ± 0.18) of the $O(^3P_{2,1,0})$ branching ratios, where the weights are the measured relative abundances. The good agreement indicates that the ionization efficiencies of the N_2 $A\ ^3\Sigma_u^+$ and $B\ ^3\Pi_g$ states must not be very different at 130.2 nm. As well, the effect of dissociation at $O(^3P_{2,1,0})$ detection wavelengths differing by 0.3 nm is shown to be insignificant.

Previous investigators[8,9] have detected visible N_2 (B $^3\Pi_g$-A $^3\Sigma_u^+$) fluorescence, following N_2O dissociation only at shorter wavelengths where the emission is from higher vibrational levels. Their experiments were not sensitive to infrared emission from the low vibrational levels of the B state populated at dissociation wavelengths near 130 nm. As a result, they grossly underestimated the B state population, reporting an A:B branching ratio of 99 at 123.6 nm. Despite the uncertainty in how the relative ionization efficiencies of the two excited electronic states of N_2 change with wavelength, it is clear from the N_2^+ images that the order of magnitude of the A/B ratio is closer to unity than to 100, with values estimated to be 0.3, 0.84, and 3.3 at dissociation wavelengths of 124.3, 130.2, and 131.05 nm, respectively. Because of uncertainties in the relative ionization efficiency mentioned above, we cannot say whether or not there is a systematic trend in the ratio with dissociation wavelength.

Combining the three branching ratios relating O(^{3}P) to NO, N(^{2}P) to N(^{2}D), and N_2(A $^3\Sigma_u^+$) to N_2(B $^3\Pi_g$), the branching between the dissociation channels (5)-(8) at 130.2 nm is

$$\mathrm{O(^3P)+\ N_2(A\ ^3\Sigma_u^+)\ :\ O(^3P)+\ N_2(B\ ^3\Pi_g)\ :\ N(^2D)+NO(X^2\Pi)\ :\ N(^2P)+NO(X^2\Pi)}$$
$$= 2.6 : 3 : 3 : 1$$

with $\pm 2\sigma$ uncertainties about 35%. Black et al. have determined the O(^{1}S) quantum yield from N_2O dissociation at 129 nm to be 0.95±0.05 by direct observation of the O(^{1}S) emission and by comparing the signal level with that from the photodissociation of CO_2 at 112 nm where the quantum yield is unity.[9] They then fixed the quantum yield to be 0.93 because they observed a 0.07 quantum yield for N_2(A $^3\Sigma_u^+$). Nee et al. also measured the O(^{1}S) quantum yield at dissociation wavelengths close to 130 nm by observing O(^{1}S) emission enhanced by

Xenon buffer gas.[10] From the data in their Fi. 3, the average quantum yield is 0.88±0.05 for wavelengths of 128, 129, 132, and 133 nm. It is reasonable and convenient to fix the O(^{1}S) quantum yield to be 0.90 at 130.2 nm and to treat our combined branching ratios as % quantum yields. At 130 nm, the quantum yield for N_2(A $^3\Sigma_u^+$) is given by Black et al. as 6±1%. Under their conditions, the N_2(B $^3\Pi_g$) would have been completely quenched to N_2(A $^3\Sigma_u^+$) at the start of the experiment,[11] so that 6% is the sum total of O(^{3}P) + N_2(A,B). This agrees well with our sum of 2.6%+3%. Their quantum yield of 3±3% for N(^{2}D) at 130 nm is also in agreement with our value. A comparison of our O(^{1}S) and O(^{3}P) signal levels after normalizing for laser powers and oscillator strengths for the atomic transitions confirmed the order of magnitude difference in quantum yields for the two electronic states. We cannot give a better estimate without quantifying the relative efficiencies for VUV generation at 121.76 and 130.2 nm and the relative ionization efficiencies of the resonantly excited O atoms.

Vibrational distributions of the N_2 and NO products are qualitatively consistent with the structures of the N_2O excited states determined by Hopper,[12] who found both the N-NO distance and the N-NO distance to be 1.3 Å. Because the N-N distance in the N_2 products is 1.094, 1.293, and 1.2123 Å for the X, A, and B states, respectively,[13] it is clear that the N_2 product will be vibrationally excited for all three channels. Similarly, the N-O bond distance is 1.1508 Å for the NO(X) product,[13] so this product also is likely to be vibrationally excited. The vibrational combs in Figs. 3.3 and 3.4 provide an indication of the excited vibrational distributions for these diatomic fragments.

3.3.2 Angular Distributions

The electronic configuration of the $^1\Sigma^+$ ground state of N_2O is $...(7\sigma)^2(1\pi)^4(2\pi)^4$. *Ab initio* calculations by Hopper[12] have confirmed that the strong absorption near 130 nm is mainly due to the electronic excitation to the linear $D^1\Sigma^+$ state the electronic configuration of which is $...(7\sigma)^2(1\pi)^4(2\pi)^3 4\pi$. The $\pi-\pi^*$ excitation weakens both the N-O and the N-N bonds. In addition to the $D^1\Sigma^+$ state, there is also a $^3\Pi_v$ state in this same energy region, just slightly higher in energy than the $D^1\Sigma^+$ state at the linear geometry. Its electronic configuration is $...(7\sigma)(1\pi)^4(2\pi)^3 3\pi$, where the last electron is in an antibonding orbital on the N-N and N-O bonds.

Let us first consider the dissociation from these states to N_2 + O. For dissociation along the NN-O coordinate, the $D^1\Sigma^+$ state correlates in the linear configuration to $N_2(X\ ^1\Sigma_g^+)$ + O(^{1}S), but in the bent configuration it becomes a $^1A'$ state and correlates to $N_2(A\ ^3\Sigma_u^+)$ + O(^{3}P). Thus, there is an avoided seam along the dissociation surface. Along this same NN-O coordinate, the $^3\Pi_v$ state correlates in the linear configuration to $N_2(A\ ^3\Sigma_u^+)$ + O(^{3}P), but in the bent configuration, the $^3\Pi_v$ state becomes two components of a Renner-Teller pair, a lower $^3A'$ state and an upper $^3A''$ state. The lower-energy $^3A'$ component correlates to $N_2(B\ ^3\Pi_g)$ + O(^{3}P), while the higher-energy $^3A''$ component correlates to $N_2(A\ ^3\Sigma_u^+)$ + O(^{3}P). Thus, there is also a seam of crossing between the $^3A'$ and $^3A''$ surface, but this crossing is allowed because the surfaces are of different symmetries. Next, consider the dissociation from the $D^1\Sigma^+$ and $^3\Pi_v$ states to N + NO. For dissociation along the N-NO coordinate, the $D^1\Sigma^+$ state correlates in the linear configuration to N(^{2}P) + NO($X^2\Pi$), and in the bent configuration it correlates to N(^{2}D) + NO(X $^2\Pi$). Thus, there is another avoided seam along this dissociation surface. Along this N-NO coordinate, the $^3\Pi_v$ state correlates in the linear configuration to N(^{2}D)

+ NO($X^2\Pi$), but in the bent configuration, again, there are two Renner-Teller components. Both the $^3A'$ component and the $^3A''$ component correlate to N(^{2}D) + NO($X^2\Pi$). Note that because, in the linear configuration, the $D^1\Sigma^+$ state, which is lower in energy than the $^3\Pi_v$ state, correlates to the more energetic N(^{2}P) + NO($X^2\Pi$) channel, while the $^3\Pi_v$ state correlates to the less energetic N(^{2}D)+ NO($X^2\Pi$), there must be a crossing between these surfaces. In the absence of spin-orbit coupling, the crossing is allowed, but in its presence the $^3A'$ and $^1A'$ components may have an avoided crossing.

The angular distributions of the products can help to determine which of these dissociation paths are the most important. In a linear molecule for prompt axial recoil, the expected values of the anisotropy parameter β are, using linearly polarized light, +2 for a parallel transition and -1 for a perpendicular transition. For the dissociation of a bent triatomic molecule, again in the axial recoil limit and for linear polarization, the anisotropy parameter is related to the angle θ between the recoil direction and the transition dipole moment $\beta = 2P_2(\cos(\theta))$, where $P_2(x)$ is the second Legendre polynomial.

We now enumerate the various product channels, note how each may be reached, and comment on the expected and measured anisotropy parameters. The $N_2(X\ ^1\Sigma_g^+)$ + O(^{1}S) channel is accessed by dissociation only from the $D^1\Sigma^+$ state in the linear configuration. For a parallel transition, such as from the N_2O ground state $X\ ^1\Sigma^+$ to the optically allowed $D^1\Sigma^+$ state, the limiting value of the anisotropy parameter β is well-known to be +2 for dissociation by linearly polarized light or -1 for dissociation by unpolarized light.[14] The angular distribution of the O(^{1}S) fragment from the 130-nm photodissociation measured by Stone et al. using an unpolarized light source is consistent with β = -1, indicating a parallel transition.[15]

Similarly, our own measurement using linearly polarized light gave β =1.3 for the O(^{1}S), consistent with a parallel transition, but perhaps not quite as high as we might have expected.

The $N_2(A\ ^3\Sigma_u^+)$ + O(^{3}P) channel is accessed (a) from the $D^1\Sigma^+$ state after it bends to become $^1A'$, (b) from the $^3\Pi_v$ state in the linear configuration, or (c) from the upper $^3A''$ Renner-Teller component of the $^3\Pi_v$ state in the bent configuration. The basic transition is again a parallel one, but two of the three possibilities come from dissociation of a bent N_2O. Thus, we might expect that β could be reduced from its limiting value of 2.0. Somewhat surprisingly, the data indicate β =2.0, so that it must be that dissociation takes place from a nearly linear configuration. The correlations calculated by Hopper would suggest that dissociation proceeds following crossing to the $^3\Pi_v$ state.

The $N_2(B\ ^3\Pi_g)$ + O(^{3}P) channel can come only from the lower $^3A'$ component of the $^3\Pi_v$, state in the bent configuration (assuming that only the $D^1\Sigma^+$ and $^3\Pi_v$ states to be involved). The data indicate that β =1.3, in general agreement with a parallel excitation followed by dissociation from a somewhat bent geometry. Witinski et al. also reported a similar value of β =1.5 for this channel.[2]

The N(^{2}D) + NO($X^2\Pi$) channel can come (a) from the $^3\Pi_v$ state in a linear configuration, (b) from either of the Renner-Teller components of the $^3\Pi_v$ state in a bent configuration, or (c) from the bent ($^1A'$) configuration of the $D^1\Sigma^+$ state. The N(^{2}D) image gives a β of 0.5, suggesting that the bent configurations dominate.

Finally, the N(^{2}P) + NO($X^2\Pi$) channel comes only from the linear configuration of the $D^1\Sigma^+$ state. We expect β =2, but the data suggest something lower, β =0.5-0.7. The value of the anisotropy parameter, based on measurement of the NO($X^2\Pi$)

channel, is also somewhat lower than expected from the measured parameters for the N(^{2}P) and N(^{2}D) , but this determination is rendered less certain due to the necessity for background subtraction in the measurement.

The variations of the anisotropy parameter β with internal energy of the diatomic fragment indicated in Table I can be understood qualitatively based on the model described by Demyanenko et al.[16] in which the transverse recoil component is calculated based on the angular momentum calculation. The principal result is given by the equation

$$\sin^2\phi = \frac{\mu_{diatom} r^2}{\mu_{A-BC} R_C^2 (\frac{E_{avl}}{E_{rot}} - 1)}$$

where ϕ is the angle between the actual and axial recoil directions, $E_{avl} = E_{trans} + E_{rot}$ is the energy available to the fragments, exclusive of internal vibrational and electronic energy, r is the diatomic bond length, and R_c is a critical distance parameter at which the angular momenta have reached their final values. Because we do not resolve the rotational energy of the fragment, we cannot perform a quantitative analysis, but it is clear from the formula that as E_{avl} decreases, assuming comparably sampled values for E_{rot}, the denominator will decrease, leading to larger predictions for ϕ. Because, in this theory, $\beta = 2P_2(\cos(\alpha \pm \phi))$, it is clear that β should decrease with decreasing E_{avl} . This behavior is observed for the O(^{1}S) + N_2(X,v) channel, the O($^3P_0$) + N_2(A,v) channel, the O + N_2(B,v) channel, and the N(^{2}P) + NO(X$^2\Pi$) channels.

3.4 Conclusions

Dissociation of N_2O near 130 nm leads to at least five product channels, (4)-(8). Based on this and previous work, it appears that channel (4) dominates, with minor contributions from (5)-(8), all of the quantum yields between 1% and 3%. Both of the diatomic products are vibrationally excited in all accessible channels. The spin-orbit ratios, relative branching ratios, and anisotropy parameters have been determined, as listed in Tables I and II. The dynamics of the dissociation appear to be consistent with the calculations of Hopper; dissociation takes place predominantly through the $D^1\Sigma^+$ state, with likely participation of the $^3\Pi_v$ state.

BIBLIOGRAPHY

[1] P. J. Crutzen *Q. J. R. Meteorol. Soc.*, vol. 96, p. 320, 1970.

[2] M. F. Witinski, M. Ortiz-Suárez, and H. F. Davis *J. Chem. Phys.*, vol. 122, p. 174303, 2005.

[3] R. J. Wilson, J. A. Mueller, and P. L. Houston *J. Chem. Phys. A.*, vol. 101, p. 7593, 1997.

[4] B. Y. Chang, R. C. Hoetzlein, J. A. Mueller, J. D. Geiser, and P. L. Houston *Rev. Sci. Instruments.*, vol. 69, p. 1665, 1998.

[5] B. R. Cosofret, H. M. Lambert, and P. L. Houston *J. Chem. Phys.*, vol. 117, p. 8787, 2002.

[6] H. M. Lambert, A. A. Dixit, E. W. Davis, and P. L. Houston *J. Chem. Phys.*, vol. 121, p. 10437, 2004.

[7] J. Miyawaki, T. Tsuchizawa, K. Yamanouchi, and S. Tsuchiya *Chem. Phys. Lett.*, vol. 165, p. 168, 1990.

[8] L. C. Lee and M. Suto *J. Chem. Phys.*, vol. 80, p. 4718, 1984.

[9] G. Black, R. L. Sharpless, T. G. Slanger, and D. C. Lorents *J. Phys. Chem.*, vol. 62, p. 4266, 1975.

[10] J. B. Nee, J. C. Yang, P. C. Lee, X. Y. Wang, and C. T. Juo *Chin. J. Phys.*, vol. 37, p. 172, 1999.

[11] R. A. Young, G. Black, and T. G. Slanger *J. Chem. Phys.*, vol. 50, p. 303, 1969.

[12] D. G. Hopper *J. Chem. Phys.*, vol. 80, p. 4290, 1984.

[13] G. Herzberg, *Spectra of Diatomic Molecules*. Van Nostrand , New York, 1950.

[14] R. N. Zare *Mol. Photochem.*, vol. 4, p. 1, 1972.

[15] E. J. Stone, G. M. Lawrence, and C. E. Fairchild *J. Chem. Phys.*, vol. 65, p. 5083, 1976.

[16] A. B. Demyanenko, B. Dribinski, H. Reisler, H. Meyer, and C. X. W. Qiane *J. Chem. Phys.*, vol. 111, p. 7384, 1999.

CHAPTER 4

THE $O(^1D)$+ N_2O REACTION: VIBRATIONAL AND ROTATIONAL DISTRIBUTIONS

4.1 Introduction

The reaction between $O(^1D)$ and N_2O is both of importance to atmospheric chemistry and interesting from the point of view of a multichannel reaction:

$$O(^1D) + N_2O \rightarrow N_2 + O_2 \qquad k = 4.9 \text{ x } 10^{-11} \text{ cm}^3 \text{ molec}^{-1} \text{ s}^{-1} \text{ (1a)}$$

$$\rightarrow NO + NO \qquad k = 6.7 \text{ x } 10^{-11} \text{ cm}^3 \text{ molec}^{-1} \text{ s}^{-1} \text{ (1b)}$$

The reaction rate increases as the relative velocity between the $O(^1D)$ and N_2O decreases. The reaction is important to atmospheric chemistry because the branching ratio between the two channels is fundamental to the steady-state concentration of ozone.[1] N_2 and O_2 are major constituents of the stratosphere, so reaction to this channel is neutral to the concentration of ozone. Production of 2 NO molecules, however, decreases the ozone concentration because NO is a catalyst in a scheme which converts two ozone molecules to three molecules of oxygen. Thus, not only is the odd oxygen species $O(^1D)$ destroyed in (1b), but the products go on to catalyze the destruction of further odd oxygen.

There is considerable uncertainty concerning the vibrational distribution of the NO products from reaction (1b); we summarize previous results briefly here and return to this issue in the discussion section. Brouard et al.[2,3] reported the stereochemistry of the reaction by probing NO in v=15 and 16. Akagi et al.[4–6]

reported that two different NO molecules were formed, a "new" one from the abstraction of an N atom by $O(^1D)$ from N_2O and the other from the "old" NO left behind. By using isotopic labeling they found that the new NO had a peak in the vibrational distribution at high vibrational levels, whereas the old one peaked at v=0. Pisano et al. reported the distribution from v=0 to v=12 and found it to peak at v=7.[7] Hancock and Haverd measured time-resolved infrared emission of NO(v=1-14) and concluded that the vibrational distribution for these states decreased monotonically from a maximum population at v=1.[8] An earlier paper using this technique was reported by Wang et al.[9] Finally, Lu, Liang, and Lin have recently investigated the translational energy distribution of the N_2 + O_2 and NO + NO products from the $O(^1D)$ + N_2O reaction.[10] For the NO + NO products, they report that the translational energy release consumes 31% of the available energy. It remains unclear from these studies both what the vibrational distribution actually is and why so many measurements differ from one another. All attempts to measure the nascent rotational distribution find that it is very hot. Kawai et al.[11] report temperatures up to 20 000 K, while Tsurumaki et al.[12] found 10 000 K.

The reaction of $O(^1D)$ with N_2O has also been investigated in clusters, typically by photodissociation of one N_2O of the N_2O dimer.[13,14] This "pre-aligned" reaction produces NO vibrational excitation, but it may be somewhat different from that of the normal reaction. In particular, it appears that the rotational temperatures of the NO products are typically colder, on the order of 60-100K, than those reported for the normal reaction above.

Theoretical investigations of the $O(^1D)$ +N_2O reaction are limited. Gonzalez and coworkers investigated it by trajectory calculations using both A′ and

A″ surfaces calculated using the CASPT2/CASSCF level.[15–17] Last et al. heve investigated the $O(^1D)$ + N_2O reaction on an ab initio surface calculated using the Møller-Plesset method.[18] More recently, Akagi et al.[19] developed a surface at the CASPT2/cc-pVDZ level for the reaction, and Takayanagi and Akagi have reported the results of classical trajectory studies.[20] Finally, Takanayagi has performed mixed quantum-classical wavepacket calculations to explore this system.[21]

In this paper we report a detailed investigation of the vibrational and rotational distribution of the NO product of (1b) using multiphoton ionization to probe the NO product following reaction of $O(^1D)$ and N_2O in a molecular beam.

4.2 Experiment

Figure 4.1 presents a schematic drawing of the experimental apparatus. The molecular beam setup is a modified version of the single beam ion imaging apparatus described elsewhere.[7] In a manner similar to the setup first described by Welge and coworkers,[22] a second nozzle has been added parallel to the first one in preparation for future reaction product imaging studies. The apparatus has been equipped with additional electrodes for DC or pulsed slice imaging capabilities when desired.

A mixture of O_3 (1%) and N_2O (6%) seeded in He (-78° C), backing pressure 2 psi) was expanded supersonically through a 500 μm diameter nozzle, and collimated with a 500 μm diameter skimmer located 2 cm from the nozzle. Two unfocused counter-propagating laser beams intersected the molecular beam at right angles in the center of repeller and extractor electrodes and 7.5 cm from the nozzle. One laser dissociated the O_3 molecules to generate $O(^1D)$ atoms, while the other state selectively ionized the resulting $NO(X^2\Pi)$ molecules formed in the

$O(^1D)+N_2O \rightarrow 2\ NO(X^2\Pi)$ reaction. The ion cloud was then extracted through an optimized velocity-map spectrometer and impinged onto a gated dual micro-channel plate coupled to a fast phosphor screen (Burle, P-47) located at the end of the TOF tube. The ion intensity was measured with a PMT (Thorn EMI) and passed to a computer, where a boxcar records the NO signal strength as a function of laser wavelength.

The O_3 molecules were dissociated by the linearly polarized 266 nm laser light generated by the fourth harmonic of a Nd-YAG laser (Spectra-Physics GCR-6) operating at 10 Hz. Typical energies were 5-6 mJ/pulse. The laser beam size was apertured to 5 mm, which gave the maximum signal to noise ratio under our detection conditions. The polarization axis of the dissociation light was vertical to the plane defined by the molecular beam and the 266 laser direction.

The $O(^1D)$ ions created by a 203.7 nm, 2+1 REMPI processes,[23] were used to check the molecular beam properties and to optimize production of this species. The 203.7 nm light was generated by doubling the output of a Nd-YAG (Spectra-Physics GCR-270) pumped dye laser (PDL-2) in a KDP crystal and then summing the fundamental with the doubled light in a BBO crystal. Typical powers were 0.9 mJ/pulse at 10 Hz.

NO molecules were state-selectively detected by a 1+1 REMPI processes.[24,25] The tunable 220-246 nm laser light used to probe the NO molecule was generated by doubling the output of a Nd-YAG (GCR-230) pumped Scanmate OPPO laser (Lambda Physik). The probe laser polarization was the same as that of the 266 nm laser. The probe laser was set to arrive 20 ns after the 266 nm laser. To generate the appropriate light, three types of dyes were used: Coumarin 450, 460 and 480. Typical energies were 0.9-1 mJ/pulse or 0.5-0.6 mJ/pulse. The pulse

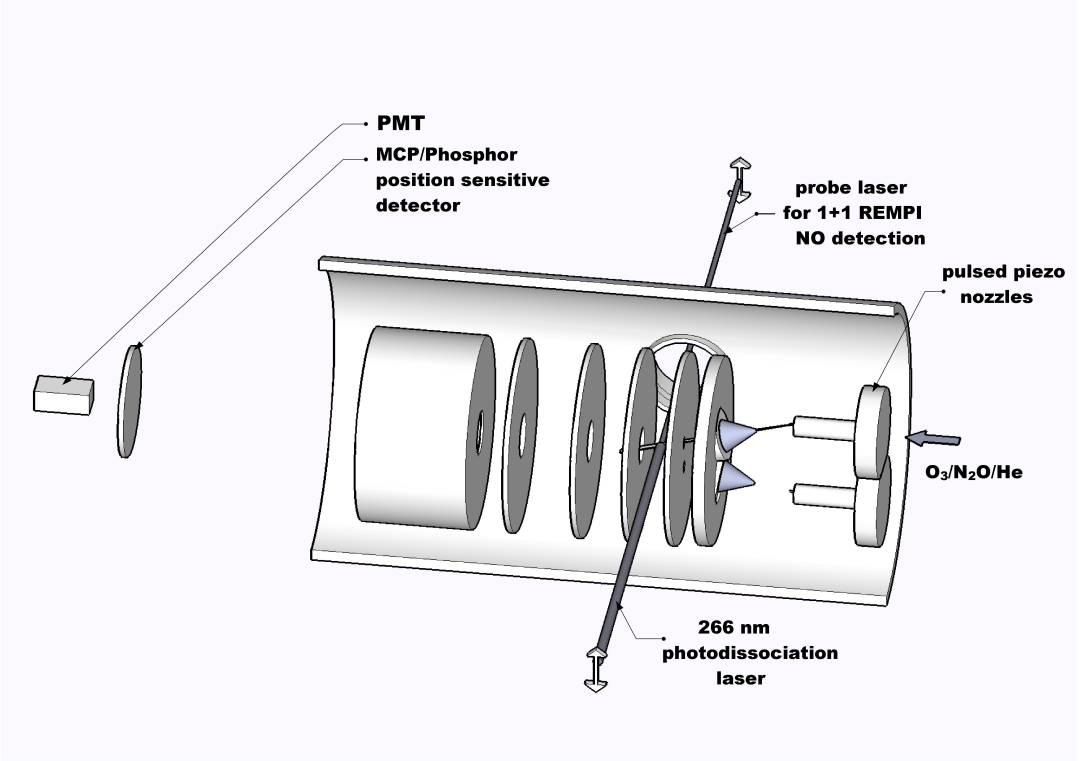

Figure 4.1: Scaled Diagram of the Experimental Apparatus

energy levels were chosen so that the NO ion signal did not saturate. Care was also taken by routinely monitoring the signal under small magnetic fields to ensure that no electrons generated by secondary processes caused any ion background. A series of overlapping 1.5 nm scans were recorded at 30 laser shots/step, monitoring the laser pulse energies before and after each scan.

Ultrahigh purity N_2O (99.99%) and He (99.999%) were purchased from Matheson Tri-Gas and Airgas, respectively, and used without any further purification. O_3 was generated by a commercial ozonator and kept in a silica gel trap at - 78

C° before mixing.[26]

4.3 Results

4.3.1 Background Sources

Molecular Beam Characterization

The molecular beam can be characterized by expanding a mixture of NO molecules and an inert gas in the beam and detecting the NO molecules with 1+1 REMPI.

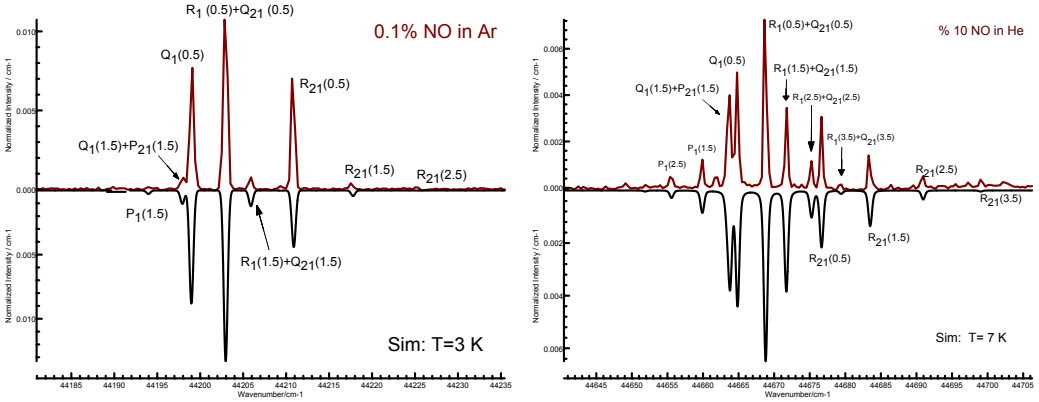

(a) γ (0-0) transition (b) γ (1-1) transition

Figure 4.2: Molecular Beam Characterization

We can measure the rotational beam temperature as 3 K for γ (0-0) and as 7 K for γ (1-1) transitions, with Ar and He mixtures respectively, as seen in Figure 4.2. This indicates a very efficient rotational cooling in the supersonic expansion.

Background Sources

There are three possible NO background sources in the experiment. First, some residual NO molecules are in thermal contact with the chamber walls. At 300 K these molecules account for almost all the thermal NO molecules populating v=0 and around 0.01% of those populating the v=1 level. This source was very small compared to our signal, 3-4% for v=0. The signal for NO($X^2\Pi$) (v=0) from this source has been characterized, as shown in Fig. 4.3(a), which is a scan of the probe laser with the molecular beam off.

A second background source is the NO generated and detected by the interaction of N_2O and the probe laser; that is the background is there even when there is no ozone in the beam mixture and when 266 nm light is blocked. The background was weak; we estimate it to account for less than 7% of the signal in v = 0. To characterize this background source for higher vibrational levels, we put pure N_2O in the beam and scanned the probe laser wavelength over strong transitions used for NO($X^2\Pi$) v=1, 2 and 3 detection. Fig.4.3(b) shows the N_2O + probe laser scan for NO($X^2\Pi$) (v=1) . Similar but much weaker beam-dependent spectra have been obtained for NO($X^2\Pi$) v=2 and 3, with rotational temperatures close to 300 K, but the signal was too weak for a proper fit.

Honma and coworkers have shown that N_2O dimers formed in the molecular beam can be photolyzed by 193 nm photons, creating NO($X^2\Pi$) through the $O(^1D).N_2O$ reactant pair.[13] Gödecke et al. have recently studied the same reaction.[14] They report rotational temperatures around 150 K, whereas Honma and coworkers report 60-100 K for all vibrational levels up to v=7. Our v=1 scan showed a rotational temperature around 350 K, much higher than found from the dimer experiments. Thus it seems unlikely that dimers are the source of this

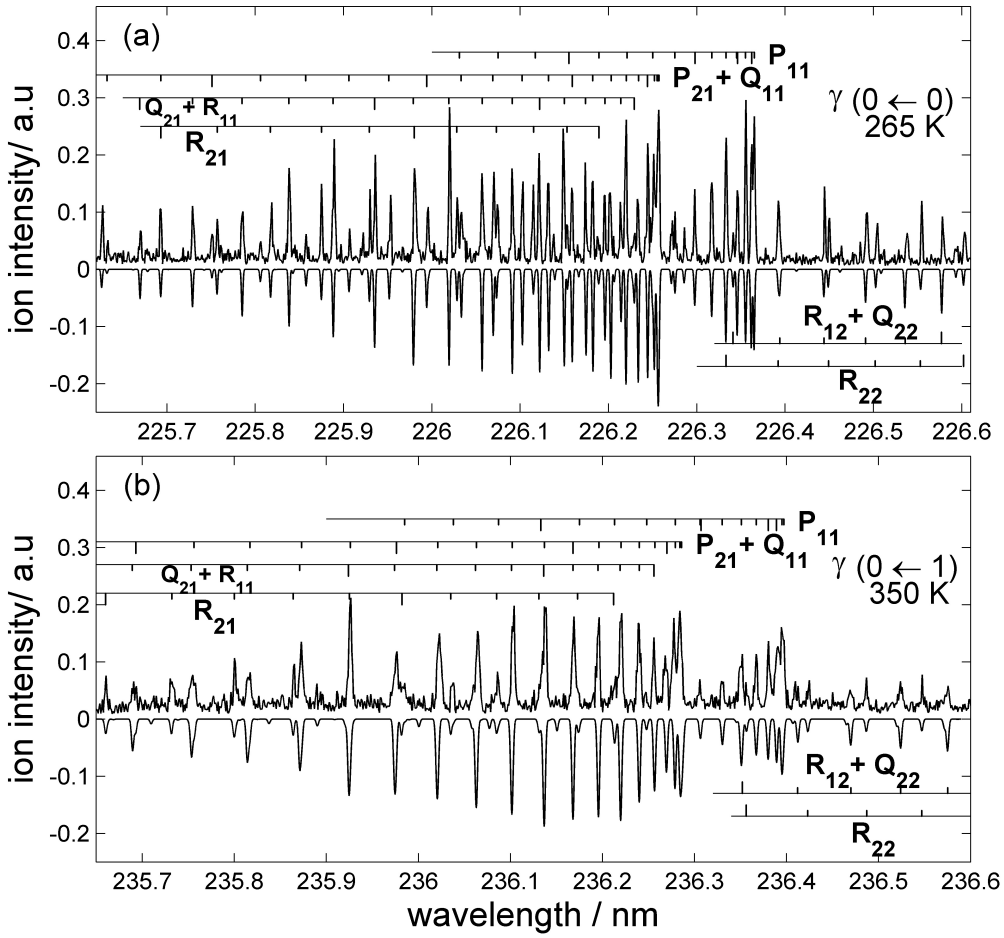

Figure 4.3: NO^+ ion signal from (a) probe laser, v=0. (b) probe + N_2O, v=1

background. We also didn't observe a direct mass spectroscopic signature of the dimer.

Whatever the source of the background, in our experiments performed under the O_3/N_2O mixture, the $v = 0$ background contribution from this beam dependent source is less than 7% of our net signal, and higher levels are absent. Apart from their small intensity in the experiment, both the first and second background sources have a T_{rot} around 300 K, much lower in comparison to that found for vibrational levels monitored in the full experiment on the O_3/N_2O mixture. In

summary, the second background makes a small contribution, but only to $v = 0$.

The total background in the scans is around 10-15%, and much of this belongs to a third source of NO. Analysis of this source shows that it is a scaled down version of our actual experimental signal. This can be understood as a result of dissociation of O_3 by the probe laser.

Dissociation of ozone is through the Hartley band, which peaks at 254 nm. Absorption of a photon in this band results mostly in a photodissociation through two channels, both of which create translationally hot $O(^1D)$ atoms.[27,28] $O_3 + h\nu \rightarrow O_2(a^1\Delta_g) + O(^1D)$ channel opens for $\lambda < 310$ nm, whereas $O_3 + h\nu \rightarrow O_2(b^1\Sigma_g^+) + O(^1D)$ channel opens for $\lambda < 267$ nm. About 90% of the dissociation in this band proceeds by the first channel. Since our probe laser scans extend to the middle of the Hartley band, it is to be expected that some O_3 molecules will dissociate by this channel after absorbing the probe laser light. The resulting $O(^1D)$ atoms would react with the N_2O, creating NO molecules, which are then ionized by the same pulse. Fortunately, this is a multiphoton process, so that the signal is not too large with our unfocused laser pulses. Furthermore, the O_3 absorption cross section at the wavelengths used for probing NO is small compared to that at 266 nm, and the probe pulse energy is a factor of 5 smaller then that of the 266 pulse. All of these factors result in small magnitude for the background signal caused by the probe laser. That this background closely mimics the actual signal is not surprising, considering that the difference between the relative collision energies of the precursor $O(^1D)$ atoms created by two lasers is much smaller then the large exothermicity of the reaction.[15,27]

4.3.2 Analysis

Spectroscopy of the Nitric Oxide Molecule

The Schrödinger Equation for a diatomic molecule can be written as follows:

$$\frac{1}{m}\sum_i\left(\frac{\partial^2\psi}{\partial^2 x_i^2}+\frac{\partial^2\psi}{\partial^2 y_i^2}+\frac{\partial^2\psi}{\partial^2 z_i^2}\right)+\frac{1}{M_k}\sum_k\left(\frac{\partial^2\psi}{\partial^2 x_k^2}+\frac{\partial^2\psi}{\partial^2 y_k^2}+\frac{\partial^2\psi}{\partial^2 z_k^2}\right)+\frac{8\pi^2}{h^2}(E-V)\psi=0 \tag{4.1}$$

where x_i, y_i and z_i are electronic coordinates (mass m) and x_k, y_k and z_k are nuclear coordinates (mass M_k). The separation of variables $\psi = \psi_e(..., x_i, y_i, z_i, ...)\psi_{vr}(..., x_k, y_k, z_k, ...)$ is possible under the Born-Oppenheimer Approximation, namely the observation that the $\frac{\partial\psi_e}{\partial x_k}$ and $\frac{\partial^2\psi_e}{\partial^2 x_k^2}$ terms can be neglected. This is possible because this amounts to the fact that the heavy nuclei move slower than the lighter electrons.

ψ_e and ψ_{vr} are then given by the solutions of the following equations:

$$\sum_i\left(\frac{\partial^2\psi_e}{\partial^2 x_i^2}+\frac{\partial^2\psi_e}{\partial^2 y_i^2}+\frac{\partial^2\psi_e}{\partial^2 z_i^2}\right)+\frac{8\pi^2 m}{h^2}(E^{el}-V_e)\psi_e=0 \tag{4.2}$$

$$\frac{1}{M_k}\sum_i\left(\frac{\partial^2\psi_{vr}}{\partial^2 x_k^2}+\frac{\partial^2\psi_{vr}}{\partial^2 y_k^2}+\frac{\partial^2\psi_{vr}}{\partial^2 z_k^2}\right)+\frac{8\pi^2}{h^2}(E-E^{el}-V_n)\psi_{vr}=0 \tag{4.3}$$

where V_e and V_n are electronic and nuclear Coulomb potentials, respectively. The first of these equations is the Schrödinger equation for electrons moving in the field of nuclei with V_e as potential energy. Since V_e is said to be a slow varying function of the nuclear coordinates, this dependency is usually altogether ignored and E^{el} can be considered independent of the nuclear coordinates. The second equation describes the dynamics of the nuclei under the potential $E^{el} + V_n$. The minimum

of this potential as a function of the nuclear coordinates is defined as the electronic energy E_e of the state associated with ψ_e.

The rotation and vibration of diatomic molecules can be modelled by the sum of the vibrational mode of an anharmonic oscillator and the rotational mode of a nonrigid rotator. However, since vibration and rotation happen simultaneously, during the vibration the internuclear distance is changing, causing a different moment of inertia at each moment. A vibrating rotator model takes this interaction into account by requiring a mean rotational constant over a vibrational period. This is justified because the period of the vibrational oscillation is much smaller compared to the period of a rotation.[29]

Pauling and Wilson have shown that a separation of variables is possible for the eigenfunctions of the "vibrating rotator", such as $\psi_{vr} = \frac{1}{r}\psi_v(r - r_e)\psi_r$ where ψ_v is the eigenfunction the linear anharmonic oscillator and ψ_r is actually the same as the rotational wave function of a hydrogen atom.[29]

With these considerations, we obtain the term values for a vibrating rotator in a particular electronic state as follows: [a]

$$\begin{aligned} T &= \frac{E_e}{hc} + G(v) + F_v(J) \\ &= \frac{E_e}{hc} + w_e(v+1/2) - w_e x_e(v+1/2)^2 + ... \\ &\quad + B_v J(J+1) - D_v J^2(J+1)^2 + ... \end{aligned} \tag{4.4}$$

$$B_v = B_e - \alpha_e(v+1/2) + ... \tag{4.5}$$

$$D_v = D_e + \beta_e(v+1/2) + ... \tag{4.6}$$

[a]Dunham did a very careful study of the interaction between vibration and rotation. He expressed the term values as $T = \sum_{l,j} Y_{l,j}(v+1/2)^l J^j(J+1)^j$ where one would expect to find $Y_{10} = w_e, Y_{20} = w_e x_e, Y_{01} = B_e, Y_{02} = D_e, Y_{11} = \alpha_e, ...$ It is found that there are very small deviations from these, typically less than 1 part in 1000 so the term values used in the text are adequate.[29]

In equation 4.4 using J=0 will give the "pure" vibrational energy levels. One should keep in mind that since E^{el} is included in the E_e term, there is an electronic energy component to this vibrational energy term. w_e is the vibrational frequency measured in cm^{-1}, $w_e x_e$ is a correction factor from the anharmonicity in the molecule's potential energy function. Rotational term values arise from nonzero J values. B_v and D_v are the mentioned mean rotational constants. α_e is small with respect to B_e and β_e is small with respect to D_e.

Orbital Angular Momentum

One can gain more insight to the diatomic molecule, if the "symmetric top" analysis in classical mechanics is considered. In general, the rotational kinetic energy T_{rot} of a rigid body can be written as $T_{rot} = \frac{1}{2}\sum_{i,j} I_{i,j} w_i w_j$ and the angular momentum is given as $L_i = \sum_j I_{i,j} w_j$ where w_i are the components of the angular momentum vector in the body coordinate system. These equations considerably simplify if a particular set of axes can be found such that the off diagonal elements of the inertia tensor are zero. These axes are called the *principal axes* and according to a theorem in classical mechanics, they coincide with the symmetry axes of a rigid body. Then we have,

$$L_i = \sum_j I_j \delta_{i,j} w_j = I_i w_i \tag{4.7}$$

$$T_{rot} = \frac{1}{2}\sum_{i,j} I_i \delta_{i,j} w_i w_j = \frac{1}{2}\sum_i I_i w_i^2 \tag{4.8}$$

From 4.7, it is seen that for any rotation around a principle axis, the angular momentum and angular velocity are aligned with that axis (This effect of the inertia tensor identifies the principle axes - if they exist - , since by definition these are the eigenvectors of the inertia tensor). When two of the three moments of

inertia are equal, $I_1 = I_2 > I_3$, we have a "symmetric top". If the finer details of the electrons in the diatomic molecule is ignored, this is a good classical model for rotations.

To describe the dynamics of the rotation, one needs to solve the Lagrange's equation. The Eulerian angles are chosen as the generalized coordinates. For the ψ coordinate we have:

$$\frac{\partial T}{\partial \psi} - \frac{\mathrm{d}}{\mathrm{d}\, t}\frac{\partial T}{\partial \dot{\psi}} = 0 \tag{4.9}$$

The angular momentum components are related to the Eulerian angles, so the derivatives involving the $\frac{\partial w_i}{\partial \psi}$, $\frac{\partial w_i}{\partial \dot{\psi}}$ can be easily evaluated in 4.9, to give the equation $(I_1 - I_2)w_1 w_2 - I_3 \dot{w}_3 = 0$. From symmetry, the index of w can be permuted to get the **Eulerian Equations** for force free motion:

$$\begin{aligned}(I_2 - I_3)w_2 w_3 - I_1 \dot{w}_1 &= 0 \\ (I_3 - I_1)w_3 w_1 - I_2 \dot{w}_2 &= 0 \\ (I_1 - I_2)w_1 w_2 - I_3 \dot{w}_3 &= 0\end{aligned} \tag{4.10}$$

Since $I_1 = I_2$ in a symmetric top, from 4.10 we get $w_3(t) =$ constant. Moreover, solving the other two equations in equation 4.10, we get $w_1(t)=$ A $cos(\Omega t)$ and $w_2(t)=$ A $sin(\Omega t)$. These two equations describe a circular path, with angular frequency $\Omega=\frac{I_3 - I_1}{I_1} w_3$. This means that the angular velocity vector $\boldsymbol{w}$ revolves around the principal axis in the body coordinate system. This motion is called *precession*. The shape defined by this motion is identified as the *body cone* and is shown in Figure 4.4.

From Equations 4.7 and 4.8 we have $T_{rot} = \frac{1}{2}\boldsymbol{w}.\boldsymbol{L}$ requiring the angle between $\boldsymbol{w}$ and $\boldsymbol{L}$ stay constant. Then to an observer in the space fixed coordinate system,

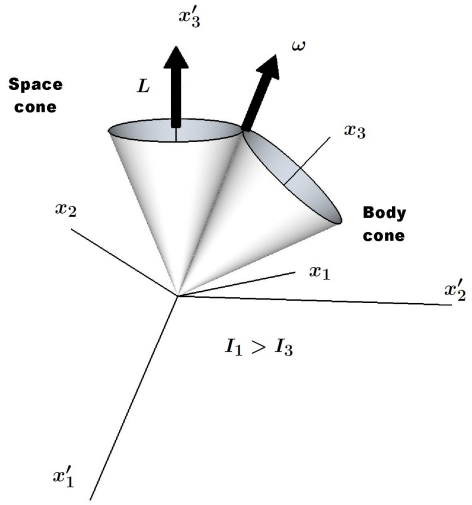

Figure 4.4: Classical Symmetric Top Motion. Also see reference.[30]

$\boldsymbol{w}$ traces another cone, around $\boldsymbol{L}$, which is a constant of motion, since there is no torque. This path is identified as the *space cone*, shown together with the body cone, in Figure 4.4. It can be easily shown that $\boldsymbol{L}$, $\boldsymbol{w}$ and the principal axis (internuclear axis for the diatomic) are all in the same plane. This results in a composite motion of two cones, one of them rolling over the other one, with angular frequency Ω. An important consequence of these considerations is that the component of the angular momentum vector along the principal axis is constant, during the composite motion of these cones.

In the quantum mechanical treatment of a diatomic molecule, the Hamiltonian, H, is no longer invariant under rotation, so the angular momentum $\boldsymbol{L}$ is not a constant of the motion. However, the system still possesses a symmetry, namely the *axial symmetry*. Just as translational symmetry (invariance of H under translation) results in the conservation of momentum, time displacement symmetry (invariance of H under the corresponding symmetry operator) results in the conservation of energy, the axial symmetry will give rise to a conserved quantity: component of the electronic angular momentum along the internuclear axis.

Due to the classical symmetric top model, it is said that a *precession* of $\boldsymbol{L}$ takes place around the principal axis (i.e. internuclear axis). Analogous to the classical model, the component of L along the internuclear axis is a constant of the motion, with the value $M_L(h/2\pi)$. One should remember that, due to the loss of spherical symmetry compared to an atom, the meaning of $\boldsymbol{L}$ is blurred as angular momentum and its value cannot be assigned, while the well defined M_L can take the values $M_L = L, L-1, L-2...0, ...-L+1, -L$. It should be expected that one can identify two degenerate electronic eigenfunctions such as to remain unchanged or change sign after a reflection operation at any plane passing thru the internuclear axis. The choice of the quantum number $\Lambda = |M_L| = 0, 1, 2, ...,$ L satisfies this, resulting in L+1 distinct quantum states with different energy. These states are designated as $\Sigma, \Pi, \Delta, \Phi$ respectively.

Spin

For states with non-zero Λ, the spin is precessing under the influence of the magnetic field of the electrons. The space quantization of total spin $\boldsymbol{S}$ along the field direction, is denoted by Σ and the allowed values are $\Sigma =$ S, S-1,..0,..-S+1, -S. The total electronic angular momentum along the principal axis is then given by the usual angular momentum addition rules in quantum mechanics: $\Omega = |\Lambda + \Sigma|$. The resulting 2S+1 components will have different energies and the multiplet can be denoted as ${}^{2S+1}\Lambda_\Omega$, each with an electronic energy of $T_e = T_0 + A\Lambda\Sigma$ where A is the spin-orbit coupling constant for a given multiplet term. Σ electronic states are also said to have the same 2S+1 multiplicity, even if the spin has no field space quantization along the internuclear axis.

Coupling of Electronic Motion and Nuclear Rotations

In the quantum mechanical modelling of a diatomic, the mutual interaction of the vibration and rotation is taken into account by the "vibrating rotator" model, culminating in the ψ_{vr} part of the total wavefunction. The interaction of vibrational and electronic motions is taken into account by the E^{el} term in equation 4.3, defining the potential energy under which the nuclear wavepacket moves. The interaction of rotational and electronic motions is subtle, in that it requires certain set of assumptions to identify the quantum numbers describing the motion.

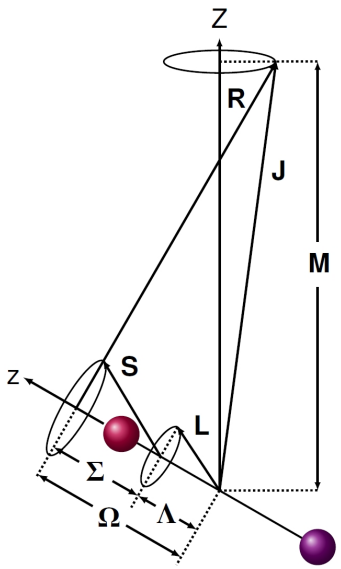

Figure 4.5: Hund's Case a Coupling

Hund first noticed that the resulting energy pattern can be classified as a function of two parameters: The electronic angular momentum and the internuclear axis coupling and Y, the ratio of the spin-orbit coupling parameter to the rotational constant, B_v. In the case of the ground state of the NO molecule, at least for small rotation, one can assume that $\boldsymbol{L}$ is coupled strongly to the internuclear axis and $\boldsymbol{S}$, being strongly coupled to $\boldsymbol{L}$, is also coupled to the internuclear axis.

Then, the addition of the $\boldsymbol{\Omega}$ and nuclear rotation $\boldsymbol{N}$ gives the resultant $\boldsymbol{J}$. This classification is called Hund's Case a and is shown in Figure 4.5. The NO($A^2\Sigma$) state has $\Lambda = 0$, so the spin is not coupled to the internuclear axis, and one should directly couple $\boldsymbol{S}$ to the nuclear rotation. This is the other limiting situation in Hund's set, namely spin-uncoupling, corresponding to a small Y value. We do not need to pursue the $\boldsymbol{L}$ uncoupling from the axis for NO molecule.

In reality, for higher rotations, the NO($X^2\Pi$) behaves as a transition from case a to b. The rotational term values for the doublets have been calculated by Hill and Van Vleck, for any spin-orbit coupling as:

$$F_1(J) = B_v\{(J+\frac{1}{2})^2 - \Lambda^2 - \frac{1}{2}\sqrt{4(J+\frac{1}{2})^2 + Y(Y-4)\Lambda^2}\} - D_v J^4 \quad (4.11)$$

$$F_2(J) = B_v\{(J+\frac{1}{2})^2 - \Lambda^2 + \frac{1}{2}\sqrt{4(J+\frac{1}{2})^2 + Y(Y-4)\Lambda^2}\} - D_v (J+1)^4 \quad (4.12)$$

where $Y = A/B_v$ and A is the spin-orbit coupling constant. F_1 and F_2 form the $X^2\Pi_{1/2}$ and $X^2\Pi_{3/2}$ multiplets for the NO molecule. For large spin-orbit coupling constant A (i.e. Hund's case a) it can be seen that these equations converge to the rotational term values in equation 4.4, with an effective rotational constant $B_{eff} = B(1 \pm \frac{B}{A\Lambda})$ for each multiplet.

Analysis Method

A preliminary analysis of the 1+1 REMPI spectrum was required due to the very hot rotational temperature observed. Pisano et al. have showed that the rotationally cooled spectrum is dominated by γ transitions.[7] A cross-correlation algorithm was written for calibrating the spectrum with γ transitions only, simulated with LIFBASE software,[31] assuming an initial rotational and vibrational temperature.

To determine the relative population of each NO($X^2\Pi$) vibrational level pro-

duced in the reaction, we modeled the NO γ and β transitions with Pgopher.[32] Fermi's golden rule states that the one photon transition probability is proportional to the square of the $<\mu.E>$ matrix element, where E is the polarization vector of our linearly polarized probe laser and μ is the molecule's transition dipole moment. Therefore, we need to use only first-order spherical transition moments in the simulation, i.e., electric dipole moments.

The spectroscopic constants for the ground state NO($X^2\Pi$) are taken from Amiot[33] and Engelman[34,35] et al., and NO($B^2\Pi$) state from Huber and Herzberg[29] and Hamilton et al.[36] NO($A^2\Sigma$) state has been recently revisited by Danielak and coworkers.[37] Since the observed spectrum is rotationally hot, the rotational constants B_v and D_v are statistically significant. For the β system, the D_v values are less certain, so we used the set of rotational constants from Hamilton et al., derived from the literature in a self consistent manner.

The following procedure had been followed for the analysis. First, a constant rotational temperature, T_{rot} is assumed for all vibrational levels. A section of the data is picked and an iterative fitting is performed for all individual γ bands extending into the chosen region. Because the γ and β bands are two competing absorption systems with different ionization efficiencies, one needs to also check for β bands in each region.[38] Thus, the same iteration is repeated for β transitions in each data segment. After an initial fit, the iteration moves to a neighboring section. Once a reasonable fit is obtained to all the data segments, the iteration set is repeated over the whole of the spectrum again, but this time including the T_{rot} as a fitting parameter in the set. The iterations are continued until satisfactory convergence is attained to the data.

The second step is to relax the universal temperature constraint for the main

bands contributing to the data; a band by band individual T_{rot} fit is performed, allowing for differences in T_{rot} with vibrational level. A Boltzmann rotational distribution is assumed in all fits.

4.4 Discussion

A portion of the recorded spectrum[39] is shown in Figure 4.6, along with the best fit that resulted from the procedure described above. Figure 4.7 shows an expanded version in more detail.

The individual T_{rot} fits showed that the observed vibrational transitions can be well represented by a Boltzmann rotational distribution with a universal T_{rot} around 4500 - 5000 K. Tsurumaki et al.[12] have measured the rotational temperature of NO(v=0) with Doppler-resolved LIF, via the γ (0,0) band for the same reaction, using 193 nm laser pulses to generate the O(^1D) precursor from N_2O. Their reported T_{rot} of 10 000 K contrasts with the 300 K reported by Brouard et al.[2] for the same system. However, both observed very high rotational temperatures for $v > 0$, with Brouard et al. reporting $T_{rot} = 5500$ K, for v=1. The discrepancy at v=0 was probably because of the thermal NO (v=0) in the chamber, dominating the LIF signal in the latter experiment. Kawai et al.[11] recently determined the rotational temperature as $\approx$ 20 000 K for NO (v=0,1,2) for the part of the distribution with $J < 80$, as measured under flow conditions. For $J > 80$, they observe a faster decrease in their distribution, corresponding to a somewhat lower rotational distribution. In our fits to the data, we didn't observe strong differences from a Boltzman distribution for $J > 80$ populations.

The contributing transitions in the 220-246 nm range were found to be only

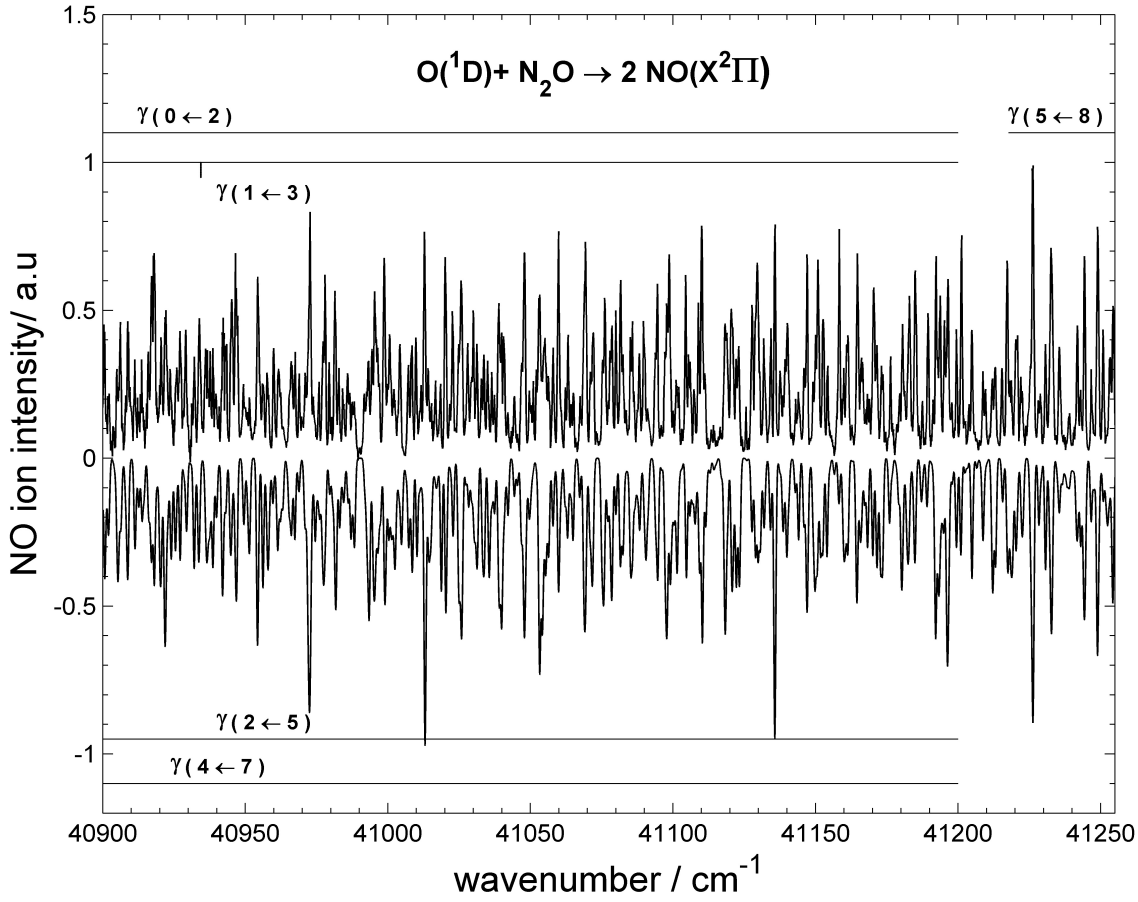

Figure 4.6: 1+1 REMPI spectra of NO($X^2\Pi$) from $O(^1D)+N_2O \rightarrow 2$ NO($X^2\Pi$) reaction. Features from the A $\leftarrow$ X (0,2); (1,3); (2,5); (4,7) bands span the whole range. The (5,8) bandhead and (1,3) band origin are also shown. The upper plot shows the data and the lower one is the simulation with T_{rot} = 4500K.

the γ transitions. Akagi et al.[4,6] have used the B $^2\Pi(v$=0-2) $\leftarrow$ X $^2\Pi(v$=11-17) transitions for the LIF detection, and Pisano et al.[7] observed the NO β system REMPI for this reaction, but both had rotationally cooled sources, allowing them to isolate these tiny signals from the otherwise congested spectrum. The NO molecule is very efficiently detected with REMPI processes,[38] so under cooled conditions the β system would be an additional source of information.

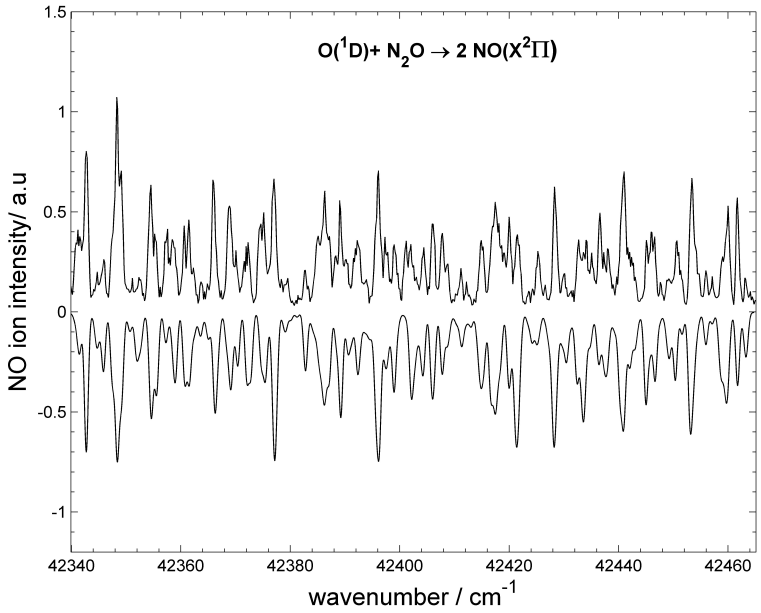

Figure 4.7: 1+1 REMPI spectra of NO($X^2\Pi$) from $O(^1D)+N_2O \rightarrow 2$ NO($X^2\Pi$) showing a smaller spectral region expanded so as to demonstrate the degree of agreement between the measured spectrum(upper plot) and the calculated one(lower plot). The γ (0,1) and γ (3,5) transitions span the entire area with contributions from the γ (4,6) transitions.

The electric dipole transition matrix element fit parameter input to the Pgopher program can be converted to relative vibrational populations for each band, using the known electronic transition moments, $R_e(r_{v',v''})$[40] and Franck-Condon factors.[40,41] The relative vibrational populations are given in Table 1.

4.4.1 Origin of Vibrational Excitation

The origin of the inverted vibrational distributions can be qualitatively understood by considering the two competing factors affecting it, the energy randomization rate in the intermediate and the available time for this randomization to take place.

Table 4.1: $NO(X^2\Pi)$ Vibrational State Distribution of the $O(^1D)+N_2O \rightarrow 2\ NO(X^2\Pi)$ reaction

Vibrational State	Observed Transition(s)	Relative Populations [b]	Weighed Averages [c]
0	γ (0,0)	0.088 ± 0.008	0.089 ± 0.008
1	γ (0,1)	0.036 ± 0.003	0.039 ± 0.010
	γ (1,1)	0.075 ± 0.014	
2	γ (0,2)	0.041 ± 0.004	0.043 ± 0.003
	γ (2,2)	0.047 ± 0.009	
3	γ (1,3)	0.125 ± 0.010	0.116 ± 0.015
	γ (2,3)	0.095 ± 0.014	
4	γ (3,4)	0.098 ± 0.015	0.100 ± 0.015
5	γ (4,5)	0.134 ± 0.021	0.212 ± 0.026
	γ (3,5)	0.220 ± 0.011	
	γ (2,5)	0.242 ± 0.019	
6	γ (4,6)	0.128 ± 0.014	0.130 ± 0.015
7	γ (6,7)	0.095 ± 0.026	0.124 ± 0.024
	γ (5,7)	0.103 ± 0.016	
	γ (4,7)	0.173 ± 0.021	
8	γ (6,8)	0.118 ± 0.025	0.093 ± 0.015
	γ (5,8)	0.084 ± 0.014	
9	γ (6,9)	0.053 ± 0.015	0.054 ± 0.015

[b] The relative vibrational distribution from each band is given before averaging and weighing the data. Since the fluctuations of error in the bands occurring in the same spectral region are correlated, about a ±15% fit precision to peak height is assumed in the error calculations. The uncertainties include the estimated uncertainty in the transition probabilities. Transition probabilities for bands $\gamma(6,7)$, $\gamma(6,8)$ and $\gamma(6,9)$ were taken from ref 40 and carry higher uncertainties because a Morse oscillator wave function is assumed. [c]The weighed mean and error in the weighed mean are calculated using eqs 4.21 and 4.22 from Bevington's Error Analysis book.[42] Following averaging, the weighed mean is normalized to a sum of unity over all observed levels.

Ab initio calculations of potential energy surfaces[16,17,43] show that the NO + NO products correlate on two $1A''$ surfaces and one $1A'$ surface to $O(^1D)$+ N_2O. All surfaces for $O(^1D)$+ N_2O leading to NO + NO products pass through a dimer configuration. The lifetime of the intermediate for this reaction is estimated to be on the order of 1 ps or less,[12,44] on the order of the rotational period of the *cis*-NO dimer.[12] Considering the large exothermicity and the barrierless PES for the reaction, with this seemingly short lived intermediate, the NO molecule can be expected to show characteristics of a nonstatistical vibrational distribution , rather like inverted vibrational distribution for the *new* OH product in the $O(^1D)$ + H_2O reaction,[45,46] as compared to the old OH from the original water , which shows a colder vibrational distribution in comparison to a statistical one. However, in the reaction we are studying, this effect is counterbalanced by the intramolecular vibrational relaxation (IVR), which is proportional to the density of states in the intermediate and to the square of the effective coupling between the vibrational states. The two similar masses of the NO molecules are likely to increase the density of states available in the intermediate, as discussed by Akagi et al.[5] Indeed, Akagi et al. found that the coupling between the two local vibrational modes increases if the hydrogen atom in the reactant is replaced by a nitrogen atom.[6] Kawai et al. confirm that the stretching modes are strongly coupled for the reaction path which passes through the trans-minimum.[43] These two competing mechanisms are likely to end up leaving NO molecules with an inverted vibrational distribution under high energy collisions with a direct mechanism, and possibly with more chance of energy redistribution at lower energy collisions.

The importance of O(^{1}D) velocity relaxation

An important question to address is why there is so much discrepancy between the various measurements of the NO vibrational distribution produced following reaction of O(^{1}D) with N_2O. Hancock and Haverd provided a very thoughtful discussion of the potential problems in each of the reported experiments, but they were still at a loss to explain the discrepancies shown in their Fig. 4.[8] These distributions, along with results from the current study (plotted as weighted averages from Table 1), are shown in Figure 4.8. An alternate approach is to ask if there might be some hidden variable that has hitherto been unaccounted for; perhaps all the measurements are correct, but there is a difference in conditions that has not been noticed. We argue here that the hidden variable is the velocity distribution associated with the collision between O(^{1}D) and N_2O.

The experiments are of two broad types. The first type are those done in a molecular beam, including that by Pisano et al.[7], that by Lu, Liang and Lin,[10] and the current experiment. The second type are those done in static or flowing bulb experiments. The conditions for the latter are as follows: Akagi et al. generated O(^{1}D) from 266 nm photolysis of O_3 and performed the experiment at a total pressure of 1.0 Torr at a delay time of 5 μs.[4,6] Brouard et al. used 193-nm photodissociation of N_2O as an O(^{1}D) source and performed the experiment at a total pressure of up to 200 mTorr with a delay time of 200 ns.[2,3] Hancock and Haverd used a similar source with total pressures of 0.3-1.0 Torr and a delay time of around 40 μs.[8]

The conditions for the molecular beam experiments are as follows. Pisano et al.[7] used a molecular beam experiment in which an O_3/N_2O mixture was photolyzed at 266 nm near the throat of a nozzle expansion. Most O(^{1}D) atoms flew

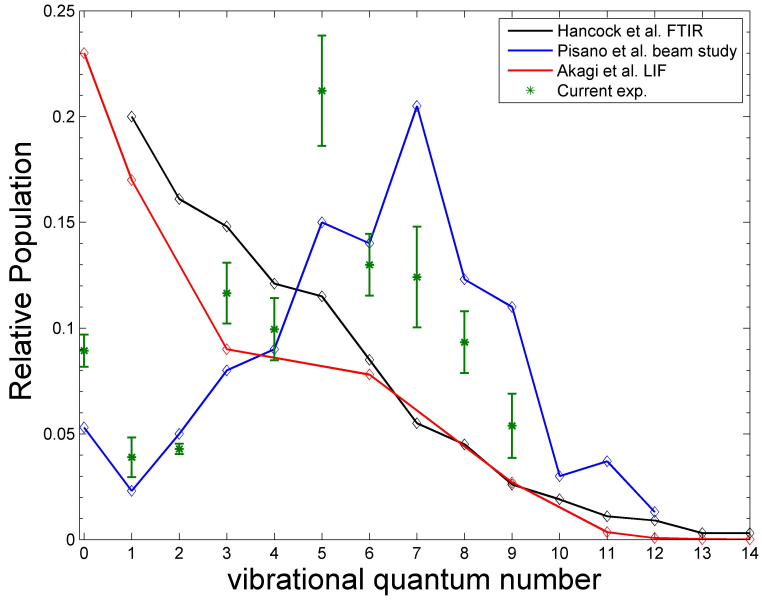

Figure 4.8: Comparison of the relative NO($X^2\Pi$) vibrational level population results from the current experiment and with those from the previous molecular beam and bulk studies. A shoulder is observed in the v = 4 - 8 range in the bulk studies, whereas an inverted population is observed in the molecular beam studies.

out of the beam before reacting, but those that reacted did so within roughly a single collision. The resulting NO was rotationally relaxed by collisions in the expansion, but vibrational relaxation under such conditions is negligible. The NO products were detected downstream, in the collisionless part of the beam, by a $1{+}1'$ REMPI scheme. Because of the rotational relaxation, the spectra were simpler to interpret than those in the current experiment. The conditions for the current experiment are similar to those used by Pisano et al. in that a molecular beam of an O_3/N_2O mixture is employed with the photodissociation at 266 nm, but both dissociation and detection are accomplished in the collisionless part of the beam. Again, most of the O(^{1}D) products escape from the beam, but a few collide with N_2O to produce NO products, which are probed within a delay time of 20ns. These products presumably have the vibrational and rotational distribu-

tions characteristic of a single collision at high velocity. The velocity distribution of the $O(^1D)$ in the current and Pisano et al. experiments is peaked at 2.2 x 10^5 cm/s. Lu, Liang and Lin used a cross molecular beam apparatus.[10] The $O(^1D)$ was produced by 157 nm photolysis of O_2 , giving a velocity of 2.1 x 10^5 cm/s.

While much attention in the bulb experiments has been focused on the possibility of vibrational relaxation of the NO, the possibility of velocity relaxation of the $O(^1D)$ has not been considered. We hypothesize that "slow" $O(^1D)$ reacts with N_2O to give a statistical vibrational distribution, perhaps through an insertion/complex-forming process, whereas "fast" $O(^1D)$ reacts to give an inverted distribution,through a more direct mechanism. For any individual experiment, the result would then be a weighted sum of the statistical distribution, given by the data of Akagi et al.,[6] in our Figure 4.8, and an inverted distribution given by the current data, also shown in our Figure 4.8. The distributions Akagi et al. (Figure 3),[6] and of Hancock and Haverd (Figure 5)[8] do seem to show a shoulder at v=4-8 on top of a more statistical distribution, albeit one that peaks at the lowest vibrational level. Thus, our hypothesis is that the $O(^1D)$ reacts from a relaxed velocity distribution in the bulb experiments, favoring the statistical branch of the NO vibrational distribution. In the beam experiments, on the other hand, if the $O(^1D)$ produced by the reaction does not react on its first collision with N_2O, it leaves the beam and doesn't react at all. Thus, it reacts with the velocity provided by the O_3 dissociation, a velocity high enough to favor the stripping branch of the NO vibrational distribution.

The only potential counterexample to this interpretation is the result by Lu, Liang, and Lin.[10] Although they do not directly measure the NO vibrational or rotational distribution, they find that the translational energy deposition in the

reaction is 31% (28 kcal/mol out of 89.7 kcal/mol available), a value to high in their view to allow for the high vibrational and rotational excitation observed in the current experiments and in those of Pisano et al. Our own measurement of the rotational temperature suggests that the total rotational energy for the two fragments is less than 20 kcal/mol (out of 91.5 kcal/mol available) That would still leave roughly 42 kcal/mol available for vibration, or about 47%. While this fraction is less than the 75-87% estimate of Pisano et al., it still means that the average NO molecule would have 21 kcal/mol in vibration and would be at v= 4, as compared to the peak of the distribution at $v = 5$ in the current experiment. To be completely consistent with our measurement, the translational energy disposal would need to be only 18 kcal/mol, as compared with their measurement of 28 kcal/mol.

Some estimates show the plausible importance of velocity relaxation. The total rate constant for reaction of $O(^1D)$ with N_2O is 1.2 x 10^{-10} cm^3 $molec^{-1}$ s^{-1}. Measurements have been made on the relaxation of $S(^1D)$ velocities in collisions with He, Ar, and Xe[47] and of $O(^1D)$ velocities in collisions with He, Ne, Ar, N_2, and O_2.[48,49] For $O(^1D)$ with N_2, the rate of velocity relaxation is 1.99 x 10^{-10} cm^3 $molec^{-1}$ s^{-1}. Assuming the velocity relaxation cross section for $O(^1D)$ + N_2O to be similar to that for $O(^1D)$ + N_2, velocity relaxation is 1.7 times faster than the reaction rate. Thus, the $O(^1D)$ in bulb experiments is cooling translationally nearly twice as fast as it is reacting. While the $O(^1D)$ + N_2O relaxation rate might be somewhat dissimilar from that for $O(^1D)$ + N_2, the fact that the rates of velocity relaxation $O(^1D)$ and $S(^1D)$ by nearly all measured partners are comparable suggests that the conclusion that velocity relaxation competes effectively with reaction is likely to be a robust one. Repetition of previous experiments but with N_2O as the target could confirm this conclusion. However, given the current state

of knowledge it appears plausible that under bulb conditions, the reaction might favor predominantly a statistical distribution whereas under beam conditions it might favor predominantly an inverted distribution.

A molecular beam experiment might be designed to check this hypothesis by using slower O(^{1}D) atoms to initiate the reaction. In such an experiment in the current apparatus, ozone would need to be dissociated with wavelengths longer than 290 nm for the reaction to have small collision energies comparable to those in a cell experiment. Unfortunately, the ozone dissociation cross section is about an order of magnitude smaller at those wavelengths. Our estimate is that the ratio of signal to "probe laser and beam background" would be around 1. Furthermore, the probe laser would still create fast O(^{1}D) atoms that would complicate the interpretation. Thus, this experiment was not attempted.

4.4.2 1+1′ Detection of NO

A two level system shown in Figure 4.9 and described by a set of rate equations is an accurate representation of the NO REMPI detection.[38,50] The applicability of the rate equations requires that the laser bandwidth is larger than the linewidth of the resonant step and either the ionization rate is much faster than the Rabi oscillation frequency or the laser phase diffusion rate (which describes the strength of the stochastic process of laser phase fluctuations) is much bigger than the Rabi frequency.[51] In REMPI detection, these requirements are satisfied and the coherence effects of the Rabi oscillations are washed out. One can assume a quasi-equilibrium in the resonant step, while the ionization step is seen as a leakage.

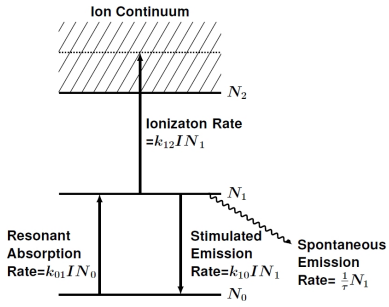

Figure 4.9: Two Level System

The rate equations show in Figure 4.9 can be solved exactly[38] to give

$$N_2(\Delta t) = N_0 F(k_{01}, k_{12}, I\Delta t) \quad where$$

$$F = (1 - \frac{1}{2B}\{(A+B)\exp[\frac{1}{2}(A-B)I\Delta t] - (A-B)\exp[\frac{1}{2}(A+B)I\Delta t]\}) \tag{4.13}$$

$$with \quad A = 2k_{01} + k_{12}\ and\ B = (4k_{01}^2 + k_{12}^2)^{\frac{1}{2}}$$

In the region where the resonant step is not saturated Equation 4.13 can be approximated[52] by $N_2 \simeq \frac{1}{2}\sigma_2 N_0 \sigma_1 I_2 I_1$ allowing for different intensities I_1, I_2 for the resonant and ionization steps. σ_1 is the absorption cross section of the resonant step and σ_2 is the ionization cross section from the intermediate level. It is seen that the ion signal will be proportional to the absorption from the ground level given that the ionization cross section from different intermediate levels is insensitive to the ionization wavelength. This has been experimentally shown to be the case for $\gamma(0,0), \gamma(1,1)$ and $\gamma(2,2)$ transitions.[53] This wavelength independence is also supported by theoretical calculations.[54,55] However, ionization cross sections are not always easy to establish from intermediate levels and it is conceivable that one

hits a particular resonance during the wavelength scans. To check this, at least in part, we look at the 1+1′ REMPI detection of NO, where the ionization step is set at a fixed laser wavelength and we compare the ion signal with the 1+1 REMPI detection.

The ionization cross section is on the order of $7\text{x}10^{-19}\text{cm}^2$ at 266 nm from the A state and the absorption cross section is around $2\text{x}10^{-16}\text{cm}^2$ for the $\gamma(0,0)$ band (similar numbers can be assumed with the wavelengths in study). The mismatch of these cross sections limits the detection capability in 1+1 REMPI, since the stimulated emission will move some of the the population back to the ground level. If the ionization and absorption steps are separated and one uses a bigger ionization laser intensity compared to the probe intensity, the ion signal can be improved as shown by Hippler et al. By solving the rate equations they showed that the 1+1′ REMPI detection designed this way, can generate an order of magnitude or more ion signal, compared to the 1+1 REMPI.[24]

We repeated the experiment under the same conditions, using a 1+1′ REMPI detection scheme, as described by Hippler et al., for a limited probe laser wavelength range. The resonant probe transition wavelength was obtained using a frequency doubled FL2002 dye laser, pumped by an excimer 308 nm laser. The ionization step uses the excimer output, 308 nm, but optically delayed so that the ionization laser arrives 10 ns later then the probe laser. 266 nm is produced by the frequency doubled output of a Nd-YAG laser. Delay between the photodissociation and probe laser is set to 20 ns. The energy of the photodissociation laser is the same as before. The probe laser energy is $\simeq$ 0.15 mJ and the 308 nm energy is $\simeq$ 1 - 2 mJ. The 308 nm laser is loosely focused with a 1 meter focal length lens. The probe laser energy is recorded during the scan, and the ion signal is normalized to

power at the end [d].

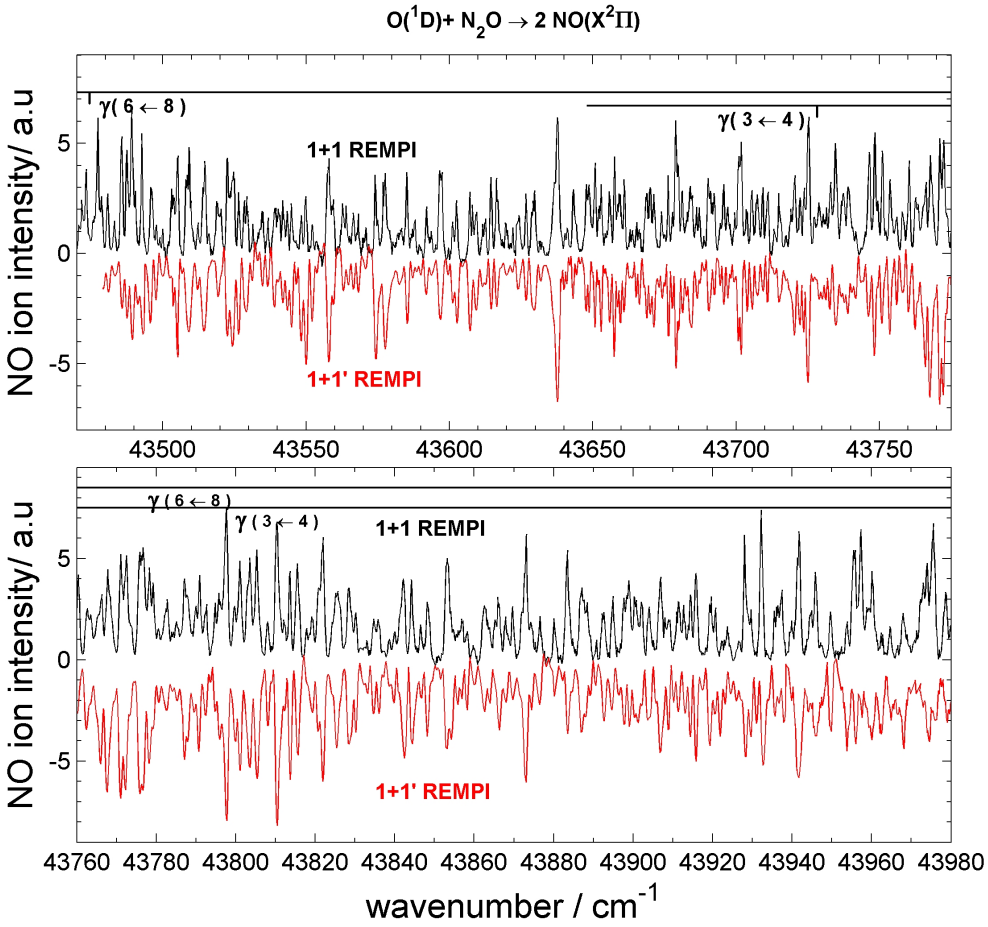

Figure 4.10: Comparison of the 1+1 REMPI and 1+1′ REMPI detection schemes for NO($X^2\Pi$) molecule from the $O(^1D)+N_2O\rightarrow$ 2 NO($X^2\Pi$) reaction. The $\gamma(6,8)$ and $\gamma(3,4)$ transitions cover the 43450^{-1} - 43980 cm^{-1} region, while $\gamma(2,3)$ and $\gamma(5,7)$ transitions also contribute to the signal. The band origin of $\gamma(6,8)$ and $\gamma(3,4)$ are indicated. $\gamma(3,4)$ transition bandhead is also seen. Positive section shows the 1+1 REMPI, whereas 1+1′ REMPI signal is inverted for easy comparison.

Figure 4.10 shows the resulting 1+1′ REMPI spectra, compared with the data recorded with the 1+1 REMPI scheme spectra, obtained in the same region. The

[d] Application of Equation 4.13 shows that the ion signal is neither linear nor quadratic in the probe laser energy. However, in the energy region of interest, Hippler et al. showed that a linear dependence can be assumed.

ion signals are normalized and given in arbitrary units.

Overlaying the two spectra shows that they fit together closely. This indicates that, for the transitions considered in Figure 4.10, the ionization step does not cause more efficient detection of one band compared to the other. All bands enjoy an increase in detection efficiency equally, but it is because of the separation of ionization and resonant steps in 1+1′ REMPI. The same argument is valid in the similar experiments of Pisano et al.[7] for this reaction, where an inverted population is observed. Therefore we can argue that the 1+1 REMPI ion signal can be modelled with the absorption in the resonant step, as is assumed in this work.

4.5 Conclusions

An inverted vibrational distribution and a very hot rotational distribution is observed in the NO product channel of N_2O collisions with fast $O(^1D)$ atoms. The translational relaxation of $O(^1D)$ in bulb experiments probing the same reaction is hypothesized to play a role in their observation of colder and more statistical NO vibrational distributions.

We conclude that an inverted vibrational distribution in this channel is likely to be the result of a direct mechanism, whereas a statistical outcome can dominate at lower collision energies through an insertion type mechanism and with the help of efficient coupling of NO stretching modes in the collision complex.

Extending the reduced dimensionality QCT calculations[44,56] to full three dimensions may shed light to the precise origins of the observed distribution. Ex-

perimentally, isotopically labeled species can be used to get more information on this channel, if a 2-fold congested spectrum can be similarly analyzed. A more informative study would be a state-selected crossed molecular beam investigation, which is currently underway in our lab. In this experiment, ozone is dissociated in one beam, and the product $O(^1D)$ flies to a beam of N_2O, where the reaction takes place. Separating the location of the probe laser from the ozone source circumvents creation of fast $O(^1D)$ by the probe laser, but the signal is still expected to be small due to the necessity of creation of slow $O(^1D)$ at wavelengths where ozone does not absorb strongly. [e]

[e]This work has been published as *$O(^1D)$ + N_2O Reaction: NO Vibrational and Rotational Distributions*, O. Tokel, J. Chen, C. K. Ulrich and P. L. Houston, The Journal of Physical Chemistry A, 114, 11292, 2010. It is reprinted with permission from The Journal of Physical Chemistry A, American Chemical Society. Copyright 2010.

BIBLIOGRAPHY

[1] J. R. Wiesenfeld *Acct. Chem Res.*, vol. 15, pp. 110–116, 1982.

[2] M. Brouard, S. P. Duxon, P. A. Enriquez, R. Sayos, and J. P. Simons *J. Phys. Chem.*, vol. 95, pp. 8169–8174, 1991.

[3] M. Brouard, S. P. Duxon, P. A. Enriquez, and J. P. Simons *J. Chem. Phys.*, vol. 97, pp. 7414–7422, 1992.

[4] H. Akagi, Y. Fujimura, and O. Kajimoto *J. Chem. Soc. Faraday Trans.*, vol. 94, pp. 1575–1581, 1998.

[5] H. Akagi, Y. Fujimura, and O. Kajimoto *J. Chem. Phys.*, vol. 110, pp. 7264–7272, 1999.

[6] H. Akagi, Y. Fujimura, and O. Kajimoto *J. Chem. Phys.*, vol. 111, pp. 115–122, 1999.

[7] P. J. Pisano, M. S. Westley, and P. L. Houston *Chem. Phys. Lett.*, vol. 318, pp. 385–392, 2000.

[8] G. Hancock and V. Haverd *Phys. Chem. Chem. Phys.*, vol. 5, pp. 2369–2375, 2003.

[9] X. B. Wang, H. Z. Li, Q. H. Zhu, F. N. Kong, and H. G. Yu *J. Chin. Chem. Soc*, vol. 42, pp. 399–402, 1995.

[10] Y. J. Lu, C. W. Liang, and J. J. Lin *J. Chem. Phys.*, vol. 125, pp. 133121–1–133121–8, 2006.

[11] S. Kawai, Y. Fujimura, O. Kajimoto, and T. Takayanagi *J. Chem. Phys.*, vol. 120, pp. 6430–6438, 2004.

[12] H. Tsurumaki, Y. Fujimura, and O. Kajimoto *J. Chem. Phys.*, vol. 111, pp. 592–599, 1999.

[13] K. Honma, Y. Fujimura, O. Kajimoto, and G. Inoue *J. Chem. Phys.*, vol. 88, pp. 4739–4747, 1988.

[14] N. Gödecke, C. Maul, A. I. Chichinin, S. Kauczok, and K. H. Gericke *J. Chem. Phys.*, vol. 131, pp. 054307–1–054307–11, 2009.

[15] M. Gónzales, D. Troya, M. P. Puyuelo, R. Sayós, and P. A. Enríquez *Chem. Phys. Lett.*, vol. 300, pp. 603–612, 1999.

[16] M. Gónzales, R. Valero, J. M. Anglada, and R. Sayós *J. Chem. Phys*, vol. 115, pp. 7015–7031, 2001.

[17] M. Gónzales, R. Sayós, and R. Valero *Chem. Phys. Lett.*, vol. 355, pp. 123–132, 2002.

[18] I. Last, A. Aguilar, R. Sayós, M. Gónzales, and M. Gilibert *J. Phys. Chem A.*, vol. 101, pp. 1206–1215, 1997.

[19] H. Akagi, A. Yokoyama, Y. Fujimura, and T. Takayanagi *Chem. Phys. Lett.*, vol. 324, pp. 423–429, 2000.

[20] T. Takayanagi and H. Akagi *Chem. Phys. Lett.*, vol. 363, pp. 298–306, 2002.

[21] T. Takayanagi *Chem. Phys.*, vol. 308, pp. 211–216, 2005.

[22] L. Schnieder, K. Seekamp-Rahn, F. Liedeker, H. Steuwe, and K. H. Welge *Faraday. Discuss. Chem. Soc.*, vol. 91, pp. 259–269, 1991.

[23] S. T. Pratt, P. M. Dehmer, and J. L. Dehmer *Phys. Rev. A.*, vol. 43, pp. 4702–4711, 1991.

[24] M. Hippler and J. Pfab *Chem. Phys. Lett.*, vol. 243, pp. 500–505, 1995.

[25] R. Uberna, R. D. Hinchliffe, and J. Cline *J. Chem. Phys.*, vol. 105, pp. 9847–9858, 1996.

[26] R. E. Stevens, C. W. Hsiao, L. L. N. J. Curro, B. J. Monton, B. Y. Chang, C. Y. Kung, C. Kittrell, and J. L. Kinsey *Rev. Sci. Instrum.*, vol. 69, pp. 2504–2508, 1998.

[27] S. M. Dylewski, J. D. Geiser, and P. L. Houston *J. Chem. Phys.*, vol. 115, pp. 7460–7473, 2001.

[28] K. Takahashi, N. Taniguchi, Y. Matsumi, and M. Kawasaki *Chem. Phys.*, vol. 231, pp. 171–182, 1998.

[29] K. P. Huber, G. Herzberg, and V. Nostrand, *Molecular Spectra and Molecular Structure: IV.Constants of Diatomic Molecules*. 1970.

[30] S. T. Thornton and J. B. Marion, *Classical Dynamics of Particles and Systems*. Brooks Cole, 2003.

[31] J. Luque and D. Crowley, "LIFBASE: Database and Spectral Simulation (version 1.5)," 1999.

[32] C. M. Western, "Pgopher, a Program for Simulating Rotational Structure."

[33] C. Amiot *J. Mol. Spectrosc.*, vol. 94, pp. 150–172, 1982.

[34] R. Engelman, P. E. Rouse, H. M. Peek, and V. D. Baiamonte, *The Beta and Gamma Systems of Nitric Oxide*. Los Alamos Scientific Report LA-4364, 1970.

[35] R. Engelman and P. E. Rouse *J. Mol. Spectrosc.*, vol. 37, pp. 240–251, 1971.

[36] P. A. Hamilton, A. J. Phillips, and R. Windsor *Chem. Phys. Lett.*, vol. 264, pp. 245–251, 1997.

[37] J. Danielak, U. Domin, R. Kępa, M. Rytel, and M. Zachwieja *J. Mol. Spectrosc.*, vol. 181, pp. 394–402, 1997.

[38] D. C. Jacobs and R. N. Zare *J. Chem. Phys.*, vol. 85, pp. 5457–5468, 1986.

[39] O. Tokel. PhD thesis, Cornell University, Ithaca, 2011.

[40] J. Luque and D. R. Crosley *J. Chem. Phys.*, vol. 111, pp. 7405–7415, 1999.

[41] H. A. Ory, A. P. Gittleman, and J. P. Maddox *Astrophys. J.*, vol. 139, pp. 346–356, 1964.

[42] P. R. Bevington and D. K. Robinson, *Data Reduction and Error Analysis for the Physical Sciences*. McGraw-Hill, Inc., 1992.

[43] S. Kawai, Y. Fujimura, O. Kajimoto, T. Yamashita, C. B. Li, T. Komatsuzaki, and M. Toda *Phys. Rev. A.*, vol. 75, pp. 022714–1–022714–11, 2007.

[44] S. Kawai, Y. Fujimura, O. Kajimoto, and T. Yamashita *J. Chem. Phys.*, vol. 124, pp. 184315–1–184315–9, 2006.

[45] C. B. Cleveland and J. R. Wiesenfeld *J. Chem. Phys.*, vol. 96, pp. 248–255, 1992.

[46] D. G. Sauder, J. C. Stephenson, D. S. King, and M. P. Casassa *J. Chem. Phys.*, vol. 97, pp. 952–961, 1992.

[47] G. Nan and P. L. Houston *J. Chem. Phys.*, vol. 97, pp. 7865–7872, 1992.

[48] Y. Matsumi, S. M. Shamsuddin, Y. Sato, and M. Kawasaki *J. Chem. Phys.*, vol. 101, pp. 9610–9618, 1994.

[49] N. Taniguchi, K. Hirai, K. Takahashi, and Y. Matsumi *J. Phys. Chem. A.*, vol. 104, pp. 3894–3899, 2000.

[50] D. C. Jacobs, R. J. Madix, and R. N. Zare *J. Chem. Phys.*, vol. 85, pp. 5469–5479, 1986.

[51] I. Schek and J. Jortner *Chem. Phys.*, vol. 97, pp. 1–11, 1985.

[52] V. S. Letokhov, V. I. Mishin, and A. A. Puetzky *Progg. Quant. Electr.*, vol. 5, pp. 139–203, 1977.

[53] H. Zacharias, F. Rougemont, T. F. Heinz, and M. M. T. Loy *J. Chem. Phys.*, vol. 105, pp. 111–117, 1996.

[54] S. N. Dixit and V. McKoy *J. Chem. Phys.*, vol. 82, pp. 3546–3553, 1985.

[55] V. McKoy, M. Braunstein, H. Rudol, J. A. Stephens, S. N. Dixit, and D. L. Lynch *J. Electron Spectrosc. Rel. Phenom.*, vol. 52, pp. 597–612, 1990.

[56] T. Takayanagi and A. Wada *Chem. Phys.*, vol. 269, pp. 37–47, 2001.

CHAPTER 5

DUAL MOLECULAR BEAM APPARATUS AND ITS APPLICATIONS TO THE VELOCITY MAP IMAGING EXPERIMENTS

5.1 Introduction

In the application of the Velocity Map Imaging Technique to crossed molecular beam studies, the image analysis could be made relatively easier if the relative velocity vector of the reactants lies in the plane of the detector. The image analysis will require the inverse Abel Transform and density-to-flux correction, but one does not need to worry about complicated Jacobians to transform the lab frame to the center of mass frame. The cylindrical symmetry of the reaction around the relative velocity vector will directly translate into the projected image. This is analogous to using the probe laser along the direction of the relative velocity in the Doppler-Selected Time-of-Flight Technique,[1–3] to take advantage of the symmetry of the problem at the projection stage. Even before the analysis stage, the inspection of the raw images can provide qualitative information as in the case of the photodissociation imaging studies.

Another appeal of the technique will be gaining all 4π solid angle center of mass recoil angular information at once, as opposed to the cross-beam experiments in which one rotates the detector in a wide range to acquire angular information.

The relative collision speed in a photo-initiated bimolecular collision experiment can be controlled by two main variables, wavelength and the temporal delay between the lasers: The initial velocity distribution of the collision partner from the photodissociation event is wavelength dependent. The temporal delay between

the photolysis laser of the precursor and the probe laser provides additional speed selectivity. The direction of this velocity vector is defined by the position of the precursor and probe lasers. However, the polarization of the photolysis laser is an essential parameter in defining the properties of the incoming species' angular distribution.

In the first few sections of this chapter, the design considerations of the apparatus will be explained and the attempts to apply the technique to $O(^1D)$ reaction studies will be described later.

5.2 Description of the Apparatus

5.2.1 General Characteristics of Molecular Beams

The most important reasons why molecular beams became standard in gas phase studies are that they provide a well defined velocity and they approach single collision conditions. Such a beam is created when a group of molecules at pressure P_0 suddenly expand into a pressure of P_1 area through a small orifice, where P_0/P_1 is larger than 2.1 . The enthalpy of the system is converted to directed translational energy, resulting in a narrow velocity distribution. This expansion is supersonic in nature and the physical behavior is very complicated. Nevertheless, the most important parameters of the beam relevant to our purposes can be calculated with the theory given by Anderson and Fenn.[4,5] In their approach, it is assumed that the molecules entering the skimmer undergo no collisions with the skimmer or among themselves, meaning that the conditions at the skimmer entrance will be the same as in the beam downstream. The average velocity and temperature in the beam is

given by

$$v = Ma = M[\frac{\gamma kT}{m}]^{\frac{1}{2}} \tag{5.1}$$
$$T = T_0(1 + \frac{\gamma - 1}{2}M^2)^{-1}$$

where M is the Mach number, which is ratio of the average speed to the local speed of the sound, γ is the specific heat ratio, C_p/C_v of the gas, k is the Boltzmann constant, T is the local temperature, T_0 is the stagnation temperature and m is the mass of the species in the beam. For an ideal gas, γ is 5/3 for monoatomics and 7/5 for diatomics. At some point during the expansion, the collisions between the atoms or molecules almost come to a stop, resulting in a terminal mach number $M_T = 1.17\ \mathrm{Kn}^{-0.4}$ where Kn is the Knudsen number.[5] It is the mean free path at the nozzle orifice (diameter D) and is given by Kn=$\frac{1}{\sqrt{2}Sn_0D}$ where S is the effective molecular collision cross section at the nozzle, a number on the order of 10^{-15} cm^{-2}. Using this M_T with equation 5.1, typical speeds can be derived:

Assuming a 0.5 mm diameter orifice with $\approx$ 2 psi backing pressure and 300 K of stagnation temperature, the speed for O_2 is 1040m/s, He is 1760m/s , N_2 is 790 m/s and Ar is 560 m/s. The corresponding M_T is 21.6.

The number density of molecules through an area normal to the propagation axis at a distance r from the axis, with $(\frac{1}{2}\gamma M_s^2)^{\frac{1}{2}}(1 + \frac{r^2}{l^2})^{-\frac{1}{2}} > 3$, is given as:[5]

$$I_r \approx A_s n_s \frac{1}{\pi l^2}[\frac{1}{2}\gamma M_s^2(1 + \frac{r^2}{l^2})^{-1} + \frac{3}{2}](1 + \frac{r^2}{l^2})^{-2} exp(-\frac{1}{2}\gamma M_s^2(1 + \frac{r^2}{l^2})^{-1}\frac{r^2}{l^2}) \tag{5.2}$$

where A_s, n_s, M_s are the skimmer area, number density and Mach number at the skimmer, respectively. l is the distance downstream from the skimmer. The number density at the skimmer can be found by the approximate formula $n_s \approx 0.16 n_0(x/D)$

where x is the distance from the nozzle. Figure 5.1 applies Equation 5.2 to N_2 beam.

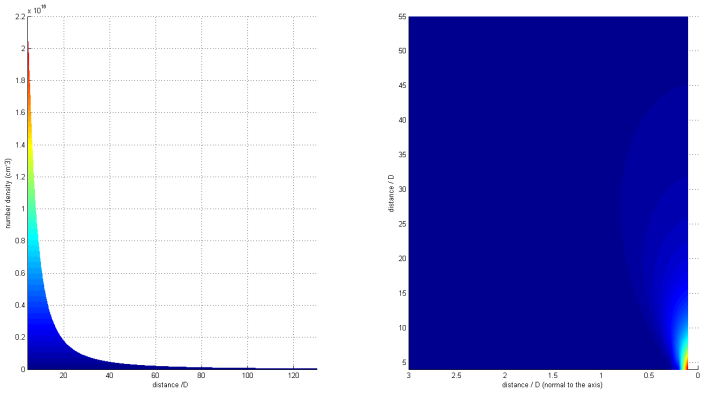

Figure 5.1: Molecular Beam Profiles for N_2. The figure on the left shows the number density on the propagation axis as a function of distance from the skimmer. The figure on the right shows the number density on any plane containing the propagation axis. 1 atm backing pressure is assumed.

In experiments, the nozzle skimmer distance is 2 cm, nozzle and skimmer diameters are 0.5 mm and the experiment takes place 7.5 cm from the nozzle. Typical beam pressures are around 2-3 psi. The cross section of the beam at this distance is given in Figure 5.2. It may be noted that the intensity does not have an explicit dependence on the mass.

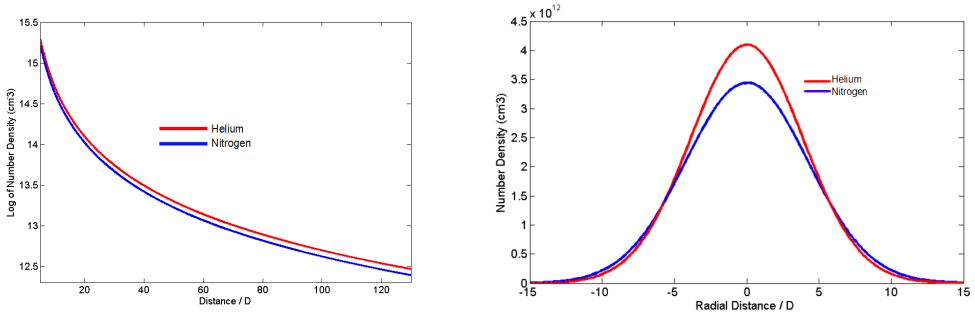

Figure 5.2: The figure on the left shows the number density of N_2 and He, on the axis as a function of distance from the skimmer, at 3 psi backing pressure. The figure on the right shows the cross sections of the molecular beam at the interaction region.

5.2.2 General Design

The vacuum level in the source chamber should be low enough so the collisions between the molecules can be ignored, i.e. the mean free path of the molecules should be greater than the characteristic dimension of the chamber. Assuming an ideal gas at room temperature and 10 cm characteristic dimension, the base pressure should be on the order of 7.7x10^{-4} torr. The required pumping speed is given[6] by $S = \frac{(\rho \Delta t) P_0 C}{P_b}$ where P_0 and P_b are the backing and base pressures, ρ is the nozzle frequency, Δt is the nozzle temporal width, C is the nozzle conductance. For typical values, and assuming 0.5 atm backing pressure, S speed must be 1100 liters/sec. This speed can be attained by a diffusion pump or a turbo-molecular pump.

The apparatus consists of two stainless steel chambers equipped with standard conflat flanges. The source chamber houses two sets of nozzles and skimmers. Because of the symmetry consideration mentioned in the previous section, the two molecular beams are chosen to be set in a parallel alignment, i.e. the plane formed by their axes is perpendicular to the plane of the detector. The source chamber is pumped by a Varian VHS-6 diffusion pump backed by a Varian DS-1002 mechanical pump (This design is modified when The Houston Lab moved to Georgia Institute of Technology. The diffusion pump is replaced by a Varian Turbo-V 2K-G turbo-molecular pump). Even if very low vapor pressure pump oil is used in the diffusion pump, it is important to minimize the possible backstream of pump oil to the chamber.. Therefore, the source chamber is also equipped with a cryotrap. The chamber part that consists of the skimmer plate and nozzles can be seen in Figure 5.3. The nickel skimmers (orifice diameter = 0.5 mm) are angled 16.26° and 9.11° with the horizontal plane, to be aligned with the ion-optics.

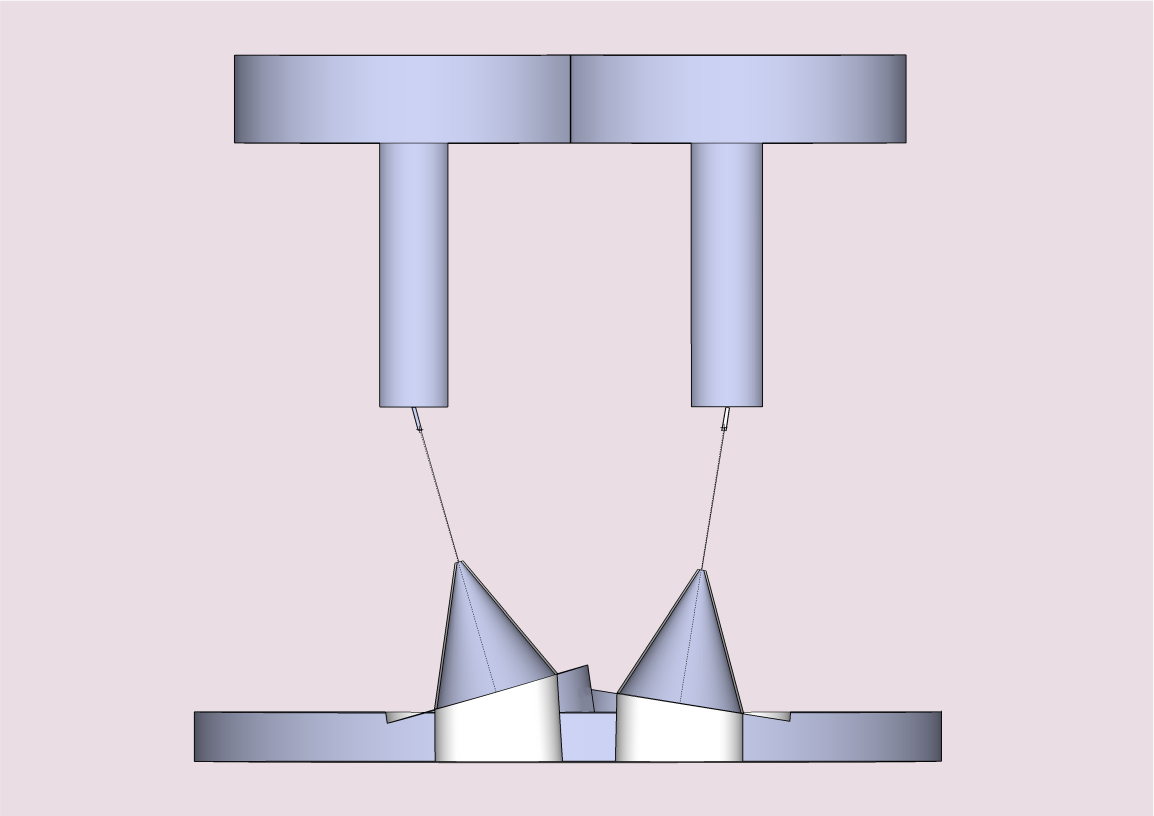

Figure 5.3: Aluminum, Angled Double Skimmer Plate with Piezoelectric Pulsed Nozzle Assembly Cross Section. Skimmer and nozzle holder aluminum plates are not shown.

The two pulsed nozzles (Precision Instruments, Inc.) are supported by an aluminum holder. The nozzles are trimmed up to the piezoelectric material, to fit in the required area. At the end of the nozzle holder plate, each nozzle orifice looks into a hole with the same area as the nozzle orifice and with an angle the same as that of the corresponding skimmer (These holes can be seen in Figure 5.3, with 3.175 mm vertical length and 0.5 mm diameter).

The source chamber is connected to the interaction chamber through the two skimmer holes, allowing them to be pumped separately. The interaction chamber is pumped by a Leybold Turbovac-1000 C backed by a Varian SD-700 mechanical pump. The interaction chamber houses the ion optics, the detector and the time of flight path, which is covered with a μ-metal to screen against low magnetic fields. The schematic of the apparatus can be seen in Figure 5.4

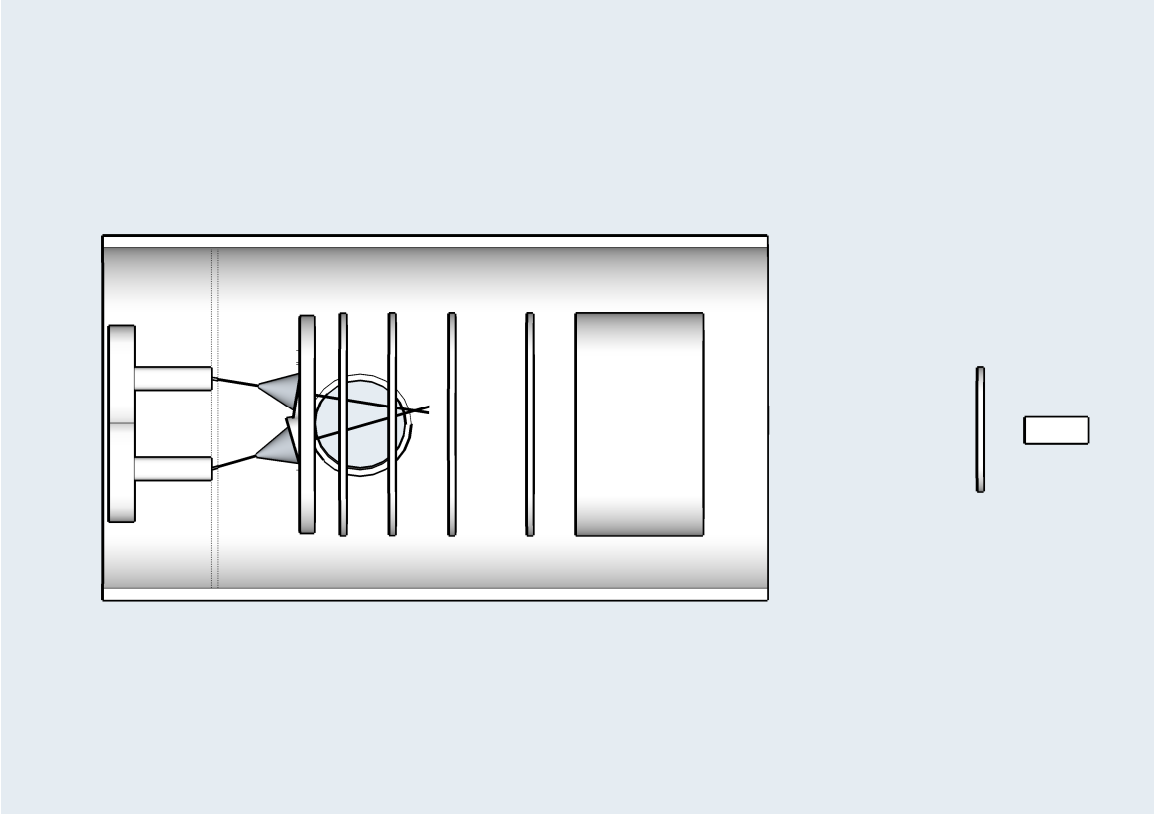

Figure 5.4: Schematic of the apparatus, showing both source and interaction chambers, pulsed nozzles, skimmers, ion optics and the MCP/phosphor detector. The dotted lines show the end of the nozzle holder plate.

The foreline tubing between the pumps are 1.5″ diameter stainless steel and standard NW hinged clamp assemblies are used when required. Ionization gauges are installed to both chambers to measure the pressure. Gate valves between the turbo/diffusion pumps and their corresponding chambers allow rapid venting of the chamber. With no gas loading the chamber is kept at around 5x10^{-8} torr. When both beams are running, the source chamber has a pressure of 10^{-5} torr to 10^{-4} torr depending on the nozzle pulse voltages and temporal widths, and the interaction chamber pressure is around 10^{-7} torr.

The alignment of the pulsed nozzle orifices with the skimmers and the alignment of the skimmers with the ion optics is constrained by a plane. This requires very careful angular positioning of the double-sided flanges holding these parts. The ion optics holes for the molecular beams are also constrained by this plane, therefore requiring care in positioning of the ion optics.

5.2.3 Nozzle Interference

One disadvantage of having two nozzles in one source chamber is that they can interfere with each other before the skimmers, if they are not properly designed. In Figure 5.5 one can see this interference and the solution to overcome this problem. The O(^{1}D) signal from the photodissociation of ozone with 285 nm in the upper beam ; detected by a 203.7 nm, 2+1 REMPI processes is shown with the red and blue curves. The lower beam timing is scanned while carrying neat N_2, to check if there is any interference to the O(^{1}D) signal in the upper beam.

The black curve in the figure shows the beam profile in the lower beam as a reference. The scan shows the O(^{1}D) signal from the photolysis of neat N_2O gas

by 203.7 nm, and detected by a 2+1 REMPI processes with the same color. The lower beam temporal profile is very similar to its profile when carrying N_2 gas as well as to the upper beam temporal profile when carrying similar gas molecules.

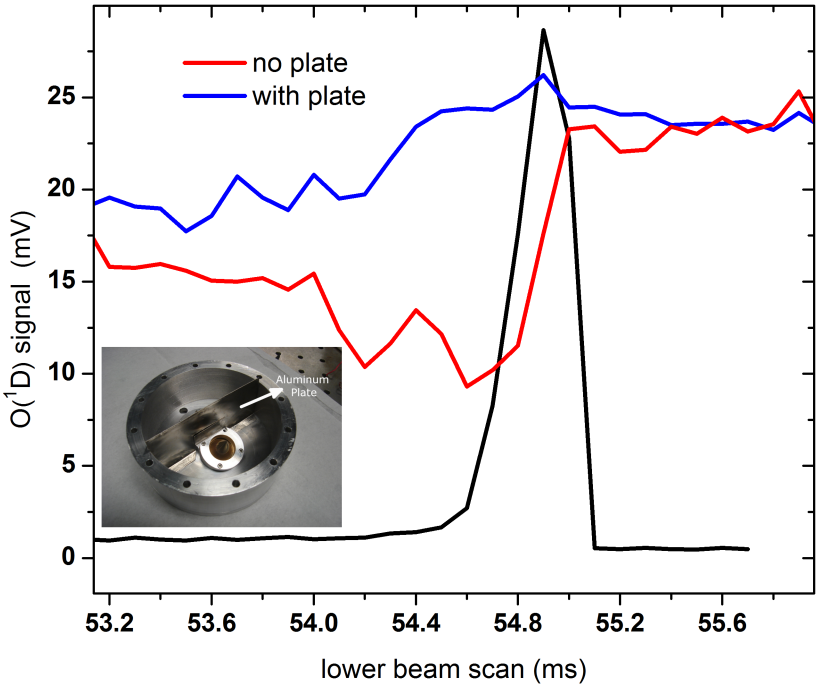

Figure 5.5: The black curve shows the temporal shape of the lower nozzle beam. The signal is obtained by monitoring the $O(^1D)$ signal from the N_2O dissociation by 203.7 nm. The red and blue curves show the $O(^1D)$ signal from ozone photodissociation in the upper beam, at 285 nm. N_2 in the lower beam decreases the signal when there is no separating plate in between the skimmers.

It is seen that, if there is no plate separating the skimmers in the source chamber, at the time when the lower nozzle fires, the signal in the upper beam is decreased. The scans showed the same effect for the analogous case, i.e. scanning the upper beam timing causes a decrease in the lower beam intensity.

This ended up not to be a big problem, after installing an aluminum plate

separating the two skimmer/nozzle pairs, as can be seen in the inset of Figure 5.5. A slight effect remains to be seen at later times, but both beam timings can be chosen in a way not to be troubled by this effect.

5.2.4 Ion Optics

Eppink and Parker introduced the use of electrostatic lenses with ion imaging, causing a substantial improvement in the velocity resolution. In this technique, the lensing of the ion-optics corrects for the finite interaction volume of the the probe laser and the molecular beam. Later Kitsopoulos et al. and Suits et al. introduced the slicing techniques that allow to experimentally slice the ion cloud rather then inverting the image.

The DC slicing technique requires one or two more electrodes in addition to the Repeller and Accelerator plates. That is to expand the ion cloud to a temporal size of about 400 ns, so the detector can be gated to slice the center of the ion cloud. We designed a 4 electrode ion-optics setup and used Simion ion trajectory simulation package to apply velocity mapping condition to DC slicing.

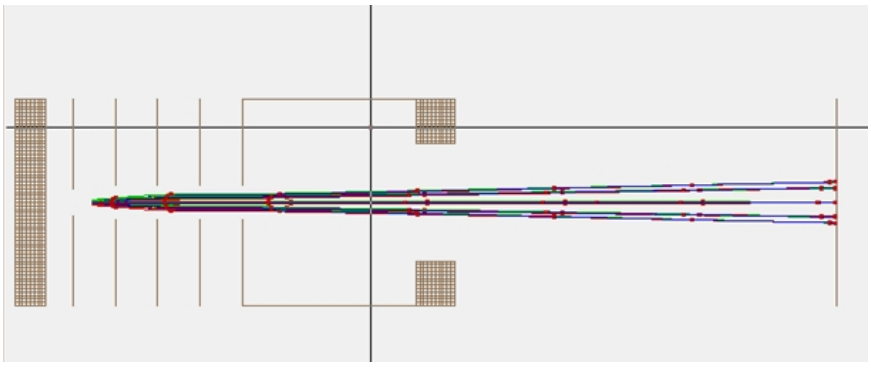

Figure 5.6: The figure shows the simulated trajectories of ions created with the same initial velocities but different spacial origins. The ion cloud cross sections at equal temporal intervals are also shown.

Figure 5.6 shows the ion trajectories for a representative case, when the velocity mapping condition is satisfied and all four electrodes are used to expand the ion cloud to be large enough for DC slicing. At the focusing plane, i.e. the detector, the ions with the same initial velocity vector are focused to the same point.

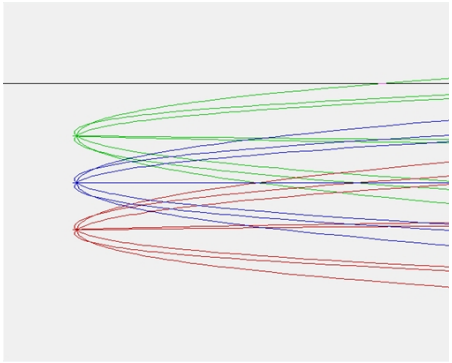

Figure 5.7: Three ion sources with ions ejecting in equally spaced angles and with the same speeds.

A detail of the ion sources used in the simulations is shown in Figure 5.7. Three ion sources with 1mm vertical separation are used. Each source has 8 ions ejected with the same initial speeds but with 45° angular spacing. Figure 5.8 shows the the detector, on which all ions with the same initial velocity vectors are focused to the same point. The grid shown on the detector has 1mm spacing.

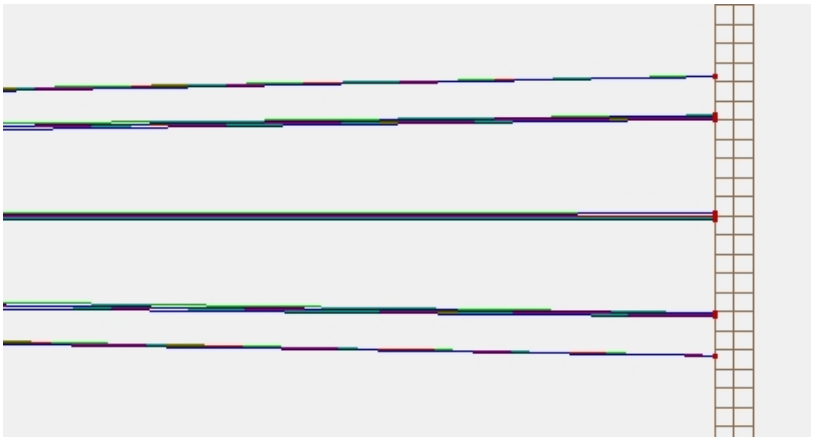

Figure 5.8: Velocity Mapping Condition on the detector plane.

In the case when there is no DC slicing, from the simulations of various initial ion positions, it is found that REP/ACC voltage ratio 1.51± 0.03 satisfies the velocity mapping condition. As is shown below, the experimental estimate is 1.48± 0.01. This uncertainty is because of the high voltage source output measurement.

The program allows estimates of the ion cloud's temporal width, Δ(Time of Flight) or Δ(TOF). When one uses only the repeller and accelerator electrodes for velocity mapping, the ion cloud is quite narrow when it impinges onto the detector, allowing a 150ns detector gate to detect all the ions. This narrow temporal case is shown in Figure 5.9(a). If desired, two additional electrodes can be used to stretch the ion cloud for heavier masses, while preserving the focusing condition. The spread is shown in Figure 5.9(b) for this case. A 40 ns mass gate would detect the expanded ion cloud's central part, which is equivalent to an inverse Abel transformed image from the preceding setting, as argued by Kitsopoulos et al.[7]

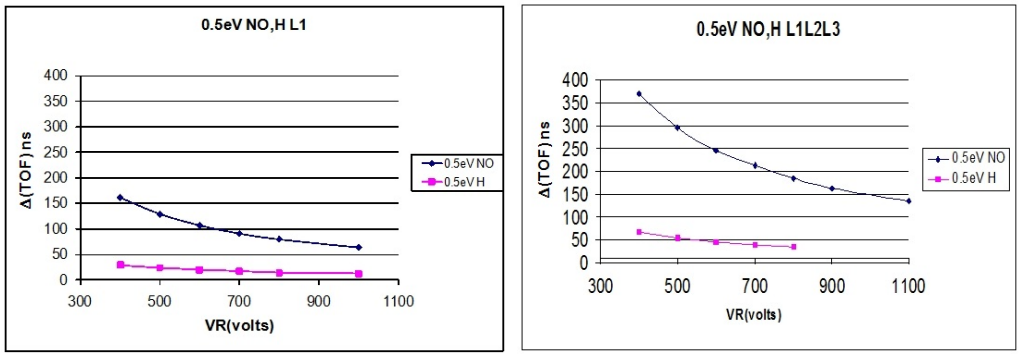

(a) TOF vs the repeller electrode voltage, for H and NO.

(b) All 4 electrodes are used in stretch the ion clouds for H and NO.

Figure 5.9:

Figure 5.10 shows how adding one or two more electrodes help keep the velocity mapping for NO ions created with different kinetic energies, while allowing for ion cloud stretching. L1 is the more common two electrode case. L1L2 shows the

effect of adding one more electrode. L1L2L3 case shows the effect of using all the electrodes.

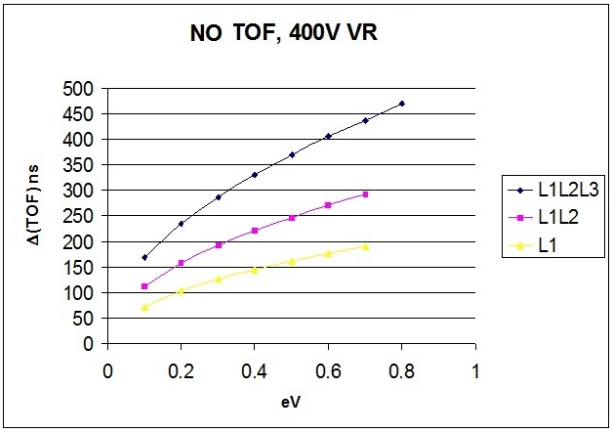

Figure 5.10: The NO ion cloud spread as a function of initial kinetic energy. The focusing condition is satisfied with 2 electrodes for L1, 3 electrodes for L1L2 and with 4 electrodes for L1L2L3

The ion cloud radius and the ΔTOF for O atom and NO molecule are shown in Figure 5.11. In the figure, R gives the radius of the ion cloud on the detector, to be read from the right ordinate. V_R is 600V for all simulation points and the MCP radius is 20mm in the setup.

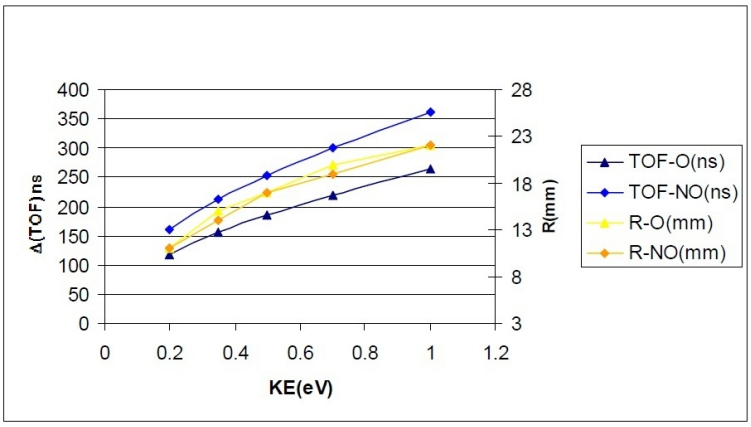

Figure 5.11: The tradeoff between the TOF and R is shown for O and NO, when all 4 electrodes are used to satisfy the velocity mapping.

Image Calibration and Focusing

The velocity focusing and the ion-optics can be calibrated by comparing our images to a well studied photodissociation event. Here we used the 285 nm photolysis of O_3 molecule:

$$O_3\ (X^1A_1) + h\nu \rightarrow O(^1D_2) + O_2(a^1\ \Delta_g)$$

The $O(^1D)$ product is detected with 2+1 REMPI, by 203.7 nm UV light. The rings in the $O(^1D)$ images, in Figure 5.12 correspond to the vibrational quanta in the $O_2(^1\Delta)$ photofragment. Such images can be used to calibrate the ion-optics by comparing the velocity distributions obtained from inverting the images, to the results found in the literature.[8]

The image on the left in Figure 5.12 shows a raw $O(^1D)$ image recorded after such a calibration, and its inverse Abel transformed image is shown on the right. This image is taken with V_{REP}=5990 V and V_{ACC}=4060 V. If V_{REP} is kept at this voltage and V_{ACC} is tuned slightly off to see the velocity mapping effect, the eye doesn't detect a change in the images for about $\pm$ 30 V. But one can quantify the effect of fine tuning by calculating the cross-correlation of an image with a given V_{ACC} and a well calibrated image. Such a calculation is shown in Figure 5.13. The red curve compares the raw images to a well calibrated image and the blue curve does the same comparison for the corresponding inverted images. In both cases the case with V_{ACC}=4060 V is seen to be the optimum, so this voltage setting is used in the experiments. By this method, the initial voltages are found by the guidance of simulation and the calibration is done by comparing calculated and measured speed distributions. The fine tuning is done by comparing the angular distributions, with the help of cross-correlation calculations, so bypassing the ef-

fects of individual lens or voltage source differences in a particular experiment.

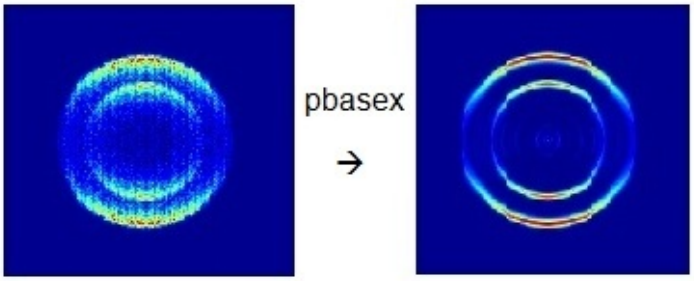

Figure 5.12: Raw image of O(^{1}D) atoms from 285 nm dissociation of ozone and their CM distribution from inverse Abel transform with polar basis functions: (pbasex) method.

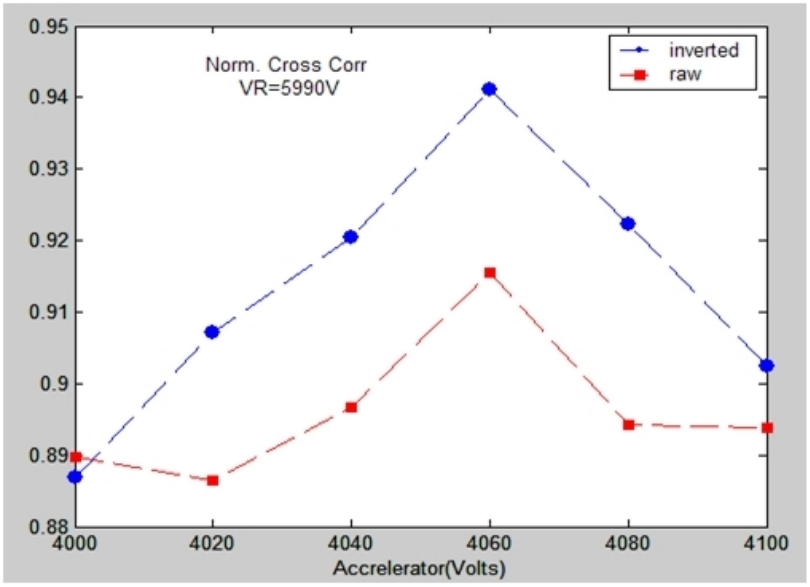

Figure 5.13: Normalized Cross-Correlations

5.3 Velocity map ion imaging in a dual-beam setup

To apply the velocity map ion imaging technique in a dual beam setup, we have tried various reactions of the $O(^1D)$ precursor. This choice, in part, is because of the fact that $O(^1D)$ has a high rate constant for its reactions, usually on the order of 10^{-11} cm^{-3} molecule $^{-1}$ s^{-1}.[9]

The O_3 $(X^1A_1) + h\nu \rightarrow O(^1D_2) + O_2(a^1\ \Delta_g)$ photolysis event is used to create $O(^1D)$ precursor. A mixture of O_3(%10) beam seeded in Argon (backing pressure 2 psi) was expanded supersonically through a 500 μm diameter nozzle and collimated with a 500 μm diameter skimmer located 2 cm from the nozzle, as seen in Figure 5.4. A collimated photolysis laser intersected the molecular beam at right angles, in the middle of the repeller and accelerator plates and 7.5 cm from the nozzle. These product oxygen atoms were then "followed" down to the lower molecular beam where the collision is supposed to take place. Initially we have used Helium as the carrier gas and kept the ozone trap at -78°C.

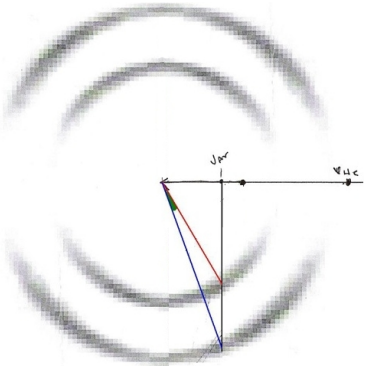

Figure 5.14: $O(^1D)$ atoms from the 285 nm dissociation of O_3 molecule.

But as seen in Figure 5.14, it is more intuitive and practical to use Argon as the carrier gas, since the composite velocities of the molecular beam and $O(^1D)$ atoms allow a vertical lab velocity vector, so one can translate the probe laser

vertically in the lab frame to "follow" these atoms. In the case of He carrier gas, the procedure has to be done at an angle causing practical problems. Also ozone has a higher vapor pressure at -40°C, so we switched the trap to this temperature.

One can calculate the minimum photolysis laser diameter that will result in using all the photons in a pulse for a given laser intensity. Using Beer-Lambert law we get the following plot for the laser diameter d_{min} and the number density of oxygen atoms. All curves for the minimum diameter for 285 nm photolysis fall on top of each other, the blue curve. d_{min} is to be read from the left ordinate. The right hand scale shows the number density of oxygen atoms for different backing pressures, assuming argon is used as carrier gas.

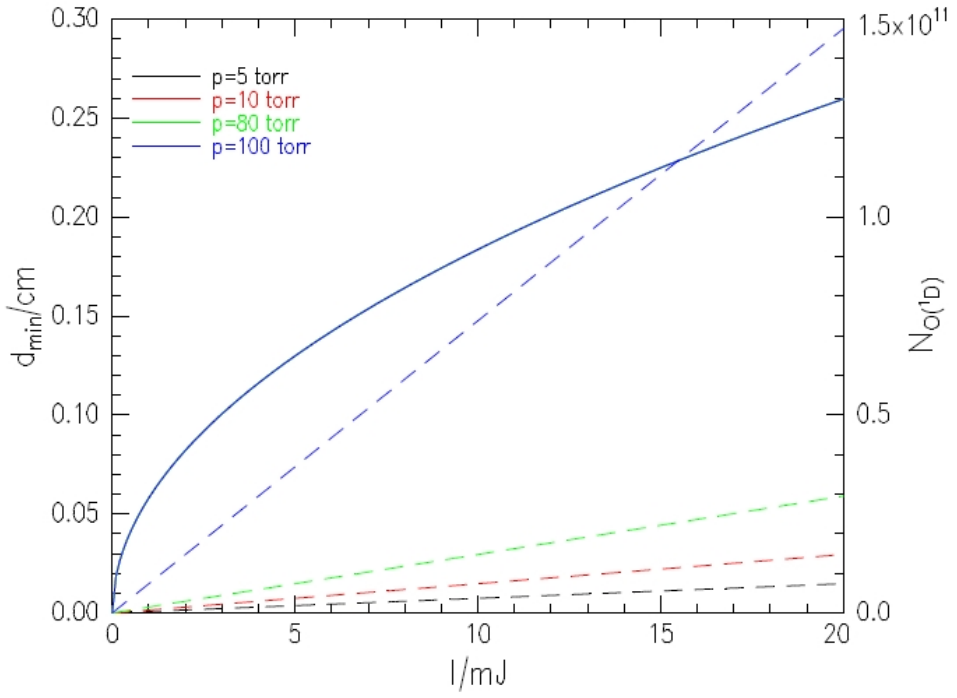

One needs to collimate the laser to 2-3 mm, use higher pressure and higher laser intensity to maximize the ion count. We use 5-10 mJ pulses and collimate the laser to 3-4 mm diameter while keeping the ozone trap at -40°C during the following experiments.

5.4 Getting O(^{1}D) atoms to the lower beam

The following figure shows a cartoon of the experiment. O_3/Ar mixture is expanded in the upper molecular beam and O_3 is dissociated by a Nd:YAG pumped dye laser in the Hartley Band, as explained in the previous section. The detection of the product O(^{1}D) atoms are, however, done in the lower molecular beam with a probe laser at 203.7 nm and 2+1 REMPI schemes, where the reaction is supposed to take place with N_2 or N_2O molecules. The 203.7 nm light is created by doubling the output of a Nd:YAG pumped dye laser in a KDP crystal and then summing the fundamental with the doubled light in a BBO crystal.

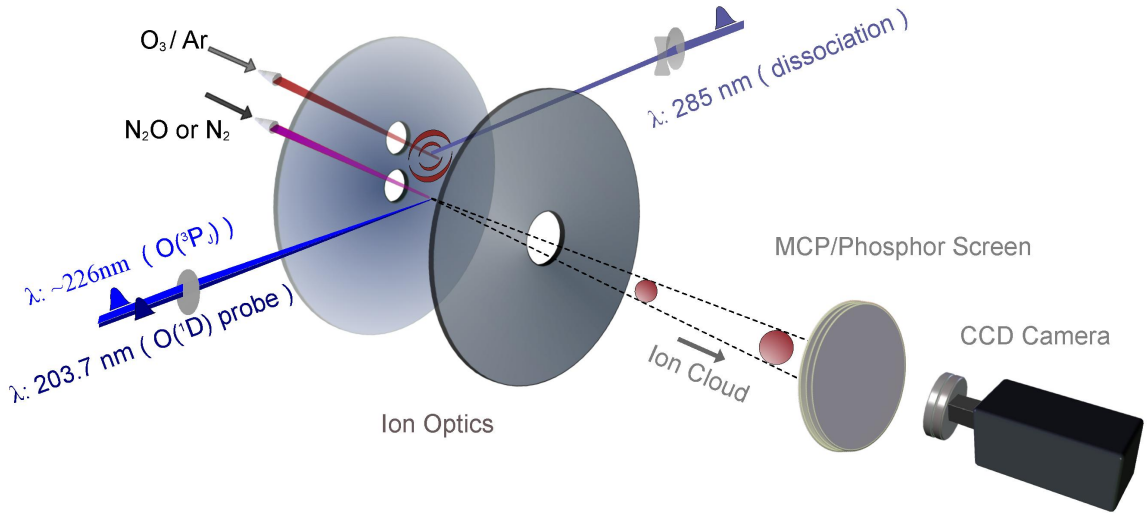

Figure 5.15: A cartoon of the experiment.

The O(^{1}D) atoms are ionized in the lower beam and the resulting ion-cloud is either detected with a Photo Multiplier Tube (PMT) for measuring the signal level and getting spectral information or with a position sensitive detector (MCP/Phosphor) coupled to a CCD camera, when the image is desired. The ion optics are optimized for the velocity map imaging conditions, as in section 3.2.4.

The photolysis of ozone is done at a number of wavelengths where the absorption cross section is highest. In Figure 5.16, the O(^{1}D) detection in the lower beam is shown, with four different photolysis wavelengths: 266 nm, 280 nm, 285 nm and 290 nm. This photolysis event was studied in our lab previously, and the speed and angular distributions of O(^{1}D) atoms had been well documented.[8]

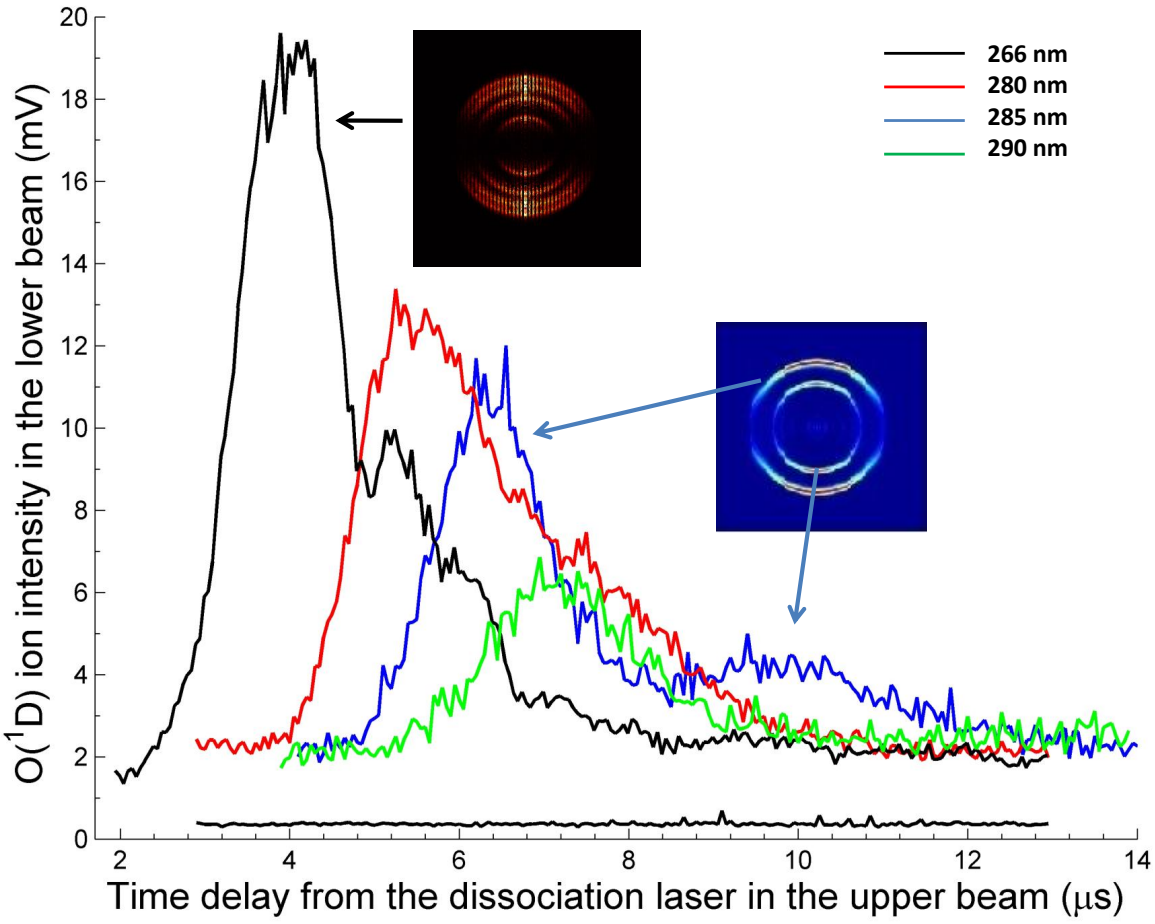

Figure 5.16: O(^{1}D) atoms in the lower beam

The captions in the figure show the inverse Abel transformed O(^{1}D) photofragment images from the 266 nm and 285 nm photolysis events of ozone, in that order from left to right. The experimental setting for these images are the same, except

that the photolysis of ozone and the detection of $O(^1D)$ atoms are done in the same molecular beam, with 20 ns temporally separated lasers. From the images, it is apparent that the linear polarization of the photolysis laser can be used as a control on the directionality of the ion spread flying to the lower beam.

For the 285 nm photolysis case in the figure, the two $O(^1D)$ peaks corresponding to the two vibrational quanta in O_2 are well resolved and are indicated with blue arrows. The 266 nm photolysis results in four rings. These are harder to resolve in the lower beam, but one can see the first three of these as small bumps in the corresponding scan. The limiting speed for $O(^1D)$ from these rings can be calculated to get a general idea about the appearance of these scans. From the 266 nm dissociation, we get v= 2280, 1930, 1510 and 920 m/s for v=0,1,2,3 in the O_2 co-fragment. From 280 nm , we have v= 1825, 1360 and 640 m/s for v=0,1,2; from 285 nm, we have v= 1640 and 1110 m/s for v=0,1 and from 290 nm, we have v= 1450 and 800 m/s for v=0,1 in O_2. The character of the signal shapes, obtained in the 203.7 nm laser trigger delay scans in the lower molecular beam fits nicely to the expected peak positions calculated for all wavelengths.

An important feature in the figure is the flat scan close to zero signal level, showing the photolysis laser background when 203.7 nm is blocked. This amounts to the full mass spectra generated by the photolysis laser, since we are scanning the 203.7 nm laser trigger during all scans shown. Any mass created by the photolysis laser in the chamber will be detected when their arrival time coincides with the mass gate set for oxygen, causing a significant background in these scans. We have developed a delay extraction scheme to get rid of this background, which will be detailed in the next section.

As another check of our control on the O(^{1}D) atoms flying down to the lower beam, we can directly image at any speed we want. In Figure 5.17, the trigger timing of the 203.7 nm laser is set to detect only the O(^{1}D) atoms that have O_2 (v=0) as a co-fragment from the 266 nm ozone dissociation. This corresponds to the biggest peak in Figure 5.16 and to the outermost ring's central part in the corresponding caption showing full speed distribution. In Figure 5.17, the blue circle is centered on the pixel that corresponds to the lab zero velocity and the radius of the circle is set to 2200 m/s, the calculated speed for this peak.

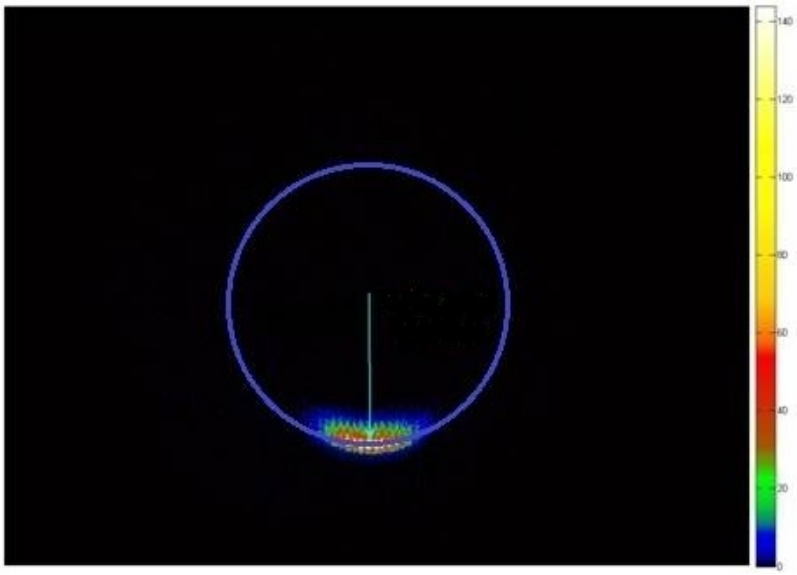

Figure 5.17: Fast O(^{1}D) atoms from the 266 nm photolysis of ozone

The polarization direction of the linearly polarized 266 nm laser is optimized for maximum signal. We get similar images by changing the delay between the two lasers or the wavelength of the dissociation laser. These parameters give us significant control on the speed and angular distributions of the incoming oxygen reagent.

5.5 Development of the Repeller Pulsing Delayed Extraction Method

In the previous section it is mentioned that the background elimination is accomplished by a delayed extraction scheme; which has proved to be critical for our purposes.

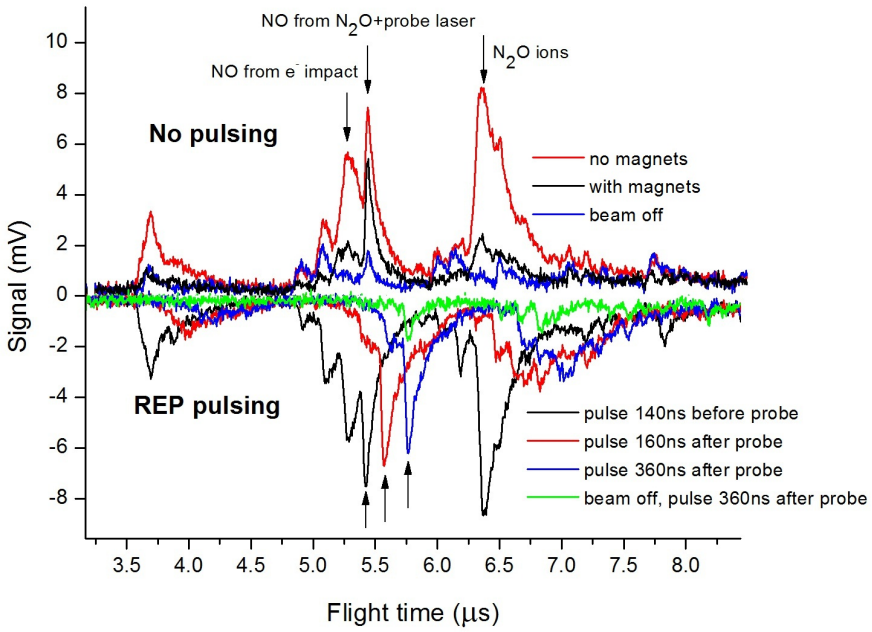

Figure 5.18: NO molecules created by electron impact ionization and from N_2O interaction with the laser. The effect of small magnetic fields is shown on the upper section of the graph. The inverted lower section shows the TOF when the Repeller Pulsing Technique is used.

The motivation for the technique is illustrated in the mass spectra shown in Figure 5.18. The data shows the TOF from the time of the probe laser's interaction with the N_2O beam. The wavelength set to a particular ro-vibrational level of $NO(X^2\Pi)(v{=}1)$. The laser energy is 1 mJ/pulse, which is a typical probe laser energy for the 1+1 NO REMPI detection scheme.

The red curve in the upper part of the figure shows two close peaks that are actually from NO molecules, indicated by the two adjacent arrows. One is from the interaction of the laser with the molecule, showing wavelength and molecular beam dependence. The other is from electrons ionizing the NO molecules and shows no wavelength dependence, even though it is entirely molecular beam dependent. One hypothesis is that electrons generated by the laser are accelerated and interact with N_2O upstream in the molecular beam to generate NO^+. These electrons can be cleared out of the way by using small magnetic fields, leaving behind only the NO molecules that are detected on resonance, as in the black curve. The same electrons also ionize O and N_2O molecules as seen in the figure.

To formalize this background reduction method, one can imagine creating a temporary electric field free region between the repeller and accelerator plates, allowing the electrons created by the laser enough time to fly away rather than be accelerated in the upstream direction of the beam. The lower section of the figure illustrates this concept. Both plates are kept at 2030 V until a certain reference time, which is the arrival time of the probe laser pulse to the interaction region. A 10 Hz voltage pulse of 1μs arrives to the repeller plate, ramping its voltage to 4000 V in 20 ns, when triggered. The black curve in the lower panel shows when this pulse is set to arrive 140 ns before the laser. As expected, the TOF is the same as the red curve of the upper plate. But when the pulse is delayed, as in the red curve of the lower panel, the effect is just like using a magnetic field to clear the electrons, except there is some change in the flight time.

But the strength of the method is not about one-laser experiments. It comes from the fact that when used in a dual beam experiment, the laser in the upper molecular beam is spatially separated from the probe laser, and the background

created by the photolysis laser can be screened entirely from the mass gate window on the detector, triggered by the probe laser.

The dramatic difference in the background is shown in Figure 5.19. The experimental setting is very similar to the case in Figure 5.16. The background TOF mass spectra created by the 285 nm laser in the upper beam is shown in the red curve. The black curve at 0 V, is the background TOF from 285 nm laser, when the repeller pulse is set to arrive 40 ns before the probe laser in the lower beam. The probe laser timing is set to detect the fast $O(^1D)$ atoms corresponding to $O_2(v{=}0)$.

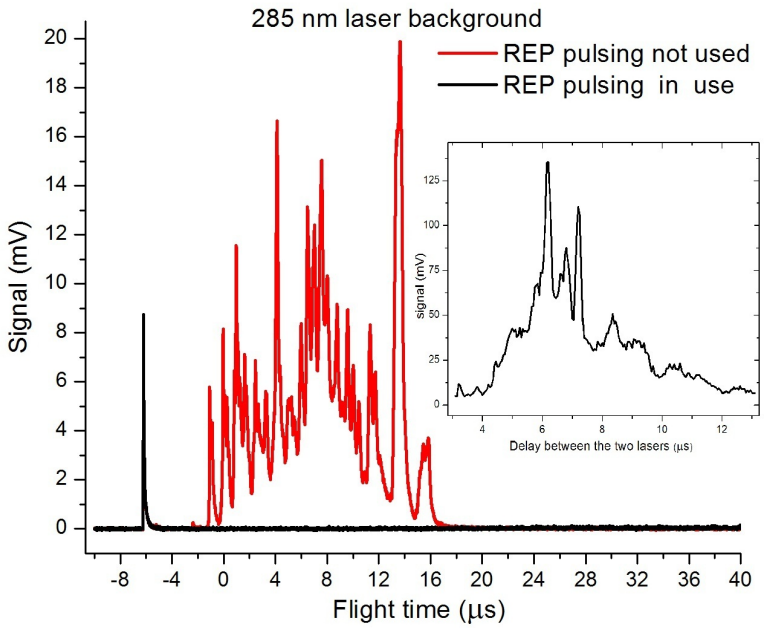

Figure 5.19: Effect of the delayed extraction method in the background: The flat black curve at zero volts shows the full screening of the background from the photolysis laser. The scope is triggered by the probe laser. The first peak is the reflected 285 nm light seen by the PMT.

The inset shows the $O(^1D)$ atoms detected in the lower beam, after being created by the 285 nm photolysis event in the upper molecular beam, when the pulsing method is not used. This scan should be compared with Figure 5.16, in particular the blue curve, which is the same experiment except the repeller pulse method is used in the latter, during the probe laser lamp timing scans.

$O(^3P)$ from the upper beam

In the Hartley, band, ozone dissociates through the spin conserved channels,

$$O_3 + h\nu \rightarrow O(^1D_2) + O_2(^1\Delta_g) \qquad (1)$$
$$O_3 + h\nu \rightarrow O(^3P_j) + O_2(^3\Sigma_g^-) \qquad (2)$$

About 90% of the ozone molecules will follow channel (1) and about 10% channel (2). One consequence of the pulsing method is that it allowed us to detect the $O(^3P)$ atoms in the lower beam, when the photolysis event took place in the upper beam. Since these atoms originate from the minor channel and considering only about 1% of them reach the lower beam, their imaging shows the power of this delayed extraction method.

The experimental conditions are the same as in the case of Figure 5.17, except that instead of detecting $O(^1D)$ atoms in the lower molecular beam from 266 nm photolysis of ozone in the upper beam, we are detecting $O(^3P_2)$ atoms in the lower beam, using a 2+1 REMPI scheme at 225.65 nm, $O(3p\ ^3P_2 \leftarrow\leftarrow 2p^3P_2)$.[10] Also, neat nitrogen gas is expanded in the lower beam, to see if there is any $O(^3P)$ after elastic or inelastic scattering of $O(^1D)$ from N_2. The small signal levels of the $O(^3P)$ atoms required imaging for 60 000 to 200 000 shots to observe these atoms. During

the data taking, the wavelength of the laser is scanned over Doppler wavelength to ensure equal detection efficiency.

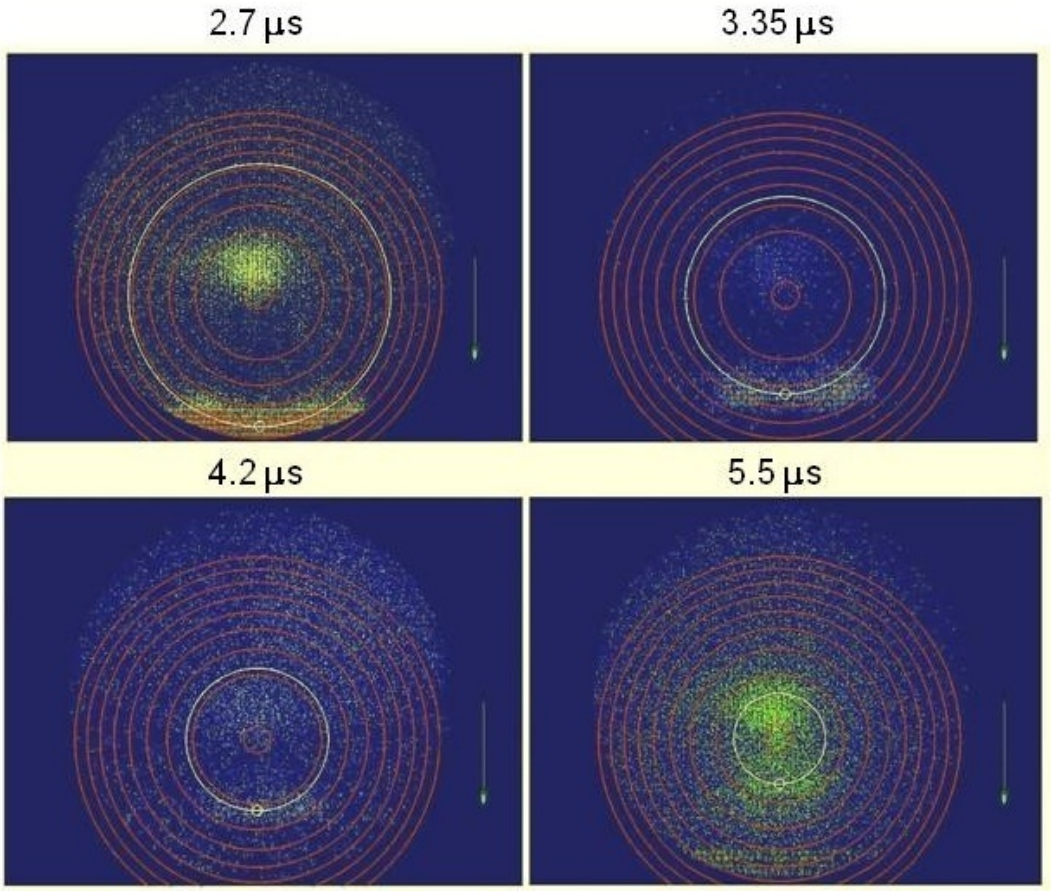

Figure 5.20: $O(^3P_2)$ atoms detected in the lower molecular beam, after flying from the upper beam. The delay between the two lasers is given for each image.

In Figure 5.20, the green arrow shows the incoming $O(^1D)$ velocity. The big white circles show the expected place of the $O(^3P)$ atoms if they are elastically scattered from N_2 molecules. The little white circle shows the expected place of the incoming $O(^3P)$ from the upper beam. The red circles show the expected position of $O(^3P)$ atoms if there is $O(^1D)+N_2$ (v=0)$\rightarrow$ $O(^3P)+ N_2(v=v')$ reaction, for each available vibrational quanta in N_2. The small white circles coincide with the larger white circles, since the center of mass collision velocity shifts the center

of the newton spheres resulting from the collision, whereas the small circle is drawn with reference to the pixel corresponding to the lab zero velocity. These images remain the same if Argon is used instead of Nitrogen. So no inelastic scattering is observed. But the fact that the small circles coincide with signal, which is a function of the delay between the two lasers is a strong indication that we can see the incoming $O(^3P)$ from the upper beam. As a final note, the last image corresponds to the delay when the biggest $O(^1D)$ signal is seen in the lower beam.

5.6 Looking for NO molecules from the $O(^1D) + N_2O \rightarrow 2\ NO(X^2\Pi)$ reaction in a dual beam experiment

We have expanded neat N_2O gas in the lower beam and looked for NO molecules from the $O(^1D) + N_2O \rightarrow 2\ NO(X^2\Pi)$ reaction in a dual-beam experiment. This reaction is studied in detail in a single molecular beam in the previous chapter, where it is shown to have a 4500 K rotational temperature in the $NO(X^2\Pi)$ product. Nevertheless, the direction of the relative velocity vector in a single molecular beam is not well defined and any NO images from those experiments are featureless. These featureless NO images can be thought as a composite of a large number of well-defined images. If the internal energy of the unobserved product is well defined, e.g. if it is an atom in a single quantum level, the images can be analyzed by the PHOTOLOC technique, to get differential cross section information.[11,12] In this case, where the product distribution is very hot and cross-correlations between different vibrational levels are not known, the technique can not be used. One has to do a two beam experiment to have a well defined initial velocity of the incoming $O(^1D)$ atoms.

We have used the Repeller Pulsing technique in conjunction with the dual-beam setup to probe for various internal energies of the NO product. Both probe laser timing scans and probe wavelength scans are incorporated for the vibrational levels searched. The wavelength scans are required to see if there is any signal over the NO background spectra and the timing scans are used to see if there is any delay between the arrival time of maximum amount of $O(^1D)$ atoms in the interaction area and the maximum amount of NO reaction product. During the probe laser scans, the repeller pulse is triggered by the probe lamp trigger just like the mass gate is triggered from the probe laser. The repeller pulse is set to arrive about 30 ns before the probe laser and all the background from the photolysis laser is eliminated, as explained in the previous section. The photolysis wavelength is used in a fashion to generate $O(^1D)$ distributions as shown in Figure 5.16. Higher signal levels were accomplished by collimating the photolysis laser in a slightly tilted fashion so as to hit the upper molecular beam closer to the lower beam. The vertical beam profiles for both molecular beams are well documented from one laser and one beam experiments, such as detecting $O(^1D)$ from N_2O photolysis by 203.7 nm laser light.

In Figure 5.21, the NO(v=1) product from the title reaction is probed. The probe laser crosses the lower molecular beam and its lamp trigger is set to make the probe laser pulse temporally coincide with the $O(^1D)$ atoms approaching from the upper beam. These oxygen atoms have about 1100 m/s speed corresponding to the v=1 in the O_2 co-fragment in the 285 nm dissociation of ozone, as seen in Figure 5.16. While the upper half of the figure shows the scan for reactive signal, the lower part shows the same scan acquired when the ozone beam is off. The lower scan is therefore our background in the experiment, which is on the order of a millivolt. The upper scan can be compared with the corresponding single

beam experiment where the reactive signal is found, i.e. Figure 4.7. Apparently, the expected hot spectra from the single beam experiment can not go over the background level in the dual beam experiment. It should be noted that, since repeller pulsing method is used in these experiments all the background is from the probe laser. In particular, probe + N_2O creates NO molecules in various vibrational levels. [a] Similar scans for the dual-beam experiment were done probing various NO vibrational levels, such as v=1,2,3 and 5 and with various photolysis wavelengths for different collision energies. The probe laser timing and N_2O beam timing were also used as a variable to account for preferential detection in all these experiments.

5.7 Conclusion

It is particularly striking that the reaction observed in a single molecular beam is not observed in the case of a dual-beam setting. In the latter case, the two beams are only separated by 10 mm. The ozone number density is about 5 times bigger and the nitrous oxide density is 10 times bigger compared to the former case, since ozone is kept at -40 °C instead of -78 °C and neat nitrous oxide is used instead of a mixture. Roughly 1% of the O(^{1}D) atoms created in the upper beam fly to the lower beam. The 10 ns probe pulse will have preferential detection for different NO speeds. Geometric arguments can be used to roughly estimate a factor of 0.1 as the fraction of O(^{1}D) atoms creating NO molecules with a detectable speed by the 10 ns pulse. Then, one can expect a signal level of 20 mV $\frac{1}{100}$ $\frac{1}{10}$ 5 10 = 1 mV.

These signal levels were hoped to be detected by the accumulation of ions in

[a] This NO source is characterized in detail in the previous chapter along with the thermal NO molecules in the chamber.

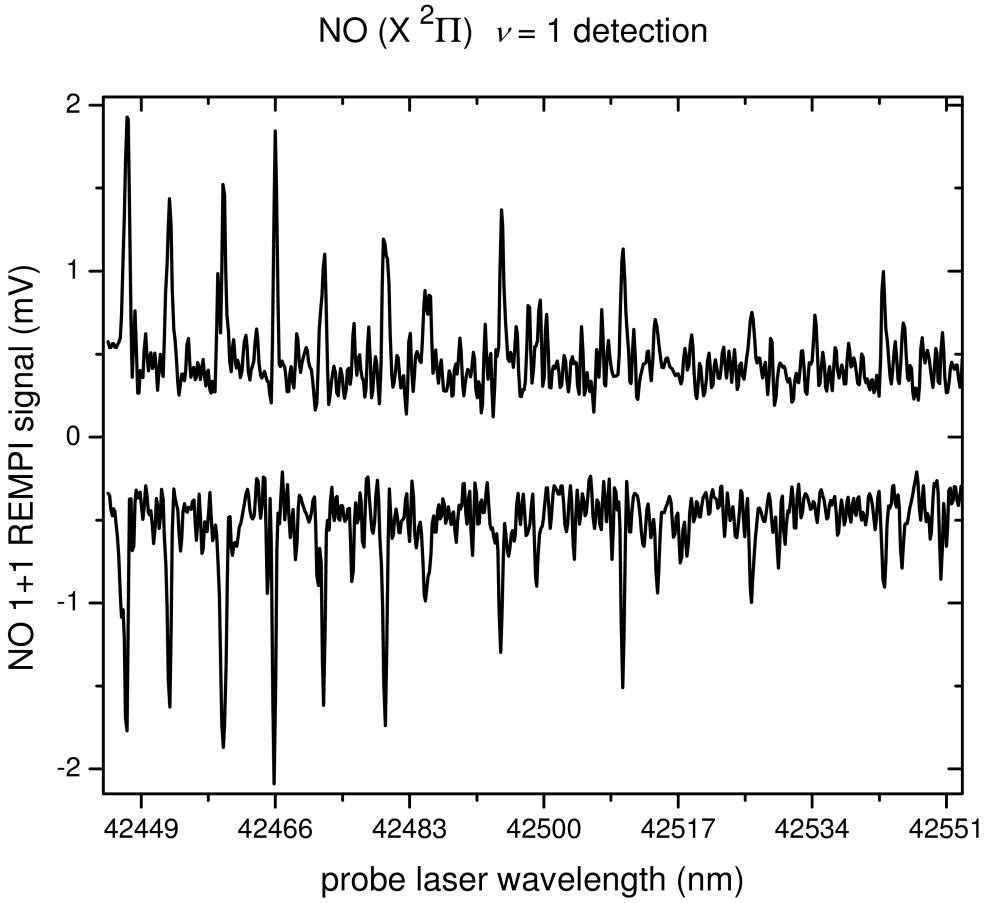

Figure 5.21: Wavelength scan probing for reactive NO product signal. The upper half shows the full experiment. The inverted lower half is the control signal, i.e. when the ozone beam is turned off.

the images with 10 hour long ion-counting and with amplified MCP settings. From simple 1D simulations, assuming an incoming Gaussian distribution of O atoms and known collision cross sections, it was estimated that about 1% of the O(^{1}D) would react with the beam. This should be similar to a single beam reaction rate. Given the larger reagent number densities, it was expected to see NO reactive scattering in the images. The disadvantage of the incoming reagent spread in three dimensions and a very high number of available quantum states in the product precluded the observation of reactive signal.

In the future, another nozzle-skimmer design may allow for a shorter vertical flight distance for the O(^{1}D) atoms, resulting in a smaller spread. This, together with the repeller pulsing delayed extraction scheme, should allow reactive signal imaging in the dual-beam apparatus. The developments in the piezo valve technology, such as new valves providing short (7μs FWHM) and strong gas pulses with high repetition rates (5kHz) may prove useful for the future of the field.[13]

BIBLIOGRAPHY

[1] J. H. Wang, Y. T. Hsu, and K. Liu *J. Phys. Chem. A.*, vol. 101, pp. 6593–6602, 1997.

[2] L. H. Lai, D. C. Che, and K. Liu *J. Phys. Chem.*, vol. 100, pp. 6376–6380, 1996.

[3] Y. T. Hsu, K. Liu, L. A. Pederson, and G. C. Schatz *J. Chem. Phys.*, vol. 111, pp. 7921–7930, 1999.

[4] J. B. Anderson, *Molecular Beams and Low Density Gas Dynamics.* Marcel Dekker Inc., New York, 1974.

[5] J. B. Anderson and J. B. Fenn *Phys. Fluids*, vol. 8, p. 780, 1965.

[6] D. A. Belle-Oudry. PhD thesis, Cornell University, Ithaca, 1997.

[7] R. L. Toomes, P. C. Samartzis, T. P. Rakitzis, and T. N. Kitsopoulos *Chem. Phys.*, vol. 301, p. 209, 2004.

[8] S. M. Dylewski, J. D. Geiser, and P. L. Houston *J. Chem. Phys.*, vol. 115, p. 7460, 2001.

[9] S. P. Sander, B. J. Finlayson-Pitts, R. R. Friedl, D. M. Golden, R. E. Huie, C. E. Kolb, M. J. Molina, G. K. Moorgat, V. L. Orkin, and A. R. Ravishankara, *Pasadena JPL Publication 02-25.* Jet Propulsion Laboratory, 2002.

[10] R. L. Miller, A. G. Suits, P. L. Houston, R. Toumi, J. A. Mack, and A. M. Wodtke *Science*, vol. 265, p. 1831, 1994.

[11] N. E. Shafer, A. J. Orr-Erwing, W. R. Simpson, H. Xu, and R. N. Zare *Chem. Phys. Letters*, vol. 212, p. 155, 1993.

[12] N. E. Shafer, A. J. Orr-Erwing, and R. N. Zare *J. Phys. Chem.*, vol. 99, p. 7591, 1995.

[13] D. Irmia, D. Dobrikov, R. Kortekaas, H. Voet, D. A. van den Ende, W. A. Groen, and M. H. Janssen *Rev. Sci. Instr.*, vol. 80, p. 113303, 2009.

Appendices

APPENDIX A

1+1 REMPI NO SPECTRA FROM THE O(^{1}D) + N_2O REACTION

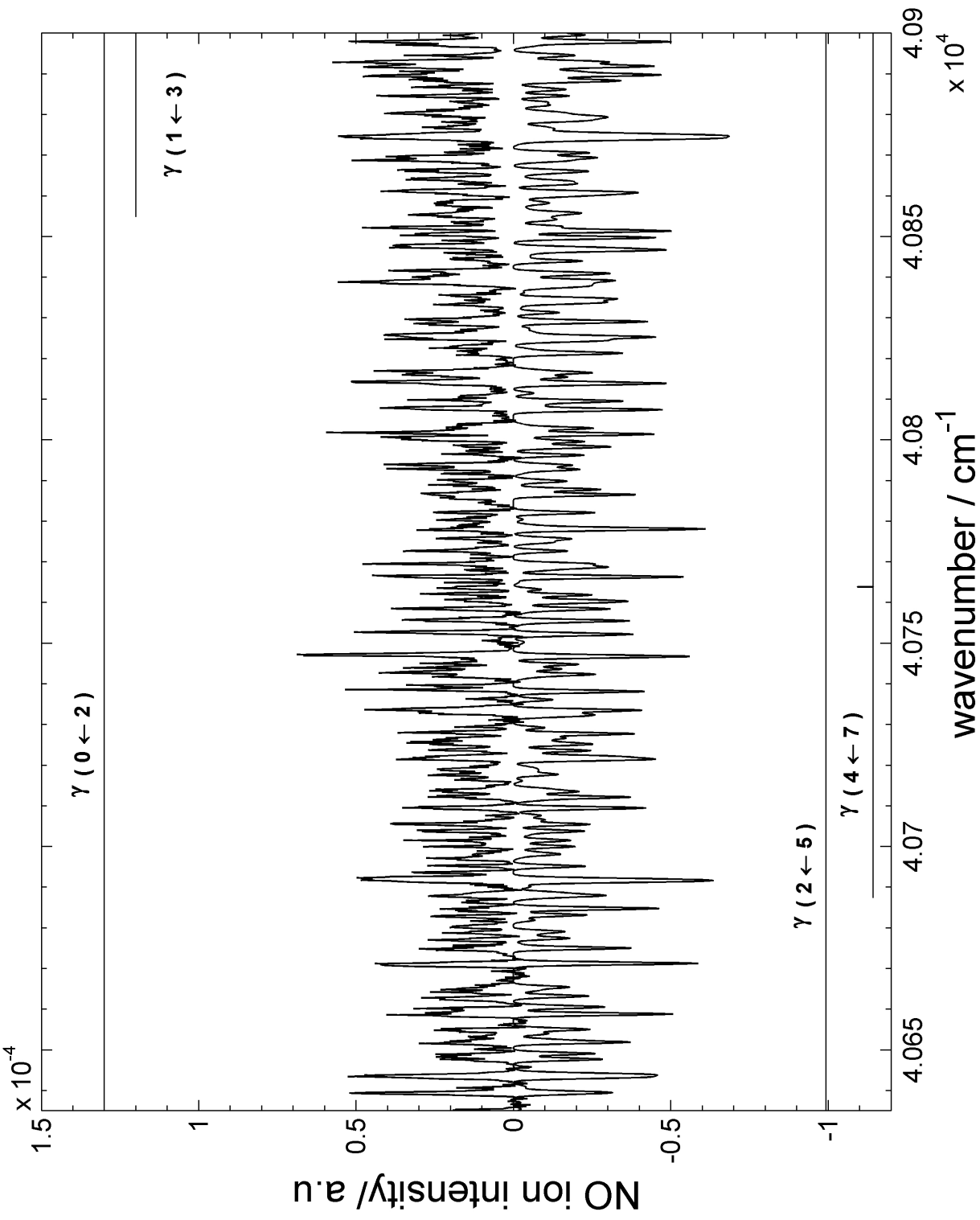
γ (0 ← 2)
γ (1 ← 3)
γ (2 ← 5)
γ (4 ← 7)
NO ion intensity/ a.u
x 10^-4
1.5
1
0.5
0
-0.5
-1
4.065
4.07
4.075
4.08
4.085
4.09
x 10^4
wavenumber / cm^-1

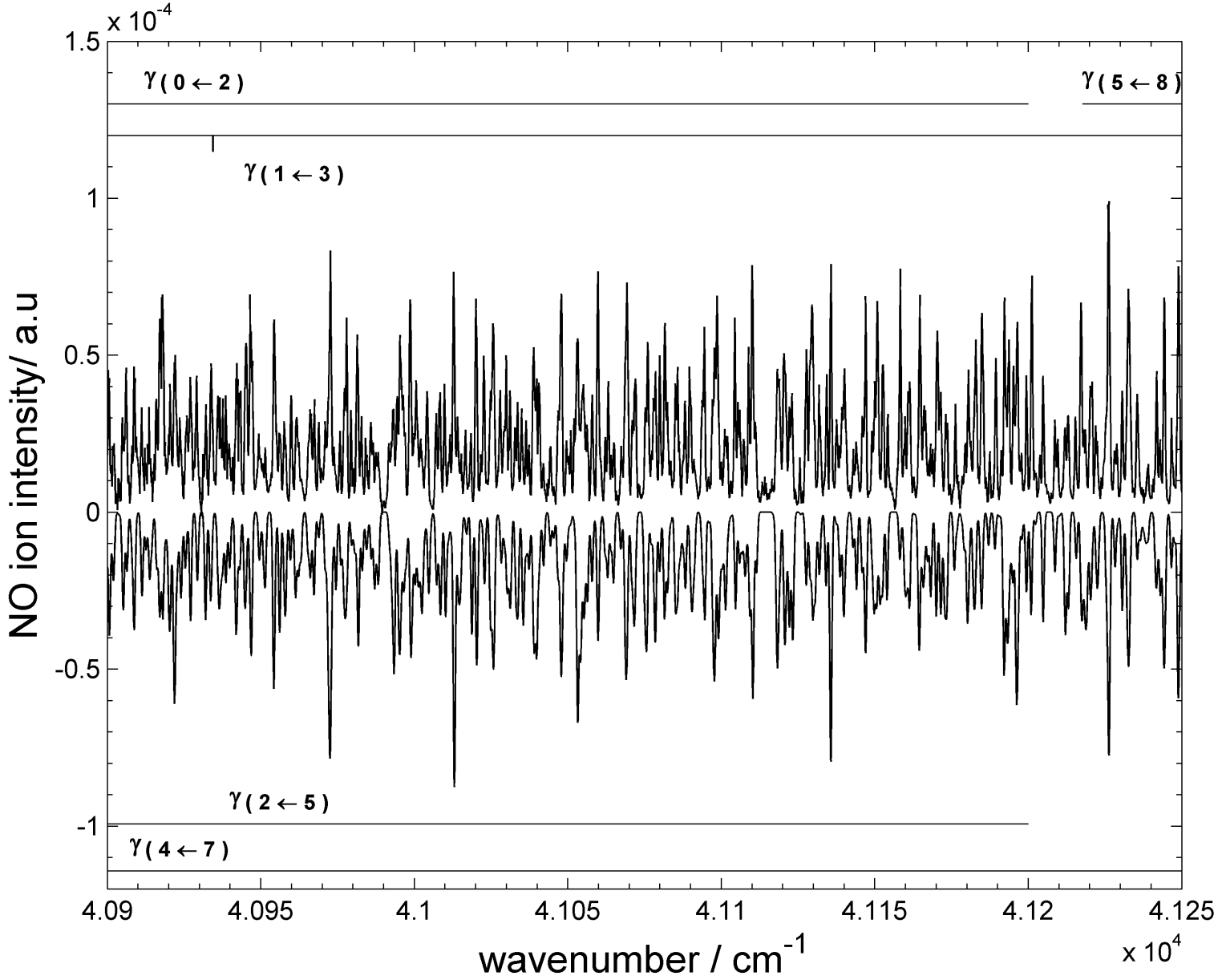
x 10^-4
1.5
1
0.5
0
-0.5
-1
γ (0 ← 2)
γ (5 ← 8)
γ (1 ← 3)
γ (2 ← 5)
γ (4 ← 7)
NO ion intensity/ a.u
4.09
4.095
4.1
4.105
4.11
4.115
4.12
4.125
wavenumber / cm^-1
x 10^4

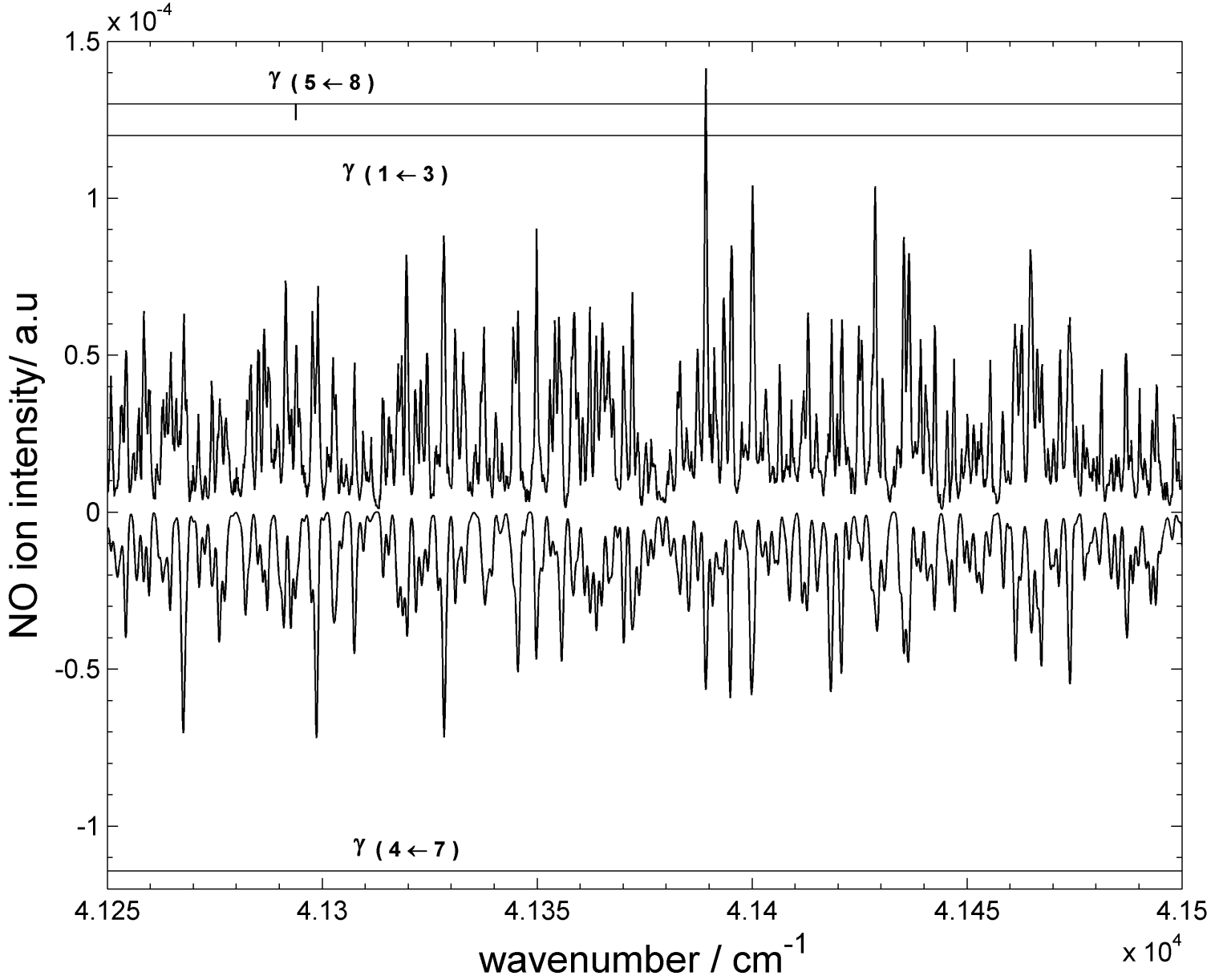
x 10^-4
1.5
γ (5 ← 8)
γ (1 ← 3)
1
0.5
0
-0.5
-1
γ (4 ← 7)
NO ion intensity/ a.u
4.125
4.13
4.135
4.14
4.145
4.15
wavenumber / cm^-1
x 10^4

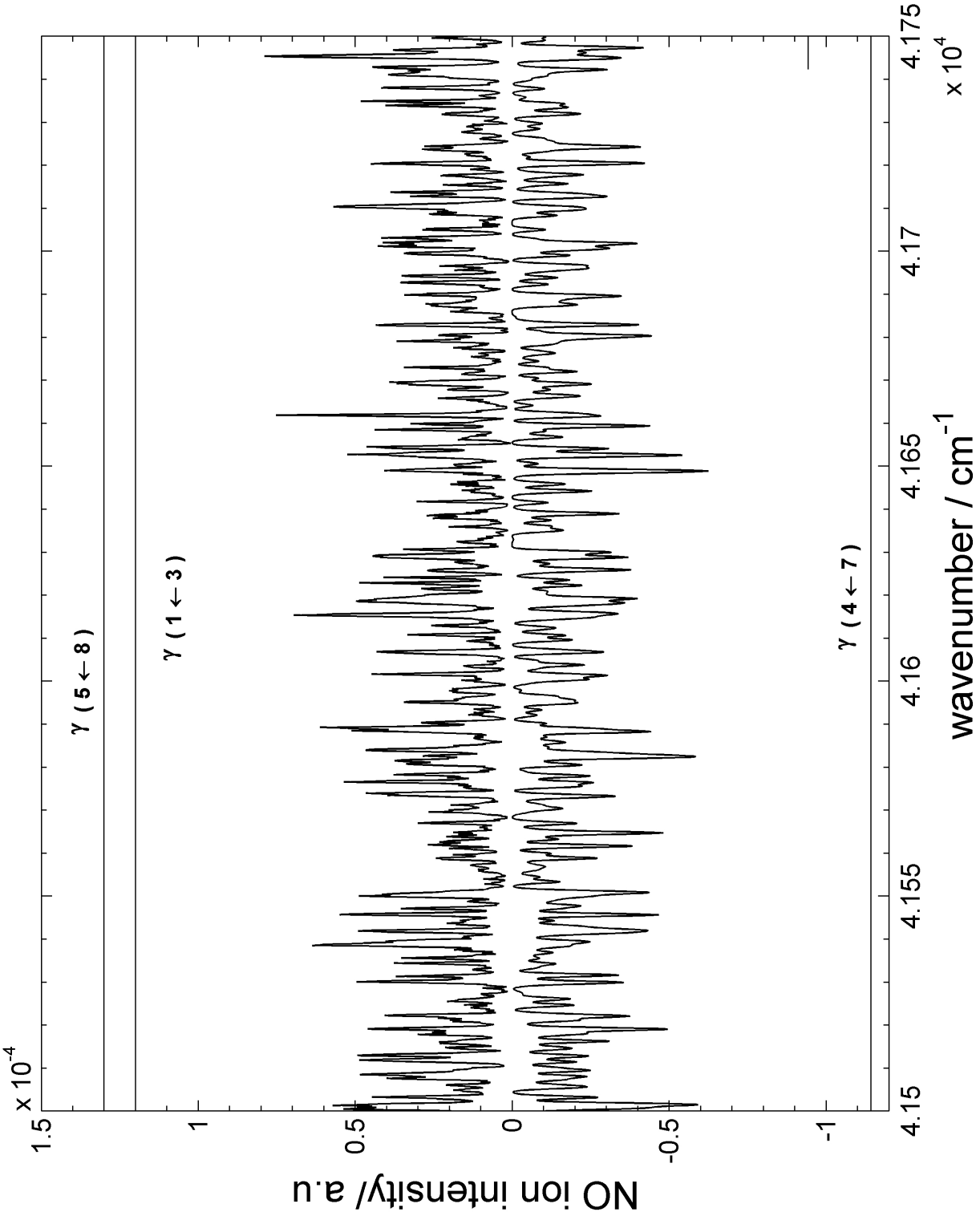
NO ion intensity/ a.u
wavenumber / cm-1
x 10-4
x 10-4
γ (5 ← 8)
γ (1 ← 3)
γ (4 ← 7)
1.5
1
0.5
0
-0.5
-1
4.15
4.155
4.16
4.165
4.17
4.175

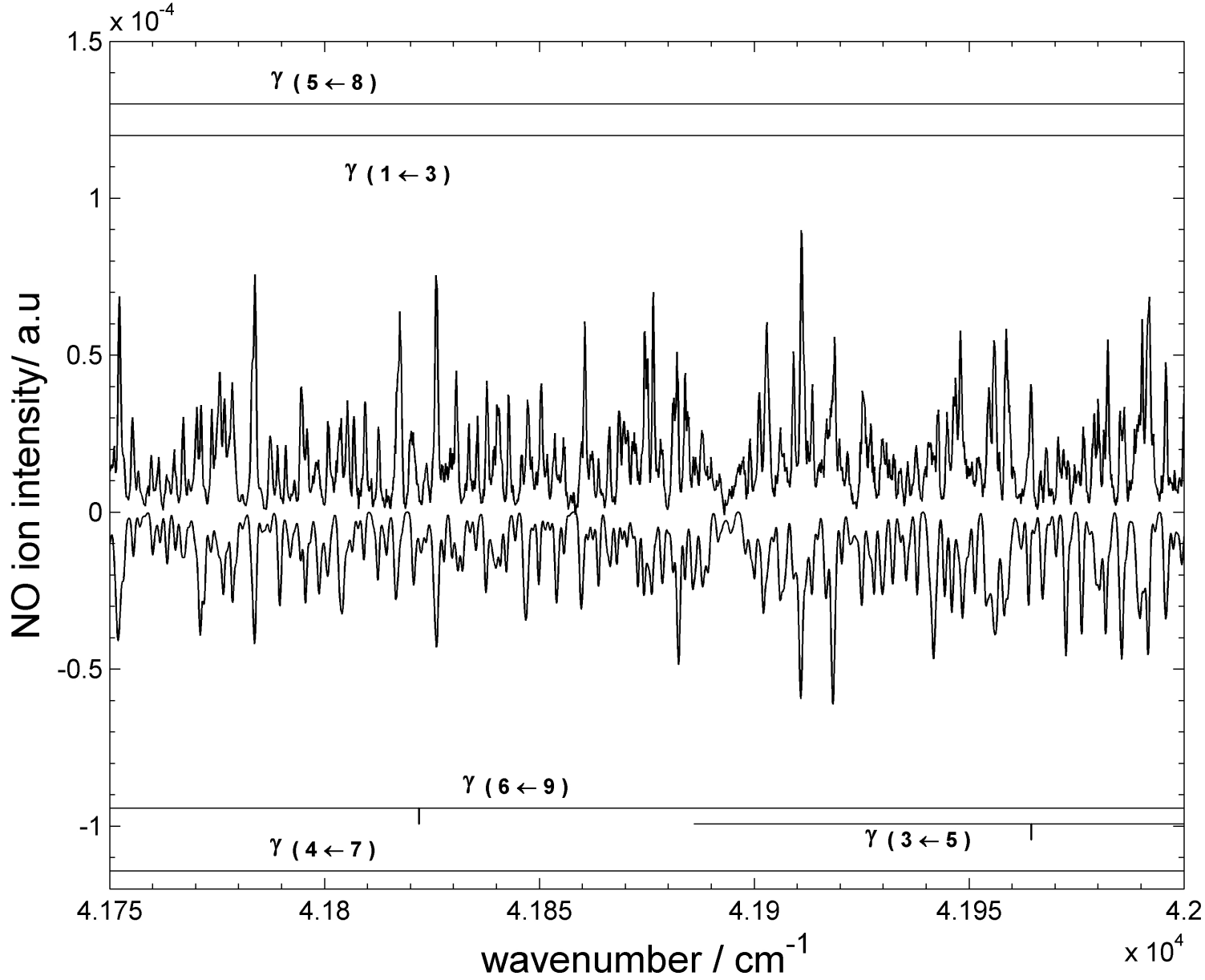
x 10^-4
1.5
γ (5 ← 8)
γ (1 ← 3)
1
0.5
0
-0.5
-1
γ (6 ← 9)
γ (4 ← 7)
γ (3 ← 5)
NO ion intensity/ a.u
4.175
4.18
4.185
4.19
4.195
4.2
x 10^4
wavenumber / cm^-1

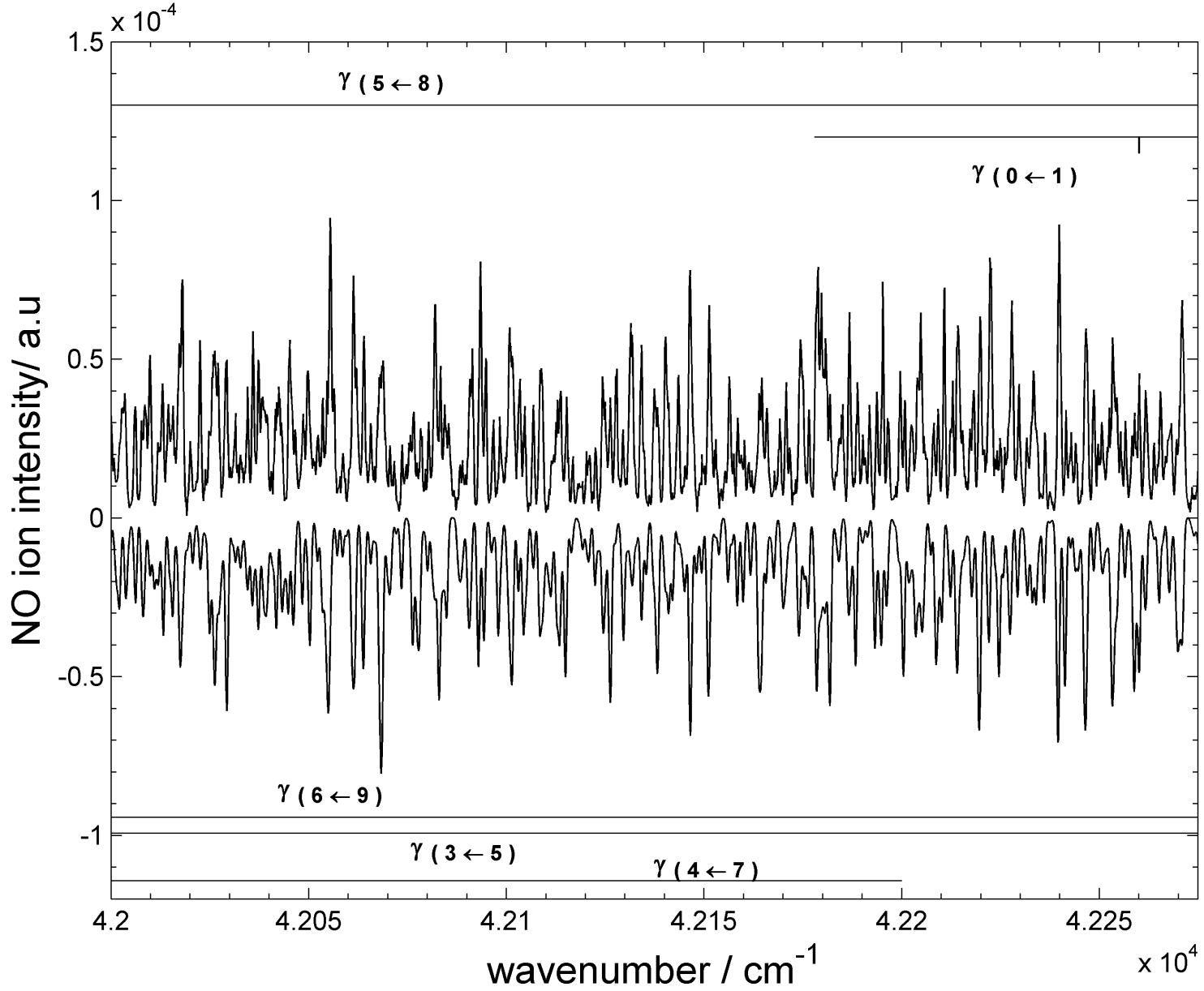
x 10^-4
1.5
1
0.5
0
-0.5
-1
γ (5 ← 8)
γ (0 ← 1)
γ (6 ← 9)
γ (3 ← 5)
γ (4 ← 7)
NO ion intensity/ a.u
4.2
4.205
4.21
4.215
4.22
4.225
wavenumber / cm^-1
x 10^4

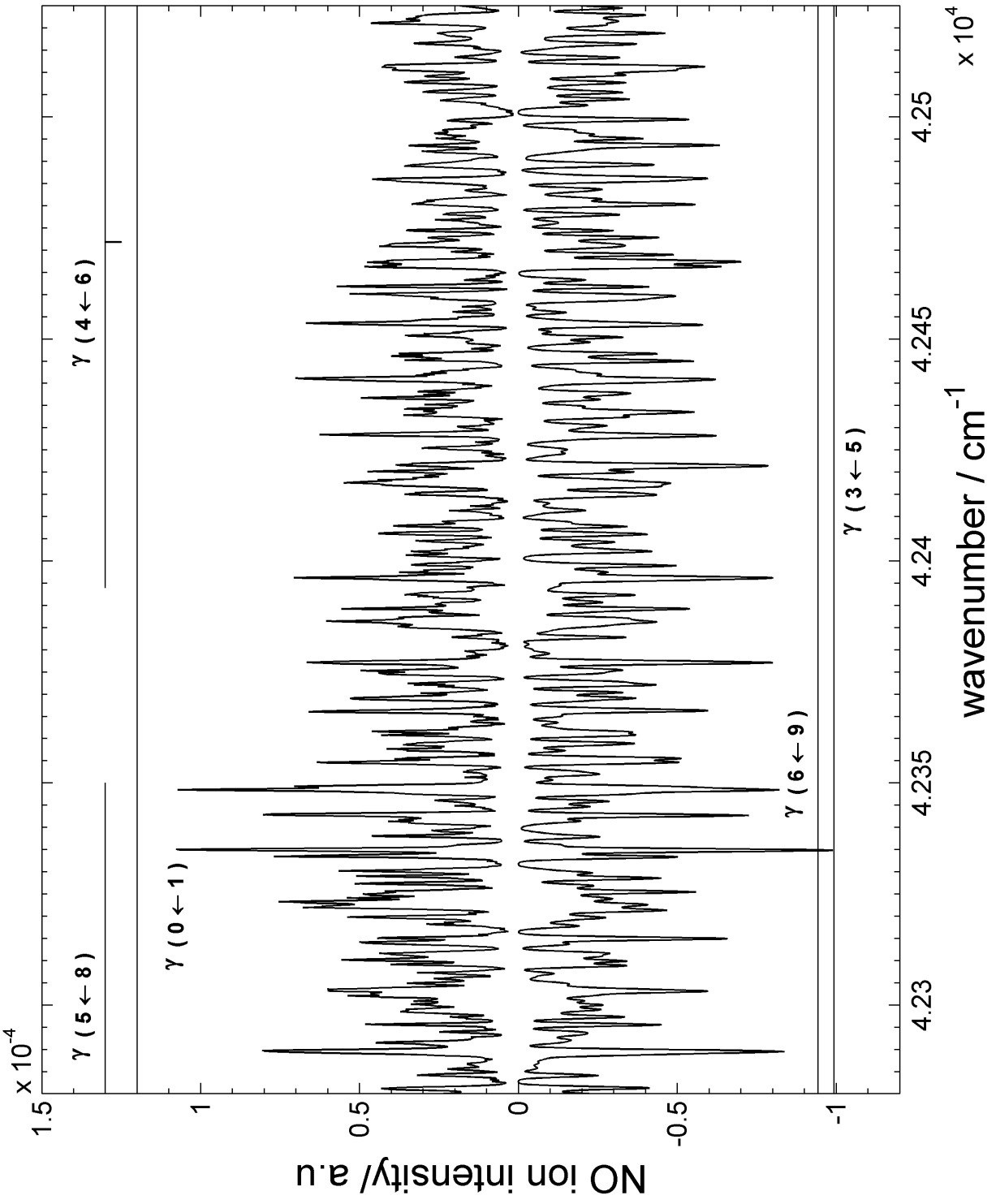
γ (5 ← 8)
γ (0 ← 1)
γ (4 ← 6)
γ (6 ← 9)
γ (3 ← 5)
x 10^-4
1.5
1
0.5
0
-0.5
-1
NO ion intensity/ a.u
4.23
4.235
4.24
4.245
4.25
x 10^4
wavenumber / cm^-1

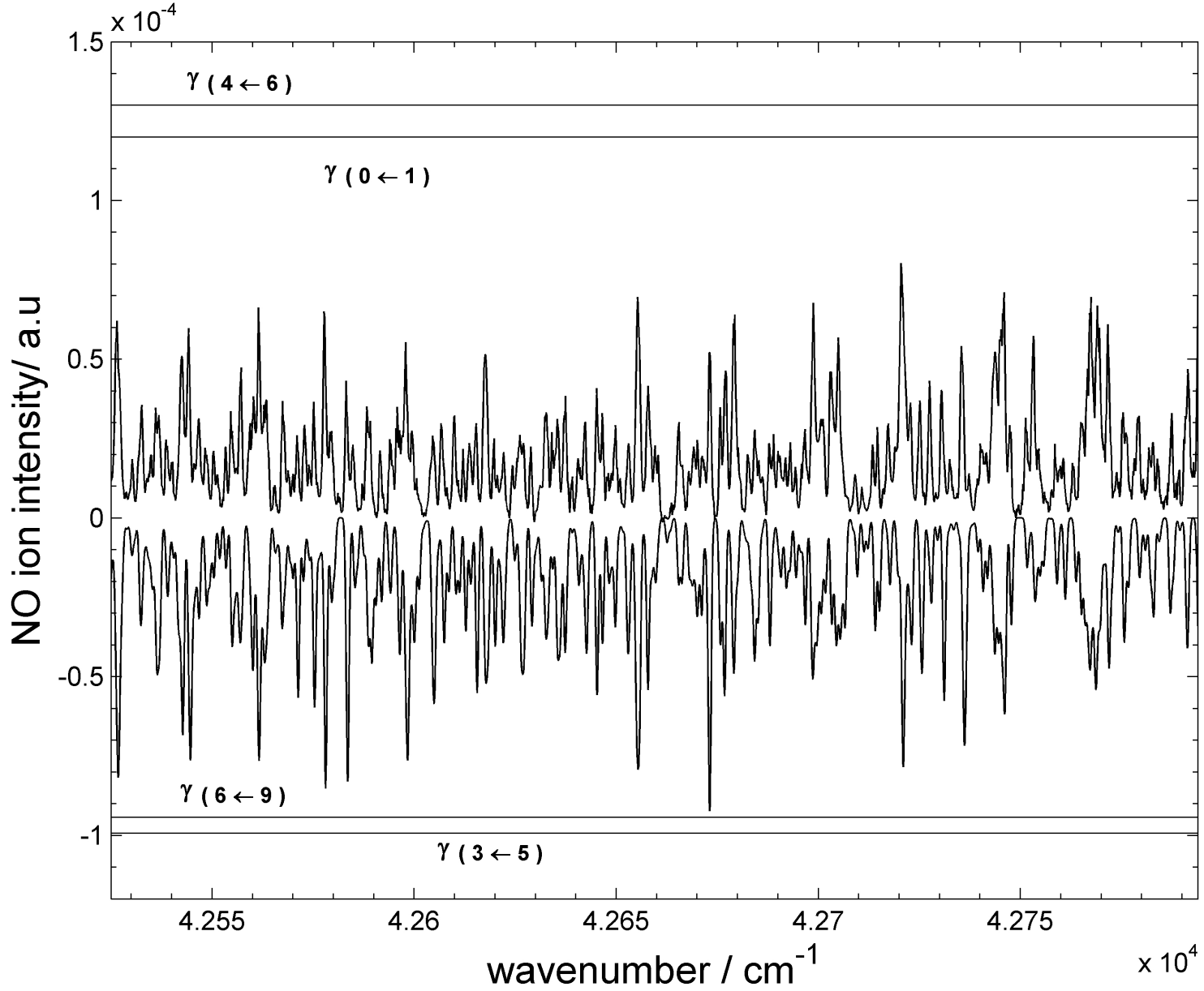
x 10^-4
1.5
1
0.5
0
-0.5
-1
γ (4 ← 6)
γ (0 ← 1)
γ (6 ← 9)
γ (3 ← 5)
NO ion intensity/ a.u
4.255
4.26
4.265
4.27
4.275
wavenumber / cm^-1
x 10^4

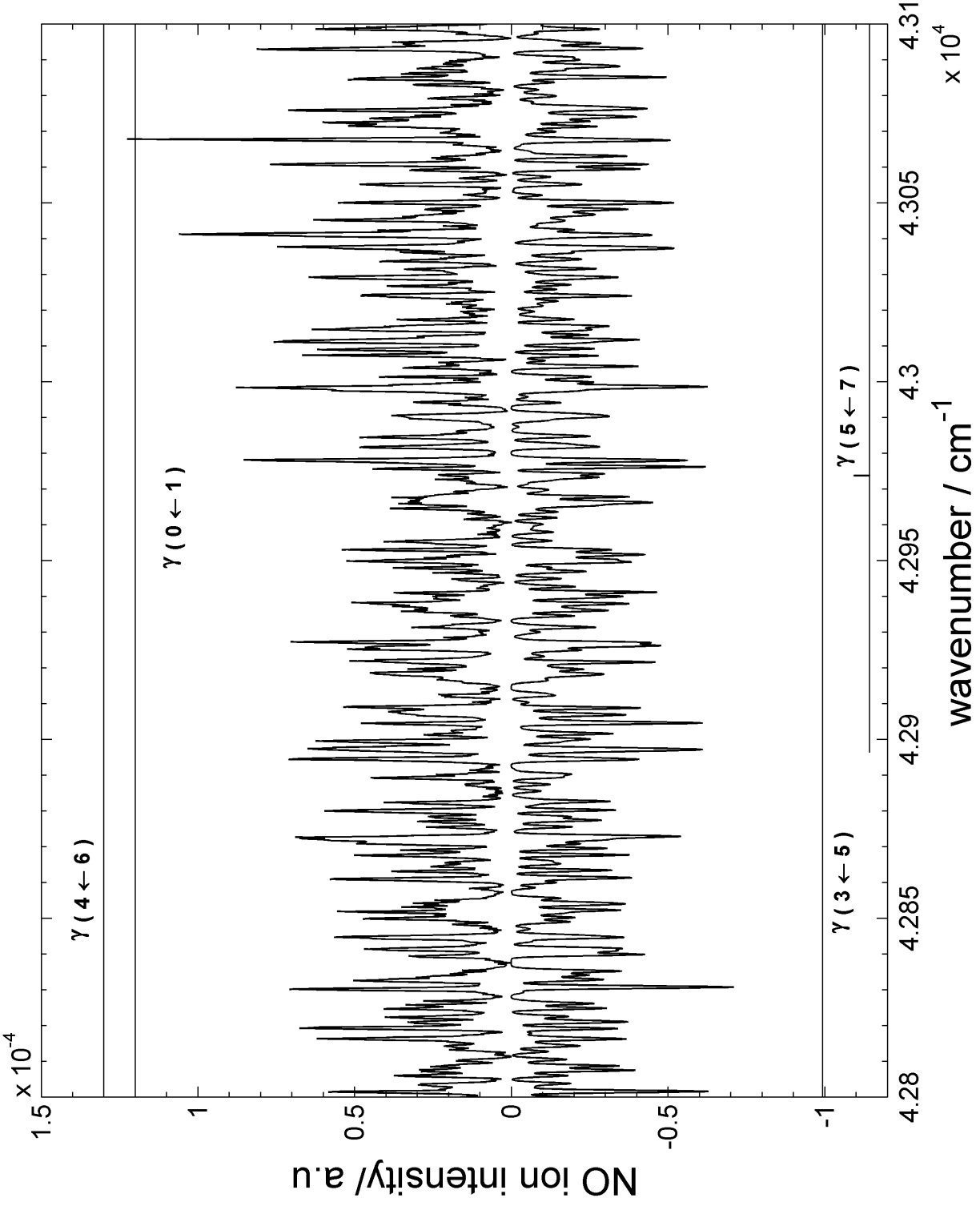
γ (4 ← 6)
γ (0 ← 1)
γ (3 ← 5)
γ (5 ← 7)
x 10^-4
1.5
1
0.5
0
-0.5
-1
NO ion intensity/ a.u
4.28
4.285
4.29
4.295
4.3
4.305
4.31
x 10^4
wavenumber / cm^-1

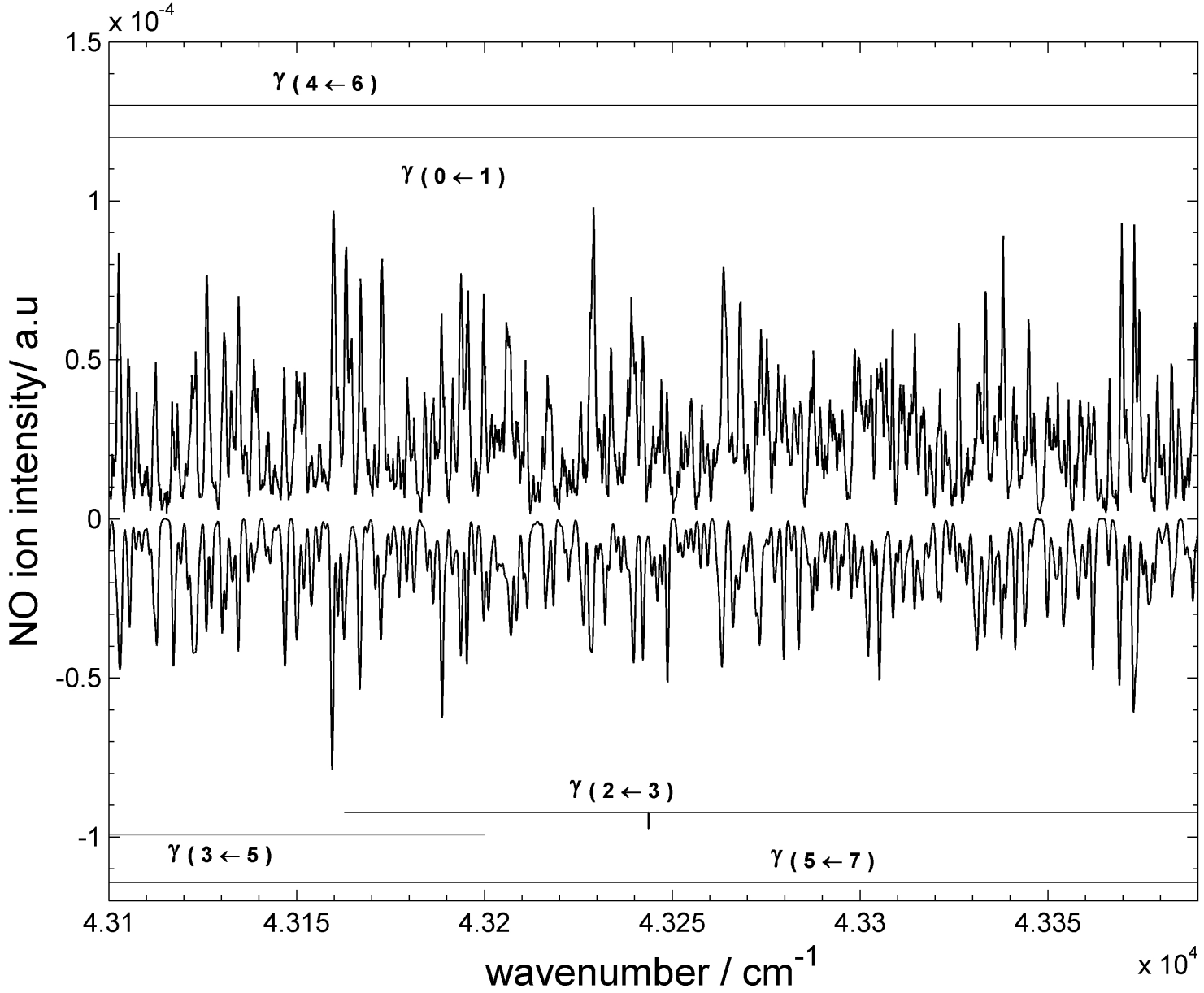
x 10^-4
1.5
γ (4 ← 6)
γ (0 ← 1)
1
0.5
0
-0.5
-1
NO ion intensity/ a.u
γ (2 ← 3)
γ (3 ← 5)
γ (5 ← 7)
4.31
4.315
4.32
4.325
4.33
4.335
wavenumber / cm^-1
x 10^4

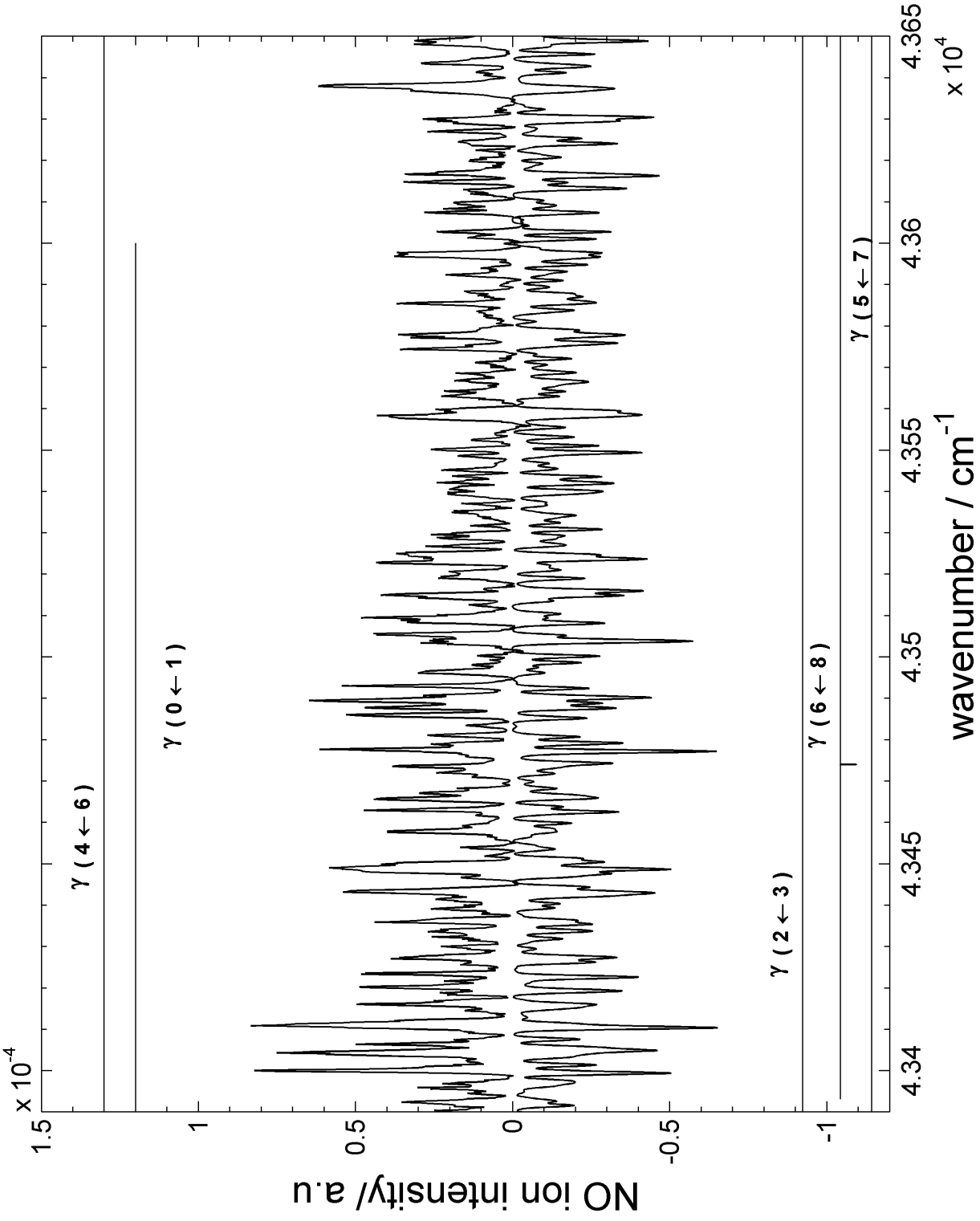
γ (4 ← 6)
γ (0 ← 1)
γ (2 ← 3)
γ (6 ← 8)
γ (5 ← 7)
x 10^-4
1.5
1
0.5
0
-0.5
-1
NO ion intensity/ a.u
4.34
4.345
4.35
4.355
4.36
4.365
x 10^4
wavenumber / cm^-1

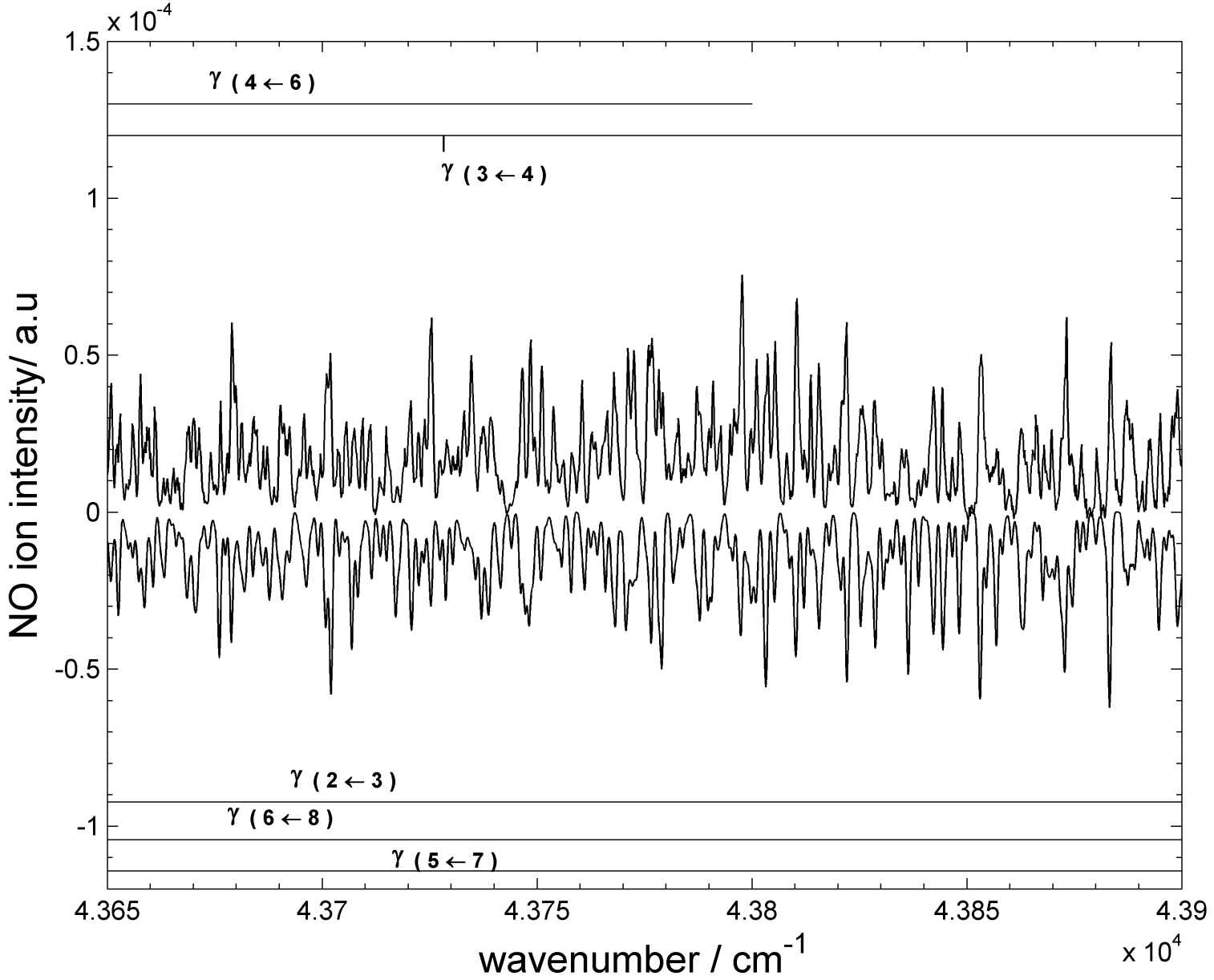
x 10^-4
1.5
γ (4 ← 6)
γ (3 ← 4)
1
0.5
0
-0.5
γ (2 ← 3)
γ (6 ← 8)
-1
γ (5 ← 7)
NO ion intensity/ a.u
4.365
4.37
4.375
4.38
4.385
4.39
wavenumber / cm^-1
x 10^4

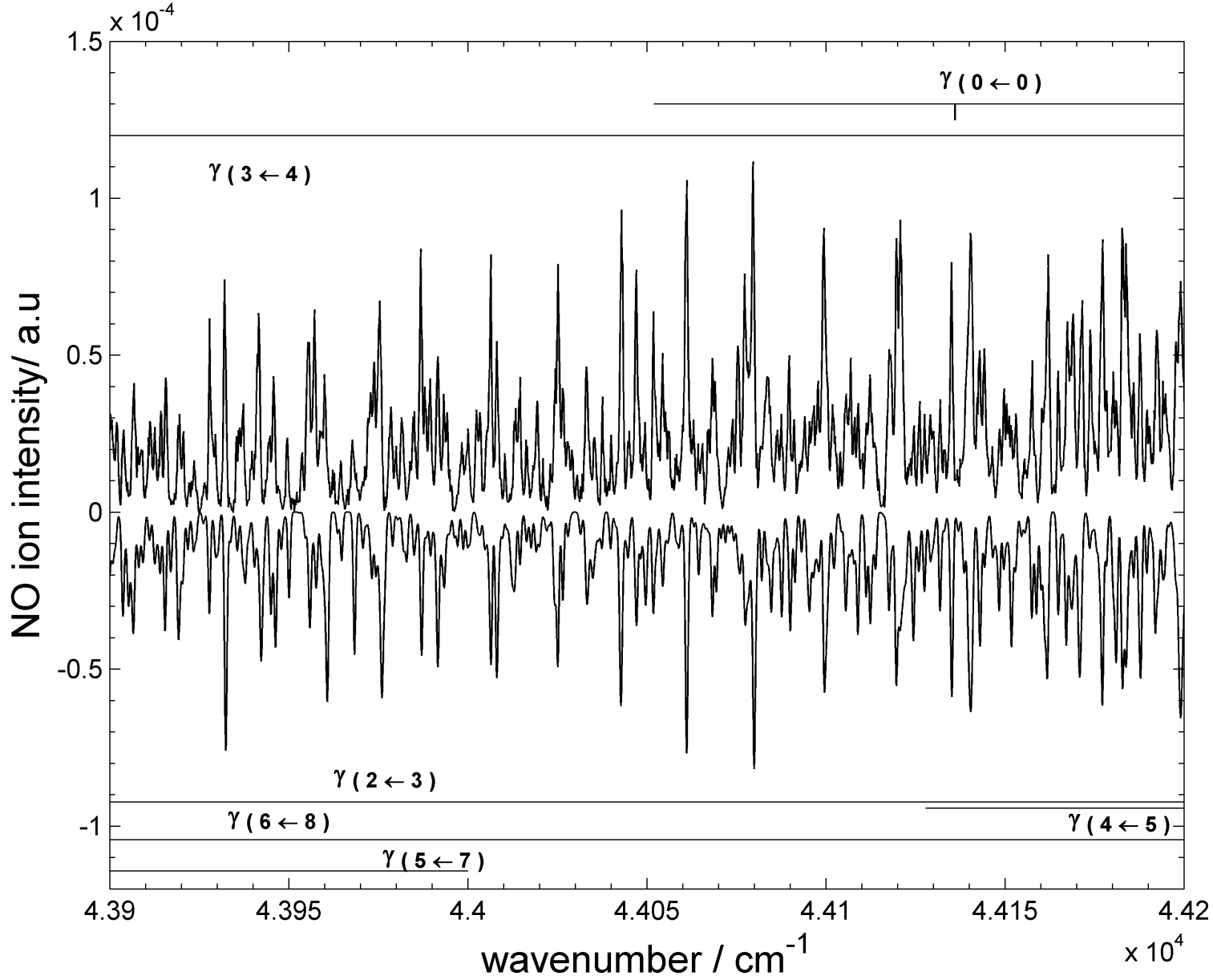
x 10^-4
1.5
1
0.5
0
-0.5
-1
γ (0 ← 0)
γ (3 ← 4)
γ (2 ← 3)
γ (6 ← 8)
γ (4 ← 5)
γ (5 ← 7)
NO ion intensity/ a.u
4.39
4.395
4.4
4.405
4.41
4.415
4.42
wavenumber / cm^-1
x 10^4

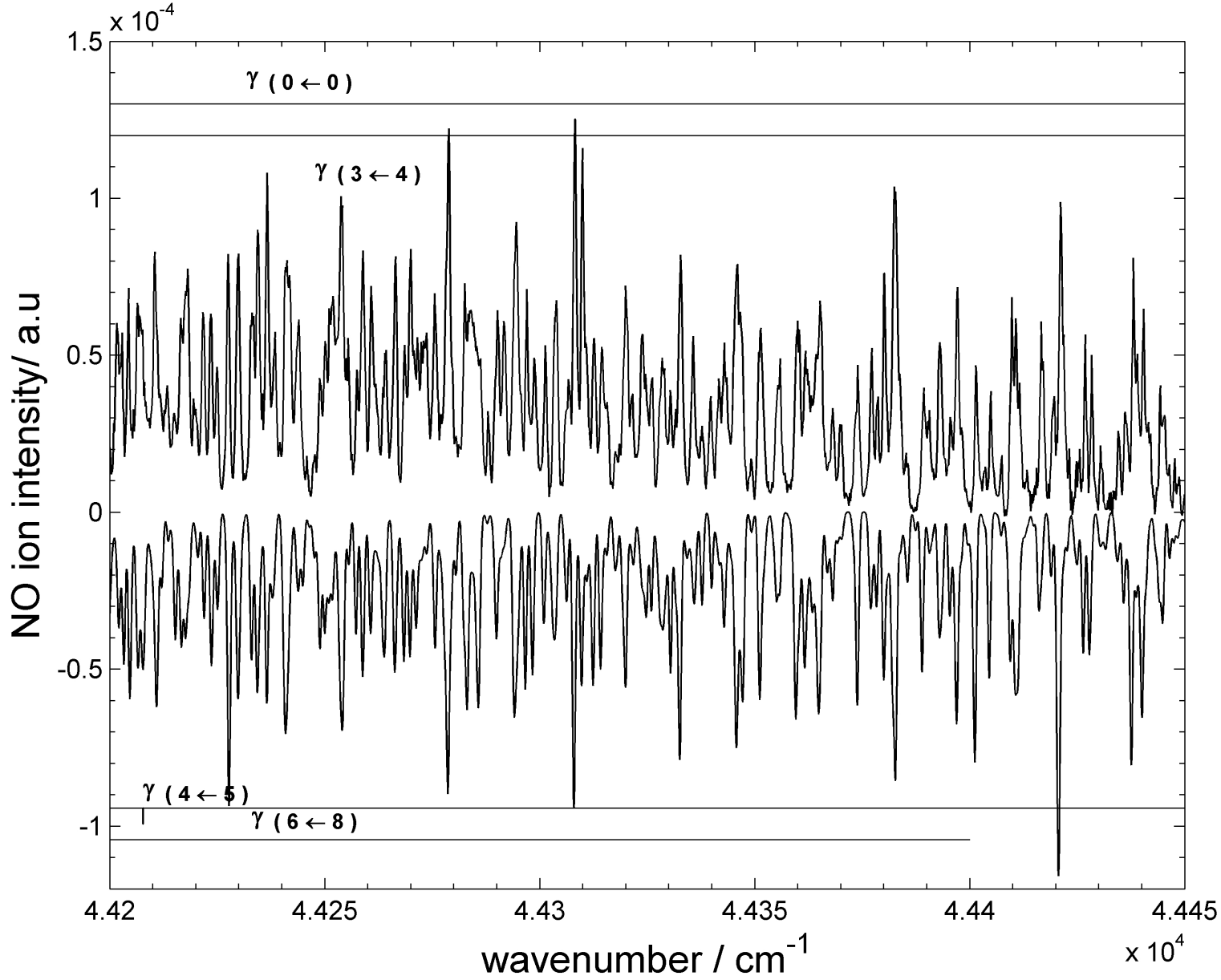
x 10^-4
1.5
1
0.5
0
-0.5
-1
γ (0 ← 0)
γ (3 ← 4)
γ (4 ← 5)
γ (6 ← 8)
NO ion intensity/ a.u
4.42
4.425
4.43
4.435
4.44
4.445
wavenumber / cm^-1
x 10^4

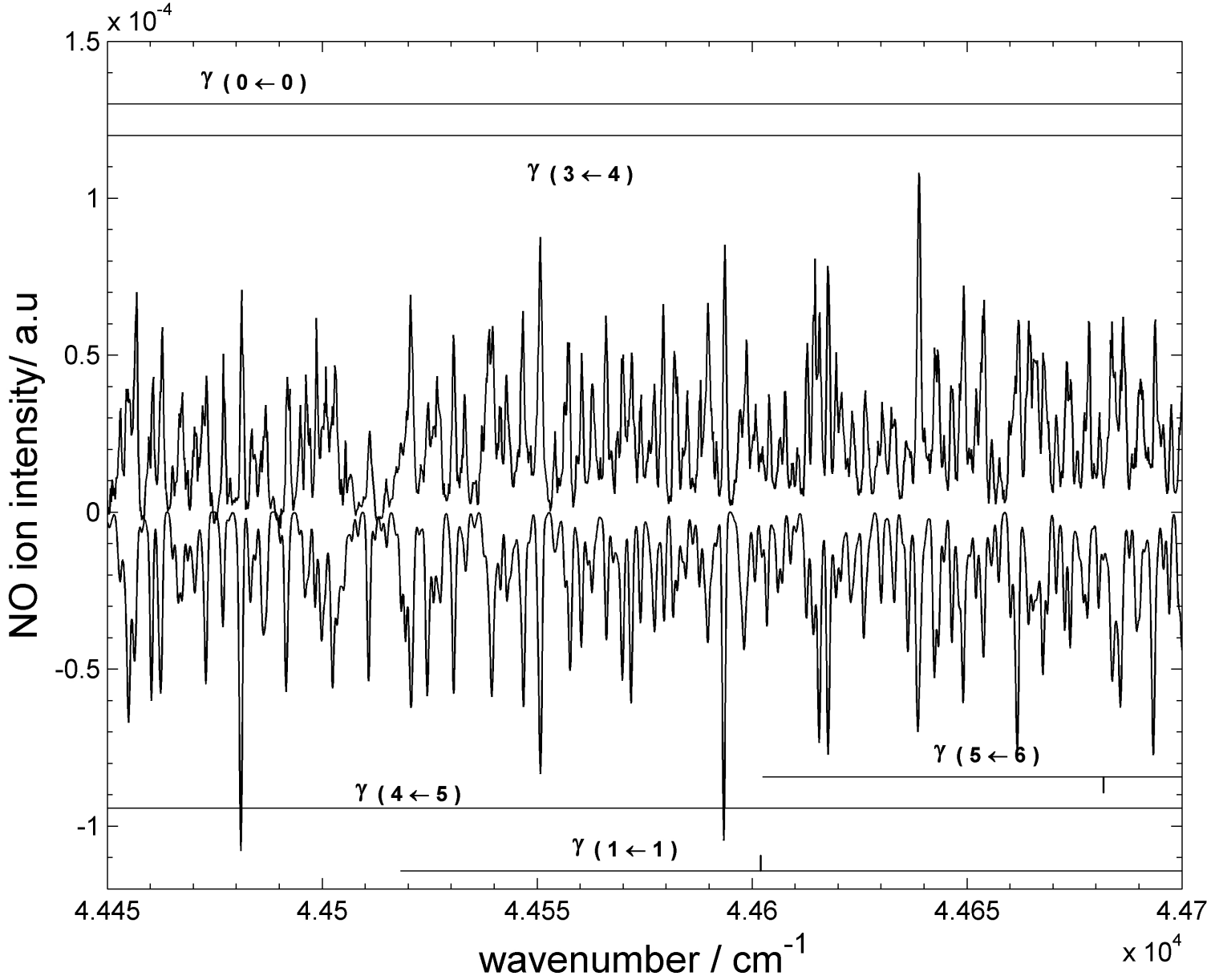
x 10^-4
1.5
γ (0 ← 0)
γ (3 ← 4)
1
0.5
0
-0.5
-1
NO ion intensity/ a.u
γ (5 ← 6)
γ (4 ← 5)
γ (1 ← 1)
4.445
4.45
4.455
4.46
4.465
4.47
x 10^4
wavenumber / cm^-1

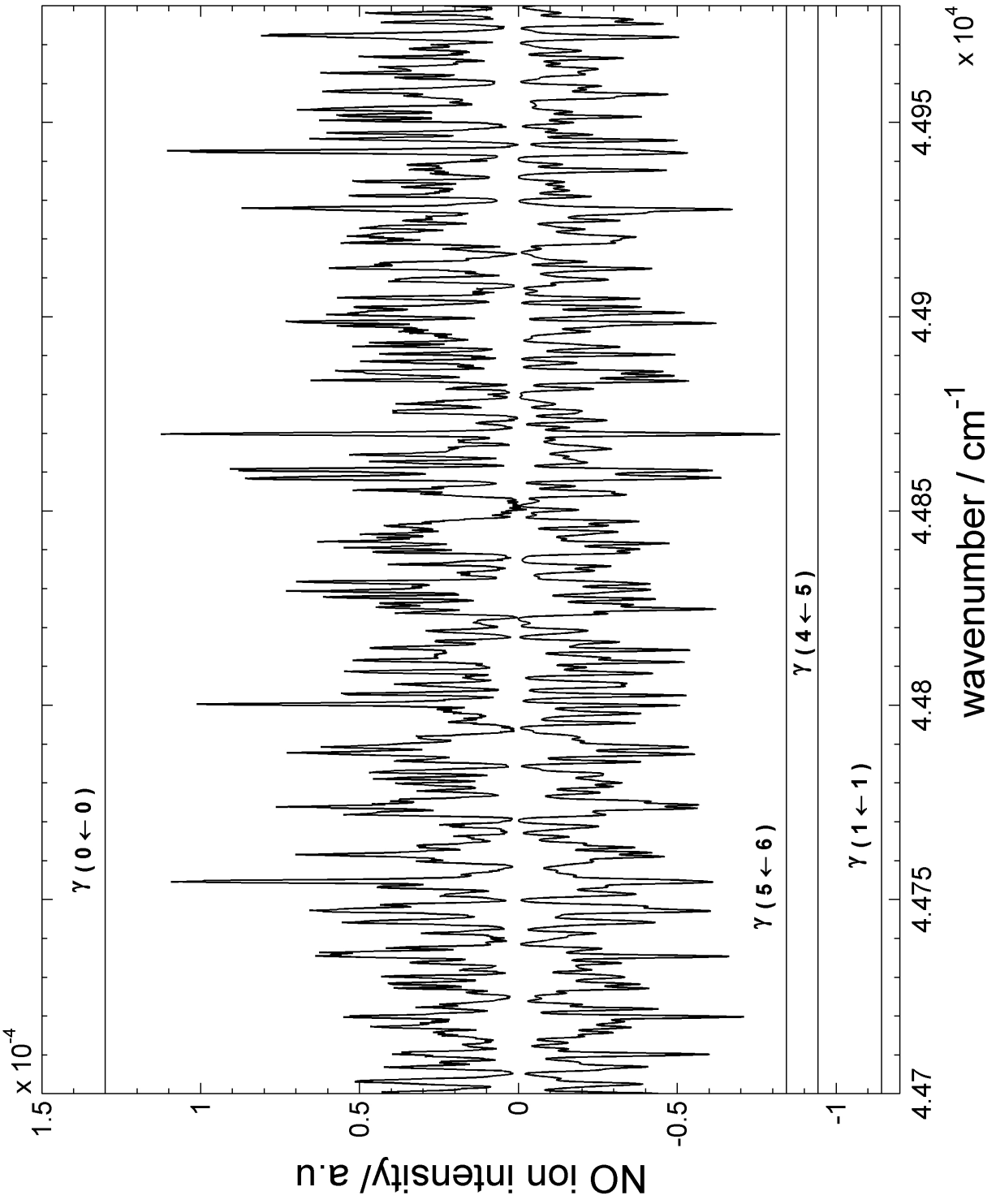
γ (0 ← 0)
γ (5 ← 6)
γ (4 ← 5)
γ (1 ← 1)
x 10^-4
1.5
1
0.5
0
-0.5
-1
NO ion intensity/ a.u
4.47
4.475
4.48
4.485
4.49
4.495
x 10^4
wavenumber / cm^-1

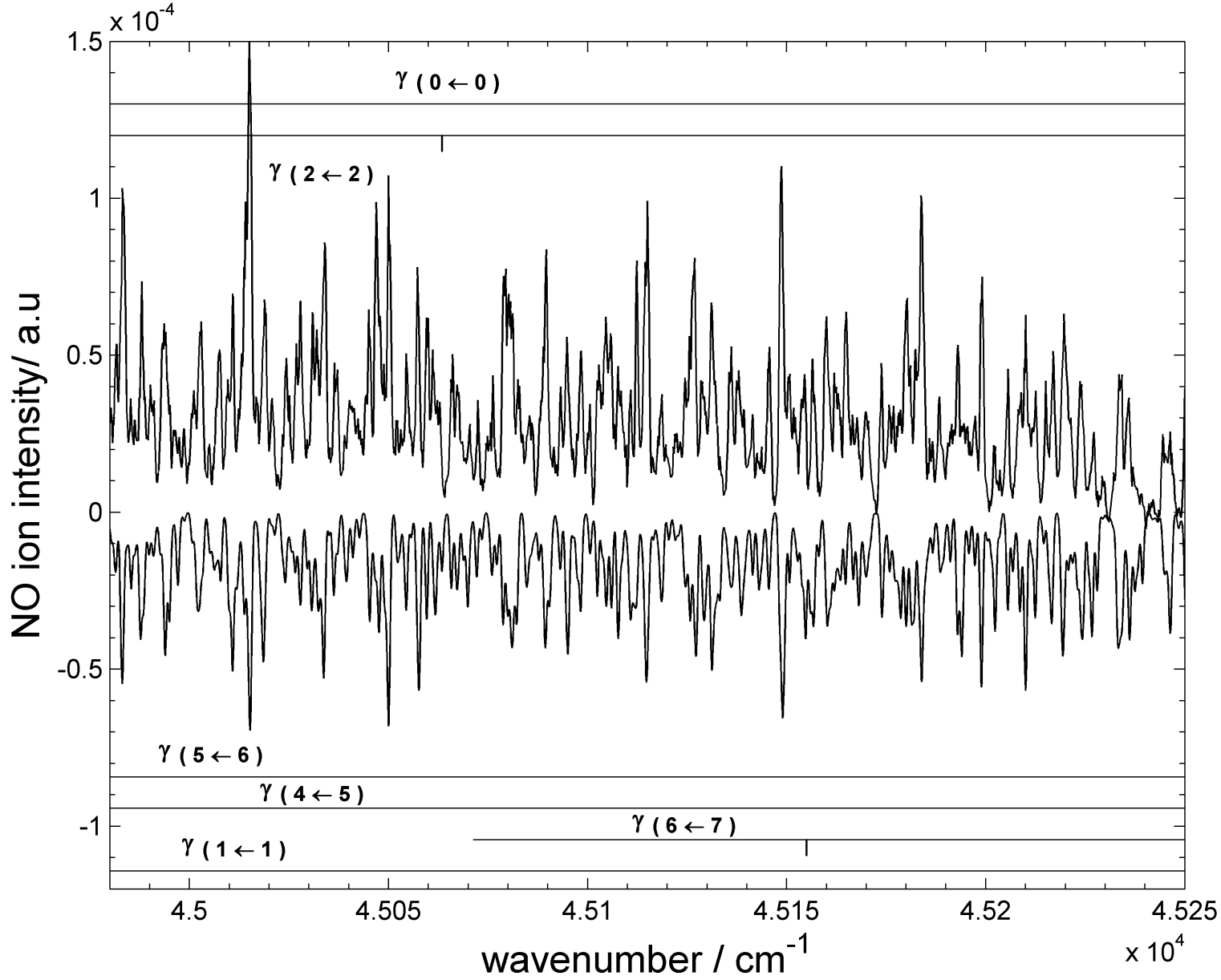
x 10^-4
1.5
1
0.5
0
-0.5
-1
γ (0 ← 0)
γ (2 ← 2)
γ (5 ← 6)
γ (4 ← 5)
γ (6 ← 7)
γ (1 ← 1)
NO ion intensity/ a.u
4.5
4.505
4.51
4.515
4.52
4.525
wavenumber / cm^-1
x 10^4

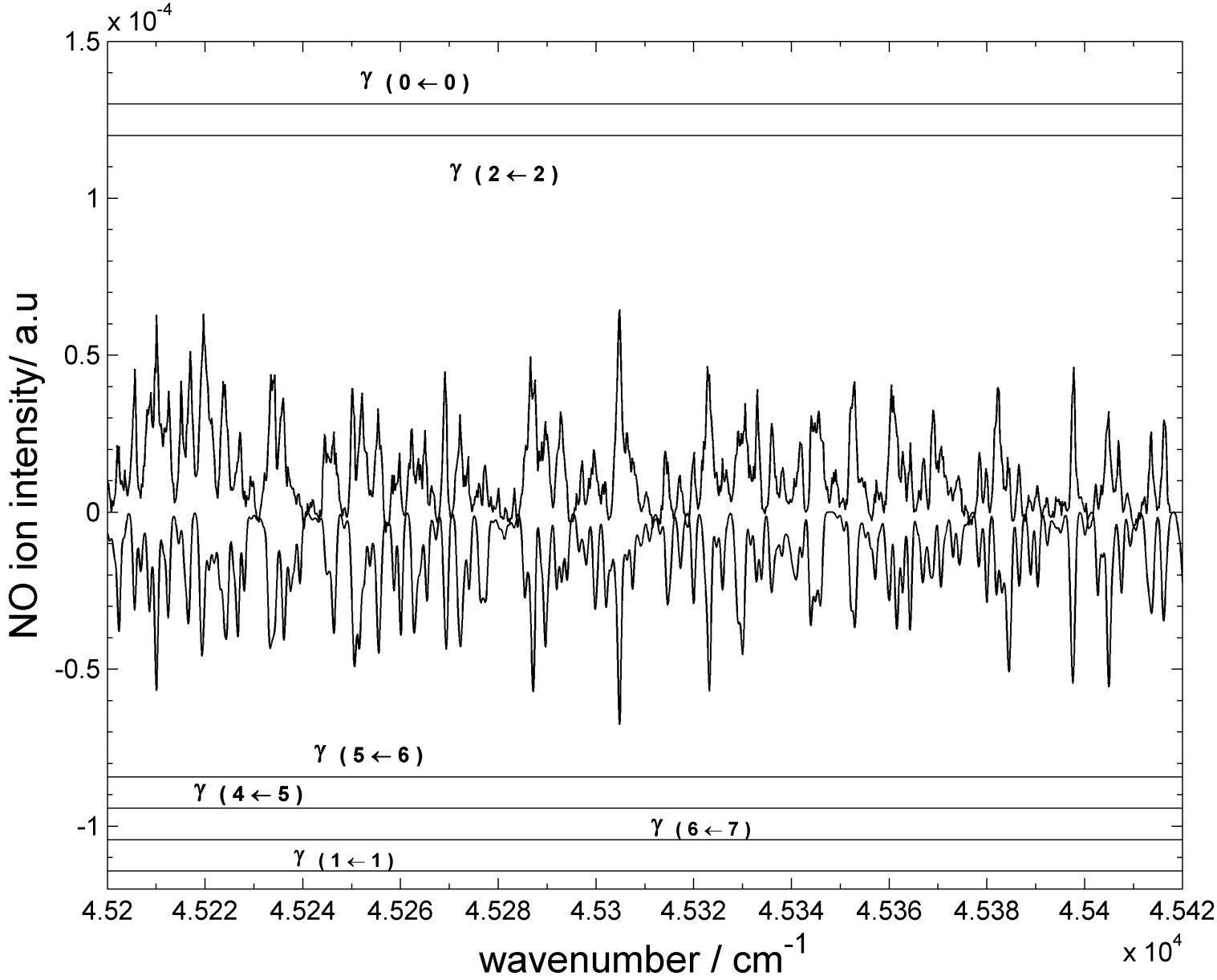
x 10^-4
1.5
1
0.5
0
-0.5
-1
γ (0 ← 0)
γ (2 ← 2)
γ (5 ← 6)
γ (4 ← 5)
γ (6 ← 7)
γ (1 ← 1)
NO ion intensity/ a.u
4.52
4.522
4.524
4.526
4.528
4.53
4.532
4.534
4.536
4.538
4.54
4.542
wavenumber / cm^-1
x 10^4

APPENDIX B

VIBRATIONAL AND ROTATIONAL LINE POSITIONS OF NO MOLECULE FOR THE γ TRANSITIONS

See Chapter 4 for the spectroscopic constants used in the Pgopher simulations. See also the LIFBase program used to generate the constants below.

QUANTITY: FREQUENCIES
UNITS : Wavenumbers
BAND (A-X)0 - 0

	P1	P2	Q1	Q2	R1	R2	P12	R12	Q12	Q21	P21	R21
0.5			44198.99		44202.97					44202.98		44210.91
1.5	44193.99	44078.07	44197.94	44086.02	44205.90	44097.93	44074.09	44086.01	44078.07	44205.91	44197.94	44217.80
2.5	44189.61	44077.41	44197.52	44089.33	44209.46	44105.22	44069.46	44089.32	44077.41	44209.47	44197.52	44225.33
3.5	44185.85	44077.29	44197.72	44093.18	44213.66	44113.04	44065.37	44093.17	44077.28	44213.67	44197.73	44233.48
4.5	44182.72	44077.70	44198.55	44097.56	44218.47	44121.39	44061.80	44097.55	44077.69	44218.48	44198.57	44242.25
5.5	44180.23	44078.65	44200.02	44102.48	44223.91	44130.28	44058.78	44102.46	44078.63	44223.93	44200.03	44251.66
6.5	44178.36	44080.13	44202.10	44107.93	44229.98	44139.70	44056.28	44107.91	44080.11	44230.00	44202.12	44261.69
7.5	44177.11	44082.14	44204.82	44113.91	44236.67	44149.64	44054.32	44113.89	44082.12	44236.70	44204.84	44272.34
8.5	44176.50	44084.69	44208.15	44120.43	44244.00	44160.13	44052.91	44120.41	44084.66	44244.02	44208.18	44283.62
9.5	44176.50	44087.78	44212.12	44127.48	44251.93	44171.15	44052.02	44127.46	44087.75	44251.96	44212.14	44295.51
10.5	44177.13	44091.40	44216.70	44135.08	44260.49	44182.70	44051.68	44135.05	44091.38	44260.52	44216.73	44308.03
11.5	44178.38	44095.57	44221.91	44143.20	44269.68	44194.79	44051.88	44143.17	44095.54	44269.71	44221.95	44321.17
12.5	44180.26	44100.27	44227.74	44151.88	44279.48	44207.42	44052.62	44151.84	44100.24	44279.52	44227.77	44334.92
13.5	44182.76	44105.52	44234.20	44161.08	44289.90	44220.58	44053.90	44161.04	44105.48	44289.94	44234.23	44349.29
14.5	44185.88	44111.30	44241.26	44170.83	44300.94	44234.29	44055.73	44170.79	44111.27	44300.98	44241.30	44364.28
15.5	44189.61	44117.64	44248.95	44181.13	44312.59	44248.53	44058.10	44181.08	44117.60	44312.63	44248.99	44379.88
16.5	44193.97	44124.51	44257.26	44191.96	44324.86	44263.31	44061.03	44191.91	44124.47	44324.90	44257.30	44396.10
17.5	44198.95	44131.93	44266.18	44203.34	44337.73	44278.63	44064.50	44203.29	44131.89	44337.79	44266.22	44412.92
18.5	44204.54	44139.91	44275.71	44215.26	44351.22	44294.50	44068.52	44215.20	44139.86	44351.28	44275.76	44430.35
19.5	44210.74	44148.42	44285.85	44227.73	44365.32	44310.91	44073.09	44227.68	44148.37	44365.38	44285.91	44448.39
20.5	44217.55	44157.49	44296.61	44240.75	44380.04	44327.86	44078.21	44240.69	44157.44	44380.09	44296.67	44467.04
21.5	44224.99	44167.11	44307.98	44254.31	44395.35	44345.36	44083.89	44254.25	44167.05	44395.41	44308.04	44486.28
22.5	44233.03	44177.29	44319.95	44268.43	44411.27	44363.41	44090.13	44268.36	44177.22	44411.33	44320.02	44506.14
23.5	44241.68	44188.01	44332.54	44283.10	44427.80	44382.00	44096.91	44283.03	44187.95	44427.86	44332.60	44526.59
24.5	44250.94	44199.29	44345.73	44298.31	44444.92	44401.13	44104.26	44298.24	44199.22	44444.99	44345.80	44547.64
25.5	44260.81	44211.13	44359.53	44314.08	44462.66	44420.82	44112.17	44314.01	44211.05	44462.73	44359.60	44569.30
26.5	44271.29	44223.52	44373.93	44330.41	44480.98	44441.06	44120.64	44330.33	44223.45	44481.06	44374.00	44591.55
27.5	44282.38	44236.47	44388.93	44347.29	44499.91	44461.85	44129.67	44347.21	44236.39	44499.99	44389.01	44614.39
28.5	44294.06	44249.98	44404.54	44364.72	44519.44	44483.19	44139.26	44364.64	44249.90	44519.52	44404.62	44637.83
29.5	44306.36	44264.04	44420.75	44382.71	44539.57	44505.08	44149.42	44382.63	44263.96	44539.65	44420.83	44661.87
30.5	44319.25	44278.68	44437.55	44401.26	44560.29	44527.52	44160.14	44401.17	44278.59	44560.37	44437.64	44686.48
31.5	44332.76	44293.87	44454.96	44420.36	44581.60	44550.52	44171.43	44420.27	44293.78	44581.69	44455.05	44711.70
32.5	44346.86	44309.62	44472.96	44440.02	44603.51	44574.07	44183.28	44439.93	44309.53	44603.60	44473.05	44737.51
33.5	44361.56	44325.93	44491.57	44460.25	44626.01	44598.18	44195.70	44460.16	44325.84	44626.10	44491.66	44763.90
34.5	44376.86	44342.82	44510.76	44481.03	44649.10	44622.84	44208.70	44480.94	44342.72	44649.19	44510.86	44790.88
35.5	44392.76	44360.26	44530.55	44502.38	44672.78	44648.05	44222.26	44502.28	44360.16	44672.88	44530.65	44818.44
36.5	44409.27	44378.27	44550.95	44524.27	44697.05	44673.82	44236.39	44524.17	44378.18	44697.15	44551.04	44846.59
37.5	44426.36	44396.84	44571.92	44546.74	44721.91	44700.14	44251.10	44546.64	44396.74	44722.01	44572.02	44875.32
38.5	44444.05	44415.99	44593.49	44569.77	44747.35	44727.03	44266.37	44569.66	44415.89	44747.46	44593.59	44904.63
39.5	44462.35	44435.70	44615.66	44593.36	44773.38	44754.46	44282.22	44593.25	44435.60	44773.49	44615.76	44934.52
40.5	44481.24	44455.98	44638.41	44617.50	44800.00	44782.46	44298.64	44617.39	44455.87	44800.11	44638.52	44965.00
41.5	44500.72	44476.82	44661.75	44642.22	44827.20	44811.01	44315.63	44642.11	44476.71	44827.31	44661.86	44996.05
42.5	44520.80	44498.25	44685.69	44667.50	44854.98	44840.13	44333.20	44667.38	44498.13	44855.10	44685.80	45027.68
43.5	44541.47	44520.23	44710.21	44693.34	44883.35	44869.79	44351.35	44693.23	44520.11	44883.46	44710.33	45059.89
44.5	44562.73	44542.79	44735.32	44719.75	44912.29	44900.02	44370.07	44719.63	44542.67	44912.41	44735.44	45092.67
45.5	44584.60	44565.91	44761.02	44746.72	44941.82	44930.80	44389.37	44746.59	44565.79	44941.95	44761.14	45126.03
46.5	44607.05	44589.60	44787.30	44774.25	44971.93	44962.14	44409.24	44774.13	44589.48	44972.06	44787.43	45159.96
47.5	44630.09	44613.87	44814.18	44802.36	45002.62	44994.04	44429.69	44802.23	44613.75	45002.75	44814.30	45194.47
48.5	44653.73	44638.71	44841.63	44831.02	45033.89	45026.50	44450.73	44830.89	44638.58	45034.02	44841.76	45229.55
49.5	44677.95	44664.12	44869.67	44860.25	45065.73	45059.52	44472.34	44860.12	44663.98	45065.87	44869.80	45265.20
50.5	44702.77	44690.10	44898.30	44890.05	45098.16	45093.09	44494.52	44889.91	44689.97	45098.29	44898.43	45301.41
51.5	44728.17	44716.66	44927.51	44920.41	45131.15	45127.22	44517.29	44920.27	44716.52	45131.29	44927.64	45338.20
52.5	44754.17	44743.78	44957.29	44951.34	45164.72	45161.91	44540.64	44951.19	44743.64	45164.87	44957.43	45375.56
53.5	44780.75	44771.48	44987.67	44982.83	45198.87	45197.16	44564.56	44982.68	44771.34	45199.02	44987.81	45413.49
54.5	44807.92	44799.75	45018.62	45014.89	45233.59	45232.96	44589.07	45014.74	44799.61	45233.74	45018.77	45451.98
55.5	44835.68	44828.60	45050.16	45047.51	45268.89	45269.33	44614.15	45047.36	44828.45	45269.04	45050.31	45491.04
56.5	44864.04	44858.02	45082.28	45080.70	45304.76	45306.25	44639.82	45080.54	44857.87	45304.91	45082.43	45530.66

57.5	44892.97	44888.01	45114.97	45114.45	45341.20	45343.73	44666.07	45114.30	44887.85	45341.36	45115.13	45570.85
58.5	44922.50	44918.57	45148.25	45148.78	45378.21	45381.77	44692.90	45148.62	44918.41	45378.38	45148.41	45611.60
59.5	44952.61	44949.71	45182.11	45183.66	45415.79	45420.36	44720.31	45183.50	44949.55	45415.96	45182.27	45652.92
60.5	44983.30	44981.42	45216.54	45219.12	45453.95	45459.52	44748.31	45218.95	44981.26	45454.11	45216.70	45694.80
61.5	45014.59	45013.71	45251.55	45255.14	45492.68	45499.22	44776.88	45254.97	45013.54	45492.84	45251.72	45737.23
62.5	45046.45	45046.57	45287.14	45291.72	45531.96	45539.48	44806.04	45291.55	45046.40	45532.13	45287.31	45780.23
63.5	45078.91	45080.00	45323.31	45328.87	45571.82	45580.31	44835.78	45328.70	45079.83	45572.00	45323.48	45823.79
64.5	45111.95	45114.00	45360.05	45366.58	45612.25	45621.69	44866.10	45366.41	45113.83	45612.43	45360.23	45867.91
65.5	45145.57	45148.59	45397.37	45404.86	45653.25	45663.62	44897.01	45404.68	45148.41	45653.43	45397.55	45912.58
66.5	45179.77	45183.74	45435.27	45443.71	45694.80	45706.11	44928.50	45443.53	45183.56	45694.98	45435.45	45957.82
67.5	45214.57	45219.46	45473.74	45483.12	45736.93	45749.15	44960.57	45482.94	45219.29	45737.12	45473.92	46003.61
68.5	45249.94	45255.77	45512.78	45523.09	45779.62	45792.75	44993.22	45522.90	45255.59	45779.81	45512.96	46049.95
69.5	45285.90	45292.64	45552.39	45563.63	45822.88	45836.91	45026.46	45563.44	45292.45	45823.07	45552.58	46096.85
70.5	45322.43	45330.09	45592.59	45604.73	45866.70	45881.62	45060.28	45604.54	45329.90	45866.89	45592.78	46144.31
71.5	45359.56	45368.11	45633.35	45646.40	45911.08	45926.88	45094.68	45646.21	45367.92	45911.28	45633.55	46192.31
72.5	45397.26	45406.71	45674.69	45688.63	45956.03	45972.70	45129.67	45688.44	45406.52	45956.22	45674.89	46240.88
73.5	45435.55	45445.88	45716.60	45731.43	46001.53	46019.07	45165.24	45731.23	45445.68	46001.73	45716.80	46289.99
74.5	45474.41	45485.62	45759.08	45774.79	46047.60	46065.99	45201.39	45774.58	45485.42	46047.80	45759.28	46339.65
75.5	45513.86	45525.93	45802.13	45818.70	46094.23	46113.47	45238.13	45818.50	45525.73	46094.43	45802.33	46389.87
76.5	45553.88	45566.82	45845.75	45863.19	46141.41	46161.50	45275.45	45862.98	45566.62	46141.62	45845.95	46440.63
77.5	45594.49	45608.28	45889.94	45908.23	46189.16	46210.08	45313.35	45908.02	45608.07	46189.37	45890.15	46491.95
78.5	45635.68	45650.31	45934.70	45953.84	46237.47	46259.21	45351.84	45953.63	45650.10	46237.68	45934.91	46543.81
79.5	45677.44	45692.92	45980.04	46000.01	46286.33	46308.89	45390.91	45999.80	45692.71	46286.55	45980.25	46596.22

QUANTITY: FREQUENCIES
UNITS : Wavenumbers
BAND (A-X)0 - 1

	P1	P2	Q1	Q2	R1	R2	P12	R12	Q12	Q21	P21	R21
0.5			42322.91		42326.89					42326.90		42334.83
1.5	42317.96	42202.25	42321.91	42210.20	42329.88	42222.11	42198.28	42210.19	42202.25	42329.89	42321.92	42341.78
2.5	42313.67	42201.69	42321.57	42213.61	42333.52	42229.50	42193.74	42213.60	42201.68	42333.53	42321.58	42349.39
3.5	42310.03	42201.69	42321.90	42217.59	42337.84	42237.45	42189.77	42217.57	42201.68	42337.85	42321.91	42357.66
4.5	42307.06	42202.27	42322.89	42222.13	42342.80	42245.96	42186.37	42222.11	42202.26	42342.82	42322.90	42366.59
5.5	42304.75	42203.41	42324.54	42227.24	42348.44	42255.04	42183.54	42227.22	42203.39	42348.45	42324.55	42376.18
6.5	42303.10	42205.12	42326.85	42232.93	42354.73	42264.69	42181.28	42232.91	42205.11	42354.75	42326.86	42386.43
7.5	42302.11	42207.41	42329.82	42239.18	42361.68	42274.91	42179.59	42239.16	42207.39	42361.70	42329.84	42397.34
8.5	42301.79	42210.26	42333.45	42246.00	42369.29	42285.70	42178.48	42245.98	42210.24	42369.31	42333.47	42408.91
9.5	42302.11	42213.70	42337.74	42253.40	42377.55	42297.06	42177.94	42253.38	42213.67	42377.58	42337.76	42421.13
10.5	42303.11	42217.70	42342.68	42261.37	42386.47	42308.99	42177.98	42261.34	42217.67	42386.50	42342.71	42434.01
11.5	42304.76	42222.27	42348.29	42269.91	42396.05	42321.50	42178.59	42269.88	42222.24	42396.08	42348.32	42447.54
12.5	42307.06	42227.43	42354.55	42279.04	42406.29	42334.57	42179.78	42279.00	42227.39	42406.32	42354.58	42461.73
13.5	42310.02	42233.16	42361.46	42288.73	42417.16	42348.22	42181.55	42288.69	42233.13	42417.20	42361.50	42476.56
14.5	42313.64	42239.47	42369.03	42299.00	42428.70	42362.45	42183.90	42298.96	42239.43	42428.74	42369.07	42492.05
15.5	42317.91	42246.36	42377.25	42309.84	42440.89	42377.25	42186.82	42309.80	42246.32	42440.93	42377.29	42508.18
16.5	42322.84	42253.83	42386.12	42321.27	42453.72	42392.63	42190.34	42321.23	42253.79	42453.77	42386.16	42524.96
17.5	42328.41	42261.88	42395.64	42333.28	42467.20	42408.57	42194.44	42333.23	42261.83	42467.25	42395.69	42542.38
18.5	42334.64	42270.52	42405.81	42345.87	42481.33	42425.11	42199.13	42345.81	42270.46	42481.38	42405.86	42560.45
19.5	42341.52	42279.73	42416.63	42359.04	42496.10	42442.21	42204.39	42358.98	42279.68	42496.16	42416.68	42579.17
20.5	42349.04	42289.54	42428.09	42372.79	42511.52	42459.90	42210.25	42372.73	42289.48	42511.58	42428.15	42598.52
21.5	42357.21	42299.93	42440.20	42387.13	42527.57	42478.17	42216.70	42387.06	42299.87	42527.63	42440.27	42618.51
22.5	42366.03	42310.91	42452.95	42402.05	42544.27	42497.02	42223.75	42401.98	42310.84	42544.33	42453.02	42639.14
23.5	42375.49	42322.47	42466.35	42417.56	42561.61	42516.46	42231.38	42417.49	42322.41	42561.68	42466.41	42660.40
24.5	42385.60	42334.63	42480.39	42433.65	42579.58	42536.48	42239.60	42433.58	42334.57	42579.65	42480.46	42682.30
25.5	42396.36	42347.38	42495.07	42450.34	42598.20	42557.08	42248.43	42450.27	42347.31	42598.27	42495.14	42704.84
26.5	42407.75	42360.72	42510.39	42467.61	42617.44	42578.27	42257.84	42467.54	42360.65	42617.52	42510.46	42728.00
27.5	42419.79	42374.65	42526.34	42485.47	42637.32	42600.04	42267.86	42485.39	42374.58	42637.40	42526.41	42751.80
28.5	42432.46	42389.18	42542.93	42503.93	42657.84	42622.40	42278.47	42503.85	42389.11	42657.91	42543.01	42776.23
29.5	42445.77	42404.30	42560.16	42522.97	42678.98	42645.34	42289.68	42522.89	42404.23	42679.07	42560.24	42801.28
30.5	42459.73	42420.03	42578.03	42542.61	42700.76	42668.88	42301.49	42542.52	42419.95	42700.85	42578.11	42826.96
31.5	42474.32	42436.34	42596.53	42562.84	42723.16	42693.00	42313.91	42562.75	42436.26	42723.25	42596.61	42853.27
32.5	42489.55	42453.26	42615.66	42583.67	42746.20	42717.71	42326.93	42583.58	42453.17	42746.29	42615.74	42880.20
33.5	42505.41	42470.77	42635.42	42605.09	42769.86	42743.02	42340.54	42604.99	42470.68	42769.96	42635.51	42907.75
34.5	42521.91	42488.89	42655.81	42627.10	42794.15	42768.91	42354.77	42627.01	42488.79	42794.25	42655.91	42935.93
35.5	42539.05	42507.60	42676.84	42649.71	42819.07	42795.39	42369.60	42649.62	42507.51	42819.16	42676.93	42964.72
36.5	42556.82	42526.92	42698.50	42672.92	42844.60	42822.46	42385.04	42672.82	42526.82	42844.70	42698.59	42994.14
37.5	42575.22	42546.83	42720.77	42696.72	42870.77	42850.13	42401.08	42696.62	42546.73	42870.87	42720.88	43024.18
38.5	42594.25	42567.35	42743.69	42721.13	42897.55	42878.39	42417.72	42721.02	42567.25	42897.66	42743.79	43054.83
39.5	42613.92	42588.47	42767.23	42746.13	42924.95	42907.23	42434.98	42746.02	42588.37	42925.06	42767.33	43086.09
40.5	42634.22	42610.20	42791.39	42771.72	42952.98	42936.68	42452.86	42771.61	42610.09	42953.09	42791.50	43117.98
41.5	42655.15	42632.52	42816.18	42797.92	42981.63	42966.71	42471.33	42797.81	42632.41	42981.74	42816.29	43150.48
42.5	42676.71	42655.46	42841.60	42824.71	43010.89	42997.34	42490.42	42824.60	42655.35	43011.00	42841.71	43183.59
43.5	42698.90	42679.00	42867.63	42852.11	43040.77	43028.56	42510.12	42851.99	42678.88	43040.89	42867.75	43217.31
44.5	42721.71	42703.14	42894.30	42880.10	43071.27	43060.37	42530.42	42879.98	42703.02	43071.39	42894.41	43251.64
45.5	42745.16	42727.89	42921.58	42908.70	43102.38	43092.78	42551.35	42908.57	42727.77	43102.51	42921.70	43286.59
46.5	42769.23	42753.25	42949.48	42937.89	43134.12	43125.79	42572.88	42937.77	42753.12	43134.24	42949.61	43322.15
47.5	42793.93	42779.21	42978.02	42967.69	43166.47	43159.38	42595.03	42967.56	42779.08	43166.59	42978.14	43358.31
48.5	42819.27	42805.78	43007.17	42998.09	43199.43	43193.57	42617.79	42997.95	42805.65	43199.56	43007.30	43395.09
49.5	42845.22	42832.95	43036.94	43029.08	43233.00	43228.35	42641.17	43028.95	42832.82	43233.13	43037.07	43432.46
50.5	42871.80	42860.74	43067.33	43060.68	43267.19	43263.72	42665.16	43060.55	42860.61	43267.32	43067.46	43470.45
51.5	42899.01	42889.13	43098.34	43092.88	43301.98	43299.70	42689.77	43092.74	42889.00	43302.13	43098.48	43509.04
52.5	42926.84	42918.13	43129.96	43125.68	43337.39	43336.26	42714.98	43125.54	42917.99	43337.54	43130.11	43548.23
53.5	42955.29	42947.74	43162.21	43159.09	43373.41	43373.42	42740.82	43158.94	42947.60	43373.56	43162.36	43588.03
54.5	42984.38	42977.96	43195.07	43193.09	43410.05	43411.17	42767.27	43192.94	42977.81	43410.20	43195.22	43628.43
55.5	43014.08	43008.79	43228.55	43227.70	43447.29	43449.52	42794.34	43227.55	43008.64	43447.44	43228.70	43669.43
56.5	43044.41	43040.23	43262.65	43262.91	43485.14	43488.45	42822.03	43262.75	43040.07	43485.29	43262.80	43711.04

57.5	43075.37	43072.27	43297.37	43298.71	43523.59	43527.99	42850.33	43298.55	43072.11	43523.75	43297.52	43753.24
58.5	43106.94	43104.92	43332.70	43335.13	43562.66	43568.12	42879.25	43334.96	43104.77	43562.82	43332.85	43796.05
59.5	43139.14	43138.19	43368.64	43372.14	43602.33	43608.84	42908.79	43371.97	43138.03	43602.49	43368.80	43839.45
60.5	43171.96	43172.06	43405.20	43409.75	43642.61	43650.15	42938.94	43409.59	43171.89	43642.77	43405.36	43883.45
61.5	43205.40	43206.54	43442.37	43447.97	43683.49	43692.05	42969.71	43447.80	43206.38	43683.66	43442.53	43928.05
62.5	43239.47	43241.64	43480.16	43486.79	43724.98	43734.55	43001.11	43486.61	43241.47	43725.15	43480.32	43973.24
63.5	43274.16	43277.34	43518.55	43526.20	43767.07	43777.64	43033.12	43526.03	43277.16	43767.24	43518.72	44019.03
64.5	43309.46	43313.65	43557.56	43566.22	43809.77	43821.33	43065.74	43566.05	43313.48	43809.94	43557.73	44065.42
65.5	43345.39	43350.57	43597.19	43606.85	43853.06	43865.61	43098.99	43606.67	43350.39	43853.24	43597.36	44112.40
66.5	43381.93	43388.10	43637.42	43648.07	43896.96	43910.48	43132.86	43647.89	43387.92	43897.14	43637.60	44159.97
67.5	43419.10	43426.24	43678.27	43689.89	43941.47	43955.93	43167.34	43689.71	43426.06	43941.65	43678.45	44208.14
68.5	43456.89	43465.00	43719.73	43732.32	43986.57	44001.98	43202.45	43732.13	43464.81	43986.75	43719.91	44256.89
69.5	43495.29	43504.36	43761.79	43775.34	44032.27	44048.63	43238.17	43775.15	43504.17	44032.46	43761.98	44306.25
70.5	43534.31	43544.33	43804.47	43818.97	44078.58	44095.86	43274.51	43818.78	43544.14	44078.77	43804.66	44356.19
71.5	43573.96	43584.91	43847.75	43863.20	44125.48	44143.68	43311.48	43863.00	43584.72	44125.68	43847.95	44406.71
72.5	43614.22	43626.10	43891.65	43908.02	44172.99	44192.09	43349.06	43907.83	43625.91	44173.18	43891.84	44457.84
73.5	43655.10	43667.90	43936.16	43953.45	44221.09	44241.10	43387.27	43953.25	43667.71	44221.29	43936.35	44509.55
74.5	43696.60	43710.32	43981.27	43999.48	44269.79	44290.69	43426.09	43999.27	43710.12	44269.99	43981.46	44561.84
75.5	43738.71	43753.34	44026.98	44046.10	44319.08	44340.87	43465.53	44045.90	43753.13	44319.29	44027.19	44614.72
76.5	43781.45	43796.96	44073.30	44093.33	44368.98	44391.64	43505.59	44093.12	43796.76	44369.18	44073.51	44668.19
77.5	43824.79	43841.20	44120.24	44141.15	44419.46	44443.00	43546.27	44140.94	43840.99	44419.67	44120.45	44722.24
78.5	43868.75	43886.05	44167.78	44189.58	44470.55	44494.95	43587.57	44189.37	43885.84	44470.76	44167.99	44776.88
79.5	43913.33	43931.51	44215.92	44238.60	44522.22	44547.48	43629.49	44238.38	43931.30	44522.44	44216.13	44832.11

QUANTITY: FREQUENCIES
UNITS : Wavenumbers
BAND (A-X)1 - 1

	P1	P2	Q1	Q2	R1	R2	P12	R12	Q12	Q21	P21	R21
0.5			44664.84		44668.79					44668.79		44676.65
1.5	44659.90	44544.15	44663.81	44552.02	44671.70	44563.82	44540.21	44552.01	44544.14	44671.71	44663.81	44683.49
2.5	44655.56	44543.51	44663.39	44555.32	44675.23	44571.06	44535.64	44555.31	44543.50	44675.24	44663.40	44690.95
3.5	44651.85	44543.40	44663.61	44559.14	44679.39	44578.81	44531.59	44559.13	44543.39	44679.41	44663.62	44699.03
4.5	44648.77	44543.83	44664.45	44563.50	44684.17	44587.10	44528.08	44563.48	44543.82	44684.19	44664.46	44707.73
5.5	44646.31	44544.78	44665.90	44568.38	44689.58	44595.92	44525.10	44568.37	44544.76	44689.60	44665.92	44717.06
6.5	44644.47	44546.27	44667.99	44573.80	44695.61	44605.27	44522.64	44573.79	44546.25	44695.63	44668.01	44727.02
7.5	44643.26	44548.29	44670.70	44579.76	44702.26	44615.15	44520.74	44579.74	44548.27	44702.28	44670.72	44737.58
8.5	44642.67	44550.84	44674.03	44586.24	44709.53	44625.57	44519.36	44586.22	44550.82	44709.55	44674.05	44748.78
9.5	44642.70	44553.93	44677.98	44593.27	44717.42	44636.52	44518.52	44593.24	44553.91	44717.45	44678.00	44760.58
10.5	44643.35	44557.56	44682.55	44600.82	44725.92	44647.99	44518.21	44600.79	44557.54	44725.95	44682.58	44773.01
11.5	44644.63	44561.72	44687.73	44608.91	44735.05	44660.01	44518.45	44608.88	44561.69	44735.08	44687.77	44786.05
12.5	44646.51	44566.43	44693.55	44617.54	44744.79	44672.56	44519.23	44617.51	44566.39	44744.83	44693.58	44799.71
13.5	44649.02	44571.67	44699.97	44626.71	44755.15	44685.64	44520.55	44626.67	44571.63	44755.19	44700.01	44813.98
14.5	44652.15	44577.45	44707.01	44636.41	44766.12	44699.27	44522.41	44636.38	44577.41	44766.16	44707.05	44828.86
15.5	44655.89	44583.77	44714.67	44646.66	44777.70	44713.42	44524.81	44646.62	44583.73	44777.75	44714.71	44844.36
16.5	44660.26	44590.64	44722.94	44657.45	44789.90	44728.12	44527.76	44657.40	44590.60	44789.95	44722.98	44860.46
17.5	44665.23	44598.05	44731.82	44668.78	44802.70	44743.36	44531.26	44668.73	44598.01	44802.75	44731.86	44877.16
18.5	44670.82	44606.01	44741.31	44680.65	44816.11	44759.13	44535.30	44680.59	44605.96	44816.16	44741.36	44894.48
19.5	44677.01	44614.51	44751.41	44693.06	44830.13	44775.45	44539.89	44693.01	44614.46	44830.18	44751.46	44912.41
20.5	44683.82	44623.56	44762.12	44706.03	44844.76	44792.31	44545.03	44705.97	44623.51	44844.81	44762.18	44930.93
21.5	44691.24	44633.16	44773.45	44719.54	44859.98	44809.71	44550.73	44719.47	44633.11	44860.04	44773.50	44950.05
22.5	44699.27	44643.31	44785.37	44733.59	44875.81	44827.66	44556.98	44733.53	44643.25	44875.88	44785.43	44969.77
23.5	44707.90	44654.01	44797.89	44748.20	44892.25	44846.15	44563.79	44748.13	44653.95	44892.31	44797.96	44990.10
24.5	44717.14	44665.27	44811.03	44763.35	44909.28	44865.19	44571.14	44763.28	44665.20	44909.35	44811.09	45011.02
25.5	44726.99	44677.07	44824.76	44779.05	44926.91	44884.78	44579.06	44778.98	44677.00	44926.98	44824.83	45032.54
26.5	44737.44	44689.43	44839.10	44795.31	44945.14	44904.91	44587.54	44795.23	44689.36	44945.21	44839.17	45054.64
27.5	44748.50	44702.35	44854.04	44812.11	44963.96	44925.59	44596.57	44812.04	44702.28	44964.04	44854.12	45077.35
28.5	44760.16	44715.82	44869.57	44829.48	44983.39	44946.82	44606.17	44829.40	44715.75	44983.46	44869.65	45100.64
29.5	44772.41	44729.86	44885.71	44847.39	45003.40	44968.59	44616.32	44847.31	44729.78	45003.48	44885.79	45124.53
30.5	44785.28	44744.45	44902.45	44865.86	45024.01	44990.92	44627.04	44865.77	44744.36	45024.10	44902.53	45149.00
31.5	44798.74	44759.59	44919.78	44884.88	45045.21	45013.80	44638.33	44884.80	44759.51	45045.29	44919.86	45174.07
32.5	44812.80	44775.30	44937.70	44904.46	45067.00	45037.23	44650.18	44904.38	44775.21	45067.09	44937.79	45199.71
33.5	44827.46	44791.57	44956.22	44924.60	45089.38	45061.21	44662.59	44924.51	44791.48	45089.47	44956.31	45225.95
34.5	44842.71	44808.40	44975.33	44945.29	45112.34	45085.74	44675.57	44945.20	44808.31	45112.44	44975.42	45252.76
35.5	44858.56	44825.79	44995.03	44966.55	45135.90	45110.83	44689.11	44966.45	44825.70	45136.00	44995.13	45280.16
36.5	44875.01	44843.75	45015.33	44988.36	45160.04	45136.46	44703.23	44988.25	44843.65	45160.14	45015.43	45308.14
37.5	44892.05	44862.27	45036.21	45010.72	45184.77	45162.66	44717.91	45010.62	44862.16	45184.87	45036.31	45336.70
38.5	44909.69	44881.35	45057.69	45033.65	45210.08	45189.41	44733.16	45033.55	44881.25	45210.18	45057.79	45365.85
39.5	44927.92	44901.00	45079.75	45057.14	45235.97	45216.70	44748.98	45057.03	44900.89	45236.08	45079.86	45395.56
40.5	44946.75	44921.21	45102.41	45081.19	45262.45	45244.56	44765.38	45081.08	44921.11	45262.56	45102.52	45425.86
41.5	44966.16	44941.99	45125.65	45105.80	45289.51	45272.96	44782.35	45105.69	44941.88	45289.62	45125.76	45456.73
42.5	44986.18	44963.34	45149.48	45130.97	45317.14	45301.93	44799.89	45130.85	44963.23	45317.26	45149.59	45488.18
43.5	45006.78	44985.25	45173.89	45156.70	45345.36	45331.45	44818.00	45156.58	44985.13	45345.48	45174.00	45520.20
44.5	45027.96	45007.73	45198.89	45182.99	45374.16	45361.52	44836.68	45182.88	45007.61	45374.28	45199.00	45552.79
45.5	45049.75	45030.78	45224.47	45209.85	45403.53	45392.15	44855.94	45209.72	45030.66	45403.66	45224.59	45585.96
46.5	45072.13	45054.39	45250.63	45237.26	45433.48	45423.34	44875.77	45237.14	45054.27	45433.61	45250.76	45619.70
47.5	45095.08	45078.57	45277.39	45265.24	45464.02	45455.07	44896.18	45265.11	45078.45	45464.15	45277.51	45654.01
48.5	45118.63	45103.33	45304.72	45293.79	45495.13	45487.37	44917.16	45293.65	45103.20	45495.26	45304.85	45688.88
49.5	45142.77	45128.66	45332.64	45322.88	45526.80	45520.22	44938.72	45322.75	45128.52	45526.93	45332.77	45724.34
50.5	45167.50	45154.54	45361.13	45352.55	45559.06	45553.63	44960.86	45352.42	45154.41	45559.20	45361.26	45760.35
51.5	45192.81	45181.00	45390.21	45382.79	45591.89	45587.59	44983.57	45382.64	45180.87	45592.03	45390.35	45796.93
52.5	45218.71	45208.04	45419.87	45413.58	45625.29	45622.11	45006.86	45413.43	45207.89	45625.43	45420.01	45834.08
53.5	45245.20	45235.64	45450.11	45444.93	45659.26	45657.18	45030.72	45444.78	45235.49	45659.41	45450.25	45871.79
54.5	45272.27	45263.80	45480.92	45476.85	45693.81	45692.80	45055.16	45476.70	45263.66	45693.96	45481.07	45910.07
55.5	45299.93	45292.55	45512.31	45509.33	45728.92	45728.99	45080.18	45509.18	45292.40	45729.07	45512.46	45948.90
56.5	45328.17	45321.86	45544.29	45542.38	45764.61	45765.73	45105.79	45542.22	45321.70	45764.76	45544.44	45988.30

57.5	45357.00	45351.74	45576.84	45575.98	45800.86	45803.02	45131.96	45575.82	45351.58	45801.02	45576.99	46028.27
58.5	45386.41	45382.19	45609.96	45610.15	45837.69	45840.87	45158.71	45609.99	45382.04	45837.85	45610.12	46068.80
59.5	45416.41	45413.21	45643.67	45644.89	45875.08	45879.27	45186.05	45644.72	45413.05	45875.24	45643.83	46109.88
60.5	45446.99	45444.81	45677.95	45680.18	45913.04	45918.23	45213.97	45680.02	45444.64	45913.20	45678.11	46151.53
61.5	45478.15	45476.97	45712.80	45716.04	45951.57	45957.73	45242.46	45715.88	45476.80	45951.73	45712.96	46193.73
62.5	45509.90	45509.71	45748.23	45752.46	45990.66	45997.80	45271.54	45752.29	45509.54	45990.83	45748.40	46236.48
63.5	45542.23	45543.02	45784.23	45789.45	46030.31	46038.42	45301.19	45789.27	45542.84	46030.48	45784.40	46279.80
64.5	45575.14	45576.89	45820.80	45827.00	46070.54	46079.59	45331.42	45826.82	45576.72	46070.71	45820.98	46323.68
65.5	45608.63	45611.34	45857.96	45865.11	46111.32	46121.31	45362.23	45864.93	45611.17	46111.50	45858.14	46368.11
66.5	45642.71	45646.36	45895.68	45903.77	46152.67	46163.59	45393.63	45903.59	45646.18	46152.85	45895.86	46413.09
67.5	45677.36	45681.95	45933.98	45943.01	46194.59	46206.42	45425.60	45942.83	45681.77	46194.77	45934.16	46458.63
68.5	45712.59	45718.11	45972.84	45982.80	46237.05	46249.80	45458.16	45982.62	45717.93	46237.24	45973.03	46504.71
69.5	45748.41	45754.84	46012.28	46023.16	46280.09	46293.74	45491.29	46022.97	45754.66	46280.28	46012.46	46551.36
70.5	45784.80	45792.15	46052.29	46064.08	46323.70	46338.22	45525.00	46063.89	45791.96	46323.88	46052.48	46598.55
71.5	45821.78	45830.02	46092.87	46105.56	46367.85	46383.26	45559.30	46105.36	45829.83	46368.04	46093.06	46646.29
72.5	45859.34	45868.46	46134.01	46147.60	46412.57	46428.85	45594.18	46147.41	45868.27	46412.76	46134.21	46694.59
73.5	45897.46	45907.48	46175.73	46190.20	46457.84	46474.98	45629.63	46190.01	45907.29	46458.04	46175.93	46743.43
74.5	45936.18	45947.07	46218.02	46233.36	46503.67	46521.68	45665.66	46233.16	45946.87	46503.88	46218.22	46792.82
75.5	45975.47	45987.22	46260.87	46277.09	46550.07	46568.91	45702.28	46276.88	45987.02	46550.27	46261.07	46842.77
76.5	46015.33	46027.95	46304.30	46321.37	46597.02	46616.70	45739.48	46321.16	46027.75	46597.23	46304.50	46893.25
77.5	46055.78	46069.24	46348.28	46366.21	46644.52	46665.03	45777.26	46366.00	46069.04	46644.73	46348.49	46944.28
78.5	46096.80	46111.11	46392.84	46411.61	46692.58	46713.92	45815.62	46411.40	46110.90	46692.79	46393.05	46995.86
79.5	46138.39	46153.54	46437.96	46457.57	46741.20	46763.36	45854.55	46457.36	46153.33	46741.41	46438.17	47047.98

QUANTITY: FREQUENCIES
UNITS : Wavenumbers
BAND (A-X)0 - 2

	P1	P2	Q1	Q2	R1	R2	P12	R12	Q12	Q21	P21	R21
0.5			40474.92		40478.91					40478.91		40486.84
1.5	40470.03	40354.54	40473.98	40362.48	40481.94	40374.40	40350.56	40362.48	40354.54	40481.95	40473.98	40493.84
2.5	40465.82	40354.06	40473.72	40365.98	40485.67	40381.87	40346.11	40365.97	40354.05	40485.68	40473.73	40501.54
3.5	40462.30	40354.19	40474.17	40370.09	40490.11	40389.95	40342.27	40370.07	40354.18	40490.12	40474.18	40509.93
4.5	40459.48	40354.93	40475.31	40374.79	40495.23	40398.62	40339.03	40374.78	40354.92	40495.24	40475.32	40519.01
5.5	40457.36	40356.27	40477.15	40380.10	40501.05	40407.91	40336.40	40380.09	40356.26	40501.06	40477.16	40528.80
6.5	40455.93	40358.22	40479.68	40386.02	40507.56	40417.79	40334.38	40386.00	40358.20	40507.58	40479.70	40539.27
7.5	40455.20	40360.78	40482.91	40392.54	40514.77	40428.28	40332.96	40392.52	40360.76	40514.79	40482.93	40550.43
8.5	40455.17	40363.94	40486.83	40399.68	40522.67	40439.38	40332.16	40399.66	40363.91	40522.70	40486.85	40562.29
9.5	40455.82	40367.71	40491.45	40407.42	40531.26	40451.08	40331.95	40407.39	40367.69	40531.29	40491.47	40574.84
10.5	40457.18	40372.09	40496.75	40415.77	40540.54	40463.39	40332.37	40415.73	40372.06	40540.57	40496.78	40588.08
11.5	40459.22	40377.08	40502.75	40424.72	40550.52	40476.31	40333.40	40424.69	40377.05	40550.55	40502.79	40602.01
12.5	40461.96	40382.68	40509.44	40434.29	40561.18	40489.83	40335.04	40434.26	40382.65	40561.21	40509.47	40616.62
13.5	40465.39	40388.91	40516.82	40444.47	40572.53	40503.97	40337.29	40444.43	40388.87	40572.57	40516.86	40631.92
14.5	40469.50	40395.73	40524.89	40455.26	40584.56	40518.71	40340.16	40455.22	40395.70	40584.60	40524.93	40647.91
15.5	40474.30	40403.18	40533.64	40466.67	40597.28	40534.07	40343.65	40466.63	40403.14	40597.32	40533.68	40664.57
16.5	40479.80	40411.25	40543.09	40478.69	40610.68	40550.04	40347.76	40478.64	40411.20	40610.73	40543.13	40681.93
17.5	40485.98	40419.93	40553.21	40491.33	40624.77	40566.62	40352.49	40491.28	40419.88	40624.82	40553.25	40699.95
18.5	40492.84	40429.23	40564.02	40504.58	40639.53	40583.82	40357.84	40504.52	40429.18	40639.59	40564.07	40718.66
19.5	40500.39	40439.14	40575.50	40518.45	40654.98	40601.63	40363.81	40518.39	40439.09	40655.04	40575.56	40738.04
20.5	40508.62	40449.69	40587.68	40532.94	40671.10	40620.05	40370.40	40532.88	40449.63	40671.16	40587.73	40758.10
21.5	40517.54	40460.85	40600.53	40548.05	40687.90	40639.09	40377.63	40547.98	40460.79	40687.96	40600.59	40778.84
22.5	40527.14	40472.64	40614.06	40563.78	40705.38	40658.76	40385.48	40563.71	40472.57	40705.44	40614.13	40800.25
23.5	40537.41	40485.05	40628.27	40580.13	40723.53	40679.03	40393.95	40580.07	40484.98	40723.59	40628.33	40822.32
24.5	40548.37	40498.09	40643.16	40597.11	40742.35	40699.93	40403.05	40597.04	40498.02	40742.42	40643.23	40845.07
25.5	40560.01	40511.75	40658.72	40614.70	40761.84	40721.45	40412.79	40614.63	40511.68	40761.91	40658.79	40868.49
26.5	40572.32	40526.04	40674.95	40632.93	40782.01	40743.59	40423.16	40632.86	40525.97	40782.09	40675.02	40892.57
27.5	40585.30	40540.96	40691.86	40651.78	40802.84	40766.34	40434.16	40651.70	40540.89	40802.92	40691.94	40917.32
28.5	40598.97	40556.51	40709.45	40671.25	40824.35	40789.73	40445.80	40671.18	40556.43	40824.43	40709.52	40942.74
29.5	40613.31	40572.69	40727.70	40691.36	40846.52	40813.73	40458.07	40691.28	40572.61	40846.60	40727.78	40968.82
30.5	40628.32	40589.51	40746.62	40712.09	40869.35	40838.36	40470.97	40712.00	40589.43	40869.44	40746.70	40995.55
31.5	40644.01	40606.95	40766.21	40733.45	40892.85	40863.61	40484.52	40733.36	40606.87	40892.94	40766.30	41022.95
32.5	40660.37	40625.03	40786.47	40755.44	40917.02	40889.48	40498.70	40755.35	40624.94	40917.11	40786.56	41051.02
33.5	40677.39	40643.74	40807.40	40778.05	40941.84	40915.98	40513.51	40777.96	40643.65	40941.94	40807.49	41079.73
34.5	40695.09	40663.09	40828.99	40801.30	40967.33	40943.12	40528.97	40801.21	40663.00	40967.43	40829.09	41109.11
35.5	40713.46	40683.08	40851.25	40825.19	40993.48	40970.87	40545.07	40825.09	40682.98	40993.58	40851.35	41139.14
36.5	40732.50	40703.70	40874.18	40849.70	41020.29	40999.25	40561.82	40849.60	40703.60	41020.39	40874.28	41169.83
37.5	40752.21	40724.95	40897.77	40874.85	41047.76	41028.25	40579.20	40874.75	40724.85	41047.86	40897.87	41201.17
38.5	40772.59	40746.85	40922.02	40900.63	41075.88	41057.89	40597.23	40900.52	40746.75	41075.99	40922.13	41233.16
39.5	40793.63	40769.39	40946.94	40927.04	41104.66	41088.15	40615.90	40926.93	40769.28	41104.77	40947.04	41265.80
40.5	40815.34	40792.56	40972.51	40954.09	41134.10	41119.04	40635.22	40953.98	40792.45	41134.21	40972.62	41299.11
41.5	40837.72	40816.37	40998.75	40981.77	41164.20	41150.56	40655.18	40981.66	40816.26	41164.31	40998.86	41333.05
42.5	40860.76	40840.83	41025.65	41010.08	41194.94	41182.71	40675.79	41009.96	40840.71	41195.06	41025.77	41367.64
43.5	40884.47	40865.92	41053.21	41039.04	41226.35	41215.48	40697.04	41038.92	40865.80	41226.46	41053.32	41402.89
44.5	40908.84	40891.66	41081.43	41068.62	41258.40	41248.89	40718.94	41068.50	40891.54	41258.52	41081.54	41438.77
45.5	40933.88	40918.03	41110.30	41098.84	41291.10	41282.92	40741.49	41098.71	40917.91	41291.23	41110.42	41475.31
46.5	40959.58	40945.05	41139.83	41129.70	41324.46	41317.59	40764.69	41129.57	40944.93	41324.59	41139.96	41512.50
47.5	40985.94	40972.71	41170.02	41161.20	41358.47	41352.88	40788.53	41161.07	40972.59	41358.60	41170.15	41550.32
48.5	41012.97	41001.02	41200.88	41193.32	41393.13	41388.80	40813.03	41193.19	41000.89	41393.26	41201.00	41588.79
49.5	41040.66	41029.96	41232.38	41226.09	41428.44	41425.36	40838.18	41225.96	41029.83	41428.57	41232.51	41627.90
50.5	41069.00	41059.55	41264.54	41259.50	41464.39	41462.54	40863.97	41259.36	41059.42	41464.53	41264.67	41667.65
51.5	41098.02	41089.79	41297.35	41293.54	41501.00	41500.36	40890.42	41293.40	41089.66	41501.14	41297.48	41708.05
52.5	41127.69	41120.67	41330.81	41328.22	41538.25	41538.80	40917.52	41328.07	41120.53	41538.39	41330.95	41749.09
53.5	41158.02	41152.19	41364.94	41363.54	41576.14	41577.87	40945.27	41363.39	41152.05	41576.29	41365.08	41790.76
54.5	41189.02	41184.36	41399.71	41399.49	41614.69	41617.57	40973.67	41399.34	41184.21	41614.84	41399.86	41833.07
55.5	41220.67	41217.17	41435.14	41436.08	41653.88	41657.90	41002.72	41435.93	41217.02	41654.03	41435.29	41876.02
56.5	41252.98	41250.63	41471.23	41473.31	41693.71	41698.86	41032.43	41473.15	41250.48	41693.87	41471.38	41919.61

57.5	41285.96	41284.73	41507.96	41511.17	41734.19	41740.45	41062.79	41511.02	41284.58	41734.34	41508.11	41963.84
58.5	41319.59	41319.48	41545.34	41549.68	41775.31	41782.67	41093.80	41549.52	41319.32	41775.47	41545.50	42008.69
59.5	41353.88	41354.88	41583.38	41588.82	41817.07	41825.52	41125.47	41588.66	41354.71	41817.23	41583.54	42054.19
60.5	41388.83	41390.91	41622.06	41628.60	41859.48	41869.00	41157.79	41628.44	41390.75	41859.64	41622.22	42100.32
61.5	41424.43	41427.59	41661.40	41669.02	41902.52	41913.11	41190.77	41668.85	41427.43	41902.69	41661.56	42147.08
62.5	41460.70	41464.93	41701.39	41710.07	41946.21	41957.84	41224.39	41709.90	41464.76	41946.38	41701.55	42194.47
63.5	41497.63	41502.90	41742.02	41751.77	41990.54	42003.21	41258.68	41751.59	41502.73	41990.71	41742.19	42242.50
64.5	41535.20	41541.52	41783.30	41794.10	42035.50	42049.21	41293.62	41793.92	41541.35	42035.68	41783.48	42291.16
65.5	41573.44	41580.79	41825.23	41837.07	42081.11	42095.83	41329.21	41836.89	41580.62	42081.29	41825.41	42340.45
66.5	41612.33	41620.71	41867.82	41880.67	42127.36	42143.08	41365.46	41880.49	41620.53	42127.54	41868.00	42390.37
67.5	41651.88	41661.27	41911.04	41924.92	42174.24	42190.96	41402.37	41924.73	41661.09	42174.43	41911.22	42440.91
68.5	41692.08	41702.48	41954.92	41969.79	42221.76	42239.46	41439.93	41969.61	41702.29	42221.95	41955.10	42492.09
69.5	41732.94	41744.33	41999.43	42015.31	42269.92	42288.60	41478.14	42015.13	41744.14	42270.11	41999.62	42543.89
70.5	41774.45	41786.83	42044.61	42061.47	42318.72	42338.36	41517.01	42061.27	41786.64	42318.91	42044.79	42596.32
71.5	41816.63	41829.98	42090.42	42108.26	42368.15	42388.75	41556.54	42108.06	41829.79	42368.34	42090.61	42649.38
72.5	41859.45	41873.77	42136.88	42155.69	42418.22	42439.76	41596.73	42155.49	41873.57	42418.41	42137.07	42703.06
73.5	41902.93	41918.21	42183.98	42203.75	42468.92	42491.40	41637.57	42203.55	41918.01	42469.12	42184.18	42757.37
74.5	41947.06	41963.29	42231.73	42252.45	42520.25	42543.66	41679.06	42252.25	41963.09	42520.45	42231.93	42812.30
75.5	41991.85	42009.02	42280.12	42301.79	42572.22	42596.56	41721.22	42301.59	42008.82	42572.42	42280.32	42867.86
76.5	42037.29	42055.40	42329.15	42351.77	42624.82	42650.08	41764.02	42351.55	42055.20	42625.03	42329.36	42924.04
77.5	42083.38	42102.42	42378.83	42402.37	42678.05	42704.22	41807.49	42402.16	42102.22	42678.27	42379.04	42980.84
78.5	42130.13	42150.09	42429.15	42453.62	42731.93	42758.99	41851.61	42453.41	42149.88	42732.14	42429.36	43038.26
79.5	42177.53	42198.41	42480.12	42505.50	42786.42	42814.38	41896.39	42505.28	42198.20	42786.64	42480.33	43096.30

QUANTITY: FREQUENCIES
UNITS : Wavenumbers
BAND (A-X)2 - 2

	P1	P2	Q1	Q2	R1	R2	P12	R12	Q12	Q21	P21	R21
0.5			45126.13		45130.04					45130.05		45137.83
1.5	45121.24	45005.68	45125.11	45013.47	45132.93	45025.16	45001.77	45013.46	45005.67	45132.93	45125.12	45144.60
2.5	45116.95	45005.05	45124.71	45016.74	45136.43	45032.33	44997.25	45016.73	45005.04	45136.44	45124.71	45152.00
3.5	45113.29	45004.95	45124.93	45020.54	45140.56	45040.02	44993.25	45020.53	45004.95	45140.57	45124.94	45160.01
4.5	45110.24	45005.39	45125.77	45024.87	45145.30	45048.25	44989.79	45024.86	45005.38	45145.32	45125.78	45168.64
5.5	45107.82	45006.35	45127.23	45029.73	45150.68	45057.00	44986.86	45029.71	45006.34	45150.69	45127.24	45177.89
6.5	45106.01	45007.85	45129.31	45035.12	45156.66	45066.29	44984.45	45035.10	45007.83	45156.68	45129.32	45187.76
7.5	45104.83	45009.88	45132.01	45041.04	45163.26	45076.10	44982.59	45041.02	45009.86	45163.29	45132.03	45198.25
8.5	45104.27	45012.43	45135.32	45047.49	45170.49	45086.44	44981.25	45047.47	45012.41	45170.51	45135.35	45209.36
9.5	45104.32	45015.53	45139.27	45054.48	45178.32	45097.31	44980.45	45054.45	45015.50	45178.35	45139.29	45221.07
10.5	45105.00	45019.15	45143.82	45062.00	45186.77	45108.71	44980.19	45061.96	45019.13	45186.80	45143.84	45233.41
11.5	45106.29	45023.31	45148.98	45070.05	45195.84	45120.65	44980.46	45070.02	45023.28	45195.88	45149.02	45246.36
12.5	45108.19	45028.01	45154.77	45078.64	45205.52	45133.12	44981.27	45078.60	45027.98	45205.56	45154.80	45259.91
13.5	45110.71	45033.25	45161.17	45087.76	45215.82	45146.13	44982.62	45087.72	45033.21	45215.86	45161.20	45274.08
14.5	45113.85	45039.02	45168.18	45097.42	45226.72	45159.66	44984.51	45097.38	45038.98	45226.76	45168.21	45288.86
15.5	45117.59	45045.34	45175.80	45107.62	45238.23	45173.74	44986.94	45107.58	45045.30	45238.27	45175.84	45304.24
16.5	45121.96	45052.20	45184.04	45118.36	45250.35	45188.35	44989.92	45118.31	45052.15	45250.39	45184.08	45320.23
17.5	45126.93	45059.59	45192.87	45129.63	45263.07	45203.49	44993.44	45129.58	45059.54	45263.13	45192.92	45336.82
18.5	45132.51	45067.53	45202.32	45141.45	45276.40	45219.18	44997.50	45141.39	45067.48	45276.46	45202.38	45354.02
19.5	45138.70	45076.02	45212.38	45153.81	45290.34	45235.41	45002.11	45153.75	45075.96	45290.39	45212.43	45371.82
20.5	45145.49	45085.05	45223.04	45166.72	45304.88	45252.17	45007.27	45166.66	45084.99	45304.94	45223.09	45390.21
21.5	45152.90	45094.63	45234.31	45180.16	45320.02	45269.47	45012.98	45180.10	45094.57	45320.08	45234.37	45409.21
22.5	45160.91	45104.75	45246.18	45194.16	45335.75	45287.32	45019.25	45194.09	45104.69	45335.82	45246.24	45428.81
23.5	45169.52	45115.42	45258.65	45208.70	45352.09	45305.71	45026.06	45208.63	45115.36	45352.16	45258.71	45449.00
24.5	45178.75	45126.65	45271.72	45223.78	45369.02	45324.64	45033.43	45223.71	45126.58	45369.09	45271.79	45469.78
25.5	45188.57	45138.42	45285.39	45239.41	45386.55	45344.12	45041.36	45239.34	45138.35	45386.63	45285.46	45491.16
26.5	45198.99	45150.75	45299.66	45255.60	45404.68	45364.14	45049.84	45255.53	45150.68	45404.76	45299.73	45513.12
27.5	45210.02	45163.63	45314.54	45272.33	45423.39	45384.70	45058.87	45272.25	45163.56	45423.47	45314.61	45535.68
28.5	45221.64	45177.06	45330.00	45289.61	45442.71	45405.82	45068.47	45289.54	45176.98	45442.79	45330.07	45558.83
29.5	45233.86	45191.05	45346.06	45307.45	45462.61	45427.48	45078.62	45307.37	45190.97	45462.70	45346.14	45582.56
30.5	45246.68	45205.60	45362.71	45325.84	45483.10	45449.68	45089.33	45325.75	45205.52	45483.18	45362.80	45606.88
31.5	45260.10	45220.70	45379.96	45344.77	45504.18	45472.44	45100.61	45344.69	45220.61	45504.27	45380.04	45631.79
32.5	45274.11	45236.36	45397.80	45364.27	45525.85	45495.74	45112.44	45364.18	45236.27	45525.94	45397.89	45657.27
33.5	45288.72	45252.57	45416.23	45384.31	45548.10	45519.59	45124.84	45384.22	45252.48	45548.20	45416.32	45683.34
34.5	45303.93	45269.35	45435.25	45404.91	45570.94	45544.00	45137.80	45404.82	45269.26	45571.04	45435.34	45709.99
35.5	45319.72	45286.69	45454.86	45426.07	45594.37	45568.95	45151.33	45425.98	45286.59	45594.46	45454.96	45737.22
36.5	45336.11	45304.58	45475.07	45447.79	45618.37	45594.45	45165.43	45447.68	45304.48	45618.47	45475.16	45765.03
37.5	45353.10	45323.04	45495.85	45470.05	45642.96	45620.50	45180.09	45469.95	45322.94	45643.06	45495.95	45793.42
38.5	45370.67	45342.05	45517.23	45492.88	45668.13	45647.11	45195.31	45492.77	45341.95	45668.24	45517.33	45822.38
39.5	45388.84	45361.64	45539.19	45516.26	45693.88	45674.26	45211.11	45516.15	45361.53	45693.99	45539.29	45851.92
40.5	45407.59	45381.78	45561.73	45540.20	45720.21	45701.97	45227.47	45540.09	45381.67	45720.32	45561.84	45882.04
41.5	45426.94	45402.48	45584.86	45564.70	45747.13	45730.23	45244.40	45564.59	45402.38	45747.24	45584.97	45912.72
42.5	45446.88	45423.76	45608.58	45589.75	45774.61	45759.04	45261.90	45589.64	45423.64	45774.73	45608.70	45943.98
43.5	45467.40	45445.59	45632.88	45615.37	45802.68	45788.41	45279.97	45615.25	45445.48	45802.80	45633.00	45975.81
44.5	45488.51	45467.99	45657.76	45641.54	45831.32	45818.32	45298.61	45641.42	45467.87	45831.45	45657.88	46008.21
45.5	45510.21	45490.96	45683.23	45668.27	45860.54	45848.79	45317.82	45668.15	45490.84	45860.66	45683.35	46041.18
46.5	45532.50	45514.48	45709.27	45695.57	45890.33	45879.81	45337.61	45695.44	45514.36	45890.46	45709.39	46074.72
47.5	45555.37	45538.58	45735.89	45723.42	45920.70	45911.39	45357.96	45723.29	45538.46	45920.82	45736.02	46108.82
48.5	45578.84	45563.24	45763.10	45751.83	45951.63	45943.51	45378.90	45751.70	45563.11	45951.77	45763.23	46143.50
49.5	45602.88	45588.47	45790.88	45780.80	45983.15	45976.19	45400.40	45780.67	45588.34	45983.28	45791.01	46178.73
50.5	45627.51	45614.26	45819.24	45810.33	46015.23	46009.42	45422.48	45810.20	45614.13	46015.36	45819.38	46214.54
51.5	45652.73	45640.63	45848.18	45840.42	46047.88	46043.21	45445.13	45840.28	45640.49	46048.02	45848.32	46250.91
52.5	45678.52	45667.55	45877.70	45871.07	46081.10	46077.54	45468.35	45870.93	45667.41	46081.25	45877.84	46287.83
53.5	45704.91	45695.05	45907.79	45902.28	46114.89	46112.43	45492.15	45902.13	45694.90	46115.04	45907.94	46325.32
54.5	45731.88	45723.11	45938.46	45934.05	46149.25	46147.88	45516.52	45933.90	45722.96	46149.40	45938.61	46363.38
55.5	45759.42	45751.73	45969.70	45966.39	46184.18	46183.87	45541.47	45966.23	45751.59	46184.34	45969.85	46401.99
56.5	45787.55	45780.93	46001.53	45999.28	46219.68	46220.41	45566.99	45999.12	45780.78	46219.84	46001.68	46441.16

57.5	45816.27	45810.70	46033.93	46032.73	46255.74	46257.52	45593.09	46032.57	45810.55	46255.90	46034.08	46480.90
58.5	45845.56	45841.03	46066.89	46066.74	46292.37	46295.16	45619.77	46066.58	45840.88	46292.53	46067.05	46521.18
59.5	45875.43	45871.94	46100.44	46101.31	46329.56	46333.37	45647.02	46101.15	45871.78	46329.72	46100.60	46562.03
60.5	45905.89	45903.40	46134.55	46136.45	46367.32	46372.12	45674.86	46136.28	45903.24	46367.48	46134.71	46603.43
61.5	45936.93	45935.44	46169.24	46172.14	46405.64	46411.43	45703.26	46171.97	45935.27	46405.81	46169.41	46645.39
62.5	45968.55	45968.05	46204.50	46208.39	46444.52	46451.28	45732.24	46208.22	45967.88	46444.70	46204.67	46687.91
63.5	46000.74	46001.22	46240.34	46245.20	46483.97	46491.69	45761.80	46245.03	46001.05	46484.14	46240.51	46730.98
64.5	46033.52	46034.96	46276.74	46282.57	46523.98	46532.64	45791.93	46282.40	46034.79	46524.16	46276.91	46774.60
65.5	46066.87	46069.27	46313.71	46320.50	46564.55	46574.15	45822.64	46320.32	46069.09	46564.73	46313.89	46818.77
66.5	46100.80	46104.15	46351.25	46359.00	46605.68	46616.21	45853.94	46358.82	46103.97	46605.86	46351.43	46863.50
67.5	46135.31	46139.59	46389.37	46398.05	46647.38	46658.82	45885.80	46397.86	46139.41	46647.55	46389.55	46908.77
68.5	46170.41	46175.61	46428.05	46437.65	46689.62	46701.97	45918.25	46437.46	46175.42	46689.81	46428.23	46954.59
69.5	46206.07	46212.19	46467.29	46477.82	46732.43	46745.68	45951.27	46477.63	46212.00	46732.62	46467.48	47000.97
70.5	46242.31	46249.34	46507.11	46518.55	46775.80	46789.93	45984.87	46518.36	46249.15	46775.99	46507.30	47047.89
71.5	46279.13	46287.06	46547.50	46559.83	46819.72	46834.73	46019.05	46559.63	46286.87	46819.91	46547.69	47095.36
72.5	46316.53	46325.34	46588.45	46601.67	46864.20	46880.08	46053.81	46601.48	46325.14	46864.40	46588.64	47143.38
73.5	46354.50	46364.19	46629.96	46644.07	46909.24	46925.98	46089.14	46643.88	46364.00	46909.44	46630.16	47191.95
74.5	46393.05	46403.61	46672.05	46687.03	46954.83	46972.42	46125.05	46686.83	46403.41	46955.03	46672.25	47241.05
75.5	46432.17	46443.60	46714.70	46730.55	47000.98	47019.41	46161.54	46730.34	46443.40	47001.18	46714.90	47290.71
76.5	46471.87	46484.16	46757.91	46774.62	47047.68	47066.95	46198.60	46774.41	46483.95	47047.88	46758.11	47340.91
77.5	46512.14	46525.28	46801.69	46819.25	47094.93	47115.04	46236.25	46819.04	46525.07	47095.14	46801.89	47391.65
78.5	46552.99	46566.97	46846.03	46864.43	47142.74	47163.67	46274.47	46864.22	46566.76	47142.95	46846.24	47442.94
79.5	46594.41	46609.23	46890.93	46910.18	47191.10	47212.84	46313.27	46909.96	46609.02	47191.32	46891.14	47494.76

QUANTITY: FREQUENCIES
UNITS : Wavenumbers
BAND (A-X)0 - 3

	P1	P2	Q1	Q2	R1	R2	P12	R12	Q12	Q21	P21	R21
0.5			38654.97		38658.95					38658.96		38666.89
1.5	38650.13	38534.87	38654.07	38542.82	38662.04	38554.73	38530.89	38542.81	38534.87	38662.05	38654.08	38673.94
2.5	38646.00	38534.48	38653.91	38546.40	38665.86	38562.29	38526.54	38546.39	38534.48	38665.86	38653.91	38681.72
3.5	38642.61	38534.74	38654.47	38550.63	38670.41	38570.49	38522.82	38550.62	38534.73	38670.42	38654.48	38690.23
4.5	38639.94	38535.64	38655.77	38555.50	38675.69	38579.33	38519.74	38555.48	38535.63	38675.70	38655.78	38699.47
5.5	38638.01	38537.18	38657.80	38561.01	38681.70	38588.81	38517.31	38561.00	38537.16	38681.71	38657.81	38709.45
6.5	38636.80	38539.36	38660.55	38567.17	38688.43	38598.93	38515.52	38567.15	38539.35	38688.45	38660.57	38720.14
7.5	38636.34	38542.19	38664.04	38573.96	38695.90	38609.70	38514.38	38573.94	38542.17	38695.92	38664.06	38731.56
8.5	38636.59	38545.66	38668.25	38581.40	38704.09	38621.10	38513.88	38581.38	38545.63	38704.12	38668.27	38743.71
9.5	38637.57	38549.77	38673.20	38589.48	38713.01	38633.14	38514.02	38589.46	38549.75	38713.04	38673.22	38756.59
10.5	38639.29	38554.54	38678.87	38598.21	38722.66	38645.83	38514.82	38598.18	38554.51	38722.69	38678.89	38770.19
11.5	38641.73	38559.95	38685.26	38607.58	38733.02	38659.17	38516.26	38607.55	38559.91	38733.05	38685.29	38784.52
12.5	38644.90	38566.00	38692.38	38617.61	38744.12	38673.14	38518.35	38617.57	38565.96	38744.16	38692.41	38799.56
13.5	38648.79	38572.70	38700.23	38628.27	38755.93	38687.77	38521.09	38628.23	38572.67	38755.97	38700.27	38815.33
14.5	38653.41	38580.05	38708.79	38639.59	38768.47	38703.04	38524.48	38639.55	38580.02	38768.51	38708.83	38831.81
15.5	38658.75	38588.06	38718.09	38651.55	38781.72	38718.95	38528.53	38651.51	38588.02	38781.77	38718.13	38849.02
16.5	38664.81	38596.72	38728.09	38664.16	38795.70	38735.52	38533.23	38664.12	38596.68	38795.74	38728.14	38866.93
17.5	38671.59	38606.03	38738.82	38677.43	38810.38	38752.73	38538.59	38677.38	38605.98	38810.43	38738.87	38885.57
18.5	38679.10	38616.00	38750.27	38691.35	38825.79	38770.59	38544.61	38691.30	38615.95	38825.84	38750.32	38904.91
19.5	38687.32	38626.62	38762.43	38705.93	38841.91	38789.11	38551.29	38705.87	38626.57	38841.96	38762.49	38924.97
20.5	38696.26	38637.90	38775.32	38721.15	38858.74	38808.27	38558.61	38721.09	38637.84	38858.80	38775.38	38945.74
21.5	38705.92	38649.84	38788.91	38737.04	38876.28	38828.08	38566.61	38736.97	38649.78	38876.34	38788.98	38967.22
22.5	38716.30	38662.43	38803.22	38753.57	38894.54	38848.55	38575.27	38753.51	38662.37	38894.60	38803.29	38989.41
23.5	38727.39	38675.69	38818.25	38770.77	38913.51	38869.68	38584.59	38770.71	38675.63	38913.57	38818.31	39012.30
24.5	38739.20	38689.61	38833.98	38788.63	38933.18	38891.45	38594.58	38788.56	38689.54	38933.25	38834.05	39035.89
25.5	38751.72	38704.19	38850.43	38807.14	38953.56	38913.89	38605.23	38807.07	38704.12	38953.63	38850.50	39060.20
26.5	38764.95	38719.43	38867.59	38826.32	38974.64	38936.98	38616.55	38826.24	38719.36	38974.71	38867.66	39085.20
27.5	38778.89	38735.34	38885.45	38846.16	38996.43	38960.72	38628.54	38846.08	38735.27	38996.51	38885.52	39110.91
28.5	38793.55	38751.91	38904.02	38866.65	39018.93	38985.13	38641.20	38866.57	38751.84	39019.00	38904.10	39137.31
29.5	38808.91	38769.15	38923.30	38887.82	39042.12	39010.19	38654.52	38887.73	38769.07	39042.20	38923.38	39164.41
30.5	38824.98	38787.06	38943.29	38909.64	39066.02	39035.91	38668.53	38909.56	38786.98	39066.10	38943.37	39192.21
31.5	38841.77	38805.64	38963.97	38932.13	39090.61	39062.30	38683.20	38932.05	38805.55	39090.70	38964.05	39220.71
32.5	38859.26	38824.88	38985.36	38955.29	39115.91	39089.34	38698.55	38955.20	38824.79	39116.00	38985.45	39249.91
33.5	38877.45	38844.80	39007.46	38979.11	39141.90	39117.04	38714.57	38979.02	38844.71	39142.00	39007.55	39279.79
34.5	38896.36	38865.39	39030.25	39003.60	39168.59	39145.41	38731.27	39003.50	38865.29	39168.69	39030.35	39310.37
35.5	38915.96	38886.64	39053.75	39028.75	39195.98	39174.43	38748.64	39028.66	38886.55	39196.08	39053.85	39341.64
36.5	38936.28	38908.57	39077.95	39054.57	39224.06	39204.12	38766.69	39054.47	38908.48	39224.16	39078.05	39373.60
37.5	38957.30	38931.17	39102.84	39081.07	39252.84	39234.48	38785.42	39080.96	38931.07	39252.94	39102.95	39406.25
38.5	38979.01	38954.45	39128.45	39108.23	39282.31	39265.49	38804.82	39108.12	38954.35	39282.41	39128.55	39439.58
39.5	39001.44	38978.40	39154.74	39136.05	39312.47	39297.16	38824.91	39135.94	38978.30	39312.58	39154.85	39473.61
40.5	39024.57	39003.03	39181.73	39164.55	39343.32	39329.51	38845.68	39164.44	39002.92	39343.43	39181.84	39508.32
41.5	39048.39	39028.33	39209.42	39193.72	39374.87	39362.52	38867.13	39193.61	39028.22	39374.98	39209.53	39543.72
42.5	39072.92	39054.31	39237.81	39223.56	39407.10	39396.19	38889.26	39223.44	39054.20	39407.22	39237.92	39579.80
43.5	39098.15	39080.96	39266.88	39254.07	39440.03	39430.52	38912.08	39253.95	39080.84	39440.14	39267.00	39616.56
44.5	39124.08	39108.29	39296.66	39285.25	39473.64	39465.52	38935.57	39285.13	39108.17	39473.76	39296.78	39654.01
45.5	39150.71	39136.30	39327.13	39317.10	39507.93	39501.19	38959.75	39316.98	39136.17	39508.06	39327.25	39692.14
46.5	39178.04	39164.98	39358.29	39349.63	39542.93	39537.52	38984.61	39349.50	39164.85	39543.05	39358.41	39730.95
47.5	39206.07	39194.34	39390.15	39382.82	39578.60	39574.51	39010.16	39382.70	39194.22	39578.73	39390.27	39770.44
48.5	39234.80	39224.39	39422.70	39416.69	39614.96	39612.17	39036.40	39416.56	39224.26	39615.09	39422.83	39810.61
49.5	39264.22	39255.11	39455.93	39451.23	39652.00	39650.50	39063.32	39451.10	39254.98	39652.14	39456.07	39851.46
50.5	39294.34	39286.51	39489.87	39486.45	39689.73	39689.49	39090.92	39486.31	39286.38	39689.87	39490.00	39892.98
51.5	39325.16	39318.59	39524.49	39522.34	39728.14	39729.15	39119.22	39522.20	39318.45	39728.28	39524.63	39935.19
52.5	39356.68	39351.35	39559.80	39558.89	39767.23	39769.48	39148.20	39558.75	39351.21	39767.38	39559.94	39978.07
53.5	39388.89	39384.79	39595.80	39596.13	39807.02	39810.46	39177.86	39595.98	39384.64	39807.16	39595.95	40021.63
54.5	39421.80	39418.91	39632.50	39634.04	39847.48	39852.12	39208.22	39633.89	39418.76	39847.63	39632.64	40065.86
55.5	39455.41	39453.71	39669.88	39672.62	39888.62	39894.45	39239.26	39672.47	39453.56	39888.77	39670.03	40110.76
56.5	39489.71	39489.20	39707.95	39711.88	39930.44	39937.43	39271.00	39711.72	39489.05	39930.59	39708.10	40156.33

57.5	39524.71	39525.36	39746.70	39751.80	39972.94	39981.08	39303.42	39751.64	39525.20	39973.09	39746.86	40202.58
58.5	39560.40	39562.20	39786.15	39792.41	40016.12	40025.40	39336.53	39792.25	39562.05	40016.28	39786.30	40249.50
59.5	39596.79	39599.73	39826.28	39833.68	40059.97	40070.38	39370.33	39833.52	39599.57	40060.14	39826.44	40297.09
60.5	39633.87	39637.94	39867.10	39875.63	40104.52	40116.04	39404.82	39875.46	39637.78	40104.68	39867.26	40345.36
61.5	39671.64	39676.83	39908.61	39918.26	40149.73	40162.35	39440.00	39918.09	39676.67	40149.90	39908.77	40394.29
62.5	39710.11	39716.41	39950.80	39961.55	40195.62	40209.32	39475.87	39961.38	39716.24	40195.79	39950.96	40443.88
63.5	39749.28	39756.66	39993.67	40005.52	40242.19	40256.97	39512.44	40005.35	39756.49	40242.36	39993.84	40494.15
64.5	39789.13	39797.60	40037.23	40050.17	40289.44	40305.28	39549.69	40049.99	39797.43	40289.61	40037.41	40545.09
65.5	39829.68	39839.22	40081.48	40095.49	40337.36	40354.25	39587.64	40095.31	39839.04	40337.54	40081.65	40596.69
66.5	39870.92	39881.52	40126.41	40141.48	40385.95	40403.89	39626.27	40141.30	39881.34	40386.13	40126.59	40648.96
67.5	39912.86	39924.51	40172.02	40188.15	40435.23	40454.20	39665.60	40187.97	39924.33	40435.41	40172.20	40701.89
68.5	39955.48	39968.18	40218.32	40235.49	40485.16	40505.16	39705.63	40235.30	39967.99	40485.35	40218.50	40755.49
69.5	39998.81	40012.52	40265.30	40283.50	40535.79	40556.79	39746.34	40283.32	40012.34	40535.98	40265.48	40809.75
70.5	40042.81	40057.56	40312.96	40332.20	40587.08	40609.09	39787.74	40332.00	40057.37	40587.27	40313.15	40864.68
71.5	40087.52	40103.28	40361.31	40381.56	40639.04	40662.05	39829.84	40381.36	40103.09	40639.24	40361.50	40920.27
72.5	40132.91	40149.68	40410.34	40431.59	40691.68	40715.67	39872.63	40431.40	40149.48	40691.88	40410.53	40976.52
73.5	40179.00	40196.76	40460.05	40482.30	40744.99	40769.95	39916.12	40482.10	40196.56	40745.19	40460.24	41033.44
74.5	40225.77	40244.53	40510.44	40533.68	40798.96	40824.90	39960.29	40533.48	40244.33	40799.16	40510.64	41091.01
75.5	40273.24	40292.98	40561.51	40585.73	40853.61	40880.51	40005.16	40585.53	40292.77	40853.81	40561.71	41149.25
76.5	40321.40	40342.10	40613.26	40638.46	40908.93	40936.78	40050.73	40638.26	40341.90	40909.14	40613.46	41208.14
77.5	40370.24	40391.92	40665.69	40691.87	40964.91	40993.72	40096.98	40691.66	40391.71	40965.13	40665.89	41267.69
78.5	40419.78	40442.42	40718.80	40745.94	41021.57	41051.31	40143.94	40745.73	40442.21	41021.79	40719.01	41327.91
79.5	40470.01	40493.60	40772.59	40800.68	41078.90	41109.57	40191.58	40800.47	40493.39	41079.11	40772.80	41388.77

QUANTITY: FREQUENCIES
UNITS : Wavenumbers
BAND (A-X)1 - 3

	P1	P2	Q1	Q2	R1	R2	P12	R12	Q12	Q21	P21	R21
0.5			40996.90		41000.85					41000.85		41008.71
1.5	40992.06	40876.77	40995.97	40884.64	41003.86	40896.44	40872.83	40884.63	40876.76	41003.87	40995.97	41015.65
2.5	40987.89	40876.30	40995.73	40888.11	41007.57	40903.85	40868.43	40888.10	40876.30	41007.57	40995.73	41023.28
3.5	40984.43	40876.45	40996.18	40892.19	41011.97	40911.86	40864.64	40892.18	40876.44	41011.98	40996.19	41031.60
4.5	40981.65	40877.20	40997.33	40896.87	41017.05	40920.47	40861.45	40896.85	40877.19	41017.07	40997.34	41040.62
5.5	40979.57	40878.55	40999.16	40902.16	41022.84	40929.70	40858.87	40902.14	40878.53	41022.86	40999.18	41050.32
6.5	40978.17	40880.51	41001.70	40908.05	41029.31	40939.52	40856.89	40908.03	40880.49	41029.33	41001.71	41060.72
7.5	40977.48	40883.07	41004.92	40914.54	41036.48	40949.93	40855.52	40914.52	40883.05	41036.50	41004.94	41071.80
8.5	40977.47	40886.24	41008.83	40921.64	41044.33	40960.97	40854.76	40921.62	40886.22	41044.36	41008.86	41083.58
9.5	40978.16	40890.01	41013.44	40929.35	41052.88	40972.59	40854.60	40929.32	40889.99	41052.91	41013.46	41096.04
10.5	40979.53	40894.40	41018.73	40937.66	41062.11	40984.83	40855.05	40937.63	40894.38	41062.14	41018.76	41109.19
11.5	40981.60	40899.39	41024.71	40946.58	41072.02	40997.68	40856.13	40946.55	40899.36	41072.05	41024.74	41123.03
12.5	40984.35	40905.00	41031.38	40956.11	41082.63	41011.13	40857.80	40956.08	40904.96	41082.66	41031.41	41137.55
13.5	40987.79	40911.21	41038.73	40966.25	41093.91	41025.19	40860.09	40966.21	40911.18	41093.95	41038.77	41152.74
14.5	40991.92	40918.04	41046.78	40977.00	41105.89	41039.85	40862.99	40976.96	40918.00	41105.93	41046.82	41168.63
15.5	40996.73	40925.48	41055.50	40988.37	41118.54	41055.13	40866.52	40988.32	40925.44	41118.58	41055.54	41185.19
16.5	41002.23	40933.54	41064.91	41000.34	41131.87	41071.02	40870.65	41000.29	40933.50	41131.91	41064.95	41202.43
17.5	41008.41	40942.21	41075.00	41012.93	41145.88	41087.51	40875.41	41012.88	40942.16	41145.93	41075.05	41220.35
18.5	41015.27	40951.50	41085.77	41026.13	41160.57	41104.62	40880.79	41026.08	40951.45	41160.62	41085.82	41238.94
19.5	41022.82	40961.40	41097.21	41039.95	41175.94	41122.34	40886.78	41039.90	40961.35	41175.99	41097.27	41258.21
20.5	41031.04	40971.93	41109.34	41054.39	41191.98	41140.68	40893.39	41054.33	40971.87	41192.04	41109.40	41278.15
21.5	41039.95	40983.07	41122.16	41069.45	41208.70	41159.62	40900.64	41069.38	40983.02	41208.76	41122.21	41298.76
22.5	41049.54	40994.84	41135.63	41085.11	41226.08	41179.19	40908.51	41085.05	40994.78	41226.14	41135.70	41320.04
23.5	41059.80	41007.23	41149.79	41101.41	41244.14	41199.37	40917.00	41101.34	41007.17	41244.21	41149.85	41341.99
24.5	41070.74	41020.24	41164.62	41118.32	41262.87	41220.16	40926.12	41118.25	41020.18	41262.94	41164.69	41364.61
25.5	41082.36	41033.88	41180.13	41135.86	41282.27	41241.59	40935.87	41135.79	41033.81	41282.34	41180.20	41387.90
26.5	41094.64	41048.14	41196.30	41154.02	41302.34	41263.62	40946.24	41153.95	41048.07	41302.41	41196.37	41411.84
27.5	41107.61	41063.04	41213.15	41172.80	41323.07	41286.27	40957.25	41172.72	41062.96	41323.15	41213.22	41436.46
28.5	41121.25	41078.55	41230.66	41192.20	41344.48	41309.55	40968.89	41192.13	41078.48	41344.55	41230.74	41461.73
29.5	41135.55	41094.70	41248.85	41212.23	41366.54	41333.44	40981.16	41212.16	41094.63	41366.62	41248.93	41487.66
30.5	41150.54	41111.48	41267.70	41232.89	41389.27	41357.95	40994.08	41232.81	41111.40	41389.35	41267.79	41514.26
31.5	41166.19	41128.89	41287.22	41254.17	41412.66	41383.09	41007.62	41254.09	41128.80	41412.74	41287.30	41541.51
32.5	41182.51	41146.92	41307.41	41276.09	41436.70	41408.85	41021.80	41276.00	41146.84	41436.80	41307.49	41569.42
33.5	41199.50	41165.59	41328.25	41298.63	41461.42	41435.23	41036.61	41298.53	41165.50	41461.51	41328.34	41597.98
34.5	41217.15	41184.90	41349.77	41321.79	41486.79	41462.24	41052.06	41321.70	41184.81	41486.88	41349.86	41627.20
35.5	41235.48	41204.83	41371.95	41345.59	41512.81	41489.87	41068.15	41345.49	41204.74	41512.91	41372.04	41657.07
36.5	41254.47	41225.41	41394.79	41370.01	41539.50	41518.12	41084.88	41369.91	41225.31	41539.60	41394.88	41687.60
37.5	41274.13	41246.61	41418.28	41395.07	41566.84	41547.00	41102.25	41394.96	41246.51	41566.94	41418.38	41718.77
38.5	41294.45	41268.45	41442.45	41420.75	41594.84	41576.51	41120.26	41420.65	41268.35	41594.94	41442.55	41750.60
39.5	41315.44	41290.93	41467.27	41447.07	41623.48	41606.63	41138.91	41446.96	41290.82	41623.59	41467.38	41783.08
40.5	41337.09	41314.05	41492.75	41474.02	41652.79	41637.39	41158.21	41473.91	41313.94	41652.90	41492.86	41816.20
41.5	41359.41	41337.80	41518.89	41501.60	41682.75	41668.77	41178.15	41501.48	41337.69	41682.86	41519.00	41849.97
42.5	41382.39	41362.19	41545.69	41529.81	41713.36	41700.78	41198.73	41529.70	41362.07	41713.47	41545.80	41884.39
43.5	41406.03	41387.21	41573.14	41558.66	41744.62	41733.41	41219.95	41558.54	41387.09	41744.73	41573.25	41919.45
44.5	41430.33	41412.88	41601.25	41588.14	41776.53	41766.67	41241.82	41588.02	41412.76	41776.65	41601.37	41955.16
45.5	41455.30	41439.19	41630.02	41618.25	41809.08	41800.55	41264.34	41618.13	41439.06	41809.21	41630.14	41991.51
46.5	41480.93	41466.13	41659.44	41648.99	41842.29	41835.07	41287.50	41648.87	41466.00	41842.42	41659.56	42028.50
47.5	41507.21	41493.71	41689.52	41680.38	41876.15	41870.21	41311.31	41680.25	41493.59	41876.28	41689.64	42066.14
48.5	41534.16	41521.94	41720.25	41712.39	41910.66	41905.97	41335.77	41712.26	41521.81	41910.79	41720.38	42104.41
49.5	41561.77	41550.80	41751.63	41745.03	41945.80	41942.38	41360.87	41744.90	41550.67	41945.94	41751.77	42143.33
50.5	41590.04	41580.31	41783.67	41778.32	41981.60	41979.39	41386.62	41778.18	41580.18	41981.74	41783.80	42182.89
51.5	41618.96	41610.46	41816.36	41812.23	42018.04	42017.05	41413.02	41812.09	41610.32	42018.18	41816.50	42223.09
52.5	41648.55	41641.25	41849.70	41846.79	42055.13	42055.32	41440.07	41846.64	41641.11	42055.27	41849.84	42263.91
53.5	41678.80	41672.68	41883.70	41881.98	42092.86	42094.22	41467.77	41881.83	41672.54	42093.01	41883.84	42305.38
54.5	41709.70	41704.75	41918.34	41917.80	42131.23	42133.75	41496.11	41917.65	41704.61	42131.38	41918.49	42347.49
55.5	41741.25	41737.47	41953.64	41954.25	42170.25	42173.91	41525.11	41954.10	41737.32	42170.40	41953.79	42390.23
56.5	41773.47	41770.83	41989.58	41991.34	42209.91	42214.70	41554.75	41991.19	41770.68	42210.06	41989.73	42433.60

57.5	41806.34	41804.83	42026.17	42029.07	42250.20	42256.11	41585.05	42028.91	41804.67	42250.36	42026.33	42477.61
58.5	41839.87	41839.47	42063.42	42067.43	42291.14	42298.15	41616.00	42067.27	41839.32	42291.30	42063.57	42522.25
59.5	41874.05	41874.76	42101.31	42106.43	42332.72	42340.81	41647.60	42106.27	41874.60	42332.89	42101.47	42567.52
60.5	41908.90	41910.69	42139.85	42146.06	42374.95	42384.11	41679.85	42145.89	41910.53	42375.11	42140.01	42613.43
61.5	41944.39	41947.26	42179.04	42186.33	42417.80	42428.03	41712.75	42186.16	41947.10	42417.98	42179.20	42659.96
62.5	41980.54	41984.48	42218.87	42227.23	42461.30	42472.57	41746.30	42227.06	41984.31	42461.47	42219.04	42707.13
63.5	42017.35	42022.34	42259.35	42268.77	42505.43	42517.74	41780.51	42268.59	42022.17	42505.61	42259.52	42754.92
64.5	42054.81	42060.84	42300.48	42310.94	42550.21	42563.54	41815.37	42310.77	42060.67	42550.39	42300.65	42803.35
65.5	42092.93	42099.99	42342.25	42353.75	42595.62	42609.96	41850.88	42353.57	42099.82	42595.80	42342.43	42852.39
66.5	42131.70	42139.78	42384.67	42397.19	42641.66	42657.01	41887.05	42397.01	42139.60	42641.84	42384.85	42902.08
67.5	42171.12	42180.21	42427.73	42441.27	42688.34	42704.68	41923.86	42441.09	42180.03	42688.53	42427.91	42952.38
68.5	42211.20	42221.29	42471.44	42485.98	42735.66	42752.98	41961.33	42485.79	42221.11	42735.84	42471.62	43003.31
69.5	42251.93	42263.01	42515.79	42531.32	42783.61	42801.91	41999.45	42531.14	42262.82	42783.80	42515.97	43054.87
70.5	42293.30	42305.38	42560.78	42577.31	42832.19	42851.45	42038.23	42577.12	42305.19	42832.38	42560.97	43107.05
71.5	42335.34	42348.39	42606.42	42623.92	42881.41	42901.63	42077.66	42623.73	42348.20	42881.60	42606.61	43159.85
72.5	42378.03	42392.04	42652.70	42671.17	42931.26	42952.42	42117.74	42670.98	42391.84	42931.45	42652.89	43213.28
73.5	42421.36	42436.34	42699.63	42719.05	42981.74	43003.84	42158.48	42718.86	42436.14	42981.94	42699.82	43267.32
74.5	42465.35	42481.28	42747.19	42767.57	43032.85	43055.89	42199.87	42767.37	42481.08	43033.05	42747.39	43322.00
75.5	42510.00	42526.86	42795.39	42816.72	43084.60	43108.55	42241.92	42816.52	42526.66	43084.80	42795.60	43377.29
76.5	42555.29	42573.09	42844.25	42866.51	43136.97	43161.84	42284.61	42866.30	42572.89	43137.18	42844.45	43433.20
77.5	42601.23	42619.96	42893.73	42916.92	43189.97	43215.75	42327.97	42916.71	42619.76	43190.18	42893.94	43489.73
78.5	42647.82	42667.48	42943.86	42967.98	43243.61	43270.29	42371.98	42967.77	42667.27	43243.82	42944.07	43546.88
79.5	42695.07	42715.63	42994.63	43019.66	43297.88	43325.45	42416.64	43019.45	42715.42	43298.09	42994.84	43604.65

QUANTITY: FREQUENCIES
UNITS : Wavenumbers
BAND (A-X)2 - 3

	P1	P2	Q1	Q2	R1	R2	P12	R12	Q12	Q21	P21	R21
0.5			43306.18		43310.09					43310.09		43317.88
1.5	43301.34	43186.01	43305.21	43193.80	43313.02	43205.49	43182.11	43193.79	43186.00	43313.03	43305.21	43324.70
2.5	43297.14	43185.47	43304.89	43197.16	43316.62	43212.75	43177.67	43197.15	43185.46	43316.63	43304.90	43332.18
3.5	43293.59	43185.50	43305.23	43201.09	43320.87	43220.57	43173.80	43201.08	43185.49	43320.88	43305.24	43340.31
4.5	43290.70	43186.10	43306.23	43205.58	43325.77	43228.96	43170.50	43205.56	43186.09	43325.78	43306.24	43349.10
5.5	43288.47	43187.26	43307.88	43210.64	43331.32	43237.91	43167.77	43210.63	43187.24	43331.34	43307.89	43358.54
6.5	43286.88	43188.99	43310.18	43216.27	43337.53	43247.43	43165.60	43216.25	43188.98	43337.55	43310.20	43368.63
7.5	43285.96	43191.29	43313.14	43222.46	43344.39	43257.51	43164.00	43222.43	43191.27	43344.42	43313.16	43379.38
8.5	43285.69	43194.16	43316.75	43229.22	43351.91	43268.16	43162.98	43229.20	43194.13	43351.93	43316.77	43390.78
9.5	43286.07	43197.59	43321.02	43236.55	43360.07	43279.38	43162.52	43236.52	43197.57	43360.10	43321.04	43402.82
10.5	43287.11	43201.60	43325.93	43244.44	43368.89	43291.16	43162.63	43244.41	43201.57	43368.92	43325.96	43415.52
11.5	43288.80	43206.17	43331.49	43252.91	43378.35	43303.52	43163.32	43252.88	43206.14	43378.38	43331.52	43428.86
12.5	43291.13	43211.32	43337.71	43261.95	43388.46	43316.43	43164.58	43261.91	43211.29	43388.50	43337.74	43442.85
13.5	43294.12	43217.05	43344.57	43271.56	43399.22	43329.92	43166.42	43271.52	43217.02	43399.26	43344.61	43457.48
14.5	43297.75	43223.34	43352.08	43281.74	43410.63	43343.98	43168.83	43281.70	43223.30	43410.66	43352.12	43472.76
15.5	43302.04	43230.22	43360.24	43292.50	43422.67	43358.62	43171.82	43292.46	43230.18	43422.71	43360.28	43488.68
16.5	43306.97	43237.67	43369.04	43303.83	43435.36	43373.82	43175.39	43303.78	43237.63	43435.41	43369.09	43505.24
17.5	43312.54	43245.70	43378.49	43315.74	43448.69	43389.60	43179.54	43315.69	43245.65	43448.74	43378.54	43522.44
18.5	43318.76	43254.30	43388.58	43328.22	43462.66	43405.95	43184.27	43328.17	43254.25	43462.71	43388.63	43540.27
19.5	43325.63	43263.49	43399.30	43341.29	43477.27	43422.88	43189.59	43341.23	43263.44	43477.32	43399.36	43558.75
20.5	43333.13	43273.26	43410.68	43354.93	43492.52	43440.38	43195.48	43354.87	43273.20	43492.58	43410.73	43577.85
21.5	43341.28	43283.61	43422.70	43369.15	43508.40	43458.46	43201.97	43369.09	43283.55	43508.46	43422.75	43597.59
22.5	43350.08	43294.55	43435.34	43383.95	43524.92	43477.12	43209.05	43383.89	43294.48	43524.98	43435.40	43617.97
23.5	43359.50	43306.07	43448.63	43399.34	43542.07	43496.35	43216.70	43399.27	43306.00	43542.14	43448.69	43638.97
24.5	43369.57	43318.17	43462.55	43415.30	43559.85	43516.16	43224.96	43415.23	43318.10	43559.92	43462.61	43660.61
25.5	43380.28	43330.86	43477.11	43431.85	43578.27	43536.56	43233.79	43431.78	43330.79	43578.34	43477.18	43682.87
26.5	43391.62	43344.14	43492.30	43448.99	43597.31	43557.53	43243.23	43448.91	43344.07	43597.39	43492.37	43705.75
27.5	43403.60	43358.01	43508.12	43466.71	43616.98	43579.08	43253.25	43466.63	43357.94	43617.06	43508.20	43729.27
28.5	43416.22	43372.46	43524.57	43485.01	43637.29	43601.22	43263.87	43484.93	43372.39	43637.36	43524.65	43753.41
29.5	43429.46	43387.51	43541.66	43503.91	43658.21	43623.94	43275.08	43503.83	43387.43	43658.30	43541.73	43778.16
30.5	43443.34	43403.16	43559.38	43523.39	43679.76	43647.24	43286.89	43523.30	43403.07	43679.85	43559.46	43803.54
31.5	43457.86	43419.38	43577.71	43543.46	43701.94	43671.13	43299.30	43543.38	43419.30	43702.03	43577.80	43829.54
32.5	43473.00	43436.21	43596.69	43564.12	43724.74	43695.59	43312.29	43564.03	43436.12	43724.83	43596.77	43856.16
33.5	43488.78	43453.63	43616.29	43585.37	43748.16	43720.65	43325.89	43585.27	43453.54	43748.25	43616.38	43883.40
34.5	43505.19	43471.64	43636.51	43607.21	43772.20	43746.29	43340.10	43607.11	43471.55	43772.30	43636.61	43911.25
35.5	43522.22	43490.25	43657.36	43629.64	43796.87	43772.52	43354.89	43629.54	43490.16	43796.96	43657.46	43939.72
36.5	43539.89	43509.46	43678.84	43652.66	43822.14	43799.32	43370.30	43652.56	43509.36	43822.25	43678.93	43968.80
37.5	43558.18	43529.26	43700.93	43676.27	43848.04	43826.73	43386.30	43676.17	43529.16	43848.14	43701.03	43998.50
38.5	43577.10	43549.66	43723.65	43700.48	43874.56	43854.71	43402.91	43700.37	43549.55	43874.66	43723.75	44028.80
39.5	43596.64	43570.65	43746.99	43725.27	43901.69	43883.28	43420.12	43725.16	43570.55	43901.80	43747.10	44059.72
40.5	43616.82	43592.25	43770.95	43750.66	43929.44	43912.44	43437.93	43750.55	43592.14	43929.55	43771.06	44091.25
41.5	43637.61	43614.44	43795.54	43776.65	43957.80	43942.19	43456.35	43776.54	43614.33	43957.91	43795.64	44123.39
42.5	43659.04	43637.24	43820.74	43803.23	43986.77	43972.52	43475.38	43803.11	43637.13	43986.89	43820.85	44156.13
43.5	43681.08	43660.63	43846.55	43830.40	44016.36	44003.45	43495.01	43830.28	43660.51	44016.48	43846.67	44189.49
44.5	43703.75	43684.62	43873.00	43858.17	44046.56	44034.95	43515.24	43858.05	43684.50	44046.68	43873.11	44223.45
45.5	43727.04	43709.22	43900.05	43886.53	44077.37	44067.05	43536.09	43886.41	43709.10	44077.49	43900.18	44258.01
46.5	43750.96	43734.41	43927.72	43915.49	44108.79	44099.74	43557.54	43915.37	43734.29	44108.92	43927.85	44293.18
47.5	43775.50	43760.21	43956.02	43945.05	44140.82	44133.02	43579.59	43944.92	43760.09	44140.95	43956.14	44328.95
48.5	43800.66	43786.61	43984.92	43975.20	44173.46	44166.88	43602.27	43975.06	43786.48	44173.59	43985.05	44365.32
49.5	43826.45	43813.61	44014.44	44005.94	44206.71	44201.34	43625.54	44005.80	43813.48	44206.84	44014.57	44402.29
50.5	43852.84	43841.21	44044.58	44037.28	44240.56	44236.38	43649.43	44037.14	43841.08	44240.70	44044.71	44439.87
51.5	43879.87	43869.42	44075.32	44069.22	44275.02	44272.01	43673.92	44069.08	43869.29	44275.16	44075.46	44478.05
52.5	43907.52	43898.23	44106.68	44101.75	44310.09	44308.22	43699.03	44101.61	43898.09	44310.23	44106.82	44516.82
53.5	43935.77	43927.64	44138.66	44134.88	44345.76	44345.03	43724.74	44134.73	43927.50	44345.91	44138.80	44556.19
54.5	43964.66	43957.66	44171.24	44168.60	44382.04	44382.43	43751.07	44168.45	43957.51	44382.19	44171.39	44596.16
55.5	43994.16	43988.27	44204.44	44202.93	44418.92	44420.41	43778.01	44202.77	43988.13	44419.07	44204.59	44636.73
56.5	44024.27	44019.50	44238.25	44237.84	44456.41	44458.98	43805.56	44237.69	44019.35	44456.56	44238.41	44677.89

57.5	44055.02	44051.33	44272.67	44273.36	44494.49	44498.14	43833.72	44273.20	44051.17	44494.65	44272.83	44719.64
58.5	44086.37	44083.76	44307.70	44309.47	44533.18	44537.89	43862.50	44309.31	44083.60	44533.34	44307.86	44761.99
59.5	44118.34	44116.80	44343.34	44346.17	44572.46	44578.23	43891.88	44346.01	44116.64	44572.63	44343.50	44804.93
60.5	44150.93	44150.43	44379.59	44383.47	44612.36	44619.15	43921.88	44383.31	44150.27	44612.52	44379.75	44848.47
61.5	44184.13	44184.68	44416.45	44421.38	44652.85	44660.66	43952.49	44421.20	44184.51	44653.02	44416.61	44892.60
62.5	44217.96	44219.52	44453.91	44459.87	44693.94	44702.76	43983.71	44459.70	44219.36	44694.11	44454.08	44937.32
63.5	44252.39	44254.98	44491.98	44498.96	44735.63	44745.45	44015.55	44498.79	44254.80	44735.80	44492.16	44982.63
64.5	44287.45	44291.03	44530.67	44538.64	44777.91	44788.72	44048.00	44538.47	44290.86	44778.09	44530.84	45028.53
65.5	44323.12	44327.70	44569.95	44578.93	44820.80	44832.58	44081.07	44578.75	44327.52	44820.98	44570.13	45075.01
66.5	44359.40	44364.96	44609.85	44619.80	44864.28	44877.02	44114.75	44619.63	44364.78	44864.46	44610.03	45122.09
67.5	44396.30	44402.83	44650.35	44661.28	44908.36	44922.05	44149.04	44661.10	44402.65	44908.54	44650.53	45169.75
68.5	44433.81	44441.30	44691.45	44703.35	44953.02	44967.67	44183.95	44703.16	44441.12	44953.21	44691.63	45218.00
69.5	44471.94	44480.38	44733.16	44746.01	44998.30	45013.88	44219.46	44745.82	44480.20	44998.48	44733.34	45266.84
70.5	44510.67	44520.07	44775.47	44789.28	45044.16	45060.66	44255.60	44789.09	44519.88	45044.35	44775.66	45316.25
71.5	44550.03	44560.36	44818.39	44833.13	45090.61	45108.03	44292.35	44832.93	44560.17	45090.81	44818.58	45366.25
72.5	44590.00	44601.25	44861.91	44877.58	45137.66	45155.99	44329.71	44877.38	44601.05	45137.86	44862.10	45416.84
73.5	44630.57	44642.74	44906.03	44922.63	45185.31	45204.53	44367.69	44922.42	44642.55	45185.51	44906.23	45468.02
74.5	44671.76	44684.85	44950.76	44968.26	45233.54	45253.66	44406.28	44968.06	44684.65	45233.74	44950.96	45519.77
75.5	44713.56	44727.55	44996.09	45014.49	45282.37	45303.37	44445.48	45014.29	44727.35	45282.57	44996.29	45572.10
76.5	44755.98	44770.86	45042.02	45061.32	45331.79	45353.66	44485.30	45061.11	44770.66	45331.99	45042.22	45625.02
77.5	44799.00	44814.77	45088.54	45108.74	45381.79	45404.53	44525.74	45108.53	44814.57	45382.00	45088.75	45678.51
78.5	44842.64	44859.29	45135.67	45156.76	45432.39	45455.99	44566.79	45156.55	44859.08	45432.60	45135.88	45732.59
79.5	44886.88	44904.41	45183.41	45205.36	45483.58	45508.03	44608.45	45205.15	44904.20	45483.79	45183.62	45787.23

QUANTITY: FREQUENCIES
UNITS : Wavenumbers
BAND (A-X)2 - 4

	P1	P2	Q1	Q2	R1	R2	P12	R12	Q12	Q21	P21	R21
0.5			41514.22		41518.13					41518.13		41525.91
1.5	41509.43	41394.34	41513.30	41402.13	41521.11	41413.82	41390.44	41402.13	41394.34	41521.12	41513.30	41532.79
2.5	41505.31	41393.89	41513.07	41405.59	41524.79	41421.18	41386.10	41405.58	41393.89	41524.80	41513.07	41540.36
3.5	41501.88	41394.05	41513.53	41409.64	41529.16	41429.12	41382.35	41409.63	41394.04	41529.17	41513.54	41548.61
4.5	41499.15	41394.81	41514.68	41414.30	41534.21	41437.67	41379.22	41414.28	41394.80	41534.23	41514.69	41557.55
5.5	41497.11	41396.17	41516.52	41419.55	41539.96	41446.82	41376.68	41419.54	41396.16	41539.98	41516.53	41567.18
6.5	41495.75	41398.14	41519.05	41425.41	41546.40	41456.58	41374.75	41425.39	41398.13	41546.42	41519.06	41577.50
7.5	41495.09	41400.71	41522.26	41431.88	41553.52	41466.93	41373.42	41431.85	41400.69	41553.54	41522.28	41588.50
8.5	41495.11	41403.88	41526.16	41438.95	41561.33	41477.89	41372.70	41438.92	41403.86	41561.35	41526.19	41600.20
9.5	41495.82	41407.66	41530.76	41446.62	41569.82	41489.45	41372.59	41446.59	41407.64	41569.85	41530.78	41612.57
10.5	41497.21	41412.05	41536.04	41454.89	41578.99	41501.61	41373.08	41454.86	41412.02	41579.02	41536.06	41625.63
11.5	41499.30	41417.04	41542.00	41463.78	41588.86	41514.38	41374.19	41463.75	41417.01	41588.89	41542.03	41639.37
12.5	41502.06	41422.64	41548.64	41473.27	41599.40	41527.75	41375.90	41473.23	41422.61	41599.43	41548.68	41653.79
13.5	41505.52	41428.86	41555.98	41483.37	41610.62	41541.73	41378.23	41483.33	41428.82	41610.66	41556.01	41668.88
14.5	41509.66	41435.68	41563.98	41494.07	41622.53	41556.32	41381.16	41494.03	41435.64	41622.57	41564.02	41684.66
15.5	41514.48	41443.11	41572.68	41505.39	41635.11	41571.51	41384.71	41505.35	41443.07	41635.16	41572.72	41701.12
16.5	41519.98	41451.16	41582.05	41517.32	41648.37	41587.31	41388.88	41517.27	41451.11	41648.42	41582.10	41718.25
17.5	41526.16	41459.82	41592.11	41529.86	41662.30	41603.72	41393.66	41529.80	41459.77	41662.36	41592.15	41736.05
18.5	41533.02	41469.09	41602.84	41543.01	41676.91	41620.73	41399.06	41542.95	41469.04	41676.97	41602.89	41754.53
19.5	41540.56	41478.98	41614.24	41556.77	41692.20	41638.37	41405.08	41556.72	41478.93	41692.26	41614.29	41773.68
20.5	41548.78	41489.49	41626.32	41571.16	41708.16	41656.61	41411.71	41571.10	41489.43	41708.22	41626.38	41793.50
21.5	41557.68	41500.62	41639.09	41586.15	41724.79	41675.46	41418.98	41586.09	41500.56	41724.85	41639.14	41813.99
22.5	41567.25	41512.36	41652.51	41601.77	41742.09	41694.93	41426.86	41601.70	41512.30	41742.15	41652.57	41835.14
23.5	41577.49	41524.73	41666.62	41618.00	41760.06	41715.01	41435.36	41617.93	41524.66	41760.13	41666.68	41856.96
24.5	41588.41	41537.71	41681.39	41634.85	41778.69	41735.71	41444.50	41634.78	41537.65	41778.76	41681.45	41879.45
25.5	41600.01	41551.32	41696.83	41652.32	41798.00	41757.02	41454.26	41652.25	41551.25	41798.07	41696.90	41902.59
26.5	41612.27	41565.56	41712.95	41670.41	41817.96	41778.95	41464.64	41670.33	41565.49	41818.04	41713.02	41926.40
27.5	41625.21	41580.42	41729.73	41689.11	41838.59	41801.49	41475.66	41689.04	41580.34	41838.67	41729.80	41950.87
28.5	41638.82	41595.90	41747.17	41708.45	41859.88	41824.66	41487.30	41708.37	41595.82	41859.96	41747.25	41976.01
29.5	41653.09	41612.01	41765.29	41728.41	41881.84	41848.43	41499.57	41728.32	41611.93	41881.92	41765.36	42001.79
30.5	41668.04	41628.75	41784.07	41748.98	41904.45	41872.83	41512.48	41748.89	41628.66	41904.54	41784.15	42028.23
31.5	41683.65	41646.11	41803.51	41770.18	41927.73	41897.85	41526.02	41770.09	41646.02	41927.82	41803.59	42055.34
32.5	41699.93	41664.10	41823.61	41792.01	41951.66	41923.49	41540.18	41791.92	41664.02	41951.75	41823.70	42083.09
33.5	41716.88	41682.73	41844.38	41814.46	41976.25	41949.75	41554.99	41814.37	41682.64	41976.34	41844.47	42111.49
34.5	41734.48	41701.98	41865.81	41837.54	42001.50	41976.63	41570.43	41837.45	41701.89	42001.59	41865.90	42140.55
35.5	41752.76	41721.86	41887.90	41861.25	42027.40	42004.13	41586.51	41861.15	41721.77	42027.50	41887.99	42170.26
36.5	41771.70	41742.38	41910.65	41885.58	42053.96	42032.25	41603.22	41885.48	41742.29	42054.06	41910.75	42200.61
37.5	41791.30	41763.53	41934.05	41910.54	42081.17	42061.00	41620.57	41910.44	41763.43	42081.27	41934.16	42231.63
38.5	41811.57	41785.31	41958.12	41936.13	42109.03	42090.37	41638.56	41936.02	41785.21	42109.14	41958.22	42263.28
39.5	41832.50	41807.73	41982.85	41962.35	42137.55	42120.35	41657.19	41962.24	41807.62	42137.66	41982.95	42295.58
40.5	41854.09	41830.78	42008.23	41989.19	42166.71	42150.97	41676.46	41989.08	41830.67	42166.82	42008.34	42328.53
41.5	41876.34	41854.46	42034.26	42016.67	42196.53	42182.21	41696.37	42016.55	41854.35	42196.64	42034.37	42362.12
42.5	41899.25	41878.78	42060.95	42044.77	42226.99	42214.06	41716.92	42044.66	41878.67	42227.11	42061.07	42396.35
43.5	41922.83	41903.74	42088.30	42073.51	42258.10	42246.55	41738.11	42073.39	41903.62	42258.22	42088.41	42431.23
44.5	41947.05	41929.33	42116.30	42102.88	42289.87	42279.66	41759.95	42102.76	41929.21	42289.99	42116.42	42466.75
45.5	41971.95	41955.56	42144.96	42132.87	42322.27	42313.39	41782.42	42132.75	41955.44	42322.40	42145.08	42502.91
46.5	41997.50	41982.42	42174.26	42163.50	42355.33	42347.75	41805.55	42163.38	41982.30	42355.45	42174.38	42539.71
47.5	42023.70	42009.93	42204.22	42194.76	42389.03	42382.73	41829.31	42194.63	42009.80	42389.16	42204.34	42577.15
48.5	42050.57	42038.07	42234.83	42226.65	42423.37	42418.34	41853.72	42226.52	42037.94	42423.50	42234.96	42615.23
49.5	42078.09	42066.85	42266.09	42259.17	42458.36	42454.57	41878.77	42259.04	42066.71	42458.49	42266.22	42653.95
50.5	42106.27	42096.27	42298.00	42292.33	42493.99	42491.43	41904.47	42292.19	42096.13	42494.13	42298.13	42693.30
51.5	42135.11	42126.32	42330.56	42326.12	42530.27	42528.91	41930.82	42325.98	42126.19	42530.41	42330.70	42733.29
52.5	42164.60	42157.02	42363.77	42360.54	42567.18	42567.01	41957.81	42360.39	42156.88	42567.32	42363.91	42773.90
53.5	42194.75	42188.35	42397.63	42395.58	42604.73	42605.73	41985.45	42395.43	42188.21	42604.88	42397.77	42815.16
54.5	42225.55	42220.32	42432.13	42431.27	42642.93	42645.09	42013.74	42431.12	42220.18	42643.08	42432.28	42857.05
55.5	42257.00	42252.94	42467.29	42467.58	42681.77	42685.07	42042.66	42467.43	42252.79	42681.92	42467.44	42899.57
56.5	42289.12	42286.19	42503.09	42504.53	42721.25	42725.67	42072.25	42504.38	42286.04	42721.40	42503.25	42942.73

57.5	42321.89	42320.09	42539.54	42542.11	42761.36	42766.90	42102.48	42541.95	42319.93	42761.52	42539.70	42986.52
58.5	42355.30	42354.62	42576.64	42580.33	42802.12	42808.75	42133.35	42580.16	42354.46	42802.28	42576.80	43030.93
59.5	42389.38	42389.80	42614.38	42619.17	42843.50	42851.23	42164.88	42619.00	42389.64	42843.67	42614.54	43075.97
60.5	42424.11	42425.61	42652.77	42658.64	42885.54	42894.33	42197.05	42658.48	42425.45	42885.70	42652.93	43121.65
61.5	42459.48	42462.06	42691.80	42698.76	42928.20	42938.05	42229.88	42698.59	42461.90	42928.37	42691.96	43167.95
62.5	42495.52	42499.16	42731.47	42739.50	42971.50	42982.39	42263.35	42739.33	42498.99	42971.67	42731.64	43214.88
63.5	42532.20	42536.90	42771.79	42780.88	43015.43	43027.37	42297.47	42780.70	42536.73	43015.61	42771.96	43262.43
64.5	42569.54	42575.27	42812.75	42822.88	43060.00	43072.96	42332.24	42822.71	42575.10	43060.18	42812.93	43310.61
65.5	42607.52	42614.29	42854.36	42865.52	43105.20	43119.17	42367.66	42865.34	42614.12	43105.38	42854.54	43359.42
66.5	42646.16	42653.95	42896.61	42908.80	43151.04	43166.02	42403.73	42908.62	42653.77	43151.22	42896.79	43408.85
67.5	42685.45	42694.25	42939.50	42952.70	43197.52	43213.48	42440.46	42952.52	42694.07	43197.70	42939.68	43458.91
68.5	42725.40	42735.20	42983.04	42997.23	43244.61	43261.56	42477.83	42997.05	42735.01	43244.80	42983.22	43509.58
69.5	42765.99	42776.78	43027.21	43042.40	43292.35	43310.27	42515.86	43042.21	42776.59	43292.54	43027.39	43560.89
70.5	42807.23	42819.00	43072.02	43088.21	43340.71	43359.59	42554.53	43088.02	42818.81	43340.91	43072.21	43612.80
71.5	42849.12	42861.87	43117.48	43134.64	43389.71	43409.54	42593.86	43134.44	42861.68	43389.90	43117.67	43665.34
72.5	42891.66	42905.37	43163.57	43181.70	43439.33	43460.11	42633.84	43181.50	42905.18	43439.53	43163.77	43718.51
73.5	42934.85	42949.52	43210.31	43229.39	43489.59	43511.30	42674.46	43229.20	42949.32	43489.79	43210.51	43772.30
74.5	42978.69	42994.31	43257.69	43277.72	43540.47	43563.12	42715.74	43277.52	42994.11	43540.68	43257.89	43826.70
75.5	43023.18	43039.74	43305.70	43326.68	43591.98	43615.55	42757.67	43326.48	43039.54	43592.19	43305.90	43881.71
76.5	43068.32	43085.81	43354.35	43376.27	43644.13	43668.61	42800.25	43376.06	43085.61	43644.34	43354.55	43937.35
77.5	43114.10	43132.52	43403.64	43426.48	43696.89	43722.28	42843.48	43426.27	43132.32	43697.10	43403.85	43993.61
78.5	43160.54	43179.88	43453.57	43477.34	43750.29	43776.58	42887.37	43477.13	43179.66	43750.50	43453.78	44050.48
79.5	43207.62	43227.87	43504.14	43528.82	43804.31	43831.48	42931.91	43528.60	43227.66	43804.52	43504.35	44107.96

QUANTITY: FREQUENCIES
UNITS : Wavenumbers
BAND (A-X)3 - 4

	P1	P2	Q1	Q2	R1	R2	P12	R12	Q12	Q21	P21	R21
0.5			43790.62		43794.49					43794.49		43802.20
1.5	43785.83	43670.70	43789.66	43678.42	43797.40	43690.00	43666.84	43678.41	43670.70	43797.41	43789.67	43808.96
2.5	43781.68	43670.18	43789.36	43681.76	43800.96	43697.20	43662.46	43681.75	43670.18	43800.97	43789.36	43816.38
3.5	43778.17	43670.22	43789.70	43685.66	43805.18	43704.95	43658.64	43685.65	43670.21	43805.20	43789.71	43824.44
4.5	43775.32	43670.83	43790.70	43690.13	43810.05	43713.27	43655.39	43690.11	43670.82	43810.06	43790.71	43833.15
5.5	43773.13	43672.00	43792.35	43695.16	43815.57	43722.16	43652.70	43695.14	43671.99	43815.58	43792.36	43842.52
6.5	43771.58	43673.74	43794.65	43700.75	43821.74	43731.61	43650.58	43700.73	43673.73	43821.76	43794.66	43852.54
7.5	43770.69	43676.05	43797.60	43706.91	43828.55	43741.63	43649.02	43706.89	43676.03	43828.57	43797.62	43863.20
8.5	43770.45	43678.92	43801.20	43713.64	43836.02	43752.20	43648.04	43713.61	43678.89	43836.04	43801.22	43874.51
9.5	43770.85	43682.36	43805.45	43720.93	43844.13	43763.34	43647.62	43720.90	43682.33	43844.16	43805.47	43886.46
10.5	43771.91	43686.36	43810.35	43728.79	43852.89	43775.05	43647.77	43728.75	43686.34	43852.92	43810.38	43899.06
11.5	43773.61	43690.94	43815.89	43737.21	43862.30	43787.33	43648.50	43737.18	43690.91	43862.33	43815.92	43912.31
12.5	43775.96	43696.08	43822.08	43746.21	43872.34	43800.16	43649.79	43746.18	43696.05	43872.38	43822.11	43926.20
13.5	43778.96	43701.80	43828.92	43755.77	43883.03	43813.57	43651.66	43755.73	43701.77	43883.07	43828.95	43940.73
14.5	43782.60	43708.09	43836.39	43765.91	43894.37	43827.55	43654.11	43765.87	43708.05	43894.41	43836.43	43955.90
15.5	43786.89	43714.95	43844.52	43776.63	43906.35	43842.09	43657.12	43776.58	43714.91	43906.39	43844.56	43971.70
16.5	43791.82	43722.39	43853.29	43787.90	43918.96	43857.21	43660.72	43787.86	43722.35	43919.00	43853.33	43988.15
17.5	43797.39	43730.40	43862.69	43799.76	43932.21	43872.90	43664.90	43799.71	43730.36	43932.26	43862.74	44005.23
18.5	43803.61	43738.99	43872.74	43812.19	43946.09	43889.16	43669.64	43812.13	43738.95	43946.15	43872.79	44022.95
19.5	43810.46	43748.16	43883.42	43825.19	43960.62	43905.99	43674.98	43825.14	43748.11	43960.68	43883.47	44041.30
20.5	43817.96	43757.91	43894.74	43838.78	43975.78	43923.39	43680.89	43838.72	43757.85	43975.84	43894.80	44060.28
21.5	43826.09	43768.23	43906.70	43852.93	43991.57	43941.37	43687.39	43852.87	43768.18	43991.63	43906.76	44079.89
22.5	43834.87	43779.14	43919.29	43867.67	44008.00	43959.92	43694.48	43867.61	43779.08	44008.06	43919.35	44100.13
23.5	43844.27	43790.63	43932.52	43882.99	44025.05	43979.05	43702.14	43882.92	43790.57	44025.12	43932.59	44121.00
24.5	43854.32	43802.71	43946.38	43898.89	44042.73	43998.76	43710.41	43898.82	43802.64	44042.80	43946.45	44142.50
25.5	43865.00	43815.36	43960.87	43915.37	44061.05	44019.04	43719.25	43915.30	43815.29	44061.12	43960.94	44164.62
26.5	43876.31	43828.61	43976.00	43932.43	44079.98	44039.90	43728.68	43932.36	43828.54	44080.06	43976.07	44187.36
27.5	43888.26	43842.44	43991.75	43950.07	44099.55	44061.34	43738.71	43949.99	43842.37	44099.63	43991.82	44210.72
28.5	43900.84	43856.86	44008.13	43968.30	44119.73	44083.36	43749.32	43968.22	43856.78	44119.81	44008.20	44234.71
29.5	43914.05	43871.86	44025.14	43987.11	44140.55	44105.96	43760.53	43987.03	43871.78	44140.63	44025.21	44259.32
30.5	43927.89	43887.45	44042.77	44006.51	44161.98	44129.14	43772.33	44006.42	43887.38	44162.07	44042.86	44284.54
31.5	43942.36	43903.64	44061.03	44026.49	44184.04	44152.90	43784.73	44026.41	43903.55	44184.13	44061.12	44310.38
32.5	43957.45	43920.41	44079.92	44047.06	44206.71	44177.24	43797.71	44046.97	43920.32	44206.80	44080.01	44336.84
33.5	43973.18	43937.78	44099.43	44068.22	44230.01	44202.17	43811.30	44068.13	43937.69	44230.10	44099.52	44363.91
34.5	43989.54	43955.73	44119.56	44089.96	44253.92	44227.68	43825.48	44089.87	43955.64	44254.02	44119.66	44391.60
35.5	44006.51	43974.29	44140.32	44112.30	44278.45	44253.77	43840.26	44112.20	43974.19	44278.55	44140.41	44419.89
36.5	44024.13	43993.43	44161.70	44135.22	44303.59	44280.44	43855.64	44135.12	43993.33	44303.70	44161.79	44448.80
37.5	44042.35	44013.17	44183.70	44158.73	44329.36	44307.70	43871.62	44158.63	44013.07	44329.46	44183.80	44478.32
38.5	44061.21	44033.50	44206.31	44182.83	44355.73	44335.54	43888.20	44182.72	44033.40	44355.84	44206.41	44508.45
39.5	44080.69	44054.43	44229.55	44207.52	44382.72	44363.96	43905.38	44207.41	44054.32	44382.83	44229.65	44539.19
40.5	44100.79	44075.95	44253.40	44232.80	44410.32	44392.97	43923.16	44232.69	44075.84	44410.43	44253.51	44570.53
41.5	44121.51	44098.07	44277.87	44258.67	44438.53	44422.57	43941.54	44258.56	44097.96	44438.64	44277.98	44602.48
42.5	44142.86	44120.79	44302.96	44285.14	44467.36	44452.75	43960.53	44285.02	44120.67	44467.47	44303.07	44635.03
43.5	44164.83	44144.10	44328.66	44312.19	44496.79	44483.52	43980.12	44312.07	44143.98	44496.91	44328.78	44668.20
44.5	44187.42	44168.01	44354.98	44339.84	44526.83	44514.86	44000.31	44339.72	44167.89	44526.95	44355.10	44701.95
45.5	44210.63	44192.52	44381.92	44368.07	44557.48	44546.80	44021.11	44367.95	44192.40	44557.60	44382.04	44736.32
46.5	44234.46	44217.63	44409.46	44396.91	44588.73	44579.32	44042.51	44396.78	44217.50	44588.86	44409.59	44771.28
47.5	44258.91	44243.34	44437.63	44426.33	44620.60	44612.43	44064.51	44426.20	44243.21	44620.73	44437.75	44806.85
48.5	44283.98	44269.64	44466.40	44456.35	44653.07	44646.12	44087.13	44456.22	44269.51	44653.20	44466.53	44843.01
49.5	44309.66	44296.55	44495.79	44486.95	44686.14	44680.40	44110.34	44486.82	44296.41	44686.27	44495.92	44879.77
50.5	44335.97	44324.05	44525.78	44518.16	44719.82	44715.27	44134.17	44518.02	44323.91	44719.96	44525.91	44917.14
51.5	44362.89	44352.16	44556.39	44549.96	44754.11	44750.72	44158.60	44549.82	44352.02	44754.25	44556.53	44955.10
52.5	44390.43	44380.86	44587.61	44582.35	44788.99	44786.75	44183.64	44582.20	44380.72	44789.14	44587.75	44993.65
53.5	44418.59	44410.16	44619.44	44615.33	44824.48	44823.38	44209.29	44615.18	44410.02	44824.63	44619.59	45032.80
54.5	44447.36	44440.07	44651.88	44648.91	44860.57	44860.59	44235.55	44648.76	44439.92	44860.72	44652.03	45072.54
55.5	44476.75	44470.58	44684.93	44683.07	44897.26	44898.38	44262.41	44682.92	44470.43	44897.41	44685.08	45112.88
56.5	44506.76	44501.68	44718.59	44717.84	44934.55	44936.75	44289.89	44717.68	44501.53	44934.71	44718.74	45153.81

57.5	44537.38	44533.39	44752.85	44753.19	44972.45	44975.72	44317.97	44753.04	44533.23	44972.60	44753.00	45195.34
58.5	44568.61	44565.70	44787.72	44789.15	45010.94	45015.27	44346.66	44788.98	44565.54	45011.10	44787.88	45237.45
59.5	44600.46	44598.62	44823.20	44825.69	45050.02	45055.40	44375.96	44825.52	44598.46	45050.19	44823.36	45280.15
60.5	44632.93	44632.13	44859.28	44862.82	45089.71	45096.13	44405.88	44862.66	44631.96	45089.88	44859.45	45323.45
61.5	44666.00	44666.24	44895.97	44900.55	45130.00	45137.43	44436.39	44900.39	44666.07	45130.16	44896.14	45367.32
62.5	44699.70	44700.96	44933.27	44938.88	45170.88	45179.31	44467.52	44938.70	44700.79	45171.05	44933.44	45411.79
63.5	44734.00	44736.27	44971.16	44977.79	45212.35	45221.79	44499.27	44977.62	44736.10	45212.52	44971.34	45456.85
64.5	44768.91	44772.19	45009.67	45017.30	45254.43	45264.84	44531.62	45017.13	44772.02	45254.60	45009.84	45502.50
65.5	44804.45	44808.71	45048.78	45057.41	45297.09	45308.48	44564.58	45057.23	44808.54	45297.27	45048.96	45548.73
66.5	44840.59	44845.84	45088.49	45098.10	45340.35	45352.70	44598.16	45097.92	44845.66	45340.53	45088.67	45595.54
67.5	44877.34	44883.55	45128.81	45139.39	45384.20	45397.51	44632.34	45139.21	44883.38	45384.39	45128.99	45642.94
68.5	44914.70	44921.89	45169.73	45181.27	45428.65	45442.90	44667.14	45181.08	44921.70	45428.84	45169.91	45690.92
69.5	44952.68	44960.81	45211.24	45223.74	45473.69	45488.87	44702.55	45223.55	44960.63	45473.88	45211.43	45739.49
70.5	44991.26	45000.34	45253.36	45266.81	45519.32	45535.43	44738.56	45266.62	45000.15	45519.51	45253.55	45788.64
71.5	45030.46	45040.47	45296.09	45310.47	45565.54	45582.56	44775.20	45310.27	45040.28	45565.73	45296.27	45838.37
72.5	45070.27	45081.20	45339.41	45354.72	45612.35	45630.28	44812.44	45354.52	45081.01	45612.55	45339.60	45888.68
73.5	45110.68	45122.54	45383.33	45399.56	45659.75	45678.58	44850.29	45399.36	45122.34	45659.95	45383.52	45939.56
74.5	45151.71	45164.48	45427.85	45444.99	45707.74	45727.45	44888.76	45444.79	45164.27	45707.95	45428.05	45991.03
75.5	45193.34	45207.01	45472.97	45491.02	45756.32	45776.92	44927.84	45490.81	45206.80	45756.52	45473.17	46043.08
76.5	45235.59	45250.15	45518.69	45537.63	45805.49	45826.96	44967.52	45537.43	45249.95	45805.70	45518.89	46095.70
77.5	45278.44	45293.89	45565.01	45584.84	45855.24	45877.58	45007.82	45584.63	45293.68	45855.45	45565.22	46148.91
78.5	45321.91	45338.23	45611.92	45632.63	45905.59	45928.78	45048.74	45632.42	45338.02	45905.80	45612.13	46202.69
79.5	45365.97	45383.17	45659.44	45681.02	45956.52	45980.56	45090.26	45680.81	45382.96	45956.73	45659.65	46257.04

QUANTITY: FREQUENCIES
UNITS : Wavenumbers
BAND (A-X)2 - 5

	P1	P2	Q1	Q2	R1	R2	P12	R12	Q12	Q21	P21	R21
0.5			39750.21		39754.12					39754.13		39761.91
1.5	39745.47	39630.65	39749.35	39638.44	39757.16	39650.13	39626.74	39638.43	39630.64	39757.17	39749.35	39768.84
2.5	39741.45	39630.29	39749.20	39641.98	39760.93	39657.57	39622.49	39641.98	39630.28	39760.93	39749.21	39776.49
3.5	39738.14	39630.57	39749.78	39646.16	39765.41	39665.64	39618.88	39646.15	39630.57	39765.43	39749.79	39784.86
4.5	39735.56	39631.50	39751.09	39650.98	39770.63	39674.36	39615.90	39650.96	39631.49	39770.64	39751.10	39793.96
5.5	39733.71	39633.06	39753.11	39656.44	39776.56	39683.71	39613.57	39656.42	39633.04	39776.58	39753.13	39803.78
6.5	39732.57	39635.26	39755.87	39662.54	39783.22	39693.70	39611.87	39662.52	39635.25	39783.24	39755.89	39814.32
7.5	39732.17	39638.10	39759.35	39669.27	39790.60	39704.33	39610.82	39669.25	39638.09	39790.63	39759.37	39825.59
8.5	39732.48	39641.59	39763.54	39676.65	39798.70	39715.59	39610.41	39676.63	39641.56	39798.73	39763.57	39837.57
9.5	39733.52	39645.71	39768.46	39684.66	39807.52	39727.50	39610.63	39684.64	39645.69	39807.55	39768.49	39850.27
10.5	39735.29	39650.48	39774.11	39693.32	39817.06	39740.04	39611.51	39693.29	39650.45	39817.09	39774.13	39863.70
11.5	39737.77	39655.89	39780.46	39702.62	39827.32	39753.23	39613.03	39702.59	39655.86	39827.36	39780.50	39877.84
12.5	39740.96	39661.94	39787.55	39712.57	39838.30	39767.05	39615.20	39712.53	39661.91	39838.34	39787.58	39892.69
13.5	39744.89	39668.64	39795.34	39723.15	39849.99	39781.52	39618.01	39723.11	39668.61	39850.03	39795.38	39908.25
14.5	39749.53	39675.99	39803.86	39734.38	39862.40	39796.63	39621.47	39734.34	39675.95	39862.44	39803.90	39924.54
15.5	39754.89	39683.98	39813.09	39746.26	39875.52	39812.38	39625.58	39746.22	39683.95	39875.57	39813.13	39941.53
16.5	39760.96	39692.63	39823.04	39758.79	39889.35	39828.78	39630.35	39758.74	39692.59	39889.40	39823.08	39959.23
17.5	39767.75	39701.92	39833.70	39771.96	39903.90	39845.82	39635.77	39771.91	39701.87	39903.95	39833.74	39977.64
18.5	39775.25	39711.86	39845.07	39785.78	39919.15	39863.51	39641.83	39785.73	39711.81	39919.20	39845.12	39996.76
19.5	39783.47	39722.46	39857.15	39800.25	39935.11	39881.85	39648.55	39800.20	39722.40	39935.17	39857.20	40016.59
20.5	39792.40	39733.71	39869.95	39815.38	39951.79	39900.83	39655.93	39815.32	39733.65	39951.85	39870.00	40037.12
21.5	39802.05	39745.61	39883.46	39831.15	39969.16	39920.46	39663.97	39831.09	39745.55	39969.22	39883.52	40058.36
22.5	39812.41	39758.17	39897.66	39847.57	39987.25	39940.74	39672.67	39847.51	39758.11	39987.31	39897.73	40080.30
23.5	39823.46	39771.38	39912.59	39864.66	40006.03	39961.67	39682.02	39864.59	39771.32	40006.10	39912.65	40102.93
24.5	39835.24	39785.26	39928.21	39882.39	40025.52	39983.25	39692.04	39882.32	39785.19	40025.59	39928.28	40126.27
25.5	39847.72	39799.79	39944.55	39900.78	40045.71	40005.48	39702.72	39900.71	39799.72	40045.78	39944.62	40150.31
26.5	39860.91	39814.98	39961.59	39919.82	40066.60	40028.36	39714.06	39919.75	39814.91	40066.68	39961.66	40175.04
27.5	39874.81	39830.83	39979.32	39939.52	40088.19	40051.90	39726.07	39939.45	39830.75	40088.27	39979.40	40200.47
28.5	39889.41	39847.34	39997.77	39959.88	40110.48	40076.09	39738.74	39959.80	39847.26	40110.55	39997.84	40226.60
29.5	39904.71	39864.51	40016.91	39980.91	40133.47	40100.93	39752.07	39980.82	39864.43	40133.55	40016.99	40253.41
30.5	39920.73	39882.35	40036.76	40002.58	40157.14	40126.43	39766.08	40002.50	39882.27	40157.23	40036.84	40280.92
31.5	39937.45	39900.84	40057.30	40024.92	40181.52	40152.59	39780.75	40024.83	39900.76	40181.61	40057.38	40309.13
32.5	39954.86	39920.01	40078.54	40047.92	40206.59	40179.40	39796.09	40047.83	39919.93	40206.68	40078.63	40338.02
33.5	39972.98	39939.84	40100.48	40071.58	40232.35	40206.86	39812.11	40071.48	39939.75	40232.45	40100.57	40367.59
34.5	39991.80	39960.34	40123.12	40095.90	40258.81	40234.99	39828.79	40095.80	39960.25	40258.91	40123.21	40397.86
35.5	40011.31	39981.50	40146.45	40120.89	40285.96	40263.77	39846.14	40120.79	39981.41	40286.05	40146.55	40428.81
36.5	40031.54	40003.34	40170.48	40146.53	40313.79	40293.20	39864.17	40146.43	40003.24	40313.89	40170.58	40460.45
37.5	40052.45	40025.84	40195.20	40172.84	40342.32	40323.30	39882.88	40172.74	40025.73	40342.42	40195.30	40492.77
38.5	40074.07	40049.00	40220.62	40199.82	40371.53	40354.05	39902.25	40199.71	40048.90	40371.64	40220.72	40525.77
39.5	40096.38	40072.84	40246.73	40227.46	40401.43	40385.46	39922.30	40227.35	40072.73	40401.54	40246.84	40559.46
40.5	40119.40	40097.35	40273.53	40255.76	40432.02	40417.54	39943.03	40255.65	40097.24	40432.13	40273.64	40593.83
41.5	40143.11	40122.52	40301.03	40284.73	40463.29	40450.27	39964.43	40284.62	40122.41	40463.41	40301.14	40628.88
42.5	40167.51	40148.38	40329.21	40314.37	40495.25	40483.66	39986.51	40314.25	40148.27	40495.37	40329.32	40664.61
43.5	40192.62	40174.90	40358.09	40344.67	40527.89	40517.71	40009.27	40344.55	40174.78	40528.01	40358.20	40701.02
44.5	40218.41	40202.09	40387.65	40375.64	40561.22	40552.42	40032.71	40375.52	40201.97	40561.34	40387.77	40738.10
45.5	40244.90	40229.96	40417.91	40407.27	40595.23	40587.80	40056.82	40407.15	40229.84	40595.35	40418.03	40775.86
46.5	40272.09	40258.50	40448.85	40439.57	40629.92	40623.83	40081.62	40439.45	40258.38	40630.05	40448.97	40814.30
47.5	40299.97	40287.71	40480.48	40472.55	40665.29	40660.52	40107.09	40472.42	40287.59	40665.42	40480.61	40853.41
48.5	40328.55	40317.60	40512.80	40506.18	40701.34	40697.87	40133.25	40506.05	40317.47	40701.48	40512.93	40893.20
49.5	40357.81	40348.16	40545.80	40540.48	40738.08	40735.88	40160.09	40540.35	40348.03	40738.21	40545.94	40933.66
50.5	40387.77	40379.40	40579.50	40575.46	40775.49	40774.56	40187.61	40575.32	40379.27	40775.63	40579.63	40974.79
51.5	40418.43	40411.31	40613.88	40611.10	40813.58	40813.89	40215.81	40610.96	40411.17	40813.72	40614.02	41016.60
52.5	40449.77	40443.89	40648.94	40647.41	40852.35	40853.89	40244.69	40647.27	40443.75	40852.50	40649.08	41059.07
53.5	40481.81	40477.16	40684.69	40684.39	40891.79	40894.54	40274.25	40684.24	40477.02	40891.94	40684.84	41102.22
54.5	40514.54	40511.09	40721.12	40722.03	40931.92	40935.86	40304.50	40721.88	40510.95	40932.07	40721.27	41146.04
55.5	40547.95	40545.70	40758.23	40760.35	40972.72	40977.84	40335.43	40760.20	40545.55	40972.87	40758.38	41190.52
56.5	40582.06	40581.00	40796.04	40799.33	41014.20	41020.48	40367.05	40799.18	40580.84	41014.35	40796.19	41235.67

57.5	40616.87	40616.96	40834.52	40838.98	41056.34	41063.78	40399.35	40838.83	40616.80	41056.50	40834.68	41281.49
58.5	40652.36	40653.60	40873.69	40879.31	41099.17	41107.73	40432.34	40879.15	40653.45	41099.33	40873.84	41327.98
59.5	40688.54	40690.93	40913.54	40920.30	41142.66	41152.36	40466.01	40920.13	40690.77	41142.83	40913.70	41375.13
60.5	40725.41	40728.92	40954.06	40961.95	41186.84	41197.64	40500.36	40961.79	40728.75	41187.00	40954.23	41422.95
61.5	40762.96	40767.59	40995.27	41004.28	41231.68	41243.58	40535.40	41004.12	40767.43	41231.85	40995.44	41471.43
62.5	40801.21	40806.94	41037.17	41047.28	41277.20	41290.18	40571.13	41047.11	40806.77	41277.37	41037.34	41520.57
63.5	40840.15	40846.97	41079.74	41090.95	41323.38	41337.44	40607.54	41090.77	40846.80	41323.55	41079.91	41570.38
64.5	40879.78	40887.67	41122.99	41135.28	41370.24	41385.36	40644.64	41135.11	40887.50	41370.42	41123.16	41620.85
65.5	40920.09	40929.05	41166.93	41180.29	41417.77	41433.94	40682.43	41180.11	40928.88	41417.95	41167.10	41671.98
66.5	40961.09	40971.12	41211.54	41225.96	41465.97	41483.18	40720.90	41225.78	40970.94	41466.15	41211.71	41723.78
67.5	41002.78	41013.86	41256.83	41272.30	41514.84	41533.08	40760.06	41272.12	41013.68	41515.02	41257.01	41776.23
68.5	41045.16	41057.27	41302.80	41319.31	41564.38	41583.63	40799.91	41319.13	41057.09	41564.57	41302.98	41829.34
69.5	41088.23	41101.37	41349.45	41366.99	41614.59	41634.86	40840.45	41366.80	41101.18	41614.77	41349.63	41883.13
70.5	41131.98	41146.13	41396.77	41415.34	41665.46	41686.73	40881.66	41415.15	41145.95	41665.66	41396.95	41937.55
71.5	41176.41	41191.59	41444.77	41464.36	41717.00	41739.26	40923.57	41464.16	41191.40	41717.20	41444.96	41992.64
72.5	41221.54	41237.71	41493.45	41514.04	41769.21	41792.46	40966.18	41513.84	41237.52	41769.41	41493.64	42048.39
73.5	41267.35	41284.52	41542.80	41564.39	41822.09	41846.31	41009.46	41564.20	41284.32	41822.29	41543.00	42104.79
74.5	41313.84	41332.01	41592.84	41615.41	41875.63	41900.81	41053.43	41615.21	41331.80	41875.83	41593.04	42161.84
75.5	41361.03	41380.17	41643.55	41667.11	41929.84	41955.98	41098.10	41666.90	41379.97	41930.04	41643.75	42219.56
76.5	41408.90	41429.01	41694.93	41719.46	41984.71	42011.80	41143.45	41719.26	41428.80	41984.91	41695.13	42277.93
77.5	41457.45	41478.53	41746.99	41772.49	42040.24	42068.29	41189.49	41772.28	41478.32	42040.45	41747.20	42336.95
78.5	41506.69	41528.73	41799.72	41826.18	42096.45	42125.43	41236.22	41825.97	41528.52	42096.66	41799.93	42396.63
79.5	41556.61	41579.60	41853.13	41880.55	42153.30	42183.21	41283.64	41880.33	41579.39	42153.52	41853.34	42456.96

QUANTITY: FREQUENCIES
UNITS : Wavenumbers
BAND (A-X)3 - 5

	P1	P2	Q1	Q2	R1	R2	P12	R12	Q12	Q21	P21	R21
0.5			42026.61		42030.48					42030.49		42038.20
1.5	42021.88	41907.01	42025.71	41914.73	42033.45	41926.30	41903.15	41914.72	41907.01	42033.46	42025.71	42045.01
2.5	42017.81	41906.58	42025.49	41918.16	42037.10	41933.59	41898.86	41918.15	41906.57	42037.11	42025.50	42052.51
3.5	42014.43	41906.75	42025.95	41922.18	42041.44	41941.48	41895.16	41922.17	41906.74	42041.45	42025.96	42060.70
4.5	42011.73	41907.52	42027.11	41926.81	42046.46	41949.96	41892.07	41926.80	41907.51	42046.47	42027.12	42069.56
5.5	42009.73	41908.89	42028.95	41932.04	42052.16	41959.05	41889.59	41932.02	41908.88	42052.18	42028.96	42079.12
6.5	42008.41	41910.86	42031.47	41937.88	42058.56	41968.73	41887.70	41937.86	41910.85	42058.58	42031.49	42089.36
7.5	42007.77	41913.45	42034.69	41944.30	42065.63	41979.02	41886.42	41944.28	41913.42	42065.66	42034.71	42100.28
8.5	42007.83	41916.62	42038.58	41951.34	42073.40	41989.91	41885.74	41951.31	41916.60	42073.42	42038.60	42111.89
9.5	42008.55	41920.40	42043.16	41958.98	42081.84	42001.39	41885.67	41958.95	41920.38	42081.87	42043.18	42124.17
10.5	42009.98	41924.79	42048.42	41967.21	42090.96	42013.48	41886.20	41967.18	41924.76	42090.99	42048.45	42137.13
11.5	42012.08	41929.78	42054.36	41976.06	42100.76	42026.17	41887.34	41976.03	41929.75	42100.79	42054.39	42150.78
12.5	42014.86	41935.38	42060.98	41985.51	42111.25	42039.46	41889.09	41985.48	41935.35	42111.28	42061.02	42165.10
13.5	42018.33	41941.59	42068.29	41995.56	42122.40	42053.36	41891.45	41995.52	41941.55	42122.44	42068.32	42180.09
14.5	42022.48	41948.40	42076.27	42006.22	42134.24	42067.86	41894.42	42006.18	41948.36	42134.28	42076.30	42195.77
15.5	42027.30	41955.82	42084.93	42017.50	42146.76	42082.97	41897.99	42017.45	41955.78	42146.80	42084.97	42212.11
16.5	42032.80	41963.86	42094.27	42029.37	42159.94	42098.68	41902.19	42029.32	41963.82	42159.98	42094.31	42229.13
17.5	42038.99	41972.50	42104.28	42041.86	42173.80	42115.00	41907.00	42041.81	41972.46	42173.85	42104.33	42246.82
18.5	42045.84	41981.77	42114.97	42054.96	42188.33	42131.93	41912.42	42054.91	41981.71	42188.38	42115.02	42265.18
19.5	42053.38	41991.64	42126.33	42068.67	42203.53	42149.46	41918.46	42068.61	41991.58	42203.59	42126.38	42284.21
20.5	42061.58	42002.13	42138.36	42082.99	42219.41	42167.61	41925.11	42082.94	42002.07	42219.46	42138.42	42303.90
21.5	42070.46	42013.23	42151.07	42097.93	42235.94	42186.36	41932.39	42097.87	42013.17	42236.00	42151.13	42324.27
22.5	42080.02	42024.95	42164.45	42113.48	42253.15	42205.73	41940.29	42113.42	42024.89	42253.21	42164.51	42345.29
23.5	42090.25	42037.29	42178.49	42129.65	42271.02	42225.71	41948.80	42129.58	42037.23	42271.09	42178.55	42366.97
24.5	42101.15	42050.25	42193.21	42146.43	42289.56	42246.30	41957.95	42146.36	42050.18	42289.63	42193.27	42389.32
25.5	42112.71	42063.83	42208.59	42163.83	42308.76	42267.51	41967.71	42163.76	42063.76	42308.83	42208.66	42412.34
26.5	42124.95	42078.03	42224.64	42181.85	42328.63	42289.32	41978.10	42181.77	42077.96	42328.70	42224.71	42436.00
27.5	42137.86	42092.85	42241.35	42200.48	42349.14	42311.75	41989.12	42200.40	42092.78	42349.22	42241.42	42460.32
28.5	42151.44	42108.29	42258.72	42219.73	42370.33	42334.80	42000.76	42219.66	42108.21	42370.41	42258.80	42485.30
29.5	42165.67	42124.36	42276.76	42239.61	42392.18	42358.46	42013.03	42239.53	42124.28	42392.26	42276.84	42510.94
30.5	42180.58	42141.05	42295.46	42260.11	42414.67	42382.74	42025.93	42260.02	42140.98	42414.76	42295.55	42537.23
31.5	42196.15	42158.38	42314.82	42281.23	42437.83	42407.64	42039.46	42281.14	42158.29	42437.91	42314.91	42564.18
32.5	42212.38	42176.32	42334.85	42302.97	42461.64	42433.15	42053.62	42302.88	42176.23	42461.73	42334.94	42591.77
33.5	42229.28	42194.89	42355.53	42325.33	42486.11	42459.29	42068.41	42325.24	42194.80	42486.20	42355.62	42620.01
34.5	42246.85	42214.09	42376.87	42348.32	42511.23	42486.04	42083.84	42348.23	42214.00	42511.33	42376.96	42648.91
35.5	42265.07	42233.92	42398.88	42371.93	42537.00	42513.41	42099.90	42371.84	42233.83	42537.10	42398.97	42678.45
36.5	42283.96	42254.38	42421.53	42396.17	42563.43	42541.39	42116.59	42396.07	42254.29	42563.53	42421.63	42708.63
37.5	42303.50	42275.47	42444.84	42421.03	42590.50	42570.00	42133.92	42420.93	42275.37	42590.61	42444.94	42739.47
38.5	42323.71	42297.19	42468.80	42446.52	42618.23	42599.23	42151.89	42446.41	42297.09	42618.34	42468.91	42770.95
39.5	42344.57	42319.54	42493.43	42472.63	42646.60	42629.07	42170.49	42472.52	42319.43	42646.71	42493.54	42803.07
40.5	42366.09	42342.52	42518.70	42499.37	42675.63	42659.54	42189.73	42499.26	42342.41	42675.73	42518.81	42835.84
41.5	42388.28	42366.13	42544.64	42526.73	42705.30	42690.63	42209.60	42526.63	42366.02	42705.41	42544.75	42869.25
42.5	42411.12	42390.38	42571.21	42554.73	42735.61	42722.34	42230.12	42554.61	42390.27	42735.73	42571.33	42903.29
43.5	42434.62	42415.26	42598.45	42583.35	42766.58	42754.68	42251.28	42583.23	42415.14	42766.70	42598.57	42937.98
44.5	42458.77	42440.77	42626.34	42612.60	42798.18	42787.63	42273.07	42612.48	42440.66	42798.30	42626.45	42973.30
45.5	42483.59	42466.92	42654.87	42642.48	42830.43	42821.20	42295.51	42642.35	42466.80	42830.55	42654.99	43009.27
46.5	42509.05	42493.70	42684.05	42672.98	42863.33	42855.40	42318.58	42672.86	42493.58	42863.45	42684.18	43045.87
47.5	42535.17	42521.12	42713.89	42704.12	42896.86	42890.22	42342.30	42703.99	42520.99	42896.99	42714.02	43083.11
48.5	42561.95	42549.17	42744.37	42735.88	42931.04	42925.65	42366.66	42735.75	42549.04	42931.18	42744.50	43120.98
49.5	42589.38	42577.86	42775.50	42768.27	42965.86	42961.71	42391.66	42768.13	42577.73	42965.99	42775.64	43159.49
50.5	42617.47	42607.18	42807.28	42801.29	43001.32	42998.40	42417.30	42801.16	42607.05	43001.46	42807.41	43198.64
51.5	42646.21	42637.14	42839.71	42834.95	43037.42	43035.71	42443.59	42834.80	42637.00	43037.56	42839.85	43238.41
52.5	42675.61	42667.74	42872.78	42869.23	43074.16	43073.63	42470.52	42869.08	42667.60	43074.31	42872.92	43278.82
53.5	42705.65	42698.97	42906.50	42904.13	43111.54	43112.18	42498.10	42903.98	42698.83	43111.69	42906.65	43319.86
54.5	42736.35	42730.84	42940.86	42939.67	43149.56	43151.35	42526.32	42939.52	42730.69	43149.71	42941.01	43361.53
55.5	42767.70	42763.34	42975.88	42975.84	43188.21	43191.14	42555.18	42975.69	42763.20	43188.36	42976.02	43403.82
56.5	42799.70	42796.49	43011.53	43012.64	43227.50	43231.56	42584.69	43012.48	42796.34	43227.66	43011.68	43446.75

57.5	42832.36	42830.27	43047.83	43050.07	43267.43	43272.60	42614.84	43049.91	42830.11	43267.58	43047.98	43490.31
58.5	42865.66	42864.68	43084.77	43088.13	43307.99	43314.25	42645.64	43087.97	42864.53	43308.15	43084.93	43534.50
59.5	42899.62	42899.75	43122.36	43126.82	43349.18	43356.53	42677.09	43126.65	42899.59	43349.35	43122.52	43579.30
60.5	42934.23	42935.44	43160.58	43166.13	43391.01	43399.43	42709.18	43165.96	42935.27	43391.18	43160.75	43624.74
61.5	42969.48	42971.77	43199.45	43206.08	43433.48	43442.95	42741.92	43205.91	42971.60	43433.64	43199.62	43670.80
62.5	43005.39	43008.74	43238.96	43246.66	43476.57	43487.09	42775.30	43246.48	43008.57	43476.74	43239.13	43717.49
63.5	43041.95	43046.34	43279.12	43287.86	43520.30	43531.86	42809.34	43287.69	43046.17	43520.47	43279.29	43764.80
64.5	43079.15	43084.59	43319.91	43329.70	43564.66	43577.24	42844.02	43329.53	43084.42	43564.84	43320.08	43812.73
65.5	43117.01	43123.48	43361.35	43372.17	43609.66	43623.24	42879.34	43371.99	43123.30	43609.84	43361.52	43861.29
66.5	43155.52	43163.00	43403.42	43415.26	43655.28	43669.87	42915.32	43415.08	43162.82	43655.46	43403.60	43910.47
67.5	43194.66	43203.16	43446.13	43458.99	43701.53	43717.11	42951.94	43458.81	43202.98	43701.72	43446.31	43960.27
68.5	43234.47	43243.96	43489.49	43503.35	43748.41	43764.98	42989.21	43503.16	43243.78	43748.60	43489.67	44010.69
69.5	43274.92	43285.40	43533.48	43548.33	43795.93	43813.46	43027.13	43548.14	43285.21	43796.12	43533.66	44061.73
70.5	43316.01	43327.48	43578.11	43593.95	43844.06	43862.56	43065.70	43593.75	43327.29	43844.26	43578.30	44113.38
71.5	43357.75	43370.19	43623.38	43640.19	43892.83	43912.28	43104.91	43639.99	43370.00	43893.03	43623.57	44165.66
72.5	43400.14	43413.55	43669.28	43687.06	43942.23	43962.62	43144.78	43686.86	43413.35	43942.43	43669.48	44218.55
73.5	43443.18	43457.54	43715.82	43734.56	43992.25	44013.58	43185.29	43734.36	43457.34	43992.45	43716.02	44272.06
74.5	43486.87	43502.17	43763.00	43782.69	44042.90	44065.15	43226.45	43782.48	43501.97	44043.10	43763.20	44326.18
75.5	43531.20	43547.44	43810.82	43831.44	44094.17	44117.35	43268.26	43831.24	43547.23	44094.38	43811.02	44380.93
76.5	43576.17	43593.34	43859.27	43880.83	44146.07	44170.16	43310.72	43880.63	43593.14	44146.28	43859.47	44436.28
77.5	43621.79	43639.90	43908.36	43930.84	44198.59	44223.59	43353.83	43930.63	43639.69	44198.80	43908.56	44492.25
78.5	43668.06	43687.08	43958.07	43981.48	44251.74	44277.63	43397.59	43981.27	43686.87	44251.95	43958.29	44548.84
79.5	43714.96	43734.90	44008.43	44032.75	44305.52	44332.29	43441.99	44032.54	43734.69	44305.73	44008.64	44606.03

QUANTITY: FREQUENCIES
UNITS : Wavenumbers
BAND (A-X)4 - 5

	P1	P2	Q1	Q2	R1	R2	P12	R12	Q12	Q21	P21	R21
0.5			44269.91		44273.75					44273.75		44281.38
1.5	44265.18	44150.27	44268.97	44157.91	44276.63	44169.38	44146.45	44157.91	44150.27	44276.64	44268.98	44288.08
2.5	44261.07	44149.77	44268.67	44161.23	44280.17	44176.52	44142.12	44161.22	44149.76	44280.18	44268.68	44295.43
3.5	44257.61	44149.82	44269.03	44165.11	44284.36	44184.21	44138.35	44165.09	44149.81	44284.37	44269.04	44303.42
4.5	44254.81	44150.44	44270.03	44169.54	44289.19	44192.46	44135.15	44169.53	44150.43	44289.20	44270.04	44312.06
5.5	44252.65	44151.62	44271.68	44174.54	44294.66	44201.28	44132.51	44174.52	44151.61	44294.68	44271.69	44321.35
6.5	44251.14	44153.36	44273.97	44180.11	44300.79	44210.66	44130.43	44180.09	44153.35	44300.81	44273.99	44331.29
7.5	44250.27	44155.67	44276.92	44186.23	44307.56	44220.60	44128.92	44186.21	44155.66	44307.59	44276.94	44341.86
8.5	44250.05	44158.55	44280.50	44192.92	44314.98	44231.11	44127.98	44192.90	44158.52	44315.00	44280.53	44353.09
9.5	44250.48	44161.98	44284.74	44200.18	44323.04	44242.17	44127.59	44200.15	44161.96	44323.06	44284.76	44364.95
10.5	44251.56	44165.99	44289.62	44208.00	44331.74	44253.80	44127.79	44207.96	44165.96	44331.77	44289.64	44377.45
11.5	44253.28	44170.56	44295.14	44216.38	44341.08	44266.00	44128.54	44216.35	44170.53	44341.11	44295.17	44390.61
12.5	44255.64	44175.70	44301.30	44225.34	44351.07	44278.75	44129.87	44225.30	44175.67	44351.11	44301.34	44404.39
13.5	44258.65	44181.41	44308.11	44234.85	44361.69	44292.07	44131.77	44234.81	44181.38	44361.73	44308.15	44418.81
14.5	44262.30	44187.69	44315.55	44244.94	44372.95	44305.96	44134.24	44244.90	44187.65	44372.99	44315.59	44433.88
15.5	44266.59	44194.54	44323.64	44255.60	44384.86	44320.42	44137.28	44255.55	44194.50	44384.90	44323.68	44449.57
16.5	44271.52	44201.96	44332.37	44266.83	44397.39	44335.45	44140.90	44266.78	44201.92	44397.44	44332.41	44465.90
17.5	44277.09	44209.96	44341.74	44278.63	44410.57	44351.04	44145.10	44278.58	44209.91	44410.62	44341.79	44482.86
18.5	44283.30	44218.53	44351.73	44291.00	44424.37	44367.20	44149.88	44290.95	44218.48	44424.42	44351.79	44500.46
19.5	44290.14	44227.68	44362.37	44303.95	44438.81	44383.94	44155.22	44303.89	44227.62	44438.86	44362.42	44518.68
20.5	44297.62	44237.40	44373.64	44317.47	44453.88	44401.24	44161.15	44317.41	44237.35	44453.94	44373.70	44537.54
21.5	44305.74	44247.70	44385.55	44331.56	44469.57	44419.11	44167.66	44331.50	44247.64	44469.64	44385.61	44557.02
22.5	44314.50	44258.58	44398.08	44346.23	44485.90	44437.57	44174.76	44346.17	44258.52	44485.96	44398.14	44577.13
23.5	44323.88	44270.04	44411.24	44361.48	44502.86	44456.59	44182.44	44361.41	44269.98	44502.93	44411.30	44597.85
24.5	44333.90	44282.09	44425.04	44377.30	44520.44	44476.18	44190.70	44377.23	44282.02	44520.51	44425.11	44619.21
25.5	44344.55	44294.70	44439.46	44393.71	44538.64	44496.35	44199.55	44393.64	44294.63	44538.71	44439.54	44641.18
26.5	44355.83	44307.91	44454.52	44410.70	44557.48	44517.10	44208.98	44410.62	44307.84	44557.55	44454.59	44663.78
27.5	44367.74	44321.70	44470.20	44428.26	44576.92	44538.42	44219.00	44428.18	44321.63	44577.00	44470.27	44686.99
28.5	44380.28	44336.07	44486.50	44446.40	44597.00	44560.32	44229.61	44446.32	44335.99	44597.08	44486.58	44710.83
29.5	44393.45	44351.03	44503.43	44465.13	44617.70	44582.79	44240.80	44465.05	44350.95	44617.78	44503.51	44735.27
30.5	44407.25	44366.58	44520.98	44484.44	44639.00	44605.84	44252.60	44484.36	44366.49	44639.09	44521.07	44760.34
31.5	44421.67	44382.70	44539.16	44504.33	44660.94	44629.48	44264.98	44504.25	44382.62	44661.02	44539.24	44786.02
32.5	44436.71	44399.43	44557.95	44524.81	44683.49	44653.70	44277.95	44524.73	44399.34	44683.58	44558.04	44812.31
33.5	44452.39	44416.74	44577.38	44545.88	44706.65	44678.48	44291.52	44545.78	44416.65	44706.74	44577.46	44839.21
34.5	44468.69	44434.64	44597.41	44567.52	44730.43	44703.86	44305.68	44567.42	44434.54	44730.52	44597.51	44866.73
35.5	44485.61	44453.12	44618.07	44589.75	44754.82	44729.80	44320.44	44589.66	44453.02	44754.92	44618.16	44894.85
36.5	44503.15	44472.20	44639.35	44612.57	44779.83	44756.34	44335.79	44612.47	44472.11	44779.93	44639.45	44923.58
37.5	44521.32	44491.87	44661.24	44635.97	44805.45	44783.45	44351.74	44635.87	44491.77	44805.55	44661.34	44952.92
38.5	44540.11	44512.13	44683.75	44659.96	44831.68	44811.14	44368.29	44659.86	44512.03	44831.79	44683.85	44982.86
39.5	44559.52	44532.99	44706.88	44684.54	44858.52	44839.41	44385.43	44684.43	44532.88	44858.63	44706.98	45013.41
40.5	44579.55	44554.43	44730.62	44709.71	44885.97	44868.27	44403.18	44709.60	44554.32	44886.08	44730.73	45044.57
41.5	44600.19	44576.47	44754.98	44735.47	44914.03	44897.71	44421.52	44735.35	44576.36	44914.14	44755.09	45076.32
42.5	44621.46	44599.11	44779.95	44761.81	44942.69	44927.73	44440.46	44761.69	44599.00	44942.81	44780.06	45108.68
43.5	44643.35	44622.34	44805.53	44788.74	44971.97	44958.34	44460.01	44788.63	44622.22	44972.09	44805.64	45141.64
44.5	44665.85	44646.16	44831.73	44816.26	45001.84	44989.52	44480.15	44816.14	44646.05	45001.96	44831.84	45175.20
45.5	44688.98	44670.59	44858.53	44844.38	45032.33	45021.29	44500.90	44844.25	44670.46	45032.45	44858.65	45209.36
46.5	44712.71	44695.60	44885.95	44873.07	45063.42	45053.64	44522.24	44872.95	44695.48	45063.54	44886.07	45244.12
47.5	44737.07	44721.21	44913.98	44902.36	45095.11	45086.58	44544.20	44902.23	44721.09	45095.24	44914.11	45279.47
48.5	44762.04	44747.42	44942.62	44932.24	45127.40	45120.09	44566.75	44932.11	44747.29	45127.54	44942.75	45315.42
49.5	44787.63	44774.22	44971.86	44962.71	45160.30	45154.20	44589.91	44962.58	44774.09	45160.44	44972.00	45351.97
50.5	44813.83	44801.62	45001.72	44993.77	45193.80	45188.88	44613.66	44993.64	44801.49	45193.94	45001.86	45389.11
51.5	44840.65	44829.62	45032.19	45025.42	45227.90	45224.14	44638.03	45025.28	44829.48	45228.04	45032.33	45426.85
52.5	44868.09	44858.21	45063.26	45057.66	45262.60	45259.99	44663.00	45057.52	44858.07	45262.75	45063.40	45465.18
53.5	44896.13	44887.41	45094.94	45090.49	45297.90	45296.42	44688.57	45090.34	44887.27	45298.05	45095.09	45504.10
54.5	44924.79	44917.20	45127.22	45123.91	45333.80	45333.44	44714.75	45123.77	44917.05	45333.95	45127.37	45543.61
55.5	44954.06	44947.59	45160.12	45157.93	45370.30	45371.04	44741.54	45157.77	44947.44	45370.45	45160.27	45583.71
56.5	44983.95	44978.57	45193.62	45192.53	45407.39	45409.21	44768.93	45192.37	44978.42	45407.55	45193.77	45624.41

57.5	45014.45	45010.16	45227.72	45227.72	45445.08	45447.98	44796.93	45227.56	45010.00	45445.23	45227.88	45665.70
58.5	45045.55	45042.34	45262.42	45263.51	45483.37	45487.32	44825.53	45263.35	45042.18	45483.53	45262.58	45707.56
59.5	45077.27	45075.13	45297.74	45299.88	45522.25	45527.25	44854.74	45299.71	45074.96	45522.41	45297.90	45750.02
60.5	45109.61	45108.50	45333.64	45336.84	45561.73	45567.75	44884.56	45336.68	45108.34	45561.89	45333.81	45793.06
61.5	45142.55	45142.48	45370.16	45374.40	45601.80	45608.84	44914.98	45374.23	45142.32	45601.96	45370.33	45836.70
62.5	45176.11	45177.06	45407.29	45412.55	45642.46	45650.51	44946.02	45412.38	45176.89	45642.63	45407.45	45880.91
63.5	45210.27	45212.23	45445.01	45451.28	45683.72	45692.77	44977.66	45451.11	45212.06	45683.89	45445.18	45925.71
64.5	45245.04	45248.01	45483.33	45490.61	45725.57	45735.60	45009.91	45490.43	45247.84	45725.75	45483.50	45971.09
65.5	45280.43	45284.38	45522.25	45530.52	45768.01	45779.01	45042.76	45530.34	45284.21	45768.19	45522.43	46017.05
66.5	45316.42	45321.36	45561.77	45571.03	45811.04	45823.01	45076.23	45570.85	45321.18	45811.22	45561.95	46063.61
67.5	45353.02	45358.93	45601.90	45612.13	45854.67	45867.58	45110.30	45611.95	45358.75	45854.85	45602.08	46110.73
68.5	45390.23	45397.10	45642.63	45653.82	45898.88	45912.73	45144.98	45653.63	45396.91	45899.07	45642.81	46158.45
69.5	45428.05	45435.87	45683.95	45696.09	45943.69	45958.48	45180.27	45695.91	45435.68	45943.88	45684.13	46206.74
70.5	45466.48	45475.23	45725.87	45738.96	45989.08	46004.78	45216.16	45738.77	45475.05	45989.27	45726.05	46255.60
71.5	45505.52	45515.21	45768.39	45782.41	46035.05	46051.68	45252.68	45782.21	45515.02	46035.25	45768.58	46305.05
72.5	45545.16	45555.77	45811.50	45826.45	46081.63	46099.15	45289.79	45826.26	45555.57	46081.82	45811.70	46355.08
73.5	45585.40	45596.93	45855.22	45871.09	46128.78	46147.20	45327.51	45870.89	45596.74	46128.98	45855.41	46405.68
74.5	45626.26	45638.70	45899.53	45916.30	46176.52	46195.83	45365.84	45916.10	45638.50	46176.72	45899.73	46456.86
75.5	45667.73	45681.06	45944.44	45962.12	46224.84	46245.04	45404.79	45961.91	45680.86	46225.05	45944.64	46508.62
76.5	45709.79	45724.02	45989.95	46008.52	46273.76	46294.82	45444.34	46008.31	45723.82	46273.97	45990.15	46560.95
77.5	45752.46	45767.59	46036.05	46055.50	46323.25	46345.18	45484.50	46055.29	45767.38	46323.46	46036.25	46613.84
78.5	45795.75	45811.74	46082.73	46103.07	46373.34	46396.12	45525.27	46102.86	45811.53	46373.55	46082.95	46667.32
79.5	45839.63	45856.49	46130.02	46151.24	46424.00	46447.63	45566.65	46151.02	45856.28	46424.21	46130.23	46721.37

QUANTITY: FREQUENCIES
UNITS : Wavenumbers
BAND (A-X)4 - 6

	P1	P2	Q1	Q2	R1	R2	P12	R12	Q12	Q21	P21	R21
0.5			42533.84		42537.68					42537.68		42545.31
1.5	42529.16	42414.53	42532.95	42422.17	42540.61	42433.63	42410.70	42422.16	42414.52	42540.62	42532.96	42552.06
2.5	42525.14	42414.11	42532.74	42425.57	42544.24	42440.86	42406.46	42425.57	42414.10	42544.25	42532.75	42559.50
3.5	42521.80	42414.30	42533.22	42429.58	42548.55	42448.68	42402.82	42429.57	42414.29	42548.56	42533.23	42567.61
4.5	42519.16	42415.08	42534.38	42434.18	42553.53	42457.10	42399.79	42434.16	42415.07	42553.55	42534.39	42576.41
5.5	42517.19	42416.46	42536.21	42439.38	42559.20	42466.12	42397.35	42439.36	42416.45	42559.22	42536.23	42585.89
6.5	42515.90	42418.44	42538.73	42445.18	42565.55	42475.73	42395.50	42445.16	42418.42	42565.57	42538.75	42596.05
7.5	42515.29	42421.02	42541.94	42451.58	42572.58	42485.95	42394.27	42451.55	42421.00	42572.61	42541.96	42606.88
8.5	42515.38	42424.20	42545.82	42458.58	42580.30	42496.76	42393.63	42458.55	42424.18	42580.32	42545.84	42618.40
9.5	42516.13	42427.98	42550.39	42466.18	42588.68	42508.17	42393.59	42466.15	42427.96	42588.71	42550.41	42630.60
10.5	42517.57	42432.37	42555.63	42474.38	42597.75	42520.18	42394.17	42474.35	42432.34	42597.78	42555.66	42643.46
11.5	42519.69	42437.36	42561.55	42483.18	42607.49	42532.80	42395.34	42483.15	42437.33	42607.52	42561.58	42657.02
12.5	42522.48	42442.95	42568.15	42492.59	42617.91	42546.00	42397.13	42492.55	42442.92	42617.95	42568.18	42671.23
13.5	42525.96	42449.16	42575.43	42502.59	42629.00	42559.82	42399.51	42502.55	42449.12	42629.04	42575.46	42686.13
14.5	42530.12	42455.96	42583.38	42513.21	42640.77	42574.23	42402.52	42513.17	42455.92	42640.81	42583.41	42701.69
15.5	42534.94	42463.37	42592.00	42524.43	42653.21	42589.26	42406.12	42524.39	42463.33	42653.26	42592.04	42717.93
16.5	42540.45	42471.39	42601.30	42536.26	42666.33	42604.88	42410.34	42536.21	42471.35	42666.38	42601.35	42734.83
17.5	42546.63	42480.03	42611.28	42548.70	42680.11	42621.11	42415.17	42548.64	42479.98	42680.16	42611.32	42752.40
18.5	42553.48	42489.27	42621.92	42561.73	42694.55	42637.94	42420.61	42561.68	42489.22	42694.61	42621.97	42770.64
19.5	42561.01	42499.12	42633.23	42575.39	42709.67	42655.38	42426.66	42575.34	42499.07	42709.73	42633.29	42789.55
20.5	42569.20	42509.59	42645.22	42589.65	42725.46	42673.43	42433.34	42589.59	42509.53	42725.52	42645.27	42809.12
21.5	42578.07	42520.67	42657.88	42604.53	42741.90	42692.08	42440.63	42604.46	42520.61	42741.96	42657.93	42829.34
22.5	42587.61	42532.36	42671.19	42620.01	42759.02	42711.35	42448.54	42619.95	42532.30	42759.08	42671.25	42850.24
23.5	42597.82	42544.67	42685.18	42636.11	42776.80	42731.22	42457.07	42636.05	42544.61	42776.86	42685.24	42871.79
24.5	42608.69	42557.60	42699.84	42652.82	42795.23	42751.70	42466.21	42652.75	42557.54	42795.30	42699.90	42894.00
25.5	42620.23	42571.14	42715.15	42670.15	42814.33	42772.79	42475.98	42670.08	42571.07	42814.40	42715.22	42916.87
26.5	42632.44	42585.31	42731.13	42688.09	42834.09	42794.50	42486.38	42688.02	42585.24	42834.16	42731.20	42940.39
27.5	42645.32	42600.09	42747.77	42706.65	42854.50	42816.81	42497.39	42706.57	42600.02	42854.57	42747.84	42964.56
28.5	42658.85	42615.50	42765.07	42725.83	42875.57	42839.75	42509.03	42725.75	42615.42	42875.65	42765.14	42989.39
29.5	42673.05	42631.52	42783.03	42745.63	42897.30	42863.29	42521.30	42745.54	42631.44	42897.38	42783.11	43014.88
30.5	42687.92	42648.17	42801.66	42766.03	42919.68	42887.44	42534.19	42765.95	42648.09	42919.76	42801.74	43041.01
31.5	42703.45	42665.44	42820.93	42787.06	42942.71	42912.21	42547.71	42786.98	42665.35	42942.80	42821.02	43067.80
32.5	42719.63	42683.33	42840.87	42808.72	42966.40	42937.60	42561.86	42808.63	42683.25	42966.49	42840.96	43095.23
33.5	42736.48	42701.86	42861.47	42830.99	42990.74	42963.60	42576.64	42830.90	42701.77	42990.84	42861.56	43123.30
34.5	42754.00	42721.00	42882.72	42853.88	43015.73	42990.22	42592.05	42853.79	42720.91	43015.83	42882.81	43152.03
35.5	42772.16	42740.77	42904.62	42877.40	43041.38	43017.45	42608.09	42877.30	42740.67	43041.47	42904.71	43181.40
36.5	42790.98	42761.16	42927.18	42901.53	43067.66	43045.30	42624.75	42901.43	42761.07	43067.77	42927.28	43211.41
37.5	42810.47	42782.19	42950.39	42926.29	43094.60	43073.77	42642.06	42926.19	42782.09	43094.70	42950.49	43242.07
38.5	42830.61	42803.84	42974.26	42951.67	43122.19	43102.85	42659.99	42951.57	42803.74	43122.29	42974.36	43273.37
39.5	42851.41	42826.13	42998.77	42977.68	43150.41	43132.55	42678.57	42977.57	42826.02	43150.52	42998.88	43305.30
40.5	42872.87	42849.03	43023.94	43004.30	43179.29	43162.87	42697.77	43004.20	42848.92	43179.40	43024.05	43337.89
41.5	42894.98	42872.57	43049.76	43031.56	43208.81	43193.81	42717.61	43031.45	42872.46	43208.93	43049.87	43371.11
42.5	42917.74	42896.74	43076.23	43059.44	43238.98	43225.36	42738.09	43059.32	42896.63	43239.09	43076.34	43404.96
43.5	42941.17	42921.54	43103.34	43087.94	43269.79	43257.54	42759.21	43087.82	42921.42	43269.90	43103.46	43439.46
44.5	42965.24	42946.97	43131.11	43117.07	43301.23	43290.33	42780.95	43116.95	42946.86	43301.35	43131.23	43474.59
45.5	42989.97	42973.04	43159.52	43146.82	43333.32	43323.74	42803.34	43146.70	42972.91	43333.45	43159.64	43510.35
46.5	43015.35	42999.73	43188.59	43177.20	43366.05	43357.77	42826.37	43177.07	42999.61	43366.18	43188.71	43546.75
47.5	43041.38	43027.05	43218.29	43208.20	43399.42	43392.42	42850.04	43208.08	43026.93	43399.55	43218.41	43583.78
48.5	43068.07	43055.01	43248.64	43239.84	43433.43	43427.69	42874.34	43239.70	43054.88	43433.56	43248.77	43621.45
49.5	43095.41	43083.60	43279.64	43272.09	43468.08	43463.58	42899.29	43271.96	43083.47	43468.21	43279.77	43659.75
50.5	43123.39	43112.83	43311.29	43304.98	43503.37	43500.09	42924.87	43304.84	43112.70	43503.50	43311.42	43698.68
51.5	43152.04	43142.69	43343.57	43338.48	43539.29	43537.21	42951.09	43338.34	43142.55	43539.43	43343.71	43738.23
52.5	43181.33	43173.18	43376.50	43372.63	43575.85	43574.95	42977.96	43372.48	43173.04	43575.99	43376.64	43778.42
53.5	43211.27	43204.30	43410.08	43407.39	43613.04	43613.32	43005.47	43407.24	43204.16	43613.19	43410.22	43819.24
54.5	43241.86	43236.06	43444.29	43442.78	43650.87	43652.30	43033.62	43442.63	43235.91	43651.02	43444.44	43860.68
55.5	43273.10	43268.46	43479.16	43478.80	43689.34	43691.91	43062.41	43478.64	43268.31	43689.49	43479.30	43902.75
56.5	43304.99	43301.48	43514.66	43515.44	43728.43	43732.13	43091.84	43515.28	43301.34	43728.59	43514.81	43945.45

57.5	43337.53	43335.15	43550.80	43552.71	43768.16	43772.97	43121.92	43552.55	43334.99	43768.32	43550.96	43988.78
58.5	43370.71	43369.45	43587.58	43590.61	43808.53	43814.42	43152.63	43590.45	43369.29	43808.69	43587.74	44032.72
59.5	43404.55	43404.38	43625.01	43629.13	43849.52	43856.50	43184.00	43628.97	43404.22	43849.69	43625.17	44077.29
60.5	43439.04	43439.95	43663.07	43668.29	43891.16	43899.20	43216.01	43668.13	43439.78	43891.32	43663.23	44122.49
61.5	43474.16	43476.15	43701.78	43708.07	43933.41	43942.52	43248.65	43707.90	43475.99	43933.58	43701.95	44168.30
62.5	43509.95	43512.99	43741.13	43748.48	43976.30	43986.45	43281.95	43748.30	43512.82	43976.47	43741.29	44214.74
63.5	43546.37	43550.47	43781.10	43789.51	44019.82	44031.00	43315.89	43789.34	43550.30	44019.99	43781.27	44261.80
64.5	43583.44	43588.57	43821.72	43831.17	44063.96	44076.16	43350.47	43831.00	43588.40	44064.14	43821.89	44309.48
65.5	43621.16	43627.32	43862.98	43873.46	44108.73	44121.95	43385.70	43873.28	43627.15	44108.91	43863.16	44357.78
66.5	43659.52	43666.70	43904.87	43916.38	44154.14	44168.35	43421.57	43916.20	43666.52	44154.32	43905.05	44406.70
67.5	43698.53	43706.71	43947.40	43959.92	44200.18	44215.37	43458.09	43959.73	43706.54	44200.36	43947.58	44456.24
68.5	43738.18	43747.38	43990.57	44004.09	44246.83	44263.01	43495.25	44003.90	43747.19	44247.02	43990.76	44506.39
69.5	43778.48	43788.66	44034.38	44048.88	44294.12	44311.27	43533.06	44048.70	43788.48	44294.30	44034.56	44557.16
70.5	43819.43	43830.59	44078.82	44094.30	44342.03	44360.13	43571.52	44094.12	43830.40	44342.22	44079.00	44608.55
71.5	43861.02	43873.15	44123.89	44140.35	44390.56	44409.62	43610.62	44140.16	43872.96	44390.75	44124.09	44660.55
72.5	43903.26	43916.34	44169.59	44187.02	44439.72	44459.73	43650.36	44186.83	43916.15	44439.91	44169.79	44713.17
73.5	43946.13	43960.18	44215.94	44234.33	44489.51	44510.44	43690.75	44234.13	43959.98	44489.71	44216.14	44766.40
74.5	43989.65	44004.65	44262.92	44282.25	44539.91	44561.77	43731.79	44282.05	44004.45	44540.11	44263.13	44820.25
75.5	44033.82	44049.75	44310.53	44330.80	44590.94	44613.73	43773.48	44330.60	44049.55	44591.14	44310.73	44874.71
76.5	44078.63	44095.49	44358.78	44379.98	44642.60	44666.29	43815.80	44379.78	44095.29	44642.80	44358.98	44929.78
77.5	44124.08	44141.87	44407.66	44429.79	44694.87	44719.46	43858.79	44429.57	44141.66	44695.08	44407.87	44985.46
78.5	44170.18	44188.88	44457.16	44480.21	44747.77	44773.26	43902.41	44480.00	44188.67	44747.98	44457.38	45041.75
79.5	44216.91	44236.52	44507.31	44531.27	44801.29	44827.66	43946.68	44531.05	44236.31	44801.50	44507.52	45098.65

QUANTITY: FREQUENCIES
UNITS : Wavenumbers
BAND (A-X)5 - 6

	P1	P2	Q1	Q2	R1	R2	P12	R12	Q12	Q21	P21	R21
0.5			44743.82		44747.61					44747.62		44755.17
1.5	44739.13	44624.46	44742.89	44632.03	44750.48	44643.38	44620.68	44632.02	44624.46	44750.48	44742.89	44761.81
2.5	44735.08	44623.97	44742.61	44635.32	44753.99	44650.45	44616.40	44635.31	44623.96	44754.00	44742.61	44769.09
3.5	44731.66	44624.04	44742.96	44639.17	44758.14	44658.08	44612.69	44639.16	44624.04	44758.15	44742.97	44777.01
4.5	44728.90	44624.67	44743.96	44643.58	44762.93	44666.27	44609.53	44643.56	44624.66	44762.95	44743.98	44785.58
5.5	44726.78	44625.86	44745.61	44648.55	44768.38	44675.02	44606.94	44648.54	44625.84	44768.39	44745.63	44794.79
6.5	44725.30	44627.61	44747.91	44654.08	44774.46	44684.33	44604.90	44654.06	44627.59	44774.48	44747.92	44804.64
7.5	44724.46	44629.92	44750.84	44660.17	44781.18	44694.20	44603.44	44660.15	44629.91	44781.20	44750.86	44815.13
8.5	44724.27	44632.80	44754.41	44666.83	44788.55	44704.63	44602.54	44666.80	44632.77	44788.57	44754.44	44826.27
9.5	44724.72	44636.23	44758.64	44674.04	44796.55	44715.61	44602.19	44674.02	44636.21	44796.58	44758.66	44838.04
10.5	44725.82	44640.24	44763.50	44681.82	44805.19	44727.16	44602.42	44681.79	44640.21	44805.22	44763.52	44850.45
11.5	44727.55	44644.80	44768.99	44690.16	44814.47	44739.28	44603.21	44690.13	44644.77	44814.50	44769.02	44863.50
12.5	44729.93	44649.93	44775.13	44699.07	44824.39	44751.95	44604.57	44699.04	44649.90	44824.43	44775.16	44877.18
13.5	44732.94	44655.64	44781.91	44708.54	44834.95	44765.19	44606.49	44708.50	44655.60	44834.99	44781.95	44891.49
14.5	44736.60	44661.91	44789.32	44718.58	44846.14	44778.99	44608.99	44718.54	44661.87	44846.18	44789.36	44906.45
15.5	44740.89	44668.74	44797.37	44729.19	44857.97	44793.36	44612.06	44729.14	44668.70	44858.01	44797.41	44922.03
16.5	44745.82	44676.15	44806.06	44740.36	44870.43	44808.29	44615.71	44740.32	44676.11	44870.48	44806.10	44938.24
17.5	44751.38	44684.13	44815.38	44752.11	44883.52	44823.79	44619.92	44752.05	44684.08	44883.57	44815.43	44955.09
18.5	44757.59	44692.68	44825.33	44764.42	44897.23	44839.85	44624.71	44764.36	44692.63	44897.29	44825.38	44972.55
19.5	44764.41	44701.80	44835.92	44777.30	44911.59	44856.49	44630.08	44777.24	44701.75	44911.64	44835.97	44990.66
20.5	44771.88	44711.50	44847.13	44790.76	44926.56	44873.69	44636.02	44790.70	44711.45	44926.62	44847.19	45009.38
21.5	44779.98	44721.77	44858.98	44804.79	44942.16	44891.45	44642.54	44804.72	44721.72	44942.22	44859.04	45028.72
22.5	44788.71	44732.62	44871.45	44819.38	44958.39	44909.80	44649.65	44819.32	44732.56	44958.45	44871.51	45048.69
23.5	44798.07	44744.05	44884.55	44834.57	44975.25	44928.71	44657.32	44834.50	44743.98	44975.32	44884.62	45069.28
24.5	44808.07	44756.05	44898.29	44850.32	44992.72	44948.19	44665.59	44850.25	44755.99	44992.79	44898.35	45090.48
25.5	44818.69	44768.64	44912.64	44866.64	45010.82	44968.25	44674.44	44866.57	44768.57	45010.89	44912.71	45112.32
26.5	44829.93	44781.80	44927.62	44883.55	45029.54	44988.88	44683.87	44883.47	44781.73	45029.61	44927.69	45134.77
27.5	44841.80	44795.55	44943.22	44901.03	45048.88	45010.07	44693.88	44900.95	44795.47	45048.95	44943.30	45157.82
28.5	44854.30	44809.88	44959.45	44919.09	45068.83	45031.85	44704.48	44919.01	44809.80	45068.91	44959.52	45181.50
29.5	44867.43	44824.78	44976.29	44937.73	45089.40	45054.20	44715.67	44937.65	44824.70	45089.48	44976.37	45205.79
30.5	44881.18	44840.27	44993.76	44956.95	45110.59	45077.13	44727.45	44956.86	44840.20	45110.68	44993.84	45230.69
31.5	44895.55	44856.35	45011.84	44976.75	45132.39	45100.63	44739.82	44976.66	44856.27	45132.48	45011.93	45256.20
32.5	44910.54	44873.02	45030.55	44997.13	45154.81	45124.70	44752.77	44997.04	44872.93	45154.90	45030.64	45282.33
33.5	44926.16	44890.27	45049.88	45018.09	45177.84	45149.35	44766.32	45018.00	44890.18	45177.94	45049.97	45309.05
34.5	44942.41	44908.10	45069.82	45039.63	45201.49	45174.59	44780.46	45039.54	44908.01	45201.58	45069.91	45336.40
35.5	44959.26	44926.52	45090.38	45061.77	45225.74	45200.39	44795.19	45061.67	44926.43	45225.84	45090.47	45364.34
36.5	44976.74	44945.53	45111.55	45084.47	45250.60	45226.77	44810.51	45084.37	44945.44	45250.70	45111.65	45392.89
37.5	44994.84	44965.13	45133.33	45107.77	45276.08	45253.74	44826.43	45107.66	44965.03	45276.18	45133.43	45422.05
38.5	45013.55	44985.32	45155.73	45131.65	45302.16	45281.28	44842.93	45131.54	44985.21	45302.27	45155.84	45451.80
39.5	45032.89	45006.10	45178.75	45156.11	45328.85	45309.40	44860.05	45156.00	45005.99	45328.96	45178.86	45482.16
40.5	45052.84	45027.46	45202.38	45181.16	45356.14	45338.10	44877.75	45181.05	45027.36	45356.25	45202.48	45513.12
41.5	45073.41	45049.42	45226.61	45206.79	45384.04	45367.38	44896.05	45206.68	45049.31	45384.16	45226.72	45544.68
42.5	45094.59	45071.97	45251.46	45233.01	45412.55	45397.24	44914.94	45232.89	45071.86	45412.66	45251.57	45576.84
43.5	45116.40	45095.12	45276.92	45259.82	45441.66	45427.68	44934.44	45259.70	45095.00	45441.78	45277.04	45609.60
44.5	45138.81	45118.85	45302.99	45287.21	45471.37	45458.70	44954.53	45287.09	45118.73	45471.49	45303.11	45642.95
45.5	45161.84	45143.18	45329.66	45315.19	45501.68	45490.29	44975.22	45315.06	45143.05	45501.81	45329.79	45676.90
46.5	45185.49	45168.09	45356.95	45343.75	45532.60	45522.47	44996.51	45343.62	45167.97	45532.73	45357.07	45711.45
47.5	45209.75	45193.60	45384.84	45372.90	45564.12	45555.23	45018.40	45372.77	45193.48	45564.25	45384.96	45746.59
48.5	45234.62	45219.71	45413.34	45402.64	45596.23	45588.56	45040.89	45402.51	45219.58	45596.37	45413.47	45782.32
49.5	45260.11	45246.41	45442.45	45432.96	45628.95	45622.48	45063.98	45432.83	45246.27	45629.09	45442.58	45818.65
50.5	45286.20	45273.70	45472.16	45463.88	45662.27	45656.97	45087.67	45463.74	45273.57	45662.40	45472.29	45855.56
51.5	45312.91	45301.59	45502.47	45495.37	45696.18	45692.05	45111.96	45495.23	45301.45	45696.32	45502.61	45893.07
52.5	45340.23	45330.06	45533.39	45527.46	45730.69	45727.70	45136.86	45527.32	45329.92	45730.83	45533.53	45931.17
53.5	45368.16	45359.14	45564.92	45560.14	45765.79	45763.94	45162.36	45559.99	45359.00	45765.94	45565.06	45969.86
54.5	45396.70	45388.81	45597.04	45593.40	45801.49	45800.76	45188.46	45593.25	45388.66	45801.64	45597.19	46009.14
55.5	45425.85	45419.08	45629.78	45627.25	45837.79	45838.16	45215.16	45627.10	45418.93	45837.95	45629.93	46049.00
56.5	45455.61	45449.95	45663.12	45661.69	45874.68	45876.13	45242.46	45661.53	45449.79	45874.84	45663.27	46089.45

57.5	45485.98	45481.40	45697.05	45696.71	45912.16	45914.68	45270.38	45696.55	45481.24	45912.32	45697.21	46130.49
58.5	45516.96	45513.45	45731.59	45732.33	45950.25	45953.82	45298.88	45732.16	45513.29	45950.41	45731.74	46172.11
59.5	45548.55	45546.10	45766.73	45768.53	45988.91	45993.53	45328.00	45768.37	45545.94	45989.08	45766.89	46214.32
60.5	45580.75	45579.34	45802.47	45805.32	46028.18	46033.83	45357.72	45805.15	45579.18	46028.35	45802.63	46257.12
61.5	45613.55	45613.18	45838.80	45842.70	46068.04	46074.70	45388.05	45842.53	45613.02	46068.20	45838.97	46300.48
62.5	45646.97	45647.62	45875.75	45880.66	46108.48	46116.14	45418.98	45880.48	45647.45	46108.65	45875.91	46344.44
63.5	45680.99	45682.65	45913.28	45919.20	46149.51	46158.17	45450.52	45919.03	45682.48	46149.68	45913.45	46388.98
64.5	45715.62	45718.27	45951.42	45958.34	46191.14	46200.77	45482.65	45958.17	45718.09	46191.31	45951.59	46434.10
65.5	45750.85	45754.49	45990.15	45998.07	46233.35	46243.96	45515.39	45997.89	45754.32	46233.53	45990.33	46479.79
66.5	45786.70	45791.31	46029.48	46038.38	46276.16	46287.72	45548.74	46038.20	45791.13	46276.34	46029.66	46526.07
67.5	45823.14	45828.73	46069.41	46079.29	46319.54	46332.05	45582.70	46079.10	45828.55	46319.73	46069.59	46572.92
68.5	45860.20	45866.74	46109.94	46120.77	46363.52	46376.97	45617.26	46120.58	45866.55	46363.70	46110.13	46620.35

QUANTITY: FREQUENCIES
UNITS : Wavenumbers
BAND (A-X)4 - 7

	P1	P2	Q1	Q2	R1	R2	P12	R12	Q12	Q21	P21	R21
0.5			40825.70		40829.53					40829.53		40837.16
1.5	40821.06	40706.72	40824.86	40714.36	40832.52	40725.82	40702.89	40714.35	40706.71	40832.52	40824.86	40843.96
2.5	40817.13	40706.39	40824.73	40717.86	40836.23	40733.14	40698.75	40717.85	40706.39	40836.24	40824.74	40851.49
3.5	40813.91	40706.71	40825.33	40721.99	40840.66	40741.09	40695.23	40721.98	40706.70	40840.67	40825.34	40859.73
4.5	40811.42	40707.66	40826.64	40726.76	40845.80	40749.68	40692.36	40726.74	40707.64	40845.82	40826.66	40868.68
5.5	40809.64	40709.23	40828.67	40732.16	40851.66	40758.90	40690.13	40732.14	40709.22	40851.68	40828.69	40878.35
6.5	40808.58	40711.45	40831.42	40738.20	40858.24	40768.75	40688.52	40738.18	40711.44	40858.26	40831.43	40888.73
7.5	40808.24	40714.31	40834.88	40744.87	40865.53	40779.23	40687.55	40744.84	40714.29	40865.55	40834.90	40899.83
8.5	40808.61	40717.80	40839.06	40752.17	40873.54	40790.36	40687.23	40752.15	40717.77	40873.56	40839.09	40911.64
9.5	40809.70	40721.93	40843.96	40760.12	40882.26	40802.12	40687.54	40760.09	40721.91	40882.29	40843.98	40924.17
10.5	40811.51	40726.70	40849.57	40768.70	40891.69	40814.51	40688.49	40768.67	40726.67	40891.72	40849.59	40937.40
11.5	40814.03	40732.11	40855.89	40777.92	40901.83	40827.54	40690.09	40777.89	40732.07	40901.86	40855.92	40951.35
12.5	40817.26	40738.15	40862.92	40787.79	40912.69	40841.20	40692.32	40787.75	40738.12	40912.73	40862.95	40966.01
13.5	40821.21	40744.85	40870.67	40798.29	40924.25	40855.51	40695.20	40798.25	40744.81	40924.29	40870.71	40981.37
14.5	40825.87	40752.18	40879.13	40809.43	40936.52	40870.45	40698.73	40809.39	40752.14	40936.56	40879.16	40997.44
15.5	40831.23	40760.15	40888.29	40821.21	40949.51	40886.04	40702.90	40821.17	40760.11	40949.55	40888.33	41014.22
16.5	40837.32	40768.78	40898.17	40833.64	40963.20	40902.26	40707.72	40833.60	40768.73	40963.24	40898.21	41031.70
17.5	40844.11	40778.05	40908.76	40846.71	40977.59	40919.13	40713.19	40846.66	40778.00	40977.63	40908.80	41049.88
18.5	40851.61	40787.96	40920.05	40860.43	40992.68	40936.63	40719.30	40860.38	40787.91	40992.73	40920.09	41068.77
19.5	40859.81	40798.52	40932.04	40874.79	41008.48	40954.78	40726.07	40874.73	40798.47	41008.54	40932.09	41088.36
20.5	40868.73	40809.73	40944.75	40889.80	41024.98	40973.57	40733.48	40889.74	40809.68	41025.04	40944.80	41108.64
21.5	40878.35	40821.60	40958.15	40905.45	41042.18	40993.01	40741.56	40905.39	40821.54	41042.24	40958.21	41129.62
22.5	40888.68	40834.11	40972.26	40921.75	41060.08	41013.09	40750.28	40921.69	40834.04	41060.14	40972.32	41151.30
23.5	40899.70	40847.27	40987.07	40938.71	41078.68	41033.81	40759.66	40938.64	40847.20	41078.75	40987.13	41173.68
24.5	40911.44	40861.09	41002.58	40956.31	41097.98	41055.19	40769.70	40956.24	40861.02	41098.05	41002.64	41196.74
25.5	40923.88	40875.56	41018.79	40974.56	41117.97	41077.21	40780.40	40974.49	40875.49	41118.04	41018.86	41220.50
26.5	40937.01	40890.68	41035.70	40993.47	41138.66	41099.87	40791.75	40993.39	40890.61	41138.73	41035.77	41244.96
27.5	40950.85	40906.46	41053.30	41013.02	41160.03	41123.18	40803.77	41012.95	40906.39	41160.11	41053.38	41270.10
28.5	40965.39	40922.90	41071.60	41033.23	41182.11	41147.15	40816.44	41033.15	40922.82	41182.18	41071.68	41295.93
29.5	40980.63	40939.99	41090.61	41054.10	41204.87	41171.76	40829.77	41054.02	40939.91	41204.95	41090.68	41322.45
30.5	40996.56	40957.75	41110.30	41075.61	41228.32	41197.02	40843.77	41075.53	40957.67	41228.41	41110.38	41349.65
31.5	41013.20	40976.16	41130.69	41097.79	41252.47	41222.94	40858.43	41097.70	40976.07	41252.55	41130.77	41377.55
32.5	41030.53	40995.23	41151.77	41120.62	41277.30	41249.50	40873.75	41120.53	40995.14	41277.39	41151.86	41406.13
33.5	41048.56	41014.97	41173.54	41144.11	41302.82	41276.71	40889.75	41144.01	41014.88	41302.91	41173.63	41435.38
34.5	41067.29	41035.36	41196.01	41168.24	41329.02	41304.58	40906.41	41168.15	41035.27	41329.12	41196.10	41465.32
35.5	41086.70	41056.41	41219.16	41193.05	41355.92	41333.10	40923.73	41192.95	41056.32	41356.02	41219.26	41495.94
36.5	41106.82	41078.14	41243.01	41218.50	41383.49	41362.27	40941.73	41218.40	41078.04	41383.59	41243.11	41527.24
37.5	41127.63	41100.52	41267.54	41244.62	41411.75	41392.10	40960.39	41244.52	41100.42	41411.86	41267.64	41559.22
38.5	41149.13	41123.57	41292.77	41271.40	41440.70	41422.57	40979.72	41271.29	41123.46	41440.80	41292.87	41591.88
39.5	41171.32	41147.28	41318.68	41298.83	41470.32	41453.71	40999.72	41298.72	41147.18	41470.43	41318.79	41625.21
40.5	41194.21	41171.66	41345.28	41326.93	41500.63	41485.50	41020.39	41326.82	41171.55	41500.74	41345.39	41659.23
41.5	41217.78	41196.70	41372.56	41355.69	41531.62	41517.93	41041.74	41355.57	41196.59	41531.73	41372.67	41693.91
42.5	41242.05	41222.41	41400.54	41385.10	41563.28	41551.03	41063.75	41384.98	41222.30	41563.40	41400.65	41729.27
43.5	41267.02	41248.78	41429.19	41415.18	41595.63	41584.78	41086.45	41415.06	41248.66	41595.75	41429.30	41765.30
44.5	41292.66	41275.83	41458.53	41445.92	41628.65	41619.19	41109.80	41445.80	41275.71	41628.77	41458.65	41802.01
45.5	41319.00	41303.54	41488.55	41477.32	41662.35	41654.24	41133.85	41477.20	41303.41	41662.48	41488.68	41839.38
46.5	41346.03	41331.91	41519.26	41509.38	41696.73	41689.96	41158.55	41509.26	41331.79	41696.86	41519.39	41877.43
47.5	41373.75	41360.96	41550.65	41542.11	41731.79	41726.33	41183.94	41541.98	41360.84	41731.91	41550.78	41916.14
48.5	41402.16	41390.68	41582.73	41575.50	41767.52	41763.35	41210.00	41575.36	41390.55	41767.65	41582.86	41955.53
49.5	41431.25	41421.06	41615.48	41609.55	41803.92	41801.04	41236.74	41609.41	41420.93	41804.05	41615.61	41995.59
50.5	41461.03	41452.12	41648.91	41644.27	41841.00	41839.38	41264.16	41644.13	41451.98	41841.14	41649.05	42036.30
51.5	41491.50	41483.84	41683.04	41679.64	41878.75	41878.37	41292.25	41679.50	41483.71	41878.89	41683.17	42077.70
52.5	41522.66	41516.23	41717.83	41715.68	41917.18	41918.02	41321.02	41715.54	41516.09	41917.32	41717.97	42119.75
53.5	41554.50	41549.30	41753.30	41752.38	41956.27	41958.32	41350.46	41752.23	41549.16	41956.42	41753.45	42162.47
54.5	41587.03	41583.04	41789.46	41789.75	41996.04	41999.28	41380.59	41789.60	41582.89	41996.19	41789.61	42205.85
55.5	41620.24	41617.45	41826.30	41827.78	42036.48	42040.89	41411.39	41827.63	41617.30	42036.63	41826.45	42249.89
56.5	41654.14	41652.52	41863.81	41866.47	42077.59	42083.16	41442.88	41866.32	41652.37	42077.74	41863.96	42294.60

57.5	41688.73	41688.27	41902.00	41905.83	42119.37	42126.09	41475.04	41905.67	41688.11	42119.52	41902.16	42339.98
58.5	41724.00	41724.69	41940.87	41945.85	42161.82	42169.67	41507.88	41945.70	41724.53	42161.98	41941.02	42386.00
59.5	41759.96	41761.79	41980.41	41986.53	42204.93	42213.91	41541.40	41986.37	41761.63	42205.09	41980.58	42432.70
60.5	41796.60	41799.55	42020.63	42027.88	42248.72	42258.80	41575.60	42027.72	41799.38	42248.88	42020.80	42480.05
61.5	41833.92	41837.98	42061.54	42069.90	42293.17	42304.34	41610.48	42069.73	41837.82	42293.34	42061.70	42528.06
62.5	41871.93	41877.09	42103.11	42112.58	42338.29	42350.55	41646.05	42112.41	41876.92	42338.46	42103.28	42576.73
63.5	41910.63	41916.88	42145.36	42155.91	42384.08	42397.41	41682.29	42155.74	41916.70	42384.25	42145.53	42626.06
64.5	41950.00	41957.33	42188.28	42199.92	42430.53	42444.91	41719.22	42199.75	41957.16	42430.70	42188.45	42676.05
65.5	41990.06	41998.45	42231.88	42244.59	42477.64	42493.08	41756.83	42244.41	41998.28	42477.82	42232.06	42726.69
66.5	42030.81	42040.25	42276.16	42289.92	42525.43	42541.91	41795.12	42289.74	42040.07	42525.61	42276.34	42777.98
67.5	42072.23	42082.72	42321.10	42335.92	42573.88	42591.38	41834.09	42335.74	42082.54	42574.06	42321.28	42829.94
68.5	42114.34	42125.87	42366.73	42382.58	42622.99	42641.51	41873.74	42382.39	42125.69	42623.18	42366.91	42882.55
69.5	42157.13	42169.69	42413.02	42429.91	42672.77	42692.29	41914.09	42429.72	42169.50	42672.95	42413.21	42935.81
70.5	42200.60	42214.18	42459.99	42477.89	42723.20	42743.73	41955.10	42477.70	42213.99	42723.40	42460.18	42989.72
71.5	42244.76	42259.34	42507.63	42526.55	42774.30	42795.81	41996.81	42526.35	42259.16	42774.49	42507.82	43044.29
72.5	42289.60	42305.18	42555.94	42575.86	42826.06	42848.56	42039.20	42575.66	42304.98	42826.26	42556.13	43099.52
73.5	42335.11	42351.69	42604.92	42625.84	42878.49	42901.96	42082.27	42625.64	42351.50	42878.69	42605.12	43155.38
74.5	42381.31	42398.88	42654.58	42676.48	42931.57	42956.01	42126.02	42676.28	42398.68	42931.77	42654.78	43211.91
75.5	42428.20	42446.73	42704.91	42727.79	42985.32	43010.71	42170.46	42727.59	42446.53	42985.52	42705.11	43269.09
76.5	42475.75	42495.27	42755.91	42779.76	43039.73	43066.06	42215.58	42779.55	42495.06	43039.93	42756.11	43326.91
77.5	42524.00	42544.48	42807.57	42832.39	43094.79	43122.07	42261.39	42832.18	42544.27	43095.00	42807.78	43385.38
78.5	42572.92	42594.35	42859.91	42885.68	43150.52	43178.73	42307.88	42885.47	42594.14	43150.73	42860.12	43444.50
79.5	42622.52	42644.91	42912.92	42939.64	43206.90	43236.04	42355.05	42939.43	42644.70	43207.11	42913.13	43504.26

QUANTITY: FREQUENCIES
UNITS : Wavenumbers
BAND (A-X)5 - 7

	P1	P2	Q1	Q2	R1	R2	P12	R12	Q12	Q21	P21	R21
0.5			43035.67		43039.46					43039.47		43047.02
1.5	43031.04	42916.66	43034.79	42924.22	43042.38	42935.57	42912.87	42924.21	42916.65	43042.39	43034.80	43053.71
2.5	43027.07	42916.26	43034.59	42927.61	43045.98	42942.73	42908.69	42927.60	42916.25	43045.98	43034.60	43061.08
3.5	43023.77	42916.45	43035.08	42931.58	43050.25	42950.49	42905.10	42931.57	42916.45	43050.26	43035.09	43069.13
4.5	43021.17	42917.25	43036.23	42936.16	43055.20	42958.85	42902.11	42936.14	42917.23	43055.21	43036.25	43077.85
5.5	43019.23	42918.63	43038.07	42941.33	43060.83	42967.80	42899.71	42941.31	42918.62	43060.85	43038.09	43087.25
6.5	43017.98	42920.63	43040.59	42947.10	43067.14	42977.34	42897.92	42947.08	42920.61	43067.16	43040.61	43097.32
7.5	43017.41	42923.21	43043.79	42953.46	43074.12	42987.48	42896.73	42953.44	42923.19	43074.14	43043.80	43108.08
8.5	43017.52	42926.39	43047.66	42960.42	43081.79	42998.23	42896.13	42960.40	42926.37	43081.81	43047.68	43119.51
9.5	43018.30	42930.18	43052.21	42967.99	43090.13	43009.55	42896.13	42967.96	42930.16	43090.15	43052.23	43131.61
10.5	43019.76	42934.56	43057.43	42976.14	43099.13	43021.48	42896.74	42976.11	42934.54	43099.16	43057.46	43144.38
11.5	43021.89	42939.55	43063.33	42984.90	43108.81	43034.02	42897.95	42984.87	42939.52	43108.84	43063.36	43157.84
12.5	43024.70	42945.13	43069.91	42994.27	43119.17	43047.15	42899.77	42994.23	42945.10	43119.20	43069.94	43171.95
13.5	43028.19	42951.33	43077.16	43004.23	43130.20	43060.88	42902.18	43004.19	42951.29	43130.23	43077.19	43186.74
14.5	43032.35	42958.13	43085.07	43014.80	43141.89	43075.21	42905.21	43014.76	42958.09	43141.93	43085.11	43202.20
15.5	43037.18	42965.52	43093.66	43025.97	43154.26	43090.14	42908.84	43025.93	42965.48	43154.30	43093.70	43218.32
16.5	43042.69	42973.53	43102.93	43037.75	43167.30	43105.67	42913.09	43037.70	42973.49	43167.34	43102.97	43235.11
17.5	43048.86	42982.15	43112.86	43050.13	43180.99	43121.81	42917.94	43050.07	42982.10	43181.05	43112.91	43252.56
18.5	43055.71	42991.37	43123.45	43063.11	43195.36	43138.54	42923.41	43063.05	42991.32	43195.41	43123.51	43270.68
19.5	43063.22	43001.20	43134.72	43076.70	43210.39	43155.89	42929.48	43076.64	43001.15	43210.45	43134.78	43289.46
20.5	43071.41	43011.64	43146.66	43090.91	43226.09	43173.83	42936.16	43090.84	43011.59	43226.15	43146.71	43308.90
21.5	43080.26	43022.70	43159.26	43105.71	43242.44	43192.38	42943.47	43105.65	43022.64	43242.50	43159.32	43329.00
22.5	43089.78	43034.36	43172.52	43121.13	43259.46	43211.54	42951.39	43121.06	43034.30	43259.52	43172.58	43349.76
23.5	43099.96	43046.64	43186.44	43137.16	43277.14	43231.30	42959.92	43137.09	43046.58	43277.20	43186.50	43371.17
24.5	43110.81	43059.54	43201.03	43153.80	43295.47	43251.68	42969.07	43153.73	43059.48	43295.54	43201.10	43393.23
25.5	43122.33	43073.05	43216.28	43171.05	43314.46	43272.66	42978.85	43170.98	43072.98	43314.53	43216.35	43415.96
26.5	43134.50	43087.17	43232.19	43188.92	43334.11	43294.25	42989.24	43188.84	43087.10	43334.18	43232.26	43439.34
27.5	43147.34	43101.92	43248.76	43207.40	43354.41	43316.45	43000.25	43207.32	43101.84	43354.49	43248.83	43463.36
28.5	43160.84	43117.28	43265.98	43226.49	43375.37	43339.25	43011.89	43226.41	43117.20	43375.45	43266.06	43488.04
29.5	43175.00	43133.25	43283.87	43246.20	43396.98	43362.67	43024.15	43246.12	43133.18	43397.06	43283.95	43513.36
30.5	43189.83	43149.86	43302.41	43266.53	43419.23	43386.70	43037.03	43266.44	43149.77	43419.32	43302.49	43539.34
31.5	43205.30	43167.07	43321.60	43287.47	43442.15	43411.35	43050.54	43287.38	43166.99	43442.23	43321.69	43565.96
32.5	43221.45	43184.91	43341.45	43309.03	43465.71	43436.60	43064.67	43308.94	43184.83	43465.80	43341.54	43593.23
33.5	43238.24	43203.38	43361.95	43331.21	43489.92	43462.46	43079.43	43331.11	43203.29	43490.02	43362.04	43621.13
34.5	43255.70	43222.46	43383.11	43354.00	43514.78	43488.95	43094.82	43353.90	43222.37	43514.87	43383.20	43649.69
35.5	43273.80	43242.17	43404.92	43377.41	43540.29	43516.04	43110.84	43377.32	43242.07	43540.38	43405.01	43678.88
36.5	43292.57	43262.51	43427.38	43401.45	43566.43	43543.75	43127.48	43401.34	43262.41	43566.54	43427.48	43708.72
37.5	43311.99	43283.46	43450.48	43426.10	43593.23	43572.07	43144.76	43426.00	43283.36	43593.33	43450.59	43739.20
38.5	43332.07	43305.04	43474.25	43451.38	43620.68	43601.01	43162.66	43451.27	43304.94	43620.78	43474.35	43770.31
39.5	43352.80	43327.26	43498.66	43477.27	43648.75	43630.56	43181.20	43477.16	43327.15	43648.86	43498.76	43802.06
40.5	43374.18	43350.09	43523.71	43503.78	43677.48	43660.73	43200.37	43503.67	43349.98	43677.59	43523.82	43834.46
41.5	43396.21	43373.55	43549.41	43530.92	43706.85	43691.51	43220.17	43530.80	43373.44	43706.96	43549.52	43867.48
42.5	43418.90	43397.64	43575.77	43558.68	43736.86	43722.91	43240.61	43558.56	43397.52	43736.97	43575.88	43901.14
43.5	43442.24	43422.36	43602.76	43587.05	43767.51	43754.92	43261.68	43586.94	43422.24	43767.63	43602.88	43935.44
44.5	43466.23	43447.70	43630.41	43616.06	43798.79	43787.55	43283.38	43615.94	43447.59	43798.91	43630.52	43970.37
45.5	43490.88	43473.68	43658.70	43645.69	43830.72	43820.79	43305.72	43645.56	43473.55	43830.84	43658.82	44005.93
46.5	43516.17	43500.28	43687.63	43675.93	43863.28	43854.66	43328.70	43675.80	43500.16	43863.41	43687.75	44042.13
47.5	43542.11	43527.51	43717.20	43706.80	43896.48	43889.13	43352.30	43706.68	43527.38	43896.61	43717.32	44078.95
48.5	43568.70	43555.38	43747.42	43738.30	43930.32	43924.23	43376.55	43738.17	43555.24	43930.45	43747.55	44116.40
49.5	43595.95	43583.87	43778.28	43770.42	43964.79	43959.94	43401.44	43770.29	43583.73	43964.92	43778.41	44154.48
50.5	43623.84	43612.99	43809.79	43803.16	43999.90	43996.26	43426.96	43803.03	43612.86	44000.04	43809.92	44193.20
51.5	43652.37	43642.74	43841.93	43836.53	44035.64	44033.21	43453.12	43836.39	43642.61	44035.78	43842.07	44232.54
52.5	43681.56	43673.13	43874.72	43870.52	44072.02	44070.77	43479.92	43870.38	43672.98	44072.16	43874.86	44272.50
53.5	43711.39	43704.14	43908.15	43905.13	44109.02	44108.94	43507.35	43904.98	43704.00	44109.17	43908.29	44313.09
54.5	43741.87	43735.79	43942.21	43940.37	44146.66	44147.73	43535.43	43940.22	43735.64	44146.81	43942.36	44354.30
55.5	43772.99	43768.06	43976.92	43976.24	44184.94	44187.14	43564.14	43976.09	43767.91	44185.09	43977.07	44396.14
56.5	43804.77	43800.98	44012.27	44012.72	44223.84	44227.16	43593.50	44012.57	43800.83	44223.99	44012.42	44438.60

57.5	43837.19	43834.52	44048.25	44049.83	44263.37	44267.80	43623.49	44049.67	43834.36	44263.52	44048.41	44481.69
58.5	43870.25	43868.69	44084.87	44087.57	44303.53	44309.06	43654.13	44087.41	43868.54	44303.70	44085.03	44525.40
59.5	43903.96	43903.50	44122.13	44125.93	44344.32	44350.93	43685.40	44125.77	43903.34	44344.49	44122.29	44569.73
60.5	43938.32	43938.94	44160.03	44164.91	44385.75	44393.42	43717.32	44164.75	43938.77	44385.91	44160.19	44614.68
61.5	43973.32	43975.01	44198.56	44204.52	44427.80	44436.52	43749.88	44204.36	43974.84	44427.96	44198.73	44660.24
62.5	44008.96	44011.72	44237.73	44244.76	44470.47	44480.24	43783.08	44244.59	44011.55	44470.64	44237.90	44706.43
63.5	44045.25	44049.05	44277.54	44285.61	44513.77	44524.58	43816.92	44285.44	44048.88	44513.95	44277.71	44753.23
64.5	44082.18	44087.02	44317.98	44327.09	44557.70	44569.53	43851.40	44326.92	44086.85	44557.88	44318.15	44800.66
65.5	44119.76	44125.63	44359.05	44369.20	44602.26	44615.09	43886.52	44369.02	44125.45	44602.44	44359.23	44848.70
66.5	44157.98	44164.87	44400.77	44411.93	44647.44	44661.27	43922.29	44411.75	44164.69	44647.62	44400.95	44897.35
67.5	44196.84	44204.73	44443.12	44455.29	44693.25	44708.06	43958.70	44455.11	44204.55	44693.43	44443.30	44946.63
68.5	44236.35	44245.23	44486.09	44499.27	44739.67	44755.47	43995.76	44499.08	44245.05	44739.86	44486.28	44996.51

QUANTITY: FREQUENCIES
UNITS : Wavenumbers
BAND (A-X)5 - 8

	P1	P2	Q1	Q2	R1	R2	P12	R12	Q12	Q21	P21	R21
0.5			41355.45		41359.24					41359.25		41366.80
1.5	41350.86	41236.80	41354.62	41244.36	41362.21	41255.71	41233.01	41244.36	41236.79	41362.21	41354.63	41373.54
2.5	41346.98	41236.49	41354.51	41247.84	41365.89	41262.96	41228.92	41247.83	41236.48	41365.90	41354.52	41380.99
3.5	41343.81	41236.81	41355.12	41251.94	41370.29	41270.85	41225.46	41251.93	41236.80	41370.30	41355.13	41389.16
4.5	41341.36	41237.77	41356.43	41256.68	41375.39	41279.37	41222.63	41256.66	41237.76	41375.41	41356.44	41398.04
5.5	41339.62	41239.36	41358.46	41262.05	41381.22	41288.52	41220.44	41262.04	41239.34	41381.23	41358.47	41407.64
6.5	41338.59	41241.58	41361.20	41268.06	41387.76	41298.30	41218.88	41268.04	41241.57	41387.77	41361.22	41417.94
7.5	41338.29	41244.45	41364.66	41274.70	41395.00	41308.72	41217.96	41274.67	41244.43	41395.02	41364.68	41428.96
8.5	41338.69	41247.94	41368.83	41281.97	41402.96	41319.77	41217.68	41281.95	41247.91	41402.98	41368.85	41440.68
9.5	41339.80	41252.07	41373.71	41289.88	41411.63	41331.45	41218.02	41289.85	41252.05	41411.66	41373.73	41453.12
10.5	41341.63	41256.84	41379.30	41298.42	41421.00	41343.77	41219.02	41298.39	41256.81	41421.03	41379.33	41466.25
11.5	41344.17	41262.25	41385.61	41307.60	41431.09	41356.72	41220.65	41307.57	41262.21	41431.12	41385.64	41480.11
12.5	41347.41	41268.29	41392.62	41317.42	41441.88	41370.30	41222.92	41317.39	41268.26	41441.92	41392.65	41494.66
13.5	41351.37	41274.98	41400.34	41327.88	41453.38	41384.52	41225.83	41327.84	41274.94	41453.42	41400.38	41509.92
14.5	41356.04	41282.30	41408.76	41338.97	41465.59	41399.38	41229.39	41338.93	41282.26	41465.63	41408.80	41525.89
15.5	41361.41	41290.27	41417.90	41350.71	41478.50	41414.88	41233.59	41350.67	41290.23	41478.54	41417.94	41542.55
16.5	41367.50	41298.88	41427.74	41363.09	41492.11	41431.02	41238.43	41363.04	41298.83	41492.16	41427.78	41559.92
17.5	41374.29	41308.13	41438.28	41376.11	41506.42	41447.79	41243.92	41376.05	41308.09	41506.47	41438.33	41577.99
18.5	41381.79	41318.03	41449.53	41389.77	41521.44	41465.20	41250.06	41389.71	41317.98	41521.49	41449.58	41596.75
19.5	41389.98	41328.57	41461.48	41404.07	41537.15	41483.26	41256.84	41404.01	41328.52	41537.20	41461.54	41616.22
20.5	41398.89	41339.76	41474.13	41419.02	41553.57	41501.95	41264.28	41418.96	41339.70	41553.63	41474.19	41636.38
21.5	41408.49	41351.60	41487.49	41434.61	41570.67	41521.28	41272.37	41434.55	41351.54	41570.73	41487.55	41657.23
22.5	41418.80	41364.08	41501.54	41450.84	41588.48	41541.26	41281.11	41450.78	41364.02	41588.54	41501.60	41678.78
23.5	41429.81	41377.22	41516.29	41467.73	41606.99	41561.88	41290.49	41467.67	41377.16	41607.05	41516.35	41701.02
24.5	41441.52	41391.01	41531.75	41485.27	41626.18	41583.14	41300.54	41485.20	41390.94	41626.25	41531.81	41723.95
25.5	41453.94	41405.45	41547.89	41503.45	41646.07	41605.05	41311.25	41503.38	41405.38	41646.14	41547.96	41747.57
26.5	41467.05	41420.53	41564.73	41522.28	41666.65	41627.61	41322.60	41522.20	41420.46	41666.73	41564.80	41771.88
27.5	41480.85	41436.28	41582.27	41541.76	41687.92	41650.80	41334.61	41541.68	41436.20	41688.00	41582.34	41796.87
28.5	41495.36	41452.68	41600.50	41561.89	41709.88	41674.65	41347.29	41561.81	41452.60	41709.96	41600.58	41822.55
29.5	41510.56	41469.73	41619.42	41582.67	41732.54	41699.14	41360.62	41582.59	41469.65	41732.62	41619.50	41848.92
30.5	41526.46	41487.44	41639.04	41604.11	41755.87	41724.29	41374.61	41604.02	41487.36	41755.95	41639.12	41875.97
31.5	41543.05	41505.80	41659.34	41626.20	41779.89	41750.07	41389.27	41626.11	41505.71	41779.98	41659.43	41903.70
32.5	41560.34	41524.82	41680.34	41648.94	41804.61	41776.51	41404.58	41648.85	41524.74	41804.70	41680.43	41932.12
33.5	41578.32	41544.51	41702.03	41672.33	41830.00	41803.59	41420.56	41672.24	41544.41	41830.09	41702.12	41961.21
34.5	41596.99	41564.85	41724.41	41696.38	41856.07	41831.33	41437.20	41696.28	41564.75	41856.17	41724.50	41990.98
35.5	41616.36	41585.84	41747.47	41721.09	41882.84	41859.71	41454.51	41720.99	41585.75	41882.94	41747.56	42021.43
36.5	41636.41	41607.51	41771.22	41746.45	41910.28	41888.75	41472.48	41746.34	41607.41	41910.38	41771.32	42052.56
37.5	41657.16	41629.83	41795.66	41772.46	41938.41	41918.44	41491.12	41772.36	41629.73	41938.51	41795.76	42084.37
38.5	41678.60	41652.81	41820.78	41799.14	41967.21	41948.77	41510.42	41799.03	41652.71	41967.32	41820.88	42116.84
39.5	41700.73	41676.46	41846.59	41826.47	41996.69	41979.76	41530.40	41826.36	41676.35	41996.80	41846.70	42150.00
40.5	41723.55	41700.76	41873.08	41854.45	42026.85	42011.40	41551.04	41854.34	41700.65	42026.96	41873.19	42183.83
41.5	41747.06	41725.73	41900.26	41883.09	42057.70	42043.69	41572.35	41882.98	41725.62	42057.80	41900.37	42218.33
42.5	41771.26	41751.37	41928.12	41912.40	42089.21	42076.63	41594.33	41912.29	41751.25	42089.33	41928.23	42253.50
43.5	41796.14	41777.66	41956.66	41942.36	42121.41	42110.23	41616.98	41942.24	41777.55	42121.52	41956.78	42289.34
44.5	41821.71	41804.63	41985.88	41972.98	42154.27	42144.48	41640.30	41972.86	41804.51	42154.39	41986.00	42325.85
45.5	41847.98	41832.26	42015.79	42004.27	42187.81	42179.37	41664.30	42004.14	41832.13	42187.94	42015.91	42363.02
46.5	41874.92	41860.55	42046.38	42036.20	42222.03	42214.93	41688.97	42036.08	41860.43	42222.16	42046.50	42400.88
47.5	41902.55	41889.51	42077.64	42068.80	42256.92	42251.13	41714.30	42068.67	41889.38	42257.05	42077.77	42439.39
48.5	41930.87	41919.13	42109.59	42102.06	42292.48	42287.98	41740.31	42101.93	41919.01	42292.62	42109.71	42478.57
49.5	41959.88	41949.43	42142.21	42135.98	42328.72	42325.50	41767.00	42135.85	41949.30	42328.86	42142.34	42518.41
50.5	41989.56	41980.39	42175.52	42170.56	42365.63	42363.66	41794.36	42170.42	41980.25	42365.77	42175.65	42558.92
51.5	42019.94	42012.02	42209.50	42205.80	42403.20	42402.48	41822.39	42205.66	42011.88	42403.34	42209.63	42600.10
52.5	42051.00	42044.30	42244.15	42241.70	42441.45	42441.95	41851.10	42241.55	42044.16	42441.60	42244.29	42641.93
53.5	42082.73	42077.27	42279.49	42278.26	42480.37	42482.07	41880.48	42278.11	42077.13	42480.52	42279.63	42684.43
54.5	42115.16	42110.90	42315.50	42315.48	42519.95	42522.85	41910.54	42315.34	42110.75	42520.10	42315.65	42727.60
55.5	42148.27	42145.20	42352.20	42353.37	42560.21	42564.28	41941.27	42353.22	42145.05	42560.37	42352.34	42771.42
56.5	42182.06	42180.17	42389.56	42391.91	42601.13	42606.36	41972.69	42391.76	42180.02	42601.29	42389.71	42815.90

57.5	42216.54	42215.80	42427.60	42431.12	42642.72	42649.09	42004.78	42430.96	42215.65	42642.88	42427.76	42861.04
58.5	42251.70	42252.11	42466.31	42470.98	42684.98	42692.48	42037.54	42470.82	42251.95	42685.14	42466.47	42906.84
59.5	42287.54	42289.09	42505.71	42511.52	42727.90	42736.52	42070.98	42511.35	42288.93	42728.06	42505.87	42953.30
60.5	42324.06	42326.73	42545.77	42552.70	42771.49	42781.21	42105.11	42552.54	42326.57	42771.65	42545.93	43000.42
61.5	42361.26	42365.05	42586.51	42594.55	42815.74	42826.56	42139.91	42594.39	42364.88	42815.91	42586.67	43048.19
62.5	42399.15	42404.03	42627.92	42637.07	42860.66	42872.55	42175.39	42636.90	42403.86	42860.83	42628.09	43096.61
63.5	42437.72	42443.69	42670.00	42680.24	42906.24	42919.21	42211.55	42680.07	42443.52	42906.41	42670.18	43145.70
64.5	42476.96	42484.01	42712.76	42724.08	42952.48	42966.52	42248.38	42723.90	42483.84	42952.66	42712.93	43195.44
65.5	42516.89	42525.00	42756.19	42768.58	42999.39	43014.47	42285.90	42768.40	42524.83	42999.57	42756.37	43245.83
66.5	42557.51	42566.67	42800.29	42813.73	43046.97	43063.08	42324.09	42813.55	42566.49	43047.15	42800.47	43296.88
67.5	42598.80	42609.00	42845.06	42859.55	43095.20	43112.33	42362.97	42859.38	42608.82	43095.38	42845.24	43348.57
68.5	42640.77	42652.01	42890.51	42906.04	43144.09	43162.24	42402.53	42905.85	42651.83	43144.28	42890.70	43400.92